Theoretical study of electronic absorption spectra and photodissociation dynamics of atmospherically relevant molecules

A thesis

submitted in fulfilment

of the requirements for the degree

of

Doctor of Philosophy in Chemistry

at

The University of Waikato

by

SARA FARAHANI

THE UNIVERSITY OF
WAIKATO
Te Whare Wānanga o Waikato

2019

Abstract

The absorption of solar radiation by atmospheric species and the corresponding photoinduced processes, define the chemistry of a planet's atmosphere. While many of these photoinduced processes and their effects are well- known, even in Earth's atmosphere there are gaps in our understanding. The focus of this thesis is the theoretical study of the absorption of sunlight by some important atmospheric species where no or minimal experimental results are available. We simulate electronic absorption spectra of atmospherically relevant sulfur-containing molecules, including sulfuric acid, which is present in Earths' atmosphere and OSSO, which was recently identified in the atmosphere of Venus. We also simulate electronic absorption spectra for a series of N_2O complexes thought to be present in Earth's atmosphere, namely Ar-N_2O, N_2O-N_2, O_2-N_2O and H_2O-N_2O. We consider how complexation affects the absorption cross section of N_2O monomer in these complexes and also undertake photodissociation dynamics simulations for the H_2O-N_2O complex. Where possible, we compare and validate our theoretical results with experiment, and in the absence of experimental data, we suggest that our results may be of use to the atmospheric modeling community.

Acknowledgments

Firstly, I would like to express my special appreciation and thanks to my supervisor Associate Professor Joseph Lane for his continuous support of my PhD study, for his patience, motivation, and knowledge. Jo, thank you for providing me an opportunity to complete my PhD thesis. Your suggestions, comments and guidance encouraged me to learn more day by day.

It has been an honor to work on some parts of my PhD study in collaboration with Professor Henrik Kjaegaard and his PhD student, Benjamin Normann Frandsen, from the University of Copenhagen. Henrik and Benjamin, thank you for all the valuable help and information you provided me on the OSSO project. The information and calculations kindly provided, are used in chapter 4 of this thesis.

My grateful thanks are also extended to Professor Scott Kable and his PhD student, Kin Long Kelvin Lee, from the University of New South Wales for providing experimental results of absorption spectra of N_2O and two of its complexes. These results are used in chapter 5 of this thesis.

I am grateful to the Royal Society of New Zealand for a Marsden financial support of my research study. I acknowledge the University of Waikato supercomputer which was extensively used in this work. I also acknowledge the New Zealand eScience Infrastructure (NeSI) for providing me access to this facility.

I would also like to thank all the lovely staff and members of the school of science who are always supportive and ready to help.

Last but not least, I would like to thank my beloved husband who was always my support during my PhD study. Farshid, thanks for your patience, love and support.

Publications

S. Farahani, B. N. Frandsen, H. G. Kjaergaard, and Lane, Joseph R., "Simulated Electronic Absorption Spectra of Sulfur-Containing Molecules Present in Earth's Atmosphere", Journal of Physical Chemistry A, **123**, 6605-6617 (2019).

Contents

List of Figures

List of Tables

List of Abbreviations

ADC(2)	Second order algebraic diagrammatic construction
BO	Born-Oppenheimer
CASSCF	complete active space self-consistent field
CASPT2	Complete active space Møller- Plesset perturbation theory
CBS	Complete basis set
CC	Coupled cluster
CCS	Coupled cluster including single excitations
CCSD	Coupled cluster including single and double excitations
CCSD(T)	Coupled cluster including single, double and perturbative triple excitations
CC2	Coupled cluster including single and perturbative iterative double excitations
CC3	Coupled cluster including single, double and perturbative iterative triple excitations
CFC-11	Trichlorofluoromethane
CFC-12	Dichlorodifluoromethane
CI	Configuration interaction
CISD	Configuration interaction singles and doubles
CN	Condensation nuclei
DFT	Density functional theory
f	Oscillator strength
EOM-CCSD	Equation of motion coupled cluster including single and double excitations
FC	Franck-Condon
FCI	Full configuration interaction
GWP	global warming potential
HF	Hartree-Fock
HWHM	Half width at half maximum
LR	Linear response
MCSCF	Multiconfigurational self-consistent field
MO	Molecular orbital
MPPT	Møller- Plesset perturbation theory
MP2	Møller-Plesset perturbation theory of the second order
MP3	Møller-Plesset perturbation theory of the third order
MP4	Møller-Plesset perturbation theory of the forth order
MRCI	Multireference
ODP	Ozone depleting potential
ODS	Ozone depleting substance
RAS	Restricted active space
RF	Radiative forcing
RI-CC2	Resolution of the identity second order approximate coupled cluster
SR	Single reference
SCF	self-consistent field
TDDFT	Time dependent density functional theory
TSH	Transition surface hopping
UV	Ultraviolet

Chapter 1

Introduction

The chemistry of Earth's atmosphere is driven by sunlight. Absorbed photons break molecules apart to produce reactive radicals that initiate most of the chemical reactions that occur in the Earth's oxidizing atmosphere. These reactions and how light is absorbed by the atmospheric constituents, not only define atmospheric chemistry but also affect its temperature profile and therefore, define the district layers of the atmosphere, including the troposphere, stratosphere, mesosphere and thermosphere from low to high altitude, respectively [1].

The interaction of light and the atmospheric species drives all the vital atmospheric phenomena that we know, such as the greenhouse effect and the formation and depletion of ozone. The Earth's atmosphere is largely transparent to visible light. This light when absorbed and re-emitted back to space in the infrared region, is then absorbed by atmospheric molecules. This so-called greenhouse gas effect, has stabilized the Earth's climate. Another example of the interaction of light with the molecules in Earth's atmosphere, is the stratosphere ozone layer. Ozone is naturally formed through photochemical reactions where oxygen molecules are broken apart by ab-

sorbing light and then, these reactive atomic oxygens react with available oxygen molecules to produce ozone. The formation of ozone is balanced by its deconstruction through absorbing light and reacting with stratospheric species. The ozone layer protects life on Earth by absorbing the light of hazardous shorter wavelengths.

1.1 Composition of the Earth's atmosphere

The main constituents of the Earth's atmosphere are N_2 (78%), O_2 (21%) and Ar (1%). With a variable concentration up to 3%, water vapour is the next most abundant atmospheric constituent. All the other atmospheric species are referred to as trace gases with lower concentrations, typically much less than 1 ppm, compared to concentration of these main species. Although existing in small amounts, trace gases can play vital roles in the chemistry and evolution of the atmosphere, including absorbing light. For example, the mixing ratio of ozone at its peak concentration is not more than 12 ppm [2].

The increase in the concentration of greenhouse gases and the lowering of the ozone concentration in Antarctica, are two examples of how trace gases have changed in recent history. Figure 1.1 shows the change in the concentration of some of major greenhouse gases, that are responsible for radiative forcing (RF), over a 40-year period of time since 1975 [3].

Some trace gases are uniformly distributed, while others are only found at distinct altitudes. This may be due to either the production of a trace gas e.g. that forms only at high altitude by absorption of high energy photons, or perhaps because the trace gas is very reactive, being consumed in the lower troposphere.

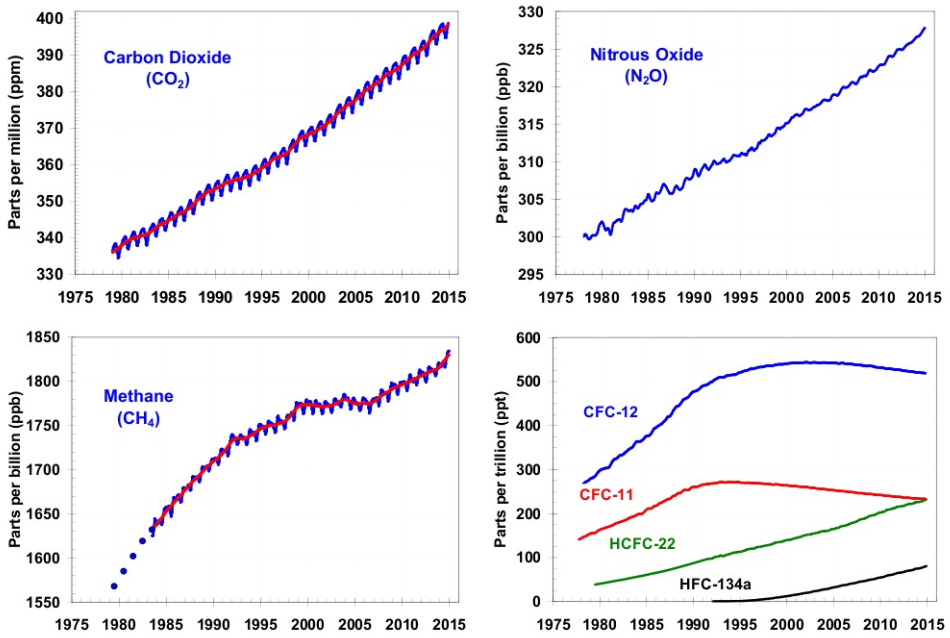

Figure 1.1: Concentration of the main greenhouse gases from 1975 to 2015 from NOAA Earth system research laboratory. [3]

1.2 Solar radiation and light absorption

The Sun radiates wavelengths over the entire electromagnetic spectrum from low frequency to Cosmic Rays. As light travels through the atmosphere, its wavelength distribution and intensity are attenuated [2]. Figure 1.2 shows the solar actinic flux (photons cm^{-2} s^{-1} nm^{-1}) in the visible and UV regions at different altitudes [4]. This attenuation is due to radiation scattering and also radiation absorption by atmospheric species. In higher altitudes, the radiation below 300 nm is absorbed by atomic and molecular oxygen and only radiation with wavelengths longer than this can reach the Earth and are available for tropospheric photochemical reactions [2].

About 30% of the Sun's light is reflected back to the atmosphere by the Earth's surface. Some of the trace gases in the atmosphere can capture and

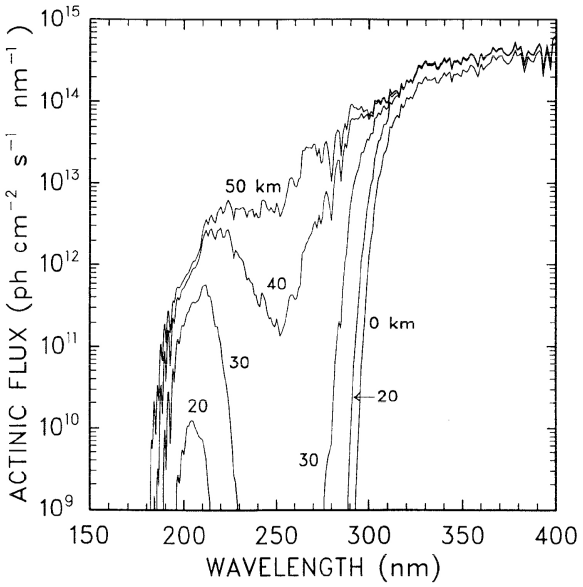

Figure 1.2: Solar actinic flux at different altitudes from DeMore *et al.* [5].

hold this radiated energy that keeps the surface of the Earth warm. Without these greenhouse gases, most radiated heat would be lost into space and the surface of the Earth would be much cooler. This natural phenomenon which acts like a blanket around the Earth, is essential for life and is referred to as the greenhouse effect. Increasing emissions of greenhouse gases due to human activities is leading to trap more of the energy radiated from the Earth and as a result, to the net global warming.

When solar radiation is absorbed by an atmospheric species, it can be electronically excited. The electronically excited molecule may go through one of the possible scenarios [2]:

absorption	$A + hv \rightarrow A^*$
dissociation	$A^* \rightarrow B_1 + B_2$
direct reaction	$A^* + B \rightarrow C_1 + C_2$
fluorescence	$A^* \rightarrow A + hv$
collisional deactivation	$A^* + M \rightarrow A + M$
ionization	$A^* \rightarrow A^+ + e$

The quantum yield of each of the processes above is calculated as the ratio of the number of excited molecules that undergo a specific process to the number of photons absorbed. The sum of the quantum yields of all the possible processes is equal to one. Quantum yield, $\Phi(\lambda)$, is used in equation 1.1 to calculate the photodissociation rate constant, J, where $I(\lambda)$ is the flux of photons of a given wavelength and $\sigma(\lambda)$ is the absorption cross-section, of a given wavelength.

$$J = \int I(\lambda)\Phi(\lambda)\sigma(\lambda)d\lambda \tag{1.1}$$

Background information about the trace gases that are studied in this thesis are described in the following sections.

1.3 Sulfur-containing molecules

Although having a concentration of less than 1 ppm in the Earth's atmosphere, sulfur-containing molecules strongly influence atmospheric chemistry and climate. Atmospheric sulfur molecules have both natural and anthropogenic sources. The majority of sulfur molecules are initially emitted to the atmosphere in the form of sulfur oxides, such as sulfur dioxide (SO_2), sulfur

trioxide (SO_3) and sulfuric acid (H_2SO_4) [6,7]. The primary natural sources of sulfur-containing molecules to Earth's atmosphere are volcanic activity (hydrogen sulfide, H_2S, and SO_2), marine microorganisms (dimethyl sulfide, DMS) and decomposition of organic matter (H_2S). The main anthropogenic source of the sulfur-containing molecules to Earth's atmosphere is combustion of fossil fuels, which is primarily in the form of SO_x molecules. Some of the other main sulfur-containing molecules in the atmosphere are carbon disulfide (CS_2) and carbonyl sulfide (OCS) [2].

Sulfur-containing molecules with lower oxidation numbers are chemically reactive and are oxidized rapidly in Earth's atmosphere, which gives them a short atmospheric lifetime. In general sulfur-containing molecules with higher oxidation numbers are of higher water solubility [2]. In the Earth's atmosphere, SO_2 has the highest concentration with SO_3 and H_2SO_4 being the second and third most abundant sulfur molecules [8]. Among the other atmospheric trace sulfur molecules such as H_2S, CS_2 and OCS, only OCS with a lifetime of 6 years can reach the stratosphere, where it is eventually oxidized to SO_2 and H_2SO_4 and incorporated into sulfate aerosol [2].

Sulfuric acid is found in different forms depending on altitude. In lower altitudes (about 15 to 35 km) and where water exists, H_2SO_4 is found in the form of sulfate aerosol, and in higher altitudes (above 35 km) it exists mostly in the gas phase [9]. Sulfur-containing molecules and their important role in forming aerosol and the condensation nuclei (CN) layer have been the subject of many atmospheric studies [10–13]. In the Earth's atmosphere, heterogeneous chemical reactions, found to be responsible for ozone layer depletion in polar regions in spring time, happen on the surfaces of aerosols [10, 13]. These particles can also scatter sunlight and affect the Earth's climate [10].

A significant enhancement is observed in the aerosol layer in the polar springtime, which is resulted from photodissociation of H_2SO_4 [10, 12, 13]. This photodissociation was first thought to happen by absorption of photons in the UV region. Later, Vaida *et al.* [10], on the basis of previous studies by Grim *et al.* [14, 15] suggested that photodissociation of H_2SO_4 occurs by absorbing photons in the visible region of energy via an OH-stretching overtone mechanism through an overtone photodissociation reaction.

The absorption spectra of most of the atmospherically-important sulfur-containing molecules are well-known [16–22]. However, despite the crucial role of H_2SO_4 in the Earth's atmosphere, its experimental spectrum is not yet available due to some inherent technical challenges. All of the previous experimental attempts to record the electronic absorption spectrum of H_2SO_4 have only led to some upper limits [9, 17] of the absorption cross section. There have been several theoretical studies of the electronic excited states of H_2SO_4, but most of these were undertaken using low level methods [17, 23, 24]. In the most recent theoretical study, Lane *et al.* [25], applied a hierarchy of coupled cluster response functions and augmented correlation basis sets to calculate electronic transitions of H_2SO_4 [26]. These calculated electronic transitions were empirically convoluted using different Gaussian half width at half maximum (HWHM) values to generate the absorption spectrum [25]. This empirically convoluted spectrum was in general agreement with the previously reported experimental upper limits and confirmed the contribution of Lyman-α photons in photodissociation of H_2SO_4 [9, 10, 17, 25].

Sulfur-containing molecules are also abundant in the atmosphere of other planets such as Venus [27–33]. Absorption spectra of the atmosphere of Venus showed strong absorption in the 320 to 400 nm region [34, 35]. Com-

paring the spectra recorded at day and night time indicated that there was an unknown absorber with a short lifetime. This absorption, for which many possible molecules have been suggested [35–44], was found to be correlated with the concentration of SO_2 [45–47]. The concentration of sulfur monoxide (SO) is high in the atmosphere of Venus, which means that molecules with equal S+O content, e.g. S_2O_2 and SO dimer, may also exist. The chemical pathways of sulfur molecules in the atmosphere of Venus are shown in Figure 1.3. Some computational studies have suggested that S_2O_2 isomers can exist in the Venusian atmosphere [48–52]. In 2012, Kransnopolsky reported the trigonal S_2O_2 as the lowest energy conformer of S_2O_2 that could be formed in the atmosphere of Venus [53]. Recently, Frandsen *et al.* suggested that the lowest energy conformers of $(SO)_2$ are *cis* and *trans*-OSSO [54]. They also suggested that these two conformers could be the unknown absorber in the 320 to 400 nm region of the Venus' absorption spectra [54]. Frandsen *et al.* proposed that the two OSSO conformers act as sulfur oxide reservoir at night time and are photodissocited by absorbing light during day time. However, these OSSO conformers do not have any experimental spectra yet. It follows that an accurate *ab initio* cross section of these two species could help future experimental investigation and identification of OSSO.

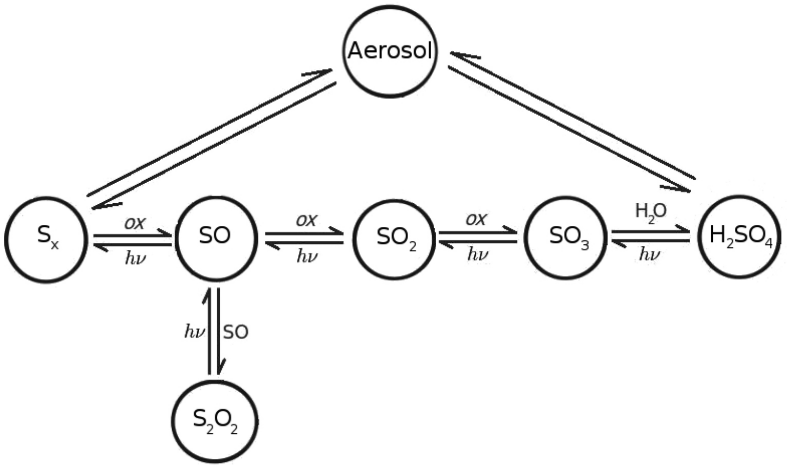

Figure 1.3: Different abundant SO_x and their chemical pathways in the atmosphere of Venus [54].

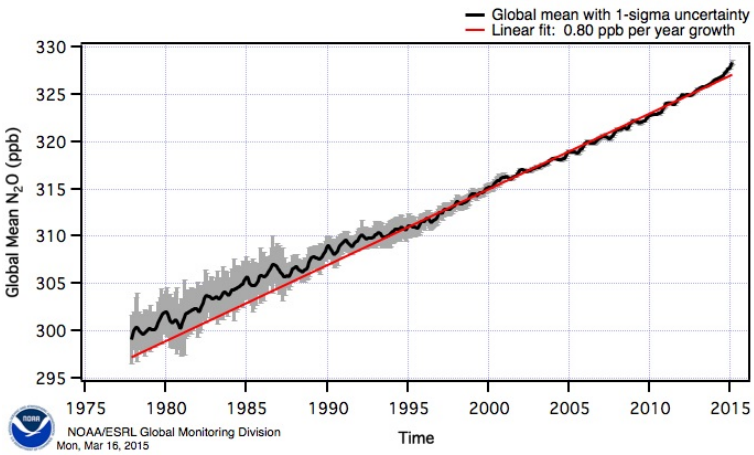

Figure 1.4: Atmospheric Concentration of N_2O [3].

1.4 N_2O monomer and complexes

Nitrous oxide is a greenhouse gas, an ozone depleting substance and a major source for stratospheric nitrogen oxides. Soils and oceans are the most important natural sources of N_2O, where it is emitted as a result of bacterial denitrification [55]. Anthropogenic emissions of N_2O primarily come from the agriculture sector and to a much lesser extent from industrial activities and fossil fuel combustion. [55, 56] Agricultural activities increase the amount and availability of nitrogen in the soil, which increases the rate of bacterial denitrification and as a consequence, more N_2O is emitted to the atmosphere [55]. The global concentration of N_2O in the Earth's atmosphere is increasing steadily, as shown in Figure 1.4.

According to a recent united nations environment program (UNEP) synthesis report, 60% of global N_2O is due to direct emission from agricultural activities and if no action is taken towards N_2O mitigation by 2050, the global N_2O emissions are projected to increase by 83% [57]. In New Zealand, most agricultural N_2O emissions come from animal grazing and the addition

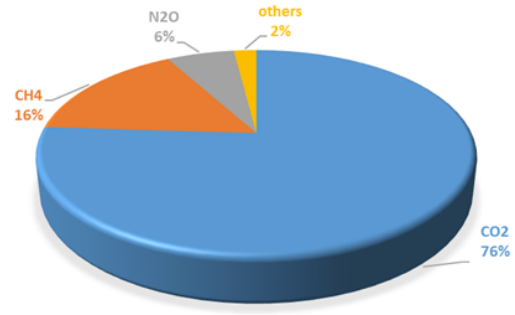

(a) Global

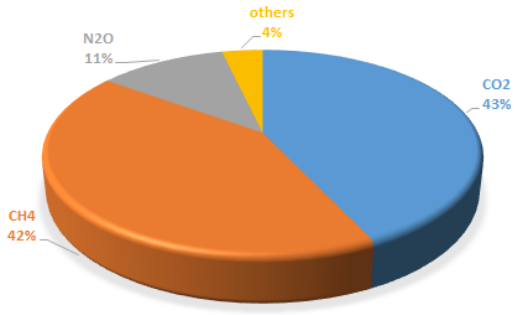

(b) New Zealand

Figure 1.5: Global and New Zealand greenhouse gas profiles with different greenhouse gases' contribution to the radiative forcing [59].

of fertilizers to the soil [58].

Nitrous oxide with a global warming potential (GWP_{100}) of 298 [a] [60] is the most significant anthropogenic climate forcing agent after CO_2 and CH_4 [60–62]. Figure 1.5 shows the global and New Zealand greenhouse gas profiles. While CO_2 makes 76% of global greenhouse gas emission, in New Zealand with an agricultural sector, N_2O and CH_4 together make up 54% of greenhouse gas emission. In the US with much fossil fuel consumption by vehicles and industry, the proportion of CO_2 is more than the global average.

[a] A certain mass of N_2O is 298 times more potent in trapping heat compared to the similar mass of CO_2 with GWP of 1.

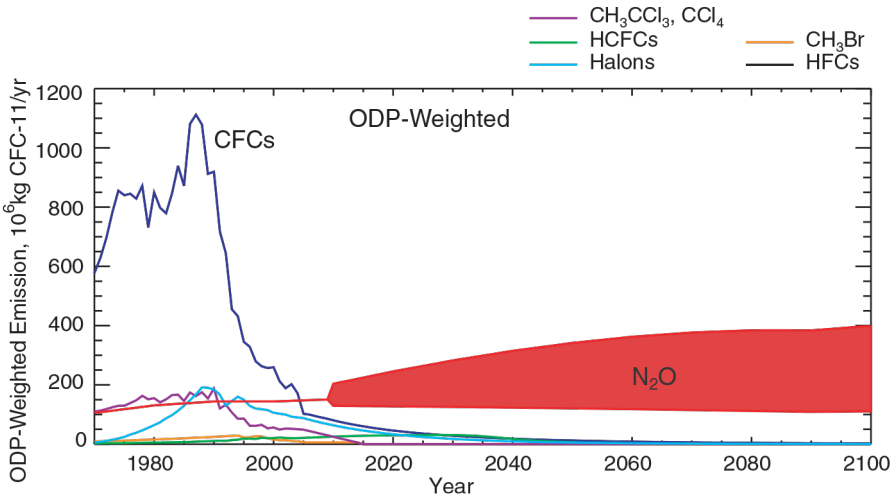

Figure 1.6: ODP-weighted emission of different ODSs from 1975-2010 and projected to 2100. [63]

Nitrous oxide is also a so-called ozone depleting substance (ODS), catalyzing the breakdown of ozone in the stratosphere. Different ozone depleting substances have different capacities in destroying ozone molecules, with CFC-11 being the reference molecule with an ozone depletion potential (ODP) of 1. Figure 1.6 shows the comparison of ODP from 1975-2010 and projected to 2100. From this figure, it is clear that N_2O is now the dominant ozone depleting substance and it is predicted to remain the single most important ozone destructive substance for the foreseeable future [63].

Although the ozone depleting effect of N_2O has been known for several years [64]; even before discovering the ozone hole and destructive effects of CFCs on ozone layer, N_2O is not yet regulated as an ODS [63]. While N_2O has recently attracted some attention, our understanding of its atmospheric chemistry requires much more research so that policy and decision makers can develop more effective actions to take. Therefore, improving our understanding of the atmospheric chemistry of N_2O, sometimes referred to as the

forgotten gas [65], is of high importance.

To the best of our knowledge, investigations into the atmospheric chemistry of N_2O have been restricted to N_2O monomer only. However, it is well established that weakly bound complexes play an important role in the Earth's atmosphere. For example, water clusters are known to be good absorbers of solar and terrestrial radiations [66, 67]. Therefore, weakly bound complexes containing water molecule/s are able to change the chemistry and radiative evolution in the atmosphere [67, 68]. Also, previous studies have shown that the formation of the oxygen dimer (O_2-O_2) and ozone water (O_3-H_2O) complexes cause a perturbation to the absorption spectra of the respective monomers (O_2 and O_3), which in turn affects the photodissociation dynamics [69, 70]. In the case of (O_3-H_2O), the atmospherically important hydroxyl radical (OH) is produced as the major product instead of atomic oxygen [70].

Recently, the abundances of a series of complexes involving N_2O and the major atmospheric components, namely nitrogen (N_2-N_2O), oxygen (O_2-N_2O), argon (Ar-N_2O) and water (H_2O-N_2O), were investigated in the Earth's atmosphere [71]. In addition, this recent research also showed that the vibrational modes of N_2O in the N_2-N_2O, O_2-N_2O, Ar-N_2O and H_2O-N_2O complexes, are perturbed as compared to those of N_2O monomer [71]. This result is significant as, the absorption cross section of N_2O in the atmospherically important 180-230 nm region is strongly dependent on coupling to the vibrational modes [72–74]. Given N_2O undergoes a direct photodissociation process [72, 75], it follows that the photodissociation rate of N_2O is also expected to be affected by complex formation. This effect has been previously observed across various isotopologues of N_2O, which have slightly different vibrational frequencies, and correspondingly, different photodisso-

ciation rates [72]. An accurate understanding of photodissociation process of N_2O while being aggregated with other atmospheric species can reveal valuable information about this atmospheric molecule and improve our knowledge about its chemistry and interaction with solar radiation. Investigating the photodissociation of N_2O complexes, can improve our understanding of the factors that affect the rate of N_2O photodissociation. This is particularly important, as most atmospheric models use this to estimate the amount of N_2O emitted to the atmosphere [76, 77].

1.5 Scope of this study

In chapter 2, we provide an overview of the theoretical methods used in simulating absorption spectra and photodissociation dynamics, and explain the specific methods and approaches used in this work.

In chapter 3, we simulate the absorption spectra of some sulfur-containing molecules, namely SO_2, H_2S, CS_2, OCS, and SO_3, and validate our results against their experimental spectra.

In chapter 4, we apply the theoretical approach developed in chapter 3 on two atmospherically relevant sulfur-containing molecules, H_2SO_4 and OSSO, where their experimental electronic absorption spectra are unknown. For H_2SO_4, we then use the simulated spectra to calculate the photodissociation rates (J-values) of H_2SO_4 in Earth's atmosphere.

In chapter 5, we investigate if formation of weakly bound complexes affects the electronic absorption spectrum of N_2O. We first simulate the electronic absorption spectrum of N_2O monomer and then, we simulate spectra of the Ar-N_2O, N_2-N_2O, O_2-N_2O and H_2O-N_2O complexes.

In chapter 6, we investigate the photodissociation dynamics of H_2O-N_2O using *ab initio* molecular dynamics simulations to show if complex formation

can open up new exit channels. For example:

$$N_2O - O_2 + h\nu \rightarrow N_2 + O_3 \tag{1.2}$$

$$N_2O - H_2O + h\nu \rightarrow N_2 + 2OH \tag{1.3}$$

Chapter 2

Theoretical methods

In this chapter, we outline the theoretical methods that are used in chapter 3-7. These methods include absorption spectrum and photodissociation dynamics simulations.

Although the experimental absorption spectrum and dynamics studies of many molecules are available, the cross section and dissociation process of some molecules are yet to be determined due to various reasons. This can be due to technical challenges *e.g.* H_2SO_4, or because of the unknown role of recently identified molecules.

We also can simulate the cross section of molecules with available experimental results for benchmarking and method validating purposes. The validated approaches can be applied later on the two previous cases where there is no experimental cross section or where the previous simulated spectrum needs to be improved.

In addition to spectral simulation, simulating the photodissociation processes of atmospheric species can help understanding the complex photochemistry of the Earth's atmosphere.

We first discuss and explain the methods and approaches that theo-

reticians use to simulate the absorption cross section and photodissociation dynamics in sections 2-1 to 2-4 and the specific approaches and packages used in this study are explained in section 2-5 of this chapter.

2.1 Electronic structure theory

It is extremely difficult to find the exact solution to the Schrödinger equation and almost impossible for most of problems. The computational complexity of solving the Schrödinger equation increases exponentially with the increase of number of particles of the system. Therefore, approximations have been introduced in computational methods to make solving the Schrödinger equation feasible and reduce the computing cost. Although applying the approximations is essential to solve the problem, they should be defined carefully not to lose the accuracy in results. Several standard models have been developed in computational quantum chemistry to describe the electronic wave functions. These models can be as simple as a single Slater determinant or as complex as defining the wave function as a superposition of all the determinants in Fock space. These models and approximations change in cost, flexibility, errors and accuracy. In Figure 2.1 the systematic approach to the exact solution of Schrödinger equation is illustrated.

A wide variety of methods are available for electronic ground state problems and depending on the size of the system and required level of accuracy, a suitable method can be selected. This variety of appropriate procedures is largely coming from one of the most basic and fundamental approximation, Born-Oppenheimer (BO) approximation [78, 79], where the motion of the electrons and nuclei of an atom can be separated which leads to a significant simplification of the wave function. In this main approximation in quantum mechanics the motions of electrons and nuclei can be separated.

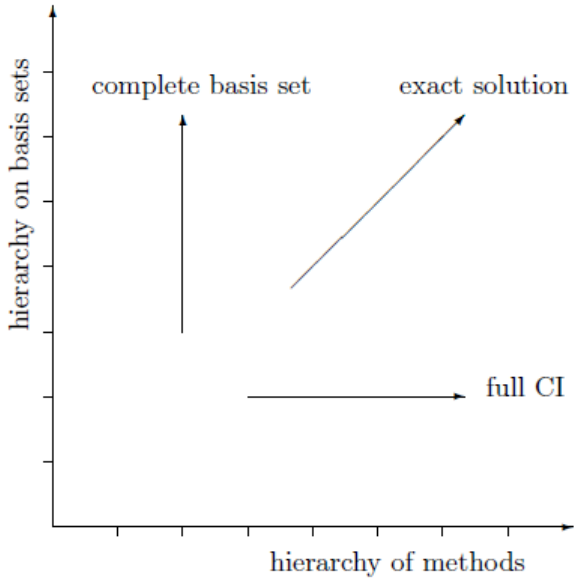

Figure 2.1: The systematic approach to the exact solution of Schrödinger equation.

This separation of nuclei and electrons wave functions, has greatly helped us to understand the electronic properties of molecules.

$$\Psi = \Psi_{electrons} \times \Psi_{nuclei} \tag{2.1}$$

The starting point of describing the electron distribution in quantum mechanics is the time independent Schrödinger equation (Equation 2.2) where it is solved for electronic problems.

$$\hat{H}\Psi = E\Psi \tag{2.2}$$

To solve this equation for systems of more than one electron, approximations must be applied. Therefore to find an approximate solution for more complicated systems, the N-electron molecular electronic wave function is defined as a linear combination of Slater determinants of one-electron

orthonormal orbitals. These Slater determinants satisfy the anti-symmetry requirement (Equation 2.3).

$$\Psi(x_1, x_2) = -\Psi(x_2, x_1) \tag{2.3}$$

As another approximation, a single Slater determinant of the N lowest spin orbitals can be used to describe the ground state of a system in Hartree-Fock method. Hartree-Fock is used as the starting point to produce more accurate models in quantum chemistry. In the following subsections Hartree-Fock and other main standard models of electronic structure theory are explained.

2.1.1 Hartree-Fock

The spin orbitals in most systems of chemical interest are not separable due to the electron-electron repulsion term in the Hamiltonian. However, applying this approximation introduces the Hartree-Fock theory (HF), the computationally simplest model that results in reasonably accurate results. In HF theory electrons are treated as independent particles and consequently the specific interaction between them is neglected. The HF wave function is written as

$$|\mathrm{HF}\rangle = exp(-\hat{k})|0\rangle \tag{2.4}$$

Where $|0\rangle$ is the reference configuration and $exp(-\hat{k})$ is the unitary transformation operator. In HF approach each electron moves independently in an average field of all other electrons and the nuclei.

In Unrestricted Hartree-Fock (UHF) wave function there are no restrictions on the spatial orbitals. If each of spatial orbitals are limited to two

electrons with one α and one β spin orbital the wave function is known as Restricted Hartree-Fock (RHF). The spin orbital restriction can be also defined in open shell system; known as Restricted Open-shell Hartree-Fock (ROHF), where the restriction is applied to doubly occupied orbitals [80] and the singly occupied orbitals are for unpaired electrons. Electron correlation, Equation 2.5, is defined as the difference between the exact energy and the HF energy of the electronic state. E_{exact} and E_{HF} (usually the energy of RHF) are both calculated in a complete basis set. It can be also solved for a given basis set. In this case E_{corr} usually increases with the size of basis set [81].

$$E_{corr} = E_{exact} - E_{HF} \tag{2.5}$$

The HF approach covers about 99% of the total energy [80]. The remaining energy matters in many chemical processes where drastic rearrangements happen in electron structures. In these cases HF approach only gives a qualitative agreement.

2.1.2 Configuration interaction theory

Configuration-interaction (CI) is the first and and conceptually the simplest model with the ability of recovering the dynamical correlation. In the CI model the wave function is defined as a linear combination of determinants or SCFs

$$|\mathrm{CI}\rangle = \sum_i C_i |i\rangle \tag{2.6}$$

where the C_i are determined by a variational optimization. The determinants in (full configuration interaction) FCI wavefunction are characterized

as single (S), double (D), triple (T), quadruple (Q), quintuple (5), sextuple (6), *etc.* Thus the wave function is written as

$$|\text{FCI}\rangle = C_0|\Psi_0\rangle + C_S|S\rangle + C_D|D\rangle + C_T|T\rangle + C_Q|Q\rangle + C_5|5\rangle + ... \quad (2.7)$$

where Ψ_0 is the HF determinant and $|S\rangle$ represents the single excitations, $|D\rangle$ represents the double excitations and so on [82]. In principle, FCI can provide the exact solution to the problem but for most of the systems it is not computationally possible to carry out the FCI calculations. Consequently, a truncated model is introduced to reduce the number of excited determinants in the CI expansion. The contribution of different excitations are not the same and the double excitations contribute most to the correlation energy. Therefore the first truncated CI with a balanced correlation energy coverage is the CI singles-and-doubles (CISD) wave function which contains all singles and doubles configurations [80–82].

2.1.3 Coupled-cluster theory

As mentioned in the previous subsection, the CI model suffers from two shortcomings: the lack of size-extensivity as a consequence of linear parametrization and slow convergence towards the full configuration interaction limit. To achieve the size-extensivity, the wave function in coupled-cluster wave function is a product model compared to the linear model in CI wave function. The coupled-cluster wave function is defined as

$$|\text{CC}\rangle = exp(-\hat{T})|\text{HF}\rangle \quad (2.8)$$

where $\hat{T}$ is the *cluster operator* (Equation 2.9).

$$\hat{T} = \hat{T}_1 + \hat{T}_2 + ... \tag{2.9}$$

where $\hat{T}_1$ and $\hat{T}_2$ are the single and double and higher-order excitations operators. The simplest CC model is coupled-cluster singles-and-doubles (CCSD) model by excluding higher than singles and doubles excitations from the cluster operator. By keeping the triple excitations term in the cluster operator the (CCSDT) wave function is created. Although the CC model can provide considerably more accurate results compared to previously discussed models, applying it to degenerate or nearly degenerate systems is difficult. For these systems MCSCF and MRCI wave functions work better. The CCSD(T) is an approximate method derived from CCSDT by applying perturbation theory arguments [80, 83]. The more recent coupled cluster method is the explicitly correlated coupled cluster singles and doubles and perturbative triples CCSD(T)-F12, from the so-called explicitly correlated methods [84–87], that was found to give significant accuracy in geometry optimization calculations when used with the associated VXZ-F12 basis sets [88–92]. In developing the F12 methods, the inter-electronic distance is applied to explicitly expand the wave function. The CCSD(T) and CCSD(T)-F12 methods are used in geometry optimization of the sulfur containing molecules discussed in chapters 3 and 4.

2.1.4 Perturbation theory

The principle idea behind the perturbation theory is breaking the problem into solvable and perturbation parts where the perturbation part is added as a small term to the exactly solvable unperturbed part to make the whole problem mathematically solvable. In Møller- Plesset perturbation theory (MPPT); introduced by Møller and Plesset in 1934 [93], the unperturbed

part is the Hartree-Fock function. In MPPT the Hamiltonian is written as

$$\hat{H} = \hat{f} + \hat{\Phi} + h_{nuc} \tag{2.10}$$

where $\hat{f}$ is the Fock operator which represents the zero-order operator, $\hat{\Phi}$ the fluctuation potential which represents the perturbation and h_{nuc} is the nuclear-nuclear term [81]. By adding the second-order correction, the second-order Møller-Plesset energy is obtained (Equation 2.11).

$$E_{MP2} = E_{MP}^{(0)} + E_{MP}^{(1)} + E_{MP}^{(2)} + h_{nuc} \tag{2.11}$$

MP2 model provides a helpful and size extensive correlation energies with balance between cost and accuracy although limited to single configuration systems. Therefore it is not applicable to degenerate or near degeneracy systems. For these systems multiconfigurational perturbation theory is more suitable.

By including third and forth-order energy corrections ($E_{MP}^{(3)}$ *and* $E_{MP}^{(4)}$), MP3 and MP4 models are generated at greater cost but less compromise of accuracy compared to MP2.

2.1.5 Density functional theory

In 1964, Hohenberg and Kohn showed that in a molecule with nondegenerate ground state, the energy of the electronic ground state is determined by the ground state probability density using functionals [94]. Later Kohn and Sham proved their variational theorem which was developed later by Kohn and Sham [95] where exchange and correlation effects were also included to make density functional theory (DFT) an accurate enough model to be used in computational chemistry. DFT has a significant lower cost which is a

result of significantly less number of coordinates compared to the wave function based models. The main difference between different DFT methods is the choice of functional. Functionals are chosen depend on the properties under investigation. Hybrid functionals, functionals with dispersion and long range corrected functionals are some of the most common types of functionals used in DFT calculations. The hybrid exchange-correlation functional CAM-B3LYP introduced by Yani *et al.* [96],combines the long-range correction and B3LYP hybrid qualities which makes it perform well for charge transfer excitations that is underestimated by B3LYP functional. At short range, the CAM-B3LYP functional consists of 0.19 HF and 0.81 Becke 1988 (B88) exchange interaction, and 0.65 HF and 0.35 B88 at long range [96]. Zhao and Truhlar introduced a new hybrid meta exchange-correlation class of functionals , M06-class, in 2008 [97,98]. The M06 functional with 27% HF exchange, is a meta-GGA exchange-correlation functional and a reoptimized functional form of M05, a global hybrid function with 28% HF exchange. has a broad applicability in thermochemistry, thermochemical interactions and excited states.The M06 functional performs well for applications where noncovalent interactions are involved [98]. The long-range corrected hybrid density wB97XD functional with damped atom-atom dispersion correction includes 100% long-range exact exchange and 22% short-range exact exchange. This functional is recommended for non-covalent interaction applications and was introduced by Chai *et al.* [99].

The functionals used in this work are wB97XD, a functional including dispersion, CAM-B3LYP, a long range corrected functional, M06, a hybrid functional. In some cases like chapter 6 where we simulate the photodissociation dynamics of N_2O molecule and H_2O-N_2O complex more than one functional are used to ensure that the results from the chosen functionals

are consistent. The functionals used in dynamics simulation in chapter 6 are CAM-B3LYP and M06. In other cases like simulating the absorption spectrum of N_2O in chapter 5, the functional with better description of our system of interest is chosen for benchmarking purposes and comparing the effectiveness of wave function methods and DFT methods.

Despite recent developments in DFT by altering the functionals and the possibility of adding terms to them to produce satisfying results [100–103], it still has difficulties describing intermolecular interactions, for example dispersion forces.

2.2 Excited states problems

Most of the properties related to the interaction of light and molecules, spectroscopic and photochemical, happen in the excited states of molecules. Molecules when in their excited states, behave differently than their ground state and this has made studying the excited states properties a very challenging task. A wide variety of methods are available for electronic ground state problems and depending on the size of the system and required level of accuracy, a suitable method can be selected. As it was discussed in section 2.1 this separation of nuclei and electrons wave functions, has greatly helped us to simplify the ground state problems and develop a variety of methods to understand the properties of molecules.

For excited states problems, the situation is very different as the electronic excited states calculations are not as straightforward as those of the ground state due to different behavior of molecules in the excited states. The main approximation for excited state problems is the Franck-Condon (FC) principle that considers that electronic transition is instantaneous compared with the time scale of changes in the position of the nuclei. The Franck-

Condon principle is formulated as the square of the overlap between the vibrational wavefunctions of the states involved in the transition. Even in the Franck-Condon (FC) excitations, there are varieties in the character of excited states. In excited state problems like direct photodissociation, where the wave packet immediately leaves the FC region the overlap with the wave packet at zero time decays to zero and it is very unlikely that the wave packet is back to its origin.Therefore, depending on the nature of the excited state problem under investigation, a suitable method is chosen. In some cases such as spectral simulation, some of the developed single reference methods such as TDDFT, CC2, EOM-CCSD, etc., can be applied while in other excited state problems where bonds are broken and formed, e.g. photodissociation dynamics, multireference approaches give more reliable description.

In the next section we explain how these excited state problems are dealt with and what the suitable procedures are to describe them.

2.2.1 Multiconfigurational self consistent field (MCSCF)

The two MCSCF and CI approaches have many common features, with the same staring point, equation 2.6. In CI the focus is on optimizing the coefficients, C_i, while in MCSCF the focus is on optimizing both the coefficients and the molecular orbitals. The MCSCF approach can be used both as a method itself for calculating electronic states or can be used to create the molecular orbitals (MOs) needed for multireference calculations. When all the possible configurations for the given orbitals and electrons are considered, it leads to complete active space self-consistent field (CASSCF) approach [104] and is specified as CAS (n, m), where n is number of electrons and m is the number of orbitals. As CAS has a factorial cost increase with the number of active orbitals, a restricted active space (RAS) has been

introduced [105]. The RAS space is usually divided in three spaces, RAS1, contains a given number of holes, RAS2, contains all of the possible allowed occupations and RAS3, contains number of electrons up to a specified number. Several techniques and approximations have been developed recently to improve the size and speed of CASSCF calculations [83].

2.2.2 Multireference perturbation theory

Another framework in which excited states can be calculated in multireference situation is many body perturbation theory (MBPT). In this approach the nondynamical electron correlation is treated as a perturbation to Hamiltonian of the ground state. However it is a challenging task to develop nondegenerate MBPT for the multireference situation [83]. The common MBPT methods are active space perturbation theory (CASPT2) [106, 107], the second-order multireference Møller-Plesset perturbation theory (MRMP2) [108–110] and N-electron valence state perturbation theory (NEVPT) [111]. Among these methods CASPT2 is the most popular. However CASPT2 is a successful approach for studying the spectroscopy and photochemical processes, it has its own disadvantages. The CASPT2 approach can be applied to only small and medium-sized systems due to high computational cost and in some cases shows a very small energy difference between the energies of doubly occupied wave function and the energy of the zeroth-order wave function [112].

The main difference between these methods, is how the zeroth-order wave function and Hamiltonian are defined [83].

2.2.3 Configuration Interaction theory

As previously discussed in section 2.1, in the CI method the wave function of the electronic states are written as as linear combinations of many-electron basis functions, equation 2.6. This method is able to cover the dynamic contribution of electron correlation associated with the correlation density for electrons [80,81]. By truncating the space, single reference (SR) methods like SR-CIS, SR-CISD, SR-CISD and SR-CISDT are introduced. The HF determinant is a good assumption as the reference. In bond breaking processes where excitations happen in a region away from FC region, one single configuration cannot describe the excited states. To have a more accurate description of a particular reaction and long bond distances multireference configuration interaction (MRCI) where an MCSCF wave function is chosen as the reference compared to SR-CI where the reference is a single determinant. The MRCI wave functions with many configurations in the MCSCF can generate very accurate wave functions, but computationally very expensive at the same time. If only the singles and doubles excitations from each reference configuration are involved, it results in multi reference singles-and-doubles CI (MRSDCI). If all the possible configurations are included, the space is named complete active space (CAS) [83]. In untruncated treatment, (*un*-MRCI [113]), where the excitation can happen from each of the reference configuration, the excited state calculation is straightforward. The truncated CI or MRCI have two main disadvantages, lack of size-extensivity and very slow convergence [114].

$$|\text{MRCI}\rangle = C_0|\Psi_0\rangle + C_S|S\rangle + C_D|D\rangle + ... \tag{2.12}$$

The second way to reduce the computational cost of MRCI calculations

is the local correlation treatment (LC) where the orbitals are localized in the space and are restricted to excitations only between the orbitals in spatial proximity [83, 115–118].

Using explicitly correlated multireference onfiguration interaction (MRCI-F12), is another way reducing the cost where significant improvement in basis set convergence is achieved resulting from introducing electron-electron distance [119].

2.2.4 Coupled cluster theory

The CC method, equation 2.8, can be approximated by truncating the cluster operator, equation 2.9, to a hierarchical set of CCD, including only doublets [120], CCSD including singles and doublets [121], CCSDT including singles, doublets and triplet excitations [122]. By applying perturbation theory arguments, other approximate approaches have been introduced such as CC2 [123], CCSD(2) [124], CCSD(T) [125] and CC3 [126].

As this approach is a single reference like SRCI, it cannot generally describe the excited states. To generalize these approaches to describe the excited states, the equation of Motion (EOM) [127, 128] and the Linear Response (LR) ways [129]. In EOM-CC and CC-LR approaches, the excited states are defined as a linear combination of ground state wave functions [83]. These two extended single reference methods are able to treat several excited states problems with high accuracy thanks to their multideterminantal description and as well as treating equivalently the excited states from the same type such as singles [83]. Also an exponential part is defined for the ground state which helps to treat the differential correlations [83, 130].

It is possible to have a hierarchical set of truncated methods from EOM-CC and CC-LR such as EOM-CCSD [130, 131] or CCSD-LR [132]. They

are based on CCSD ground state but the single and double excitations are included in the diagonalization of the Hamiltonian [83]. By using the perturbation arguments it is possible to develop methods like CC2-LR [123], EOM-CCSD(2) [124] and Algebraic Diagrammatic Construction (ADC) [133–135] family of methods are developed when doublets are approximated iteratively [83]. When only double excitations are included in the equations, only states with dominant single excitations can be correctly described and to include triple excitations CC3-LR and EOM-CCDSDT-3 methods should be used [83]. However the CC methods are powerful in describing the excited states specially for the problems where the excitations happen around the FC region [136], they fail if the excited states cannot be well described by the CC wave function [83].

Generalizing the CC theory to a multideterminantal case is not as straightforward as it is in CI theory. The most challenging part is defining a reference to classify the occupied and virtual orbitals in CC approach. The attempts to tackle this problem have led to two approaches, JM ansatz [137] and the second approach is basically internal contraction (IC) [138, 139]. Third MRCC approach is using SR-CC with higher excited excitation included. This approach despite benefiting from properties like size extensivity of SR-CC theory, can describe a certain class of excitations [83]. However many attempts were put on MRCC methods they do not have yet found routine applications [83].

2.2.5 Time-dependent density functional theory

Several approaches based on the single reference DFT have been developed to treat the nondynamical electron correlation [140]. To investigate the dynamics of many body systems, an extension of density functional theory

(DFT) was developed. Time-dependent density functional theory (TDDFT) [141,142] method is used to calculate excitation energies, frequency-dependent response properties and absorption spectra. However, this method cannot describe the strong coupling regions between the ground state and the first excited state. This method has been recently developed to TDDFT with tight-binding approximation (TD-DFTB) to tackle some the problems related to the regular TDDFT [143]. Despite great success of these approaches, they are not able to describe some the excited states.

2.3 Basis sets

In quantum chemistry the wave functions are generated from antisymmetric products of the molecular orbitals (MOs). These MOs can be expanded as a set of known functions or basis sets and an approximation is introduced if the basis sets are not complete [114]. The size and type of the chosen basis set can affect the accuracy and cost of the calculations. An expansion of basis sets where each single function can better represent the physics of the system, fewer basis functions are necessary to achieve to a certain level of theory. On the other side a larger basis set can give better results and represent the wave function more accurately. Therefore it is important to achieve a level of satisfying accuracy and efficiency as well. Different types of the basis sets have been introduced and in following subsections the main basis sets in quantum chemistry are introduced.

2.3.1 Gaussian type basis sets

Equation 2.13 shows the Gaussian type orbitals (GTO) [144].

$$\chi_{\zeta,n,l,m}(r,\theta,\varphi) = NY_{l,m}(\theta,\varphi)r^{2n-2-l}e^{-\zeta r^2} \tag{2.13}$$

where N and Y_l, m are normalization constants and spherical harmonic functions respectively. GTOs can not describe the tail of the wave function well and they represent poorly its behavior near the nucleus. It means that more GTOs are needed to achieve a certain level of theory but GTOs have computational efficiency. The smallest number of functions to make the wave function is the minimum basis set. For example, for hydrogen the minimum basis set is a single s-function. At the next step, the basis set can be improved by doubling all of the basis sets to produce a double zeta (DZ). In the case of hydrogen, a double zeta basis set includes two s-functions. By involving three, four and five times as many functions as the minimum basis, triple zeta (TZ), quadruple zeta (QZ) and quintuple zeta (QZ) basis sets are produced.There is other type of DZ type basis that only doubles the number of valance orbitals to produce a split valence basis. Again, by saving the core orbitals and splitting the valence orbitals their split valence equivalent are produced. In the next step, higher angular momentum functions are also involved which are defined as polarization functions. For example, adding p-functions on hydrogen an d-functions on heavy atoms to the DZ basis set produces a double zeta plus polarization (DZP) type basis [80].

2.3.2 Contracted basis sets

After deciding on the number of basis functions, the values of the exponents are chosen variationally. The energy of these optimized basis sets primarily depend on the inner-shell electrons. Therefore the basis set is more optimum for the core electrons and less for the valance electrons. The valence electrons are of chemical importance while core electrons are energetically important. To tackle this problem and involve the valance electrons, energy optimized basis set are augmented with diffuse functions which are functions

with small exponents. Diffuse functions are necessary to better describe a system with loosely bond electrons for example anions and excited states. To prevent spending most of the computational effort on the less chemically important orbitals, the variational coefficients in the inner shell are considered as constants and therefore they are no longer parameters and the core orbitals are described by a fixed linear combination of basis functions. By doing this; known as contraction, the number coefficients to be calculated variationally is reduced. Contraction of the primitive GTOs results in the contracted GTOs (CGTOs).

2.3.3 Pople style basis sets

Pople *et al.* designed the split valance k-nlmG basis sets [145]. For example 6-31G is a split valence basis where six PGTOs construct the core orbitals and three PGTOs are used to build the inner part of the valence orbitals and one PGTO for the outer part. Diffuse and polarized functions can be added to these basis. By adding diffuse and polarized functions to the previous example the split valence basis 6-31+G(d) is produced where one set of diffuse sp-functions and one d-type polarization are added on heavy atoms [80].

2.3.4 Dunning type basis sets

Dunning has used the Huzinaga primitive uncontracted energy optimized Gaussian type basis sets (PGTOs) and contracted them resulting in Dunning-Huzinaga (DH) type basis sets [146]. In Dunning-Huzinaga contracted basis sets the exponents for the s- and p-functions do not have to be equal alike Pole style basis sets. This makes the Dunning-Huzinaga more flexible but at the same time computationally more expensive [80].

Also due to slow convergence of correlation methods with one electron basis sets, auxiliary basis sets (ABS) were developed to be used with F12 explicitly correlated methods [147–149].

2.3.5 Basis sets for excited state problems

In photochemical processes excitation happen in the region far a way from FC region. These processes involve bond breaking and more loosely bound electrons compared to the ground state situations. To be able to describe processes like photodissociation or other photoinduced reactions, a proper description of highly excited states, so-called Rydberg states, is required.

To tackle this problem, one approach is augmenting the basis sets with diffuse functions to have a better description of highly excited states [80,150].

2.4 Simulation approaches

Absorption spectra and photodissociation processes of molecules are of great importance in characterizing material and their chemistry. In theoretical chemistry, characterization of the absorption spectrum of molecules is restricted to vertical excitations and transitions dipole moments. A schematic illustration in Figure 2.2 shows the difference between vertical excitation energy, in which the excited state has the same geometry as the ground state, and the adiabatic excitation energy, in which the excited state is in its lowest energy.

In the literature, the band maxima of experimental results are often compared with the calculated vertical excitations. This comparison, however valid for checking the general quality of the calculations, can be also misleading as the experimental band maxima are normally red shifted compared to vertical excitations. This while using the spectrum simulation

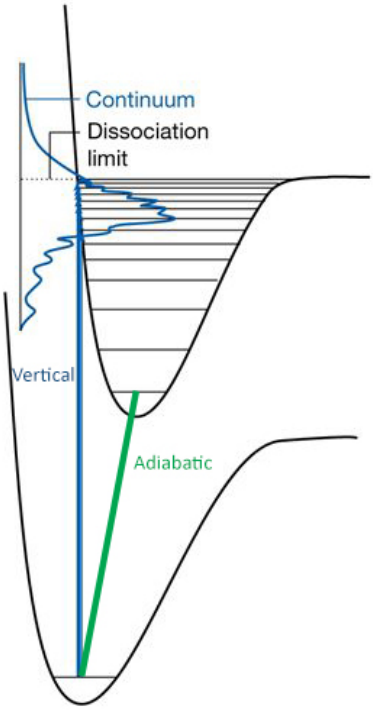

Figure 2.2: Vertical and adiabatic excitation energy and the absorption spectrum.

these shifts are also calculated and more accurate theoretical values can be provided to be compared with the experimental results [151].

2.4.1 Simulating spectra

To simulate the spectrum these transitions are empirically convoluted to produce the spectrum. These approaches, however helpful in assigning the measured spectra, are very simplistic. The spectra of the molecules in this thesis involve direct photodissociation, where the wave packet immediately leaves the FC region, and therefore the conventional FC overlap approaches do not work as there are no bound vibrational states for the excited states. Hence, a full simulation of the spectrum is much more complicated than just simply calculating the vertical excitations. It demands very expensive

procedures like propagating the excited state nuclear wave packets or determining the FC factors. These full spectrum simulations are restricted by nuclear degrees of freedom and number of excited states [151].

Some methods have been recently developed to simulate the spectrum. One method with increasing popularity is the nuclear ensemble approach (NEA), where it is assumed that the ground state nuclear geometry determines the shape of the spectral band. If this assumption is fulfilled, the simulated spectrum from this approach can provide good results. Also in this approach, all the degrees of freedom are included and there is no restriction on the number of excited states [151]. Despite the simple concept behind this approach and relatively low computational cost, which makes this approach popular and routine, there are barriers such as dependence on arbitrary parameters.

Historically, the first application of the nuclear ensemble approach goes back to 1980s when Heller *et al.* simulated the absorption spectrum based on the molecular dynamics results [152]. Saven *et al.* have also improved the nuclear ensemble approach by providing a better description of homogeneous and heterogeneous broadening and the transition between them [153].

In the nuclear ensemble approach, a distribution of nuclear phase is constructed in the electronic ground state. This distribution will be then projected to the excited states. There are two main ways to prepare the initial conditions, by either a ground state trajectory simulation or by a probabilistic sampling. In the latter case which is mainly used in this thesis, a classical phase space contribution is constructed using a Wigner distribution to sample the normal modes coordinates for the quantum harmonic oscillator [75,154]. This sampling approach, results in a total energy broadly distributed around harmonic zero point energy (ZPE). The distribution is

projected to the excited state, by calculating the cross section at the first order of time-dependent perturbation theory [155]. In the cross section calculation, the integration over quantum states is replaced by a classical average over the ensemble in terms of oscillator strengths and and transition energies. Finally a line shape is used to normalize the intensity peaked at the transition energy and broadened by phenomenological broadening constant δ. The choice of the line shape depends on the nature of the problem under investigation. For collisions or thermal broadening, a Gaussian shape is used and for finite lifetime or natural decay, a Lorentzian shape is used [155].

One advantage of the nuclear ensemble approach is that different contributions of the full spectrum can be analyzed. There are previous works on analyzing different contributions like diabatic contributions [155], symmetry contributions [156], isomeric contributions [157] and electronic density contributions [151]. Other main advantage of the nuclear ensemble approach is that the geometries displaced form the equilibrium geometry are involved in the simulation and the vibronic contributions of these geometries are considered. This makes the nuclear ensemble approach a naturally post-FC approximation [151]. Thank to this advantage, even describing the dark transitions in the absorption spectrum is possible [158]. In a previous work by Crespo-Oteroi *et al.* the absorption spectra of benzene, furan, and 2-phenylfuran in gas phase were simulated using the nuclear ensemble approach and good performance were reported and several features of this approach were discussed [151]. The main limitation of the current nuclear ensemble approach is that the vibrational resolution is missed from the simulated spectra [151] .

In the last section of this chapter, we will discuss the simulation parameters from the arbitrary parameters to the electronic structure methods in

more details where we explain the parameters and methods used in simulating the absorption spectrum of our molecules of interest.

2.4.2 Simulating photodissociation dynamics

In photodissociation one or several bonds are broken after absorbing the light. In a single photodissociation, where the bonds are broken by absorbing a single photon, the molecule is promoted to an excited from its ground state which is schematically showed in Figure 2.3. In a direct photodissociation, where immediate dissociation occurs, the molecule leave the Franck-Condon (FC) region. In indirect photodissociation, the molecule is trapped by a barrier before it gains enough energy for dissociation and bond breaking [75]. In photodossociation studies, the molecular dynamics of the molecule and its lifetime in excited state, breaking bonds and possible exit channels are studied.

High quality potential energy surface which is the key quantity for a realistic understanding of molecular processes like photodissociation is the bottleneck in dynamics studies [75]. The challenges in nonadiabatic time-dependent processes like photodissociation, were dealt with using on-the-fly calculation of surfaces. To be able to move between the surfaces transition surface hopping (TSH) is used. In the TSH approach, the time evolution of a wave packet in the branching region of the PES is approximated by an ensemble of semi-classical trajectories which are distributed among the branches [159]. In the TSH method the dissociation process is treated by a mixed quantum-classical approach (MQCD). In nonadiabatic phenomena where branching of population occur, a stochastic algorithm is used and the exchange in the electronic states is allowed. This approach is schematically shown in Figure 2.4.

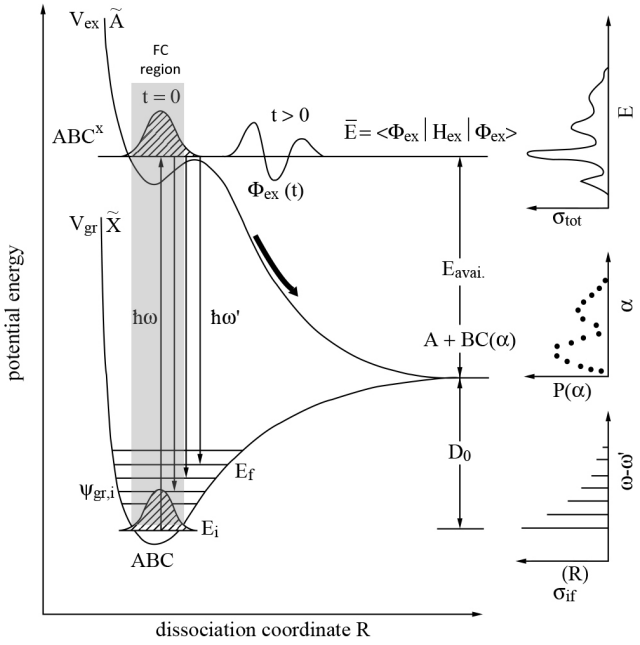

Figure 2.3: Schematic illustration of photodissociation by Schinke [75].

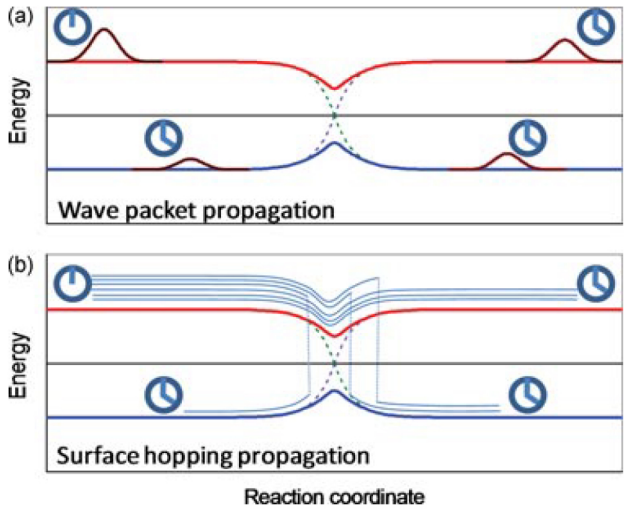

Figure 2.4: Adiabatic (solid) and nonadiabatic potential energy curves of the ground state and the first excited state of a molecule with avoiding crossing (a) wave packet propagation and (b) trajectory surface hopping approach [159].

The main difference among different TSH models comes from the transition probability calculations. The fewest approach proposed by Tully [160] in 1990s is probably the most common model which extended TSH approach to arbitrary number of states [159]. Initial condition used in TSH approach should naturally represent the initial state of the system of interest. For example, for photochemical processes the molecule is prepared in the ground state by either running a long ground state trajectory simulation and then taking snapshots of this trajectory for the initial conditions in the excited states or by sampling using defined distribution such as Wigner distribution [155]. The ground state is then projected to one or more excited states. The fewest-switches TSH model is based on on-the-fly electronic structure calculations, where the time-independent Schrödinger equation is solved for energies, energy gradients and nonadiabatic coupling terms for a specific nuclear frame, which determines the cost of the whole procedure. Consequently, the number of trajectories in the ensemble also dominates the computational cost. This number is thousands with available analytical surfaces and is reduced to few hundreds and less than one hundreds when semi-empirical and *ab initio* methods are applied consecutively [159, 161, 162].

The electronic structure method should be able to provide reasonably accurate results for distorted geometries, where the nonadibatic couplings are strong. At the same time these methods should be fast enough as there are hundreds to thousands of points in the simulations. As it was discussed in the electronic structure methods section, there is no method that can meet these two requirements. For example, mutireference methods are among the best methods for dynamics simulations but the computational cost for these methods are often very high, therefore, they can only be applied to small molecules.

Single reference methods, both wave function based and density functional theory based, are also commonly used for dynamics simulations. The main problem with these methods, is that the crossing between the ground state and the first excited state cannot be well described, however the crossings between excited states are normally described [159]. In the cases of molecules with interaction between them or solid state matter, time-dependent density functional method (TDDFT) works very efficiently. In TDDFT method the Kohn-Sham orbitals are directly propagated [163,164]. This approach is much less expensive compared to full quantum wave packet propagation. Thanks to the local character of TSH approach, there is no need to determine the multidimensional PES and states' energies and nonadiabatic couplings are calculated by means of the on-the-fly calculations. As the trajectories are independent, the trivial parallelization calculations of calculations is allowed. However, there are some cases that this approach cannot work well, such as treatment of tunneling effect and zero point energy and propagating trajectories for more than few picoseconds [159].

Photoinduced processes, both photophysical and photochemical processes, are the field where TSH has been applied the most. Figure 2.5 shows the basic concept of this process, where it is considered that at the time of photoexcitation, the molecule is in its ground state. The molecule either return to the ground state (T_1) or forms a new product (T_2). Photodissociation is one of the main photochemical processes studied by the TSH method and is studied in chapter 6 of this study for H_2O-N_2O complex.

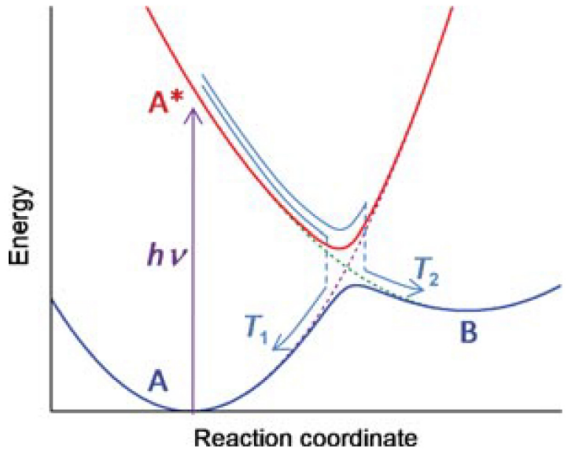

Figure 2.5: Adiabatic (solid) and nonadiabatic potential energy curves of the ground state and the first excited state of a molecule. Trajectory T_1 undergoes a photophysical process producing A, while trajectory T_2 undergoes photochemical process producing B [159].

2.5 Summary of the simulation methods used in this work

In this study, we simulate both absorption cross section and dynamics. The absorption spectrum is simulated for a range of molecules using nuclear ensemble approach as their spectra involve direct photodissociation. The molecules under investigation in this thesis are mostly atmospheric species, for which we simulate the spectra in chapters 3-5, and dynamics simulation of an atmospheric complex, H_2O-N_2O, is studied in chapter 6. The molecules for which we simulate the spectrum, were chosen for several purposes such benchmarking, validating and introducing new approximation approaches, providing the first simulated spectrum, improving the current simulated spectrum or investigating the changes on the simulated spectrum upon processes like complex formation.

For geometry optimization and vibrational frequency calculations, de-

pending on the system under investigation and the required level of theory, we use different electronic structure packages. For MRCI calculations, Molpro [165], for RASSCF calculations, MOLCAS [166], for CCSD(T) calculations, CFOUR [167] and for the rest of methods used in this work to calculate the equilibrium geometry and vibrational frequencies, Gaussian 09 [168] was used.

In chapter 3, we simulate the absorption cross section of some sulfur molecules, namely SO_2, H_2S, CS_2, OCS and SO_3. For these simulations, we use Newton-X program [169] for nuclear ensemble approach. Depending on the electronic structure method used to calculate the vertical excitations, either Gaussian 09 [168] for EOM-CCSD method or Turbomole [170] for RI-CC2 and ADC(2) methods are used interfaced with Newton-X [169].

In chapter 4 and for two conformers of H_2SO_4 and OSSO, we simulate the absorption cross section in Newton-X program [169] using EOM-CCSD method in Gaussian 09 [168] and RI-CC2 and ADC(2) methods in Turbomole [170]. The simulation approach is the same as the approach used in chapter 3, i.e. nuclear ensemble.

In chapter 5, we simulated the absorption spectra of monomeric N_2O and some of its atmospheric complexes. A variety of electronic structure methods, both wave function and density functional, implemented in Gasussian 09 [168] are used to simulate the cross section of N_2O monomer and complexes, namely Ar-N_2O, N_2-N_2O, O_2-N_2O and -H_2O-N_2O complexes in Newton-X [169]. In the electronic structure calculations, different Pople and Dunning type basis sets are applied.

Photodissociation dynamics simulation is investigated in chapter 6, where we simulate the dissociation dynamics of monomeric N_2O and N_2O-H_2O complex in stratosphere using transition surface hopping approach as im-

plemented in Newton-X [169]. The on-the-fly electronic structure calculations are done using a hybrid exchange-correlation functional, CAM-B3LYP and a Minnesota functional, M06, with aug-cc-pVDZ basis set in Gaussian 09 [168]. For the monomeric N_2O, the RASSCF photodissocition dynamics is also simulated using MOLCAS [166].

Chapter 3

Benchmarking sulfur-containing molecules

In this chapter, we simulate the electronic absorption spectra of some small atmospherically relevant sulfur-containing molecules, where there are known experimental spectra. We benchmark the accuracy of a range of different theoretical methods to determine an appropriate balance between cost and accuracy. The molecules considered are SO_2, H_2S, CS_2, OCS and SO_3, which are relatively small in size and similar in structure to the molecules in chapter 4, where the experimental spectra are unknown.

In section 3.1, we provide a description of the theoretical details used in this chapter. In section 3.2, we first benchmark our theoretical results for SO_2, and compare this with the experimental cross section to validate our simulation parameters. In section 3.3, we then test the recommended combination from SO_2 on the other molecules with known spectra (H_2S, CS_2, OCS and SO_3). The findings from this chapter are then used in chapter 4 to simulate the electronic absorption spectra of H_2SO_4 and OSSO. The benchamrking results were recently published in paper [171].

3.1 Theoretical details

We first optimize the geometry of SO_2, H_2S, CS_2, OCS and SO_3 at the CCSD(T)/aug-cc-pV(T+d)Z level of theory. The mass-weighted vibrational frequencies of the optimized geometries are also calculated at the same level of theory. The nuclear ensemble approach is used to generate the electronic absorption spectra from an ensemble of geometric structures sampled from the ground vibrational state of the ground electronic state. Vertical excitation energies and oscillator strengths are calculated for each geometric structure using the EOM-CCSD, RI-CC2 and ADC(2) methods, with different correlation consistent basis sets.

It was previously shown by Lane *et al.* [25] that adding three sets of very diffuse functions to the center of mass of the sulfur-containing systems can describe their Rydberg states better. However, because of limitations with Newton-X, we place these very diffuse functions on the central atom of the molecule, i.e. S in SO_2 and C in CS_2, rather than the center of mass. To check that this does not significantly affect the results, we investigate this for SO_2 and present the results in Table 3.1. We find that the vertical excitation energies and oscillator strengths change negligibly when moving the diffuse functions from the center of mass to the central atom.

3.2 SO_2

Sulfur dioxide (SO_2) is one of the smallest sulfur-containing atmospheric molecules where the experimental absorption spectrum is well-known [16]. At atmospheric SO_2 emissions come from both natural, e.g. volcanic eruption, and anthropogenic, e.g. fossil fuel combustion, sources. Sulfur dioxide, is oxidized to sulfate aerosol which plays an important role in the forma-

Table 3.1: EOM-CCSD/aug-cc-pV(D+d)Z+3 vertical excitations (eV) and oscillator strengths of SO_2 molecule.

	extra functions on center of mass		extra functions on S atom		difference	
state	E/eV	f	E/eV	f	$\|\Delta E\|/eV$	$\|\Delta f\|$
1	4.37	0.0054	4.37	0.0053	0.0008	0.0001
2	4.81	0.0000	4.81	0.0000	0.0015	0.0000
3	6.47	0.0797	6.47	0.0801	0.0003	0.0004
4	8.40	0.0294	8.40	0.0304	0.0007	0.0010
5	8.75	0.0023	8.74	0.0024	0.0009	0.0001
6	8.87	0.0000	8.87	0.0000	0.0007	0.0000
7	8.95	0.0020	8.95	0.0020	0.0011	0.0000
8	9.07	0.0445	9.07	0.0442	0.0014	0.0003
9	9.10	0.0000	9.10	0.0000	0.0005	0.0000
10	9.40	0.0006	9.40	0.0004	0.0006	0.0002
11	9.66	0.0342	9.66	0.0344	0.0009	0.0002
12	9.73	0.2270	9.73	0.2270	0.0005	0.0000
13	9.99	0.0166	9.99	0.0170	0.0013	0.0004
14	10.06	0.1115	10.06	0.1112	0.0011	0.0003
15	10.26	0.0000	10.26	0.0000	0.0013	0.0000
16	10.28	0.0369	10.28	0.0365	0.0016	0.0004
17	10.29	0.0429	10.29	0.0431	0.0011	0.0002
18	10.37	0.0000	10.37	0.0000	0.0008	0.0000

tion of condensation nuclei (CN) layer and acid rain. The formation of aerosol layer can significantly influence the global climate and chemistry of the atmosphere. Sulfur dioxide has attracted high attention in fundamental sciences and astronomical and environmental studies [16].

The availability of SO_2 experimental spectra, its relatively small size and similar structure to the sulfur-containing molecules studied in chapter 4, make this molecule a good candidate for benchmarking purposes. This allows us to investigate a wider range of theoretical parameters than could be done for the larger sulfur molecules in chapter 4.

3.2.1 Newton-X parameters benchmark

In this section, parameters affecting the simulated electronic absorption spectra are studied and the calculated results are compared with the experimental spectra. The simulation parameters that we benchmark in this section are: sampling approach, number of geometries in the ensemble, the phenomenological broadening of the spectrum (δ) and the band shape.

The first parameter that we consider, is the sampling type where we try three distributions, classic harmonic oscillator (distribution 1), Wigner distribution (distribution 2) and correlated quantum harmonic oscillator (distribution 3). We compare spectra simulated using these three distributions in Figure 3.1. These spectra are obtained using EOM-CCSD/aug-cc-pV(D+d)Z+3 electronic transitions, with an ensemble of 2000 geometries, convoluted with δ= 0.1 eV. We find that the three spectra simulated from the different sampling types, yield spectra that are similar near the band maxima but very different in between. This difference is much more significant in the lower energy region, below 8.0 eV.

In Figure 3.2, we plot the difference between the two S-O bond distances

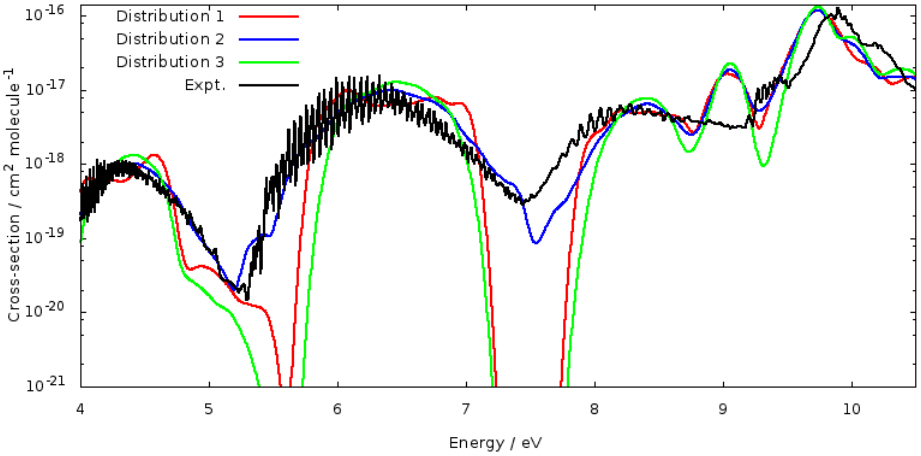

Figure 3.1: EOM-CCSD/aug-cc-pV(D+d)Z+3 simulated spectra of SO_2 from 2000 points and δ of 0.1 eV using three distributions, Classic harmonic oscillator (distribution 1), Wigner distribution (distribution 2) and correlated quantum harmonic oscillator(distribution 3) and the experimental spectrum at 293 K from Manatt *et. al.* [172].

of each geometry in the ensemble from its equilibrium. We find that the S-O bond distances from the Wigner samples are distributed in a slightly wider range compared to those from the other two approaches.

This suggests that the Wigner distribution can generate an ensemble of geometries that is a better representative of the molecule under investigation and as a result produces the simulated spectrum in closest agreement with experiment. It also suggests that it is convenient to assume that the motion of the ground state is harmonic and to use a Wigner distribution to sample the normal coordinates for the quantum harmonic oscillator [173]. This result is consistent with previous studies of the electronic absorption spectrum of benzene, furan and 2-phenylfuran which also found that the Wigner distribution performed best [151]. Hence, we will use a Wigner distribution when constructing an ensemble for the spectral simulations in this thesis and all the molecules are assumed to be in their ground vibrational

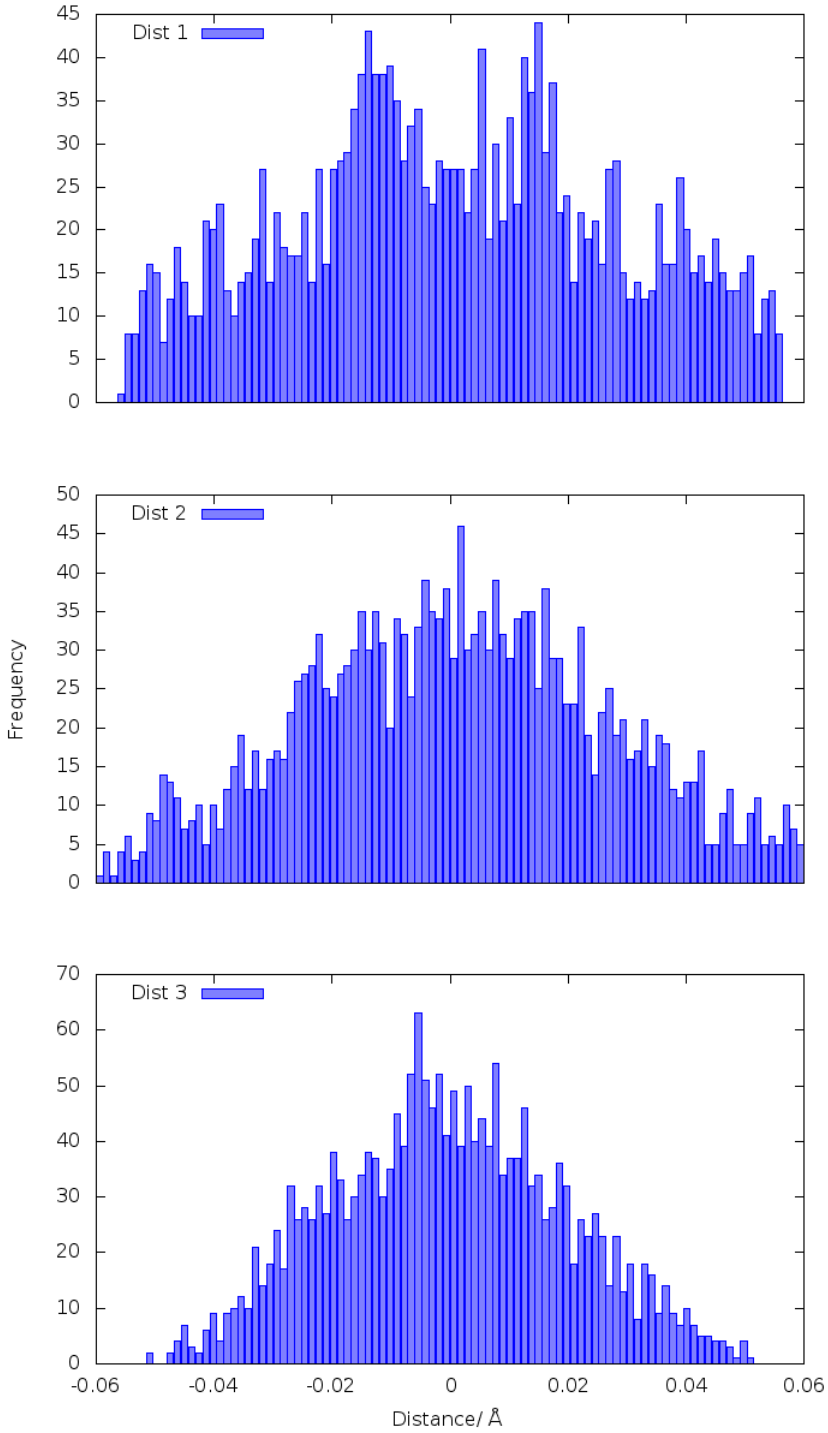

Figure 3.2: Three distributions, Classic harmonic oscillator (distribution 1), Wigner distribution (distribution 2) and correlated quantum harmonic oscillator(distribution 3).

state.

An ensemble with more geometries is a more realistic representation of the system; however, the more geometries that are included in the ensemble, the more CPU-demanding the overall spectrum is. Therefore, the least number of sampled geometries which gives results with reasonable accuracy is needed. Figure 3.3 shows the EOM-CCSD/aug-cc-pV(D+d)Z+3 absorption cross section and the numerical integration error associated with the cross section calculation for ensembles of 100, 1000, 2000 and 5000 geometries. As expected, the numerical integration error reduces as the number of points in the ensemble increases. While the 5000 point ensemble shows the smoothest spectrum, the results obtained from an ensemble of 2000 points is also smooth enough, and is 2.5 times less expensive to simulate.

The next parameter to be considered is the band shape used for convoluting each transition to construct the spectra. To benchmark this parameter, we convolute the calculated electronic transitions with a Lorentzian or a Gaussian function using the fact that the width of these functions is related to the excited state lifetime [173]. The results are presented in Figure 3.4. Again we use the underlying EOM-CCSD/aug-cc-pV(D+d)Z+3 results, simulated from 2000 geometries and δ of 0.1 eV. There is not a clearly best band shape to use, with the Gaussian the cross section is often underestimated and with the Lorentzian, the cross section is often overestimated. However, the Lorentzian gives an unphysical convergence to a cross section of approximately 10^{-19} cm^2 molecule^{-1} at 3.0 eV. In chapter 4, we are particularly interested in the lowest energy region and the Gaussian gives noticeably better results for SO_2 here and hence, we choose the Gaussian band shape over the Lorentzian.

The last simulation parameter that is benchmarked, is the phenomeno-

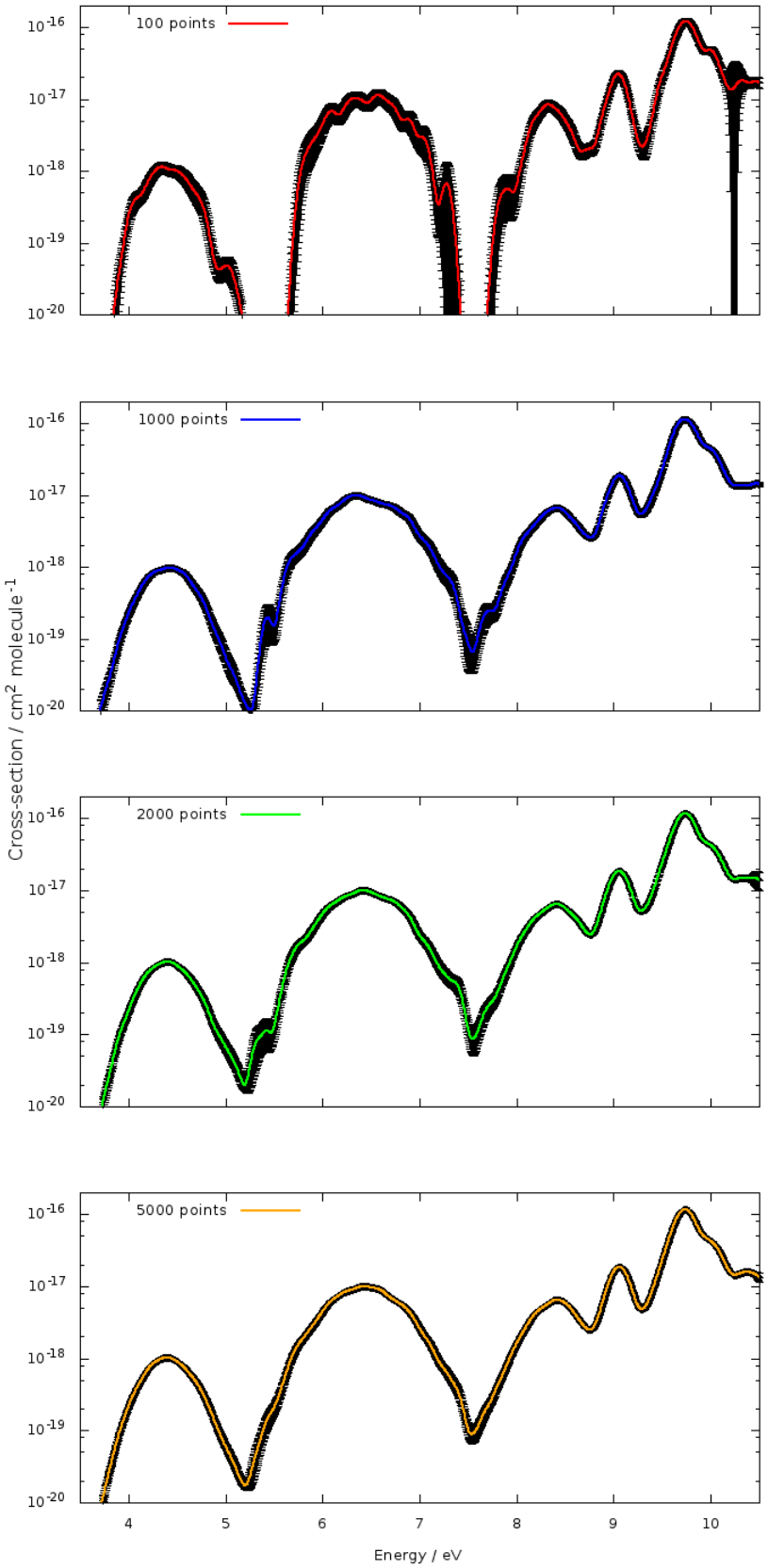

Figure 3.3: EOM-CCSD/aug-cc-pV(D+d)Z+3 absorption cross sections convoluted to a Gaussian band shape of 0.1 eV, and error bars for 100, 1000, 2000 and 5000 points included in the ensemble for SO_2.

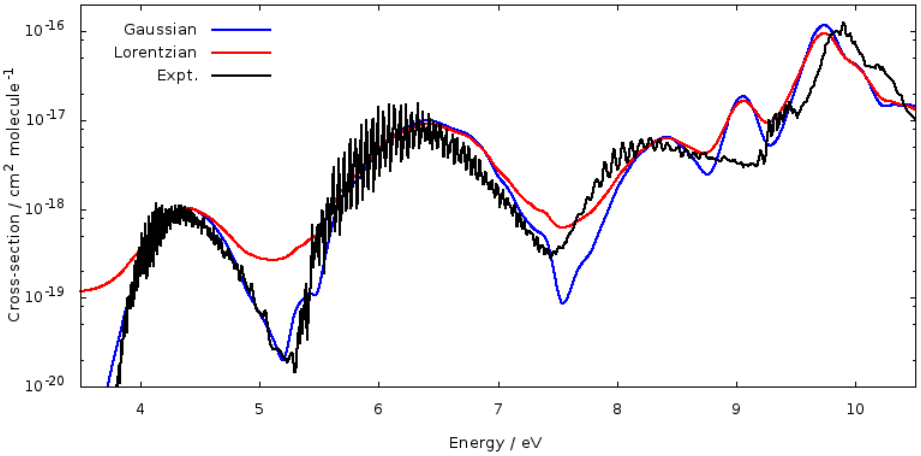

Figure 3.4: EOM-CCSD/aug-cc-pV(D+d)Z+3 absorption cross sections of SO_2 from 2000 points and δ of 0.1 eV with the two Gaussian and Lorentzian band shapes compared with the experimental spectrum at 293 K from Manatt *et. al.* [172].

logical broadening of the spectrum (δ), full-width half maximum (FWHM). The SO_2 spectra simulated from different δ values from 0.01 eV to 0.2 eV are presented in Figure 3.5 and compared with the experimental cross section from Manatt *et al* [172]. We find that the spectra simulated from 0.1 and 0.2 eV broadenings are the closest to the experimental spectrum and hence, we choose the narrower 0.1 eV broadening to use later in spectra simulation.

The most balanced combination of Newton-X parameters is achieved by an ensemble of 2000 geometries, sampled with a Wigner distribution, with the electronic transitions convoluted with a Gaussian band shape of 0.1 eV.

3.2.2 Electronic structure parameters benchmark

In this section, we benchmark the *ab initio* method and basis set, to find the most balanced combination for simulating the electronic absorption spectra. These parameters can significantly affect the overall computational cost of the simulated spectra.

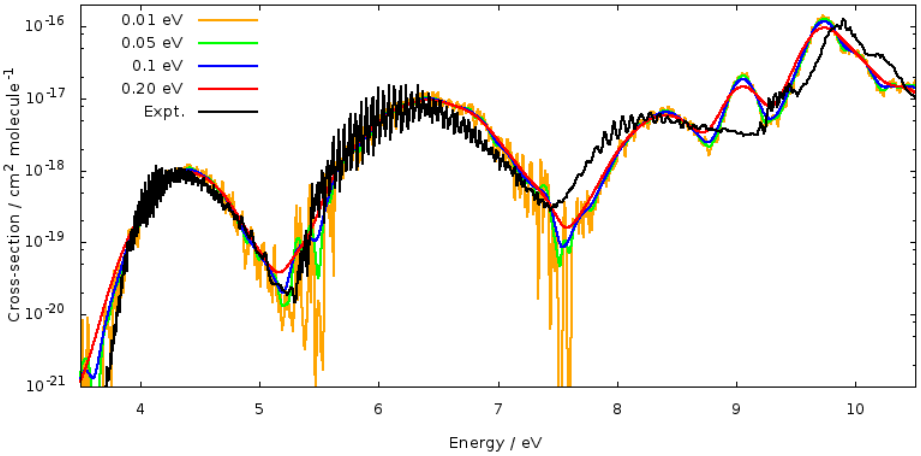

Figure 3.5: SO_2 absorption cross sections convoluted to the Gaussian band shape and from four phenomenological broadening of the spectrum values (eV), for 2000 points at EOM-CCSD/aug-cc-pV(D+d)Z+3 level of theory compared with the experimental spectrum at 293 K from Manatt *et. al.* [172].

In Figure 3.6, the generated spectra of SO_2 from different *ab initio* methods, EOM-CCSD, RI-CC2 and ADC(2), with the aug-cc-pV(D+d)Z+3 basis set are presented and compared. We find that while in lower energy regions the calculated cross sections from the three *ab initio* methods are not very different, the RI-CC2 and ADC(2) methods are poor in describing the higher energy bands. For these, the shape of the high energy bands are reasonable but the position is too low in energy. Among the investigated methods, EOM-CCSD shows the best agreement with the experimental spectrum.

The other electronic structure parameter that we benchmark in this section is the basis set. We pick the best *ab initio* method from previous comparison, *i.e.* EOM-CCSD, and benchmark different basis sets and compare the results with the experimental spectra in Figure 3.7. The chosen basis sets are aug-cc-pV(X+d)Z+3, where X=D, T and Q. Comparing the simulated spectra from these three basis sets with the experimental results in

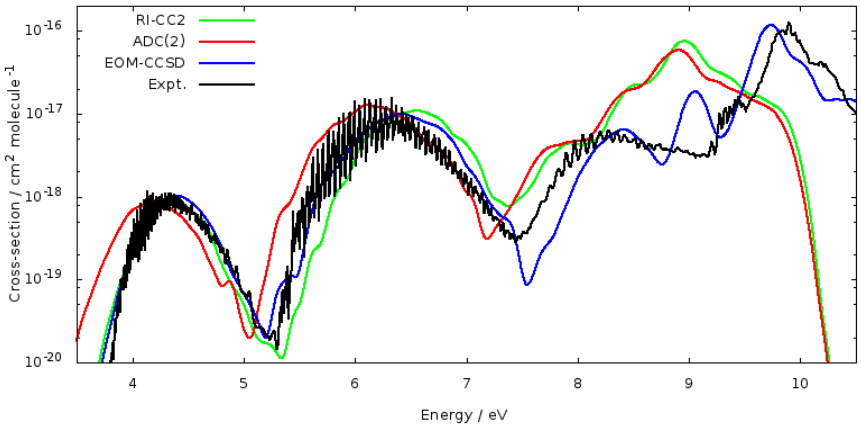

Figure 3.6: SO_2 simulated spectra from EOM-CCSD, RI-CC2 and ADC(2) methods with aug-cc-pV(D+d)Z+3 basis set and the experimental spectrum at 293 K from Manatt *et. al.* [172].

Figure 3.7, shows that both aug-cc-pV(T+d)Z+3 and aug-cc-pV(Q+d)Z+3 spectra exhibit better agreement with the experiment than the cross section calculated from the aug-cc-pV(D+d)Z+3 results. Also, we see good convergence in calculated energies with increasing size of the basis set. The aug-cc-pV(Q+d)Z+3 cross section is not very different from the aug-cc-pV(T+d)Z+3; however, the computational cost of the spectrum simulated from the aug-cc-pV(Q+d)Z+3 energy results is significantly higher; 17 hours versus 72 hours of CPU time per point for aug-cc-pV(T+d)Z+3 and aug-cc-pV(Q+d)Z+3, respectively.

Considering the two electronic structure benchmark results, *i.e. ab initio* method and basis set, we find EOM-CCSD/aug-cc-pV(T+d)Z+3 level of theory as the most balanced electronic structure parameter combination, which can generate cross sections in close agreement to the experimental results.

In a previous work by Crespo-Otero *et al.* [151], absorption spectra of benzene, furan and 2-phenylfuran, were benchmarked using the nuclear en-

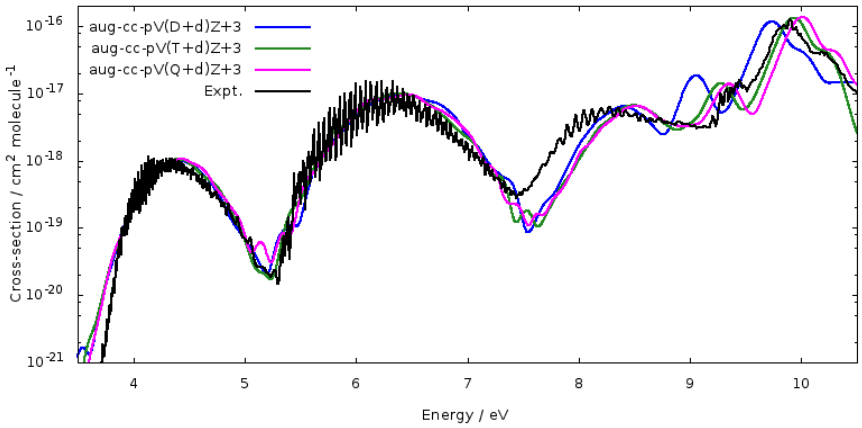

Figure 3.7: EOM-CCSD simulated cross sections of SO_2 from three aug-cc-pV(D+d)Z+3, aug-cc-pV(T+d)Z+3 and aug-cc-pV(Q+d)Z+3 basis sets and the experimental spectrum at 293 K from Manatt *et. al.* [172].

semble approach and different Newton-X and electronic structure parameters. For furan, an ensemble of 350 geometries was used and the cross sections were convoluted to the Gaussian band shape with a phenomenological broadening of 0.05 eV. For benzene and 2-phenylfuran, an ensemble of 500 and 850 geometries were used to simulate the spectra and the cross sections were convoluted to the Gaussian band shape of broadening of 0.05 eV. These simulated spectra were shown to be in reasonable agreement with the experimental spectra especially for the bright bands [151].

3.2.3 Approximation approach

Calculating excited states energies and oscillator strengths at EOM-CCSD/aug-cc-pV(T+d)Z+3 level of theory for 2000 geometries in the ensemble can be very cost demanding for medium size molecules and almost impossible for large molecules with many electrons. To achieve reasonably good accuracy close to EOM-CCSD/aug-cc-pV(T+d)Z+3 but at much lower cost, we introduce an approximate approach in this section and validate our results

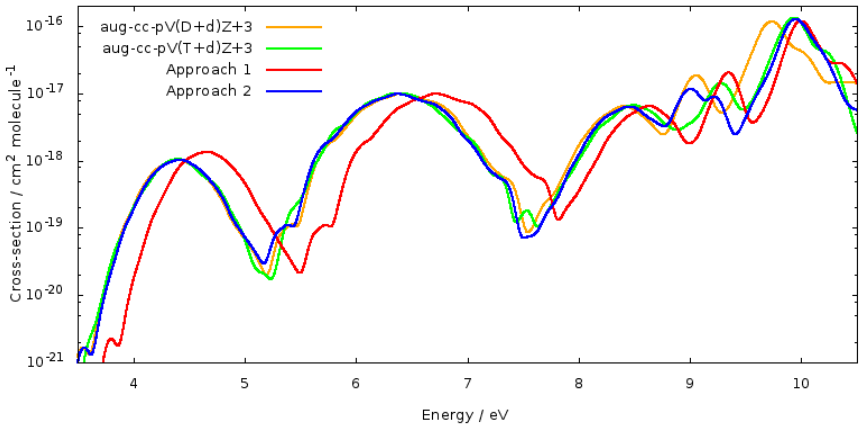

Figure 3.8: Approximated EOM-CCSD/ aug-cc-pV(T+d)Z+3 cross section of SO_2 from approaches 1 and 2 compared with EOM-CCSD calculated cross section from aug-cc-pV(T+d)Z+3 and aug-cc-pV(D+d)Z+3 basis sets.

against the fully calculated SO_2 results. We consider two separate but related approaches to do this.

In approach 1, we take the ground state geometry optimized at the CCSD/aug-cc-pV(D+d)Z+3 and CCSD/aug-cc-pV(T+d)Z+3 levels of theory. Then we calculate the vertical excitations and oscillator strengths with the EOM-CCSD method using the aug-cc-pV(D+d)Z+3 and aug-cc-pV(T+d)Z+3 basis sets, respectively and compare the results rigorously to identify any ordering switches. The absolute difference in the vertical excitation energies and the percentage change of the oscillator strengths of each state are calculated. The energies and intensities of each individual state of each of the 2000 EOM-CCSD/aug-cc-pV(D+d)Z+3 geometries in the ensemble, are then shifted applying the differences in the vertical excitation energies and oscillator strengths from comparing the energies and oscillator strengths of EOM-CCSD/aug-cc-pV(D+d)Z+3 and EOM-CCSD/aug-cc-pV(T+d)Z+3 results. These individually corrected vertical excitations and oscillator strengths are later summed over the states to produce the

final approximate EOM-CCSD/aug-cc-pV(T+d)Z+3 spectrum of SO_2 (approach 1).

In approach 2, we randomly pick 10 geometries from the previously distributed 2000-point ensemble. We run two EOM-CCSD excited states energy calculations on each of these 10 geometries using aug-cc-pV(D+d)Z+3 and aug-cc-pV(T+d)Z+3 basis sets, respectively. We compare the excited states energies and oscillator strengths from the two levels of theory and calculate the averaged absolute vertical excitation difference and the percentage change of the oscillator strengths for each individual state. Similar to approach 1, these averaged vertical excitation differences and oscillator strength percentage changes are then applied to the 2000 EOM-CCSD/aug-cc-pV(D+d)Z+3 vertical excitation energies and oscillator strengths of the individual states. These corrected electronic transitions are then summed over the states to produce the second approximate EOM-CCSD/aug-cc-pV(T+d)Z+3 spectrum of SO_2 (approach 1).

The approximate spectra generated from these two approaches are presented and compared with the full uncorrected EOM-CCSD/aug-cc-pV(D+d)Z+3 and EOM-CCSD/aug-cc-pV(T+d)Z+3 spectra in Figure 3.8. To more clearly distinguish between the two approaches, the differences between these two approximate spectra and the full uncorrected EOM-CCSD/aug-cc-pV(T+d)Z+3 spectra are plotted and shown in Figure 3.9. This comparison shows a smaller difference between the spectrum simulated from approach 2 and the original calculated EOM-CCSD/aug-cc-pV(T+d)Z+3, compared to that simulated from approach 1. This means that the EOM-CCSD/aug-cc-pV(T+d)Z+3 spectra is more accurately approximated with approach 2, where 10 random points in the ensemble are used for correcting the vertical excitations and oscillator strengths. In other words, correcting with 10 random points can

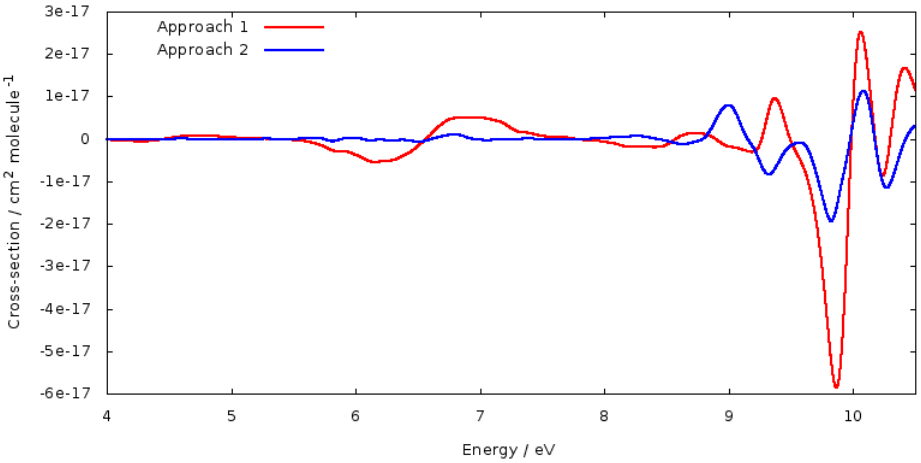

Figure 3.9: The difference graphs of the approaches 1 and 2 spectra from the calculated EOM-CCSD/ aug-cc-pV(T+d)Z+3 spectrum of SO_2.

sample the ensemble better than correcting with just one equilibrium geometry.

Finally and in Figure 3.10, we present our approximate EOM-CCSD/aug-cc-pV(T+d)Z+3 spectrum of SO_2 with the calculated EOM-CCSD/aug-cc-pV(D+d)Z+3 and experimental spectrum from Manatt *et. al* [172]. This approximate spectrum is in good agreement with the fully calculated EOM-CCSD/aug-cc-pV(T+d)Z+3 spectrum, but computationally costs much less. In our SO_2 cross section calculation, it takes 17 hours of CPU time to calculate the EOM-CCSD electronic transitions of each geometry in the ensemble with the aug-cc-pV(T+d)Z+3 basis set and 2 hours for the same calculation with the smaller aug-cc-pV(D+d)Z+3 basis set. This means that the fully calculated aug-cc-pV(T+d)Z+3 spectrum takes approximately 34000 hours whereas the approximate spectrum calculated with approach 2 takes only 4170 hours. This is a significant reduction that would be even larger for molecules with more electrons due to the formal N^6 scaling of EOM-CCSD.

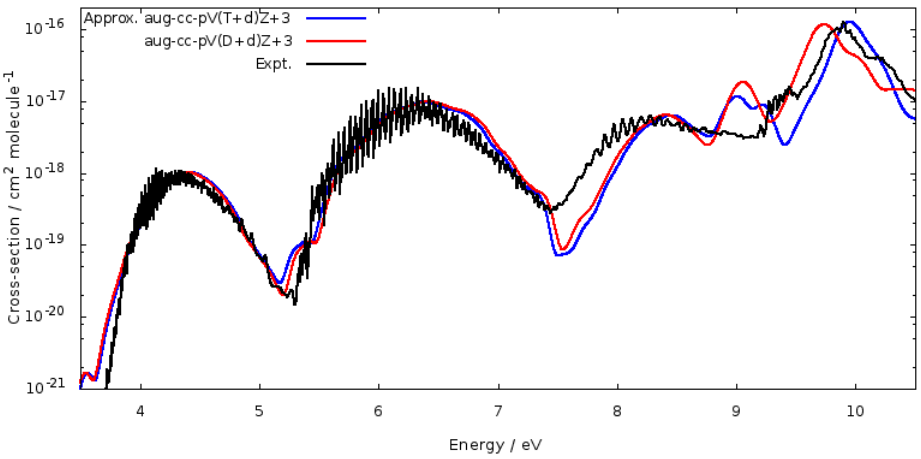

Figure 3.10: Approximate EOM-CCSD/aug-cc-pV(T+d)Z+3 and calculated EOM-CCSD/aug-cc-pV(D+d)Z+3 cross section of SO_2 compared with the experimental results at 293 K from Manatt *et. al.* [172].

3.3 Testing a molecule: H_2S, CS_2, OCS and SO_3

A thorough investigation of the individual parameters is given in appendices (A.2-A.24) and a brief comparison for each parameter is given in the related subsection for each molecule. As the trends in the mentioned benchmarking graphs are almost the same as those presented and discussed for SO_2, they are not discussed in detail here.

3.3.1 H_2S

Hydrogen sulfide (H_2S), with astronomical and atmospheric importance is a reduced form of sulfur found in the atmosphere of the Earth and some other planets like Jupiter [174] and IO [175] as well as in interstellar medium [176] and star forming regions [177]. It plays an important role in the global cycle of sulfur and it is mainly emitted to the atmosphere by volcanic eruption and biogenic emissions. The experimental absorption cross section of H_2S has been extensively studied [19, 178–181]. The absorption spectrum of H_2S recorded by Feng *et al.* [19], is shown in Figure 3.11. The main features of the experimental spectrum of H_2S are an absorption continuum from 5.2-7.7 eV and a series of sharp Rydberg transitions from about 8.0 to 9.0 eV [19]. The most intense peak in this experimental spectrum is at about 8.9-9.0 eV. In Figure 3.12, we compare our final approximate EOM-CCSD/aug-cc-pV(T+d)Z+3 spectrum with the full calculated EOM-CCSD/aug-cc-pV(D+d)Z+3 spectrum and the experimental spectrum of Grosch *et. al* [20] (5.0-6.3 eV) at 294.8 K, Wu and Chen [182] (6.3-7.7 eV) at 295 K and Feng *et al.* (7.7-9.6 eV) [19]. Our approximate EOM-CCSD/aug-cc-pV(T+d)Z+3 shows good agreement in terms of band position, however compared to the experimental spectrum, it is less structured as we do not simulate the vibrational fine structures.

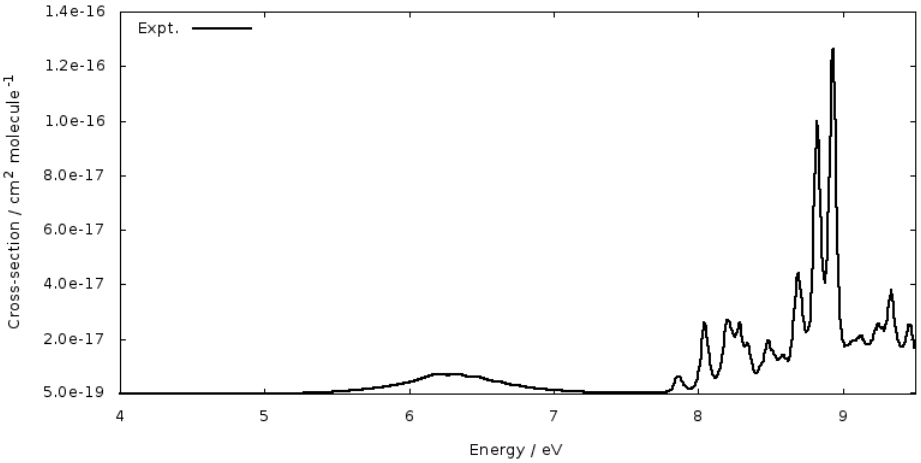

Figure 3.11: Experimental absorption cross section of H_2S from Grosch *et. al* [20] (5.0-6.3 eV) at 294.8 K, Wu and Chen [182] (6.3-7.7 eV) at 295 K and Feng *et al.* (7.7-9.6 eV) [19].

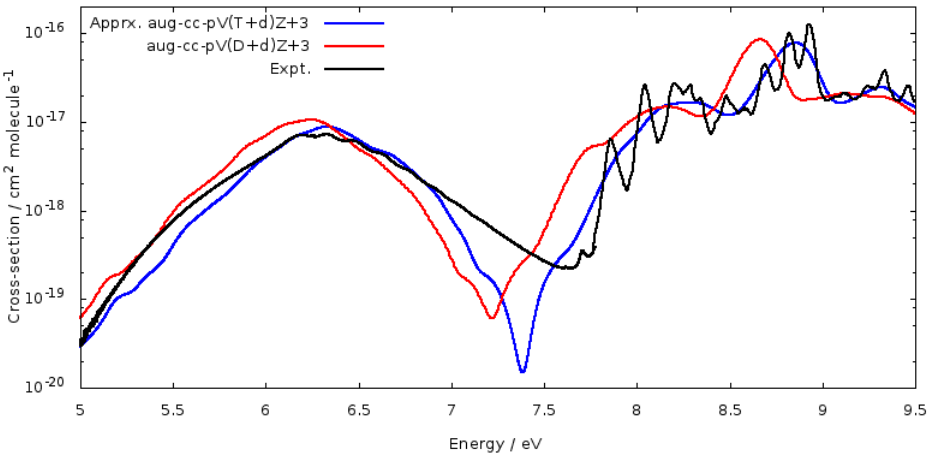

Figure 3.12: Approximate EOM-CCSD/aug-cc-pV(T+d)Z+3 and calculated EOM-CCSD/aug-cc-pV(D+d)Z+3 cross sections of H_2S compared with the experimental results from Grosch *et. al* [20] (5.0-6.3 eV) at 294.8 K, Wu and Chen [182] (6.3-7.7 eV) at 295 K and Feng *et al.* (7.7-9.6 eV) [19].

For H_2S, we include the 18 lowest energy electronic excited states in our spectra simulations. The full benchmarking results can be found in the appendices, including the number of points in the ensemble (A.1), the phenomenon broadening width (A.2), and the electronic structure method

(A.3).

We compare the calculated EOM-CCSD/aug-cc-pV(T+d)Z+3 spectrum for H_2S and the experimental spectrum which shows a good agreement (Figure A.4). We also compare the calculated EOM-CCSD/aug-cc-pV(D+d)Z+3 and EOM-CCSD/aug-cc-pV(T+d)Z+3 spectra. This comparison shows a clear shift in the bright band of the spectrum (Figure A.5). In Figure A.5, the two approximate spectra are also compared and found to be in good agreement with the full calculated EOM-CCSD/aug-cc-pV(T+d)Z+3 spectrum. We calculate the difference between the two approximate spectra and the full EOM-CCSD/aug-cc-pV(T+d)Z+3 and compare the calculated surface under the two difference graphs. We find approach 2 to produce spectrum 1.2 times closer to the full calculated EOM-CCSD/aug-cc-pV(T+d)Z+3 spectrum, showing the two approximate approaches yield similar results (Figure A.6).

3.3.2 CS_2

Carbon disulfide (CS_2), is also an atmospheric sulfur compound with indirect greenhouse gas effect that can contribute to CO_2 production [183]. It can also react with OH and produce SO_2 [184]. The absorption spectrum of CS_2 is quite structured and shows both valence and Rydberg characters [22]. The 5.5-7.0 eV region shows richly structured bands which are assigned to valence transitions. The weak bands in the 7.0-7.6 eV region belong to a dipole forbidden ($X^1\ {\Sigma_g}^+ \rightarrow {}^1\Pi$) and the region between 7.6-8.1 eV belong to Rydberg transitions [22].

For CS_2, we include the 18 lowest energy electronic excited states in our spectra simulations. The full benchmarking results can be found in the appendices, including the number of points in the ensemble (A.7), the

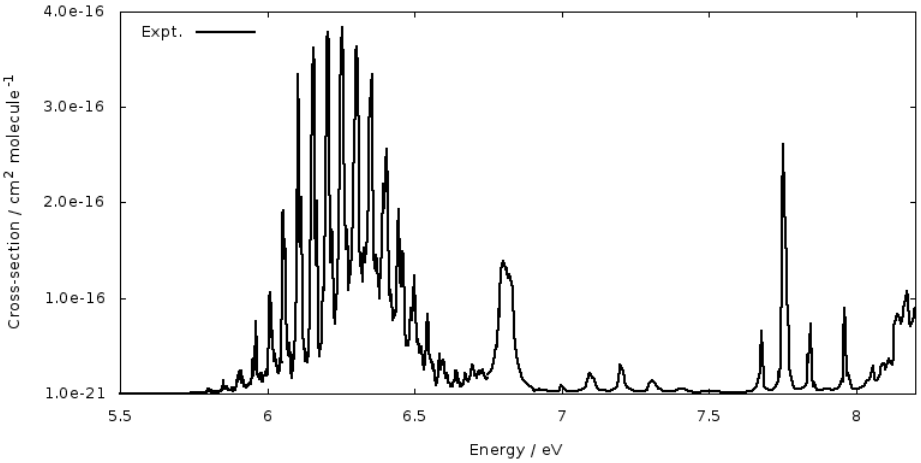

Figure 3.13: Experimental absorption cross section of CS_2 from Grosch *et. al* [20] (3.3-6.0 eV) at 294.8 K, Sunanda *et. al* [22] (6.0-6.7 eV) at 298 K and Rabalais *et. al* [185] (6.7-8.2 eV) at 298 K.

phenomenon broadening width (A.8), and the electronic structure method (A.9). In Figure 3.14, we compare our final approximate EOM-CCSD/aug-cc-pV(T+d)Z+3 spectrum of CS_2 with the experimental spectrum from Grosch *et. al* [20], Sunanda *et. al* [22] and Rabalais *et. al* [185]. While the agreement with the experimental spectrum in lower energy region is generally good, in the region of forbidden bands and higher energy region, some structures of the spectrum are missed from the calculated spectrum. The experimental spectrum has an unreasonable background absorption of 10^{-16} cm^2 $molecule^{-1}$. This is not noticeable on a linear scale but is evident on a log scale.

We compare the calculated EOM-CCSD/aug-cc-pV(T+d)Z+3 spectrum for CS_2 and the experimental spectrum from Grosch *et. al* [20] and Sunanda *et. al* [22] which shows a good agreement in terms of band position (Figure A.10). We also compare the calculated EOM-CCSD/aug-cc-pV(D+d)Z+3 and EOM-CCSD/aug-cc-pV(T+d)Z+3 spectra. This comparison shows that the two calculated spectra are similar in lower energy regions and they show

a clear shift in the higher energy bands (Figure A.11). Also in Figure A.11, the two approximate spectra are compared and found to be in good agreement with the full calculated EOM-CCSD/aug-cc-pV(T+d)Z+3 spectrum. We calculate the difference between the two approximate spectra and the full EOM-CCSD/aug-cc-pV(T+d)Z+3 and compare the calculated surface under the two difference graphs. We find approach 2 to produce spectrum 2.7 times closer to the full calculated EOM-CCSD/aug-cc-pV(T+d)Z+3 spectrum, showing approach 2 yields much closer results to EOM-CCSD/aug-cc-pV(T+d)Z+3 spectrum (Figure A.12).

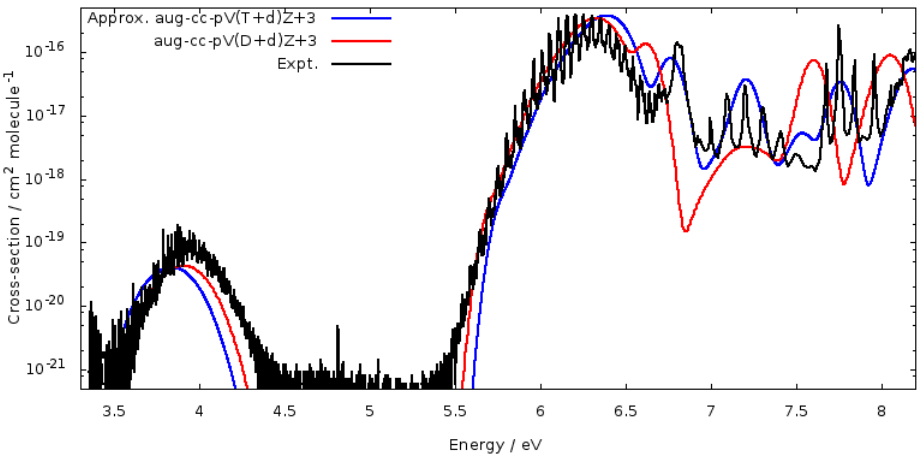

Figure 3.14: Approximate EOM-CCSD/aug-cc-pV(T+d)Z+3 and calculated EOM-CCSD/aug-cc-pV(D+d)Z+3 cross sections of CS_2 compared with the experimental results from Grosch *et. al* [20] (3.3-6.0 eV) at 294.8 K, Sunanda *et. al* [22] (6.0-6.7 eV) at 298 K and Rabalais *et. al* [185] (6.7-8.2 eV) at 298 K.

3.3.3 OCS

Carbonyl sulfide (OCS) is another sulfur molecule with important role in global cycle of sulfur [186] and has both natural [187] and anthropogenic sources [21, 188]. The experimental absorption spectrum of OCS, presented

in Figure 3.15, shows three bands around its three excitations and are centered at about 5.5, 7.4 and 8.1 eV [21]. Also a series of Rydberg transitions are observed in this spectrum from about 9.0 eV The first weak structureless band is due to the dipole forbidden transition.

In Figure 3.16, we compare our final approximate EOM-CCSD/aug-cc-pV(T+d)Z+3 spectrum of OCS with the experimental spectrum from Feng *et. al.*

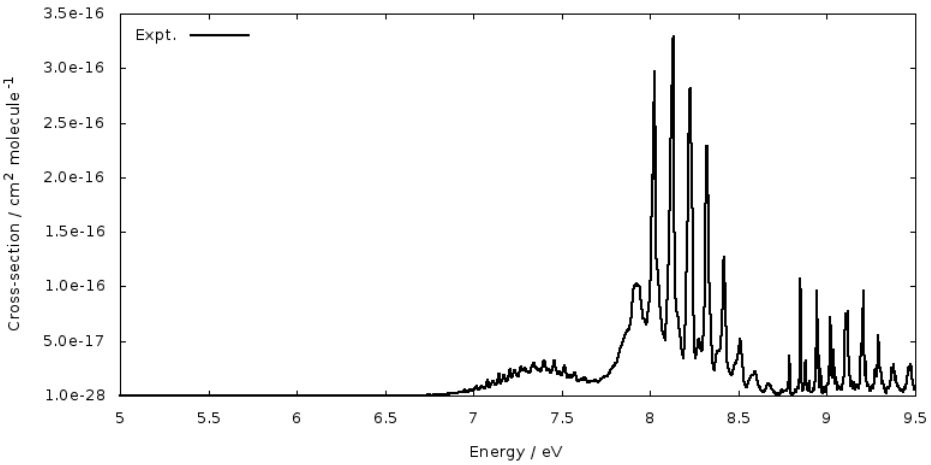

Figure 3.15: Experimental absorption cross section of OCS from Molina *et al.* [189] (4.1-4.8 eV) at 295 K and Limao-Vieira *et al.* [190] (4.8-9.3 eV) at 298 K.

For OCS, we include the 18 lowest energy electronic excited states in our spectra simulations. The full benchmarking results can be found in the appendices, including the number of points in the ensemble (A.13), the phenomenon broadening width (A.14), and the electronic structure method (A.15).

We compare the calculated EOM-CCSD/aug-cc-pV(T+d)Z+3 spectrum for OCS and the experimental spectrum from Molina *et al.* [189] (4.1-4.8 eV) at 295 K and Limao-Vieira *et al.* [190] (4.8-9.3 eV) at 298 K which shows a an excellent agreement (Figure A.16). We also compare the calculated

EOM-CCSD/aug-cc-pV(D+d)Z+3 and EOM-CCSD/aug-cc-pV(T+d)Z+3 spectra. This comparison shows that the simulated spectrum of OCS is not as sensitive as that of H_2S to the basis set, resulting in similar spectra with aug-cc-pV(D+d)Z+3 and aug-cc-pV(T+d)Z+3 basis sets (Figure A.17). Also in Figure A.17, the two approximate spectra are compared and found to be in good agreement with the full calculated EOM-CCSD/aug-cc-pV(T+d)Z+3 spectrum. We calculate the difference between the two approximate spectra and the full EOM-CCSD/aug-cc-pV(T+d)Z+3 and compare the calculated surface under the two difference graphs. We find approach 2 to produce spectrum 2.1 times closer to the full calculated EOM-CCSD/aug-cc-pV(T+d)Z+3 spectrum, showing approach 2 yields closer results to EOM-CCSD/aug-cc-pV(T+d)Z+3 spectrum (Figure A.18).

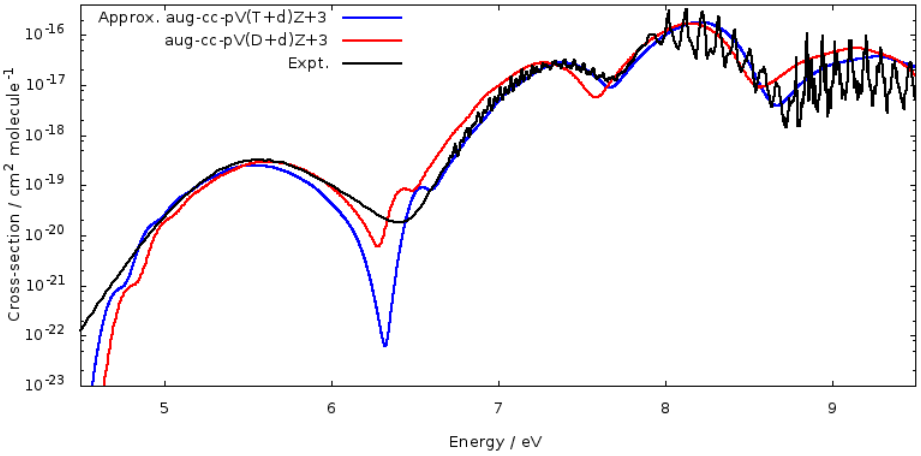

Figure 3.16: Approximate EOM-CCSD/aug-cc-pV(T+d)Z+3 and calculated EOM-CCSD/aug-cc-pV(D+d)Z+3 cross sections of OCS compared with the experimental results from Molina *et al.* [189] (4.1-4.8 eV) at 295 K and Limao-Vieira *et al.* [190] (4.8-9.3 eV) at 298 K.

3.3.4 SO_3

Sulfur trioxide (SO_3) the most abundant sulfur compound after SO_2 , reacts quickly with water to produce sulfate aerosol layer in lower altitude and where water exists [6]. It was also found to be an intermediate in the oxidation of SO_2 to H_2SO_4 [18]. In higher altitudes where water vapor is not available, SO_3 undergoes photodissociation by absorbing photons in the UV region [18]. There are some technical challenges in recording the absorption cross section of SO_3 due to the interfere of SO_2 absorption [18]. The experimental spectra recorded by Burkholder *et al.* [10, 18] are presented in Figure 3.17 with an intense peak at about 8.5 eV. We compare our final approximate EOM-CCSD/aug-cc-pV(T+d)Z+3 spectrum of SO_3 with the experimental spectra Burkholder *et al.* in Figure 3.18. In the regions where the experimental results are available, good agreement is observed between our simulated spectrum and the experimental results. However, this agreement is better in the lower energy region and worse for the intense peak.

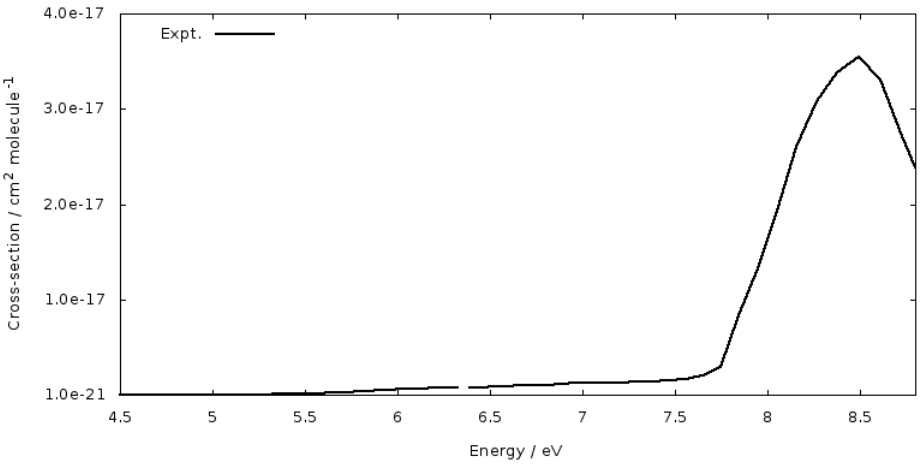

Figure 3.17: Experimental absorption spectra of SO_3 from Burkholder *et. al* [18] (4.8-6.4 eV) and Hintz *et. al* [17] (6.4-8.9 eV) at 403 K.

For SO_3, we include the 18 lowest energy electronic excited states in our spectra simulations. The full benchmarking results can be found in the appendices, including the number of points in the ensemble (A.19), the phenomenon broadening width (A.20), and the electronic structure method (A.21).

We compare the calculated EOM-CCSD/aug-cc-pV(T+d)Z+3 spectrum for SO_3 and the experimental spectra from Burkholder *et al.* [10, 18], which shows a reasonable agreement between the two spectra in terms of band position (Figure A.22). We also compare the calculated EOM-CCSD/aug-cc-pV(D+d)Z+3 and EOM-CCSD/aug-cc-pV(T+d)Z+3 spectra. This comparison shows that the two calculated spectra are very similar specially in energy regions lower than 10 eV (Figure A.23). Also in Figure A.23, the two approximate spectra are compared and found to be in much less agreement with each other compared with the other testing molecules in terms of band position. We calculate the difference between the two approximate spectra and the full EOM-CCSD/aug-cc-pV(T+d)Z+3 and compare the calculated surface under the two difference graphs. We find approach 2 to produce spectrum 2.7 times closer to the full calculated EOM-CCSD/aug-cc-pV(T+d)Z+3 spectrum, showing approach 2 yields much closer results to EOM-CCSD/aug-cc-pV(T+d)Z+3 spectrum (Figure A.24).

3.4 Conclusion

We investigated various theoretical parameters for simulating the electronic absorption spectrum of SO_2. The combination of the parameters that gave the best agreement with the experimental spectrum of SO_2 was then applied to four other molecules, namely H_2S, CS_2, OCS and SO_3. We found that with EOM-CCSD/aug-cc-pV(T+Z)+3 results, the cross section calculated

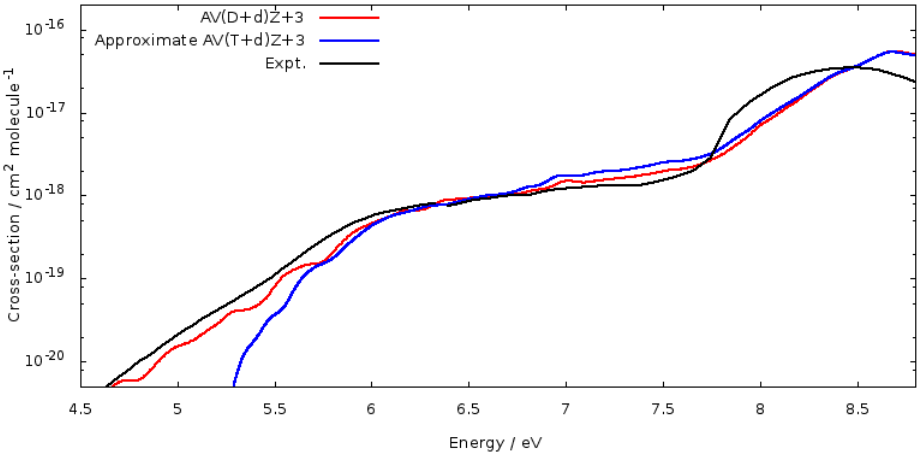

Figure 3.18: Approximate EOM-CCSD/aug-cc-pV(T+d)Z+3 and calculated EOM-CCSD/aug-cc-pV(D+d)Z+3 cross sections of SO_3 compared with the experimental results from Burkholder *et. al* [18] (4.8-6.4 eV) and Hintz *et. al* [17] (6.4-8.9 eV) at 403 K.

from an ensemble of 2000 points sampled using a Wigner distribution and convoluted to a Gaussian band shape of phenomenological broadening of 0.1 eV, can produce the closest spectrum to the experimental spectrum.

We also developed and introduced two approximate approaches that use a combination of EOM-CCSD/aug-cc-pV(D+Z)+3 and EOM-CCSD/aug-cc-pV(T+Z)+3 results. For each molecule, we compared the two approximated spectra with the full calculated EOM-CCSD/aug-cc-pV(T+Z)+3 spectrum to determine the most efficient approach between the two. In all the cases, approach 2 showed better agreement with the full calculated EOM-CCSD/aug-cc-pV(T+Z)+3 spectrum.

In chapter 4, we will apply our approximate approach on two sulfur-containing molecules, where the experimental spectra are unknown, namely H_2SO_4 and OSSO.

Chapter 4

Unknown sulfur molecules

In this chapter, we simulate the electronic absorption spectra of some important sulfur-containing molecules, where experimental spectra are not yet available. To simulate the spectra of C_2 and C_s-H_2SO_4 and *cis* and *trans*-OSSO molecules, we use the approximate approach developed and discussed in chapter 3, to present the most efficient results in terms of accuracy and computational cost. The results on sulfuric acid together with the benchmarking results from chapter 3 are published in a journal article [171].

4.1 Sulfuric acid

Sulfuric acid (H_2SO_4) is the third dominant atmospheric sulfur molecule after SO_2 and SO_3 in the Earth's atmosphere [9, 10] with important atmospheric roles. There is no experimental electronic absorption cross section for this molecule and the previous experimental efforts could only set some upper limits [9, 17]. There are technical challenges with regarding gas-phase spectra of H_2SO_4, including its low vapor pressure, high corossivity and its low absorption in the UV region, coupled with interference of absorption of SO_3 and H_2O molecules [17]. The only and first available theoretical spec-

trum of H_2SO_4 is from Lane *et al.*, where they convoluted vertical excitation energies and intensities [25] to simulate the spectrum. This spectrum, however simplistic, was in general agreement with the experimental upper limits for the cross section from Hintze *et al.* [17].

In the present work, we make several improvements to the earlier calculated spectrum of Lane *et al.* [25]. Firstly, we use the nuclear ensemble approximate approach to simulate the width of the electronic absorption bands. Also, we consider the two lowest energy conformers of H_2SO_4 whereas in the previous spectrum from Lane *et al.* [25], only the most stable conformer was considered. This improved spectrum, which is the first pure *ab initio* absorption spectrum of H_2SO_4, can be used in the future experimental investigation on sulfuric acid and in atmospheric modeling.

4.1.1 Theoretical details

The equilibrium geometry and vibrational frequencies of H_2SO_4 are calculated with the CCSD(T) method and aug-cc-pV(T+d)Z basis set for sulfur atom and aug-cc-pVTZ basis set for other atoms. As previously discussed in chapter 2, we use nuclear ensemble approach to simulate the cross section. To do so, using a Wigner distribution, an ensemble of geometries around the equilibrium geometry is created in the ground vibrational state of ground electronic state. These geometries are promoted to the 18 excited states and the vertical excitations and oscillator strengths are calculated at different levels of theory, EOM-CCSD, RI-CC2 and ADC(2) methods and different Dunning's correlation consistent basis sets.

4.1.2 Absorption cross section

It was previously shown that H_2SO_4 has two low energy conformers, C_2 and C_s-H_2SO_4 as shown in Figure 4.1, with calculated 3-8 kJ/mol energy difference, and with C_2-H_2SO_4 being the more stable conformer [191]. Using statistical mechanics and the CCSD(T)/aug-cc-pV(T+d)Z rotational constants and the vibrational frequencies, we calculate the Gibbs free energy and the population percentages of the two conformers in different altitudes with different temperatures and pressures as well as the equilibrium constants. The results are tabulated in Table 4.1. The Gibbs free energy of the two conformers are plotted against altitude in Figure 4.2 and the population percentage of the C_2 conformer is plotted in different altitudes in Figure 4.3. The equilibrium constant of these two conformers are also calculated in different altitudes and presented in Figure 4.4. These results show that the contribution of C_s-H_2SO_4 to the atmospheric concentration of sulfuric acid is significant, with 24-26 % of the total atmospheric H_2SO_4. Consequently, this contribution of the C_s-H_2SO_4 cross section should be considered in the spectra simulation.

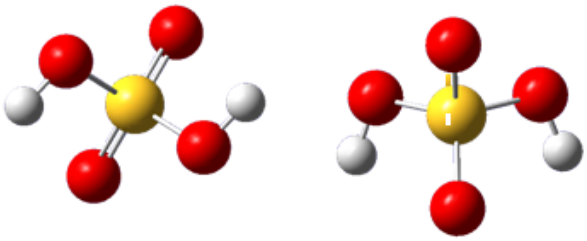

Figure 4.1: The two lower energy conformers of sulfuric acid, C_2- H_2SO_4 (left) and C_2- H_2SO_4 (right).

For both C_2 and C_s-H_2SO_4 conformers, we include the 18 lowest electronic excited states in the spectra simulations. Although there is no exper-

Table 4.1: Difference in Gibbs free energy and equilibrium constant and population percentages of C_2 and C_s conformers of sulfuric acid in different altitudes, temperatures and pressures.

Altitude(km)	$T(K)$	$P(Pa)$	$\Delta G(Jmol^{-1})$	$C_2\%$	$C_s\%$	K
0	288.15	101325	2452.587	73.57	26.43	0.359
5	255.68	54050	2395.703	75.53	24.47	0.324
10	223.25	26500	2140.585	76.01	23.99	0.316
15	216.65	12110	2089.492	76.13	23.87	0.313
20	216.65	5225	2089.492	76.13	23.87	0.313
25	221.55	2549	2127.395	76.04	23.96	0.315
30	226.51	1197	2165.936	75.95	24.05	0.317
35	236.51	574.6	2244.138	75.79	24.21	0.317
40	250.35	287.1	2353.361	75.59	24.41	0.323
45	264.20	149.1	2463.677	75.43	24.57	0.326
50	270.65	79.779	2515.360	75.36	24.64	0.327
60	247.02	21.96	2326.984	75.64	24.36	0.322
70	219.58	5.2	2112.135	76.08	23.92	0.315
80	198.64	1.1	1951.828	76.53	23.47	0.307
90	190	0.2	1886.824	76.75	23.25	0.303
100	210	0.04	2038.346	76.27	23.73	0.311

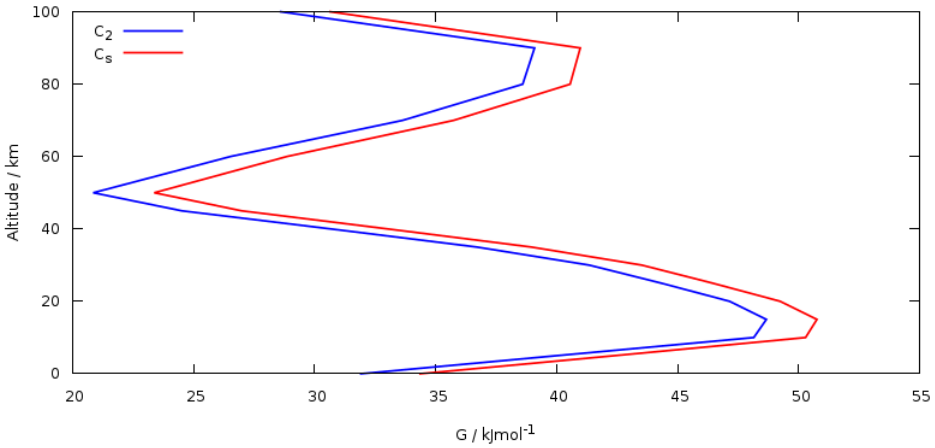

Figure 4.2: Gibbs free energy of C_2- H_2SO_4 and C_s- H_2SO_4 in different altitudes.

imental spectrum of H_2SO_4 to be compared with the simulated spectra, we benchmark the Newton-X and electronic structure parameters for the more stable conformer, C_2-H_2SO_4, to see if the trend is the same as those observed for the sulfur benchmarking molecules in chapter 3. The full benchmarking results for the C_2-H_2SO_4 conformer are found in the appendices, including the number of points in the ensemble (Figure A.25), the phenomenological broadening of spectrum (Figure A.26) and electronic structure method (Figure A.27).

Using our validated approximate approach 2 that was discussed in chapter 3, we simulate the approximate EOM-CCSD/aug-cc-pV(T+d)Z+3 spectra for the two conformers of sulfuric acid, where we have added three very diffuse functions to S atom for a better description of Rydberg states as discussed in section 3.1. In Figures A.28 and A.29, we present our calculated EOM-CCSD/aug-cc-pV(D+d)Z+3 and approximate EOM-CCSD/aug-cc-pV(T+d)Z+3 spectra of C_2 and C_s- H_2SO_4 consecutively. The simulated EOM-CCSD/aug-cc-pV(T+d)Z+3 spectra are slightly blue shifted com-

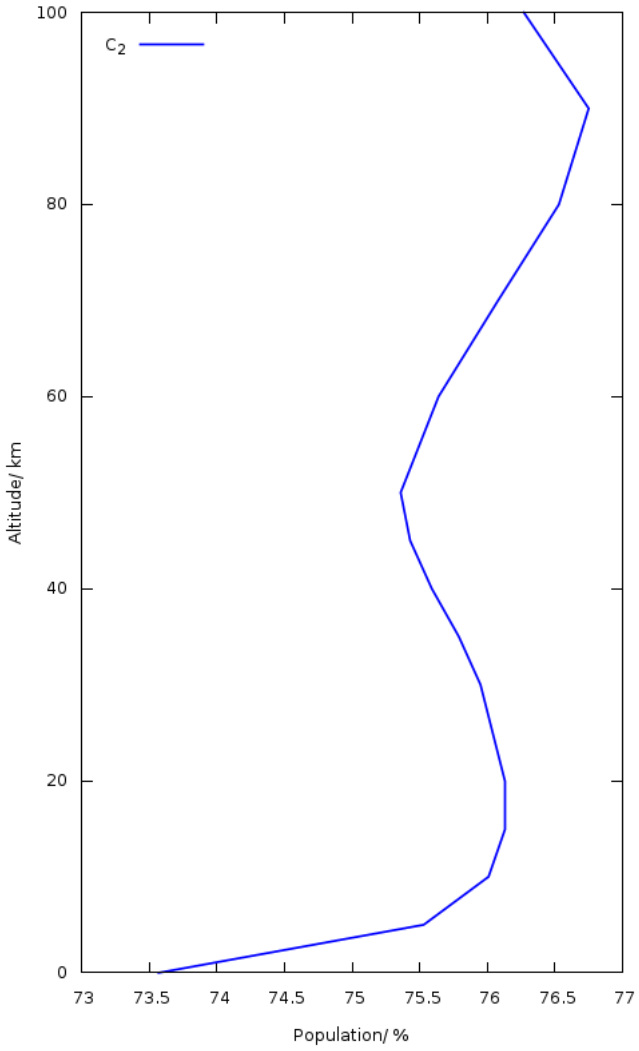

Figure 4.3: Population percentage of C_2- H_2SO_4 in different altitudes.

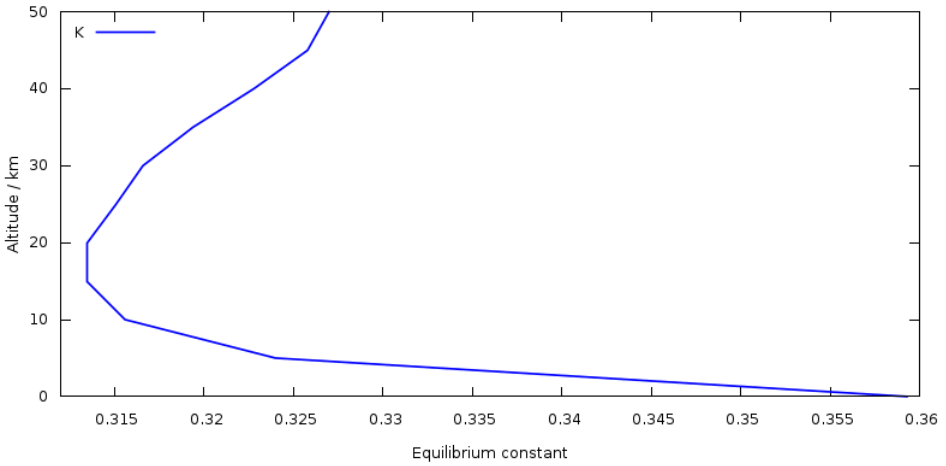

Figure 4.4: Equilibrium constant of C_2-H_2SO_4 and C_s-H_2SO_4 in different altitudes.

pared to the calculated EOM-CCSD/aug-cc-pV(D+d)Z+3 spectra.

As the population percentage of C_s-H_2SO_4 is significant, we calculate the cross section of a mixture of C_2 and C_s-H_2SO_4 by weighting their cross section respecting to their population percentages. The population percentages of the conformers are calculated at standard temperature and pressure, i.e. 273.15 K and 1.01325 $\times 10^5$ Pa. These percentages are 75.3% and 24.7% for C_2 and C_s conformers respectively. The approximate EOM-CCSD/aug-cc-pV(T+d)Z+3 spectrum of each conformer is weighted to its population percentage and are summed at each energy to produce the weighted spectrum of sulfuric acid at standard temperature and pressure as an example. The weighted spectrum with the cross section of the two conformers are shown in Figure 4.5.

The spectra of both conformers show some oscillations, which is due to smaller number of geometries in the ensemble that contribute to this region. Weighting these two spectra slightly improves the oscillations by reducing the uncertainty as the included number of geometries in the ensemble is

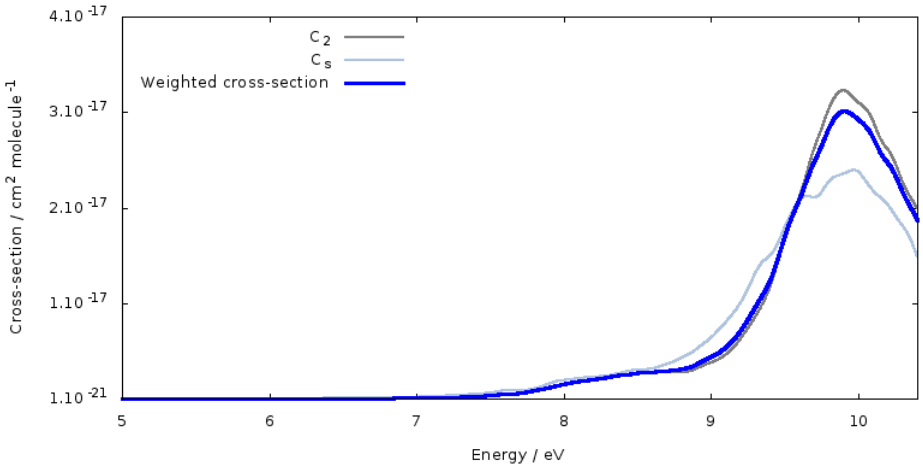

Figure 4.5: Approximate C_2 and C_s-H_2SO_4 cross section and their weighted cross section proportional to their abundance at 30 km and at 226.5 K temperature and 1197 Pa pressure.

effectively doubled (4000). We assess the accuracy of our results by three sensitivity analyses. In the first analysis shown in Figure 4.6, we use double (0.2 eV) or half (0.05 eV) of the width of the Gaussian function used for convolution. As expected, the oscillation in the spectrum increases if the width is decreased to half and decreases if the width is doubled.The integrated cross section in 3 to 7 eV varies slightly from 1.4 $\times 10^{-15}$ cm molecule^{-1} (0.05 eV) to 1.5 $\times 10^{-15}$ cm molecule^{-1} (0.10 eV), and 1.6 $\times 10^{-15}$ cm molecule^{-1} (0.20 eV).

In the second analysis, presented in Figure 4.7, a second ensemble of 4000 geometries (both C_2 and C_s conformers) is constructed and is separately sampled including four excited states. As expected, no significant difference is seen near the band maximum at 8.5 eV or approximately down to 7.0 eV. Below 7 eV, more variation between the cross sections from the ensembles is observed, although there is little difference between the overall integrated cross sections, 1.5 $\times 10^{-15}$ cm molecule^{-1} for the first and 1.5 $\times 10^{-15}$ cm molecule^{-1} for the second ensemble.

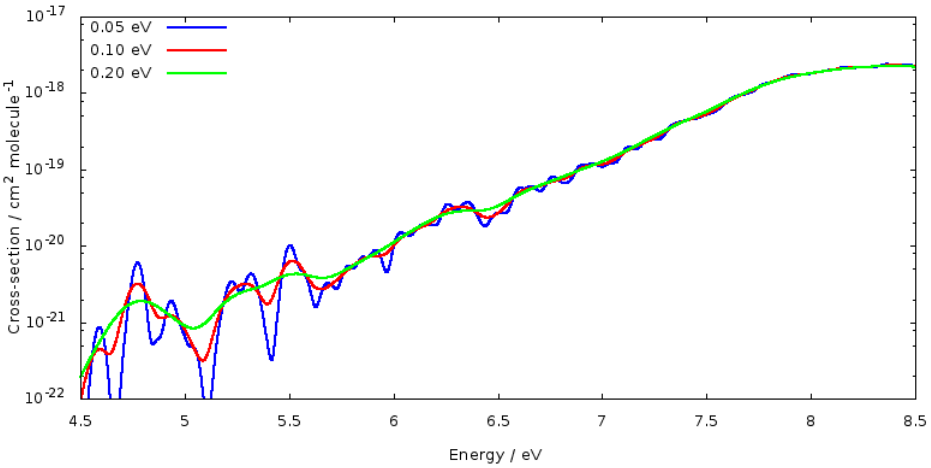

Figure 4.6: EOM-CCSD/aug-cc-pV(T+d)Z+3 weighted spectrum of H_2SO_4 at 30 km altitude with different broadening widths for the four lowest excited states.

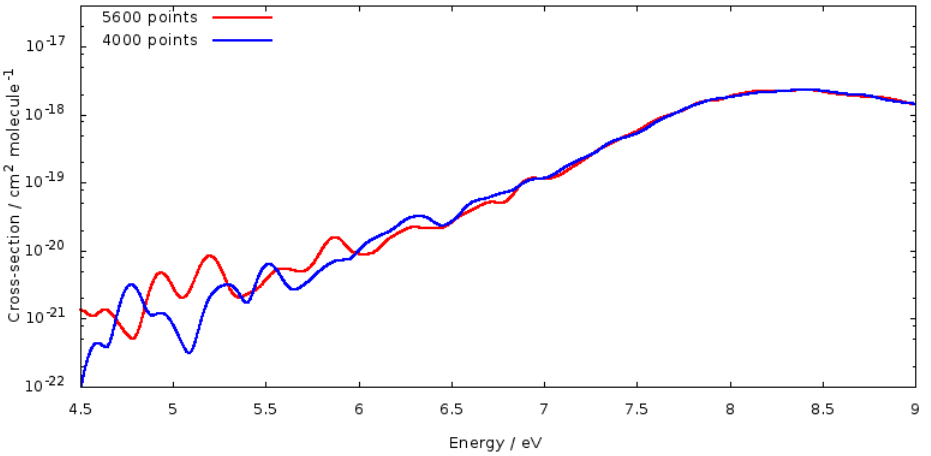

Figure 4.7: EOM-CCSD/aug-cc-pV(T+d)Z+3 weighted spectrum of H_2SO_4 at 30 km altitude with two independently sampled ensembles of 4000 geometries for the four lowest excited states.

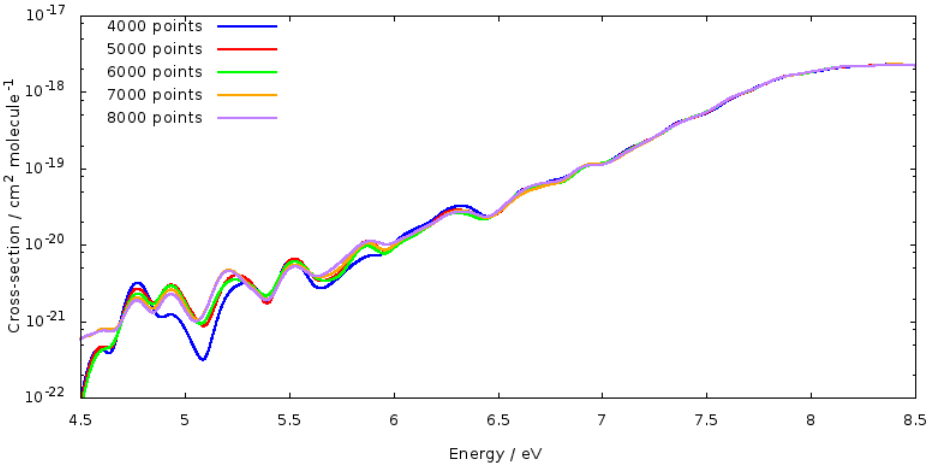

Figure 4.8: EOM-CCSD/aug-cc-pV(T+d)Z+3 weighted spectrum of H_2SO_4 at 30 km altitude with different sized ensembles of geometries for the four lowest excited states.

Finally, in the third analysis, shown in Figure 4.8, we take the original ensemble of 4000 geometries (C_2 and C_s conformers) and progressively include 1000 additional geometries (C_2 and C_s conformers) from the second ensemble, to give spectra sampled with a total of 4000, 5000, 6000, 7000 and 8000 geometries. As expected, we that the oscillation in the cross sections decreases as the number of geometries included in the ensemble increases, although even with ensemble of 8000 geometries, oscillation still remains. The integrated cross section in the region below 7.0 eV is found to be 1.5 $\times 10^{-15}$ cm molecule^{-1} (4000 geometries), 1.5 $\times 10^{-15}$ cm molecule^{-1} (5000 geometries), 1.4 $\times 10^{-15}$ cm molecule^{-1} (6000 geometries), 1.5 $\times 10^{-15}$ cm molecule^{-1} (7000 geometries) and 1.5 $\times 10^{-15}$ cm molecule^{-1} (8000 geometries).

We compare our simulated spectrum of H_2SO_4 with the empirical spectrum of Lane *et al.* [25] in Figure 4.9 where a compilation of results is used In the region above 8.0 eV 4000 geometries and 18 excited states are used and in the region below 8.0 eV 8000 geometries and only four excited states

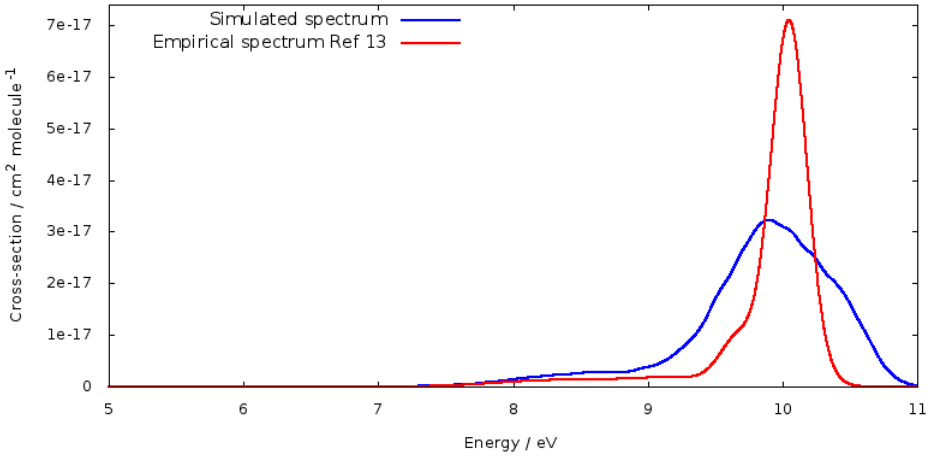

Figure 4.9: Approximate EOM-CCSD/aug-cc-pV(T+d)Z+3 of H_2SO_4 and empirically convoluted cross section from Lane *et al.* [25].

are involved. Comparing these two spectra, we find that the two spectra are in agreement in terms of band position; however, the empirically convoluted spectrum shows a sharper band with higher intensity at around 10 eV and lower cross section in the lower energy regions, compared to our simulated spectrum. The simulated spectrum from Lane *et al.* [25] was based on convolution of the vertical excitation and oscillator strengths of the experimental equilibrium geometry using wide Gaussian functions of 0.9 eV for the lower energy region and 0.3 eV for the higher energy region.

4.1.3 Atmospheric implications

In Figure 4.10 we present our improved cross section of H_2SO_4 with the averaged solar flux at 80 km in log scale. It is critical to simulate and analyze accurately the spectrum in the lower energy regions as the overlapped region between the averaged solar flux and cross section determines the photodissociation rate of sulfuric acid. In Figure 4.11, we compare our simulated spectrum and the empirically convoluted spectrum of Lane *et al.* [25]

with the experimental upper limits from Burkholder *et al.* [9] and Hintze *et al.* [17]. The experimental upper limits for cross section of H_2SO_4 were reported as 10 $\times 10^{-21}$, 10 $\times 10^{-19}$ and 10 $\times 10^{-18}$ cm^2 molecule^{-1} for the 330-195 nm (3.8-6.4 eV), 195-160 nm (6.4-7.8 eV) and 160-140 nm (7.8-8.9 eV) energy regions respectively [9, 17]. While the empirical spectrum in 7.0-10.0 eV range is more consistent with the experimental upper limits, it predicts much lower intensity in the lower energy region and below 7.0 eV and basically drops to near zero cross section. In the third region , i.e. 330-195 nm (3.76-6.52 eV), our simulated spectrum shows more agreement with the experimental upper limits, indicating that the absorbance of H_2SO_4 in this region is not zero. This result is significant, as it indicates that the observed absorbance in this region is not the measurement noise, as it was suggested by Hintze *et al.* [17], Figure 4.12, but it could actually be the low energy tail of the absorption spectrum.

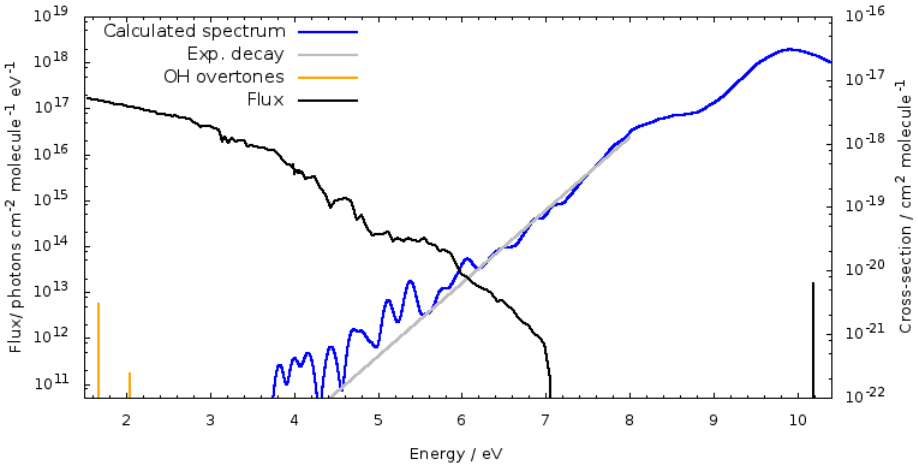

Figure 4.10: Approximate EOM-CCSD/aug-cc-pV(T+D)Z+3 cross sections of H_2SO_4 with the exponential decay in the 5.5-8.0 eV region and, the solar flux at 80 km.

The J-values for photodissociation of H_2SO_4 via the visible (vibrational photodissociation), UV and Lyman-α mechanisms (electronic photodisso-

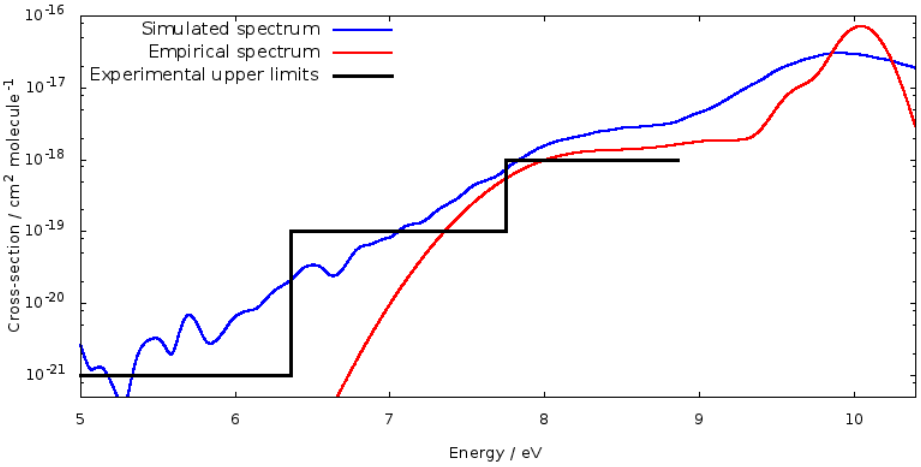

Figure 4.11: H_2SO_4 approximate EOM-CCSD/aug-cc-pV(T+D)Z+3 spectrum, empirically convoluted spectrum of Lane *et al.* [25] compared with the experimental upper limits from Burkholder *et al* [9] and Hintze *et al.* [17].

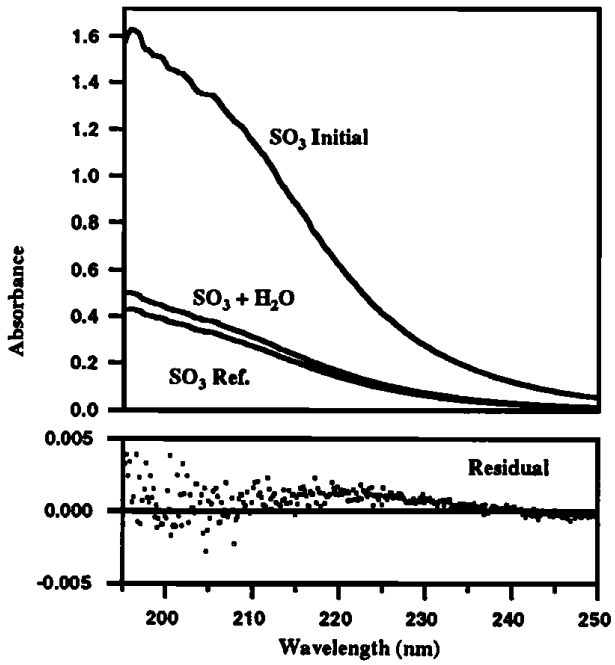

Figure 4.12: The experimental absorption spectra of a mixture of H_2O, SO_3 and H_2SO_4 recorded by Hintze *et al.* [17].

ciation), are presented in Figure 4.13. These are calculated in the same manner Lane *et al.* [25] used in their J-values calculations [25], but with the updated absorption cross section from our spectra simulation results. The vibrational J-values in the visible region were calculated from the experimental integrated cross sections from Feierabend *et al.* and the quatum yield estimates from Miller *et al.* [192], [193].

For the UV region and due to the poor sampling, the cross sections are fitted to an exponential function in the 5.5-8.0 eV to provide a reasonable estimation of the cross section in this region. The Lyman-α J-values were calculated from our approximate EOM-CCSD/aug-cc-pV(T+d)Z+3 cross sections using the solar flux from Lane *et al.* [25], calculated from the TUV model, and assuming a quantum yield of unity for all altitudes. The Lyman-α photodissociation rate was also calculated from our simulated cross section and solar flux in the region of Lyman-α radiation.

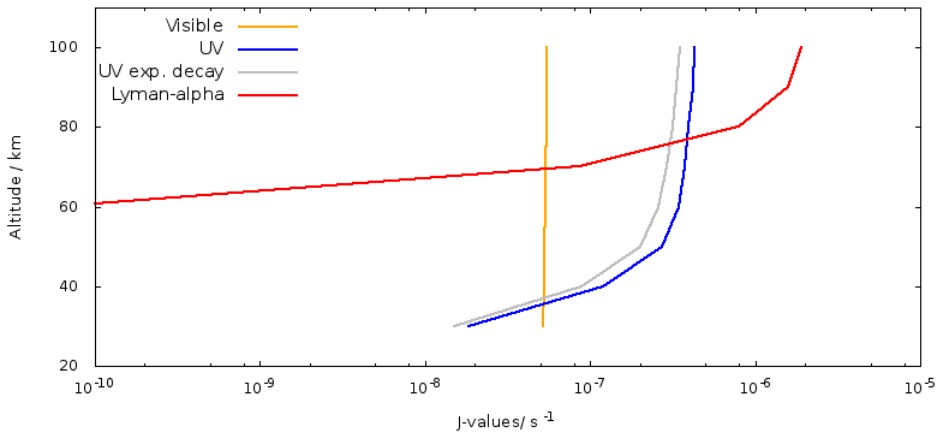

Figure 4.13: Visible, UV (from both calculated cross section and the cross section from exponential decay) and Lyman-alpha J values of H_2SO_4 in different altitudes.

We find that in lower altitudes up to 35 km, where the CN layer is found, the visible overtone vibrational photodissociation mechanism is dominant.

This result is consistent with the previous atmospheric studies where the very weak OH-stretching overtone transitions, were found to provide enough energy for the photodissociation of H_2SO_4 and consequently, a source for stratospheric polar sulfate aerosol [10, 11]. In altitudes above 35 km, the UV J-values overtakes the visible J-values and stays the main photodissociation mechanism up to altitude about 70 km, where Lyman-α J-values gradually increases and becomes the second highest after those of UV. From altitude 75 km above, the Lyman-α photodissociation rate is the highest followed by UV and visible photodissociation rates consecutively. While the main photodissociation mechanism from our results in altitudes above 75 km and below 35 km are consistent with those reported by Lane *et al.*, the order of our calculated photodissociation rates and as a result, the significance of the photodissociation mechanisms in different altitudes differ from those calculated by Lane *et al.*. In the study from Lane *et al.*, the UV photodissociation rate is the lowest in all altitudes due to the much lower absorption cross section they calculated in the energy region below 7.0 eV.

4.2 OSSO

Sulfur compounds of the atmosphere of Venus have been of increasing interest, and many aspects of Venusian atmosphere have been studied [27–33]. In a recent study, Frandsen *et al.* [54] investigated the possible conformers of S_2O_2 molecule [54]. These S_2O_2 conformers and their calculated relative energies are presented in Figures 4.14 and 4.15. This work identified two conformers of the S_2O_2 molecule in the atmosphere of Venus that could explain the absorption between 320 to 400 nm, after more than 40 years since the absorption cross section [54] of an unknown sulfur-containing molecule was recorded. They suggested *cis* and *trans*-OSSO as the main near-UV absorber of the Venus' absorption spectrum.

Frandsen *et al.* reported the percent yield of S_2O_2 conformers and showed that the two *cis* and *trans*-OSSO, with percent yields of 70.6% and 29.4%, respectively at 64 km, are the most abundant conformers of S_2O_2 in the Venusian atmosphere. This study also approximated the cross section of the two stable isomers by empirically convoluting the electronic transitions using a Lorentzian function [54], similar to the earlier approach by Lane *et al.* for H_2SO_4 [25].

In this section, we again apply the approach developed in chapter 3, to simulate the absorption spectrum of OSSO and calculate the weighted cross section for a mixture of the *cis* and *trans* conformers. This weighted spectrum can be used in the future experimental investigations and in the atmospheric modeling of Venus. We first benchmark some of the simulation parameters in section 4.2.1 and then, will present the final simulated spectra of these molecules in section 4.2.2.

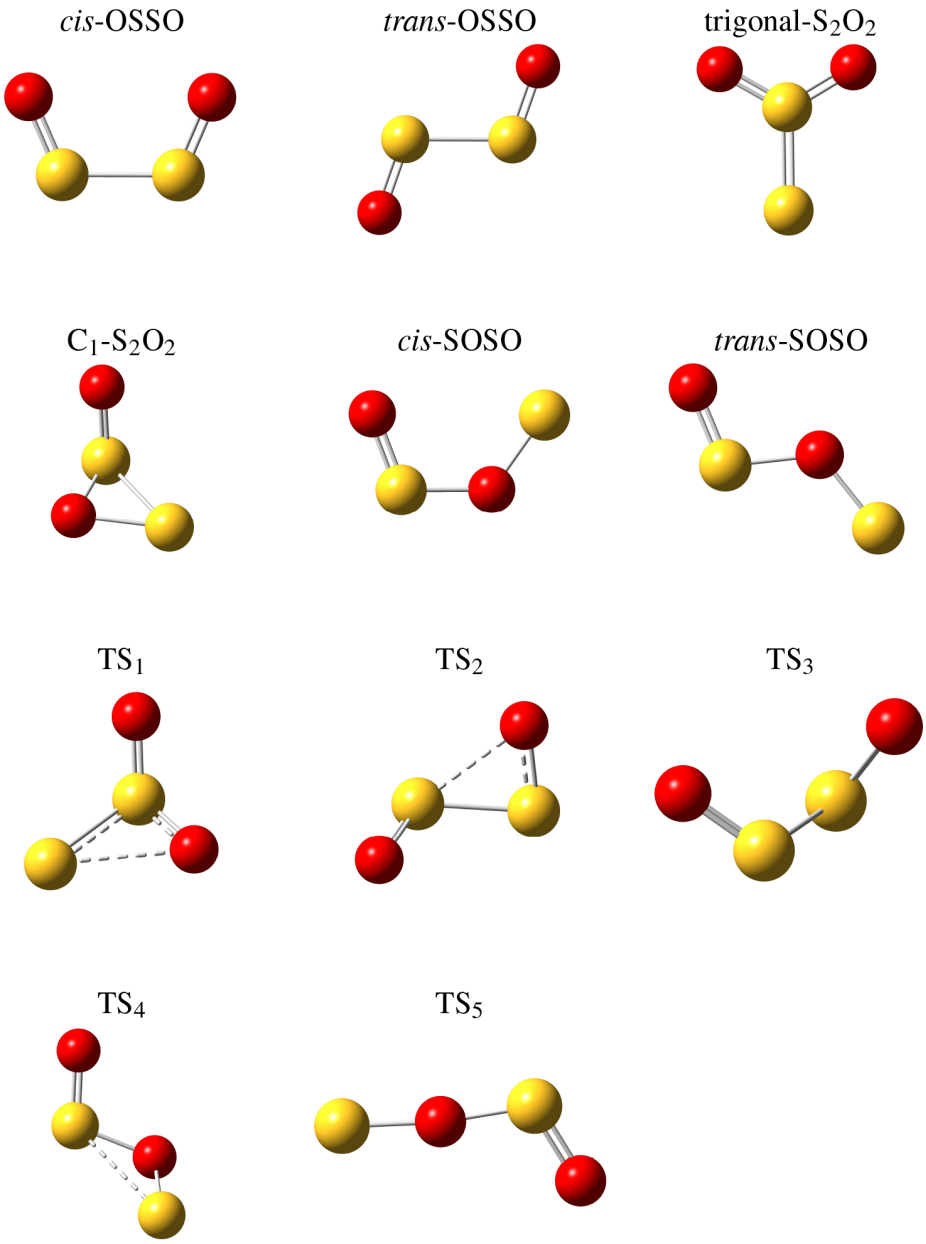

Figure 4.14: Different isomers of $(SO)_2$ molecule [54].

4.2.1 Theoretical details

We optimize the geometry of both conformers at CCSD(T)/aug-cc-pV(T+d)Z level of theory and calculate the vibrational frequencies with the same method

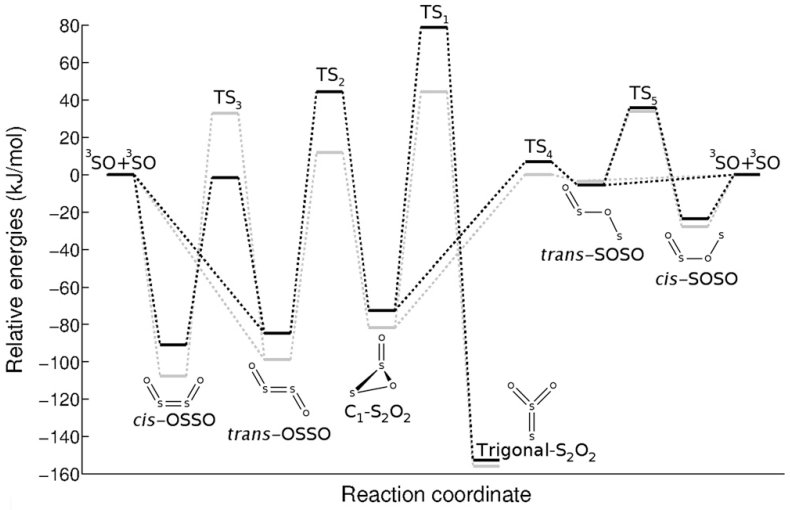

Figure 4.15: Stable conformers of S_2O_2 and the transitions states [54].

and basis set. We use this optimized geometry and the harmonic frequencies along with the Wigner distribution to construct an ensemble of a certain number of geometries around the equilibrium geometry. These geometries are promoted to the 18 excited states and the vertical excitations and oscillator strengths are calculated at different levels of theory, EOM-CCSD, RI-CC2 and ADC(2) methods and different Dunning's correlation consistent basis sets.

The calculated cross sections are convoluted to either Gaussian or Lorentzian function with defined phenomenological broadenings of spectrum to generate the final simulated absorption spectrum and approach 2 from chapter 3 is applied to produce the simulated spectra.

4.2.2 Absorption cross section

Although there is no experimental spectrum of OSSO to be compared with the simulated spectra, we benchmark the main Newton-X and electronic

structure parameters for these two conformers, to see if the trend is the same as those observed for the sulfur benchmarking molecules in chapter 3. The full benchmarking results on *cis* and *trans*-OSSO conformers are found in the appendices, including the number of points in the ensemble (Figure A.30) and the electronic structure method (Figure A.31).

In Figure A.32, we present our calculated EOM-CCSD/aug-cc-pV(D+d)Z+3 and approximate EOM-CCSD/aug-cc-pV(T+d)Z+3 spectra of *cis* and *trans*-OSSO. The bright bands of the approximate EOM-CCSD/aug-cc-pV(T+d)Z+3 spectra are slightly blue shifted compared to the calculated EOM-CCSD/aug-cc-pV(D+d)Z+3 spectra.

We compare our final simulated spectra of the two conformers with the empirically convoluted spectra of Frandsen *et al.* in Figure 4.16. There is reasonable agreement between our simulated spectra and those of Frandsen *et al.*. However, despite very similar methods for the vertical excitation energies, it is noticeable that the band maxima of our simulated spectra are 0.1-0.2 eV lower in energy. Our ground state CCSD(T)/aug-cc-pV(T+d)Z+3 optimized geometry is not very different from the MRCI/cc-pV(T+d)Z used in the vertical excitation energy calculation by Frandsen *et al.*. This suggests that the excited states potentials of these two conformers are steep and more sensitive to geometry than the ground state, which is not surprising given the excited states in question are generally dissociative. In Tables 4.2 and 4.3, we present the EOM-CCSD excited states energies of *cis* and *trans*-OSSO, optimized with the MRCI/cc-pV(T+d)Z [54] (geometry 1), and CCSD(T)/ aug-cc-pV(T+d)Z (geometry 2) using the aug-cc-pV(D+d)Z+3 and aug-cc-pV(D+d)Z basis sets. The difference between the vertical excitation energies of the two geometries with each basis set are also presented in these tables. These differences show that for each basis set, the vertical excitation energies

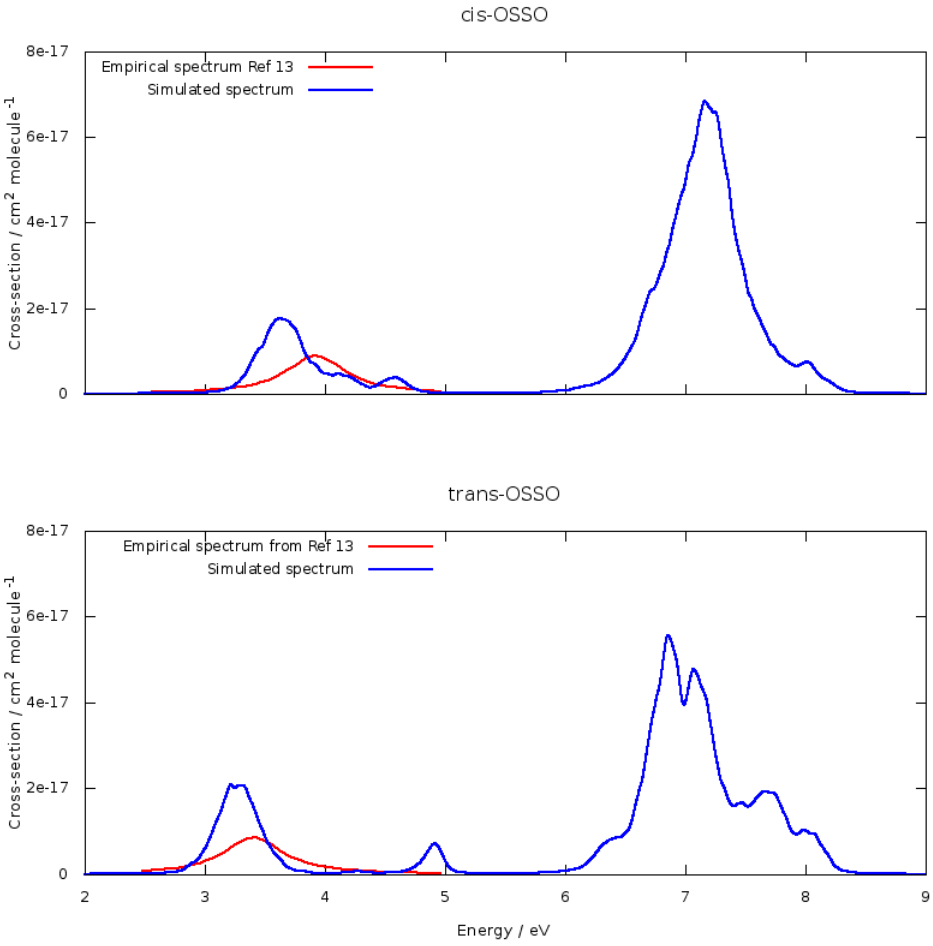

Figure 4.16: Approximate EOM-CCSD/aug-cc-pV(T+d)Z+3 and empirically convoluted spectra of *cis* and *trans*-OSSO of Frandsen *et al.* [54].

of geometry 1 is slightly higher than vertical excitation energies calculated for geometry 2, which has caused the slight shift in the simulated spectra. This difference between the vertical excitations of the two geometries is the highest at about 5.0-7.0 eV.

Table 4.2: EOM-CCSD excited states energies of geometry 1 of *cis*-OSSO (optmized at MRCI/cc-pV(T+d)Z level of theory [54]) and geometry 2 (optimized at CCSD(T)/ AV(T+d)Z using two AV(D+d)Z+3 and AV(D+d)Z basis sets.

	AV(D+d)Z+3					AV(D+d)Z				
	geometry 1		geometry 2			geometry 1		geometry 2		
state	E	f	E	f	$\lvert\Delta E\rvert$	E	f	E	f	$\lvert\Delta E\rvert$
1	2.87	0.0000	2.67	0.0000	0.21	2.87	0.0000	2.67	0.0000	0.21
2	4.00	0.1028	3.76	0.0895	0.24	4.00	0.1027	3.76	0.0893	0.25
3	4.22	0.0001	4.15	0.0003	0.07	4.25	0.0002	4.17	0.0005	0.07
4	4.66	0.0046	4.62	0.0048	0.05	4.68	0.0046	4.64	0.0048	0.05
5	5.27	0.0009	4.95	0.0006	0.32	5.28	0.0011	4.95	0.0008	0.32
6	6.00	0.0343	5.58	0.0000	0.42	6.01	0.0000	5.58	0.0000	0.42
7	6.68	0.0343	6.61	0.0157	0.07	6.98	0.0040	6.68	0.0005	0.31
8	7.00	0.0055	6.70	0.0410	0.30	7.13	0.0086	6.71	0.0455	0.42
9	7.10	0.0070	6.71	0.0214	0.39	7.15	0.0432	6.96	0.0263	0.19
10	7.10	0.0003	6.94	0.0222	0.17	7.20	0.0551	7.12	0.3405	0.08
11	7.19	0.0988	7.10	0.3338	0.08	7.36	0.3365	7.14	0.0509	0.22
12	7.33	0.3153	7.13	0.0451	0.20	7.65	0.0729	7.56	0.0000	0.09
13	7.49	0.0196	7.44	0.0000	0.05	7.74	0.0000	7.63	0.0565	010
14	7.56	0.0000	7.47	0.0272	0.09	7.94	0.0459	7.79	0.0000	0.15
15	7.78	0.0000	7.76	0.0001	0.02	8.17	0.0010	7.93	0.0533	0.24
16	7.88	0.0161	7.77	0.0000	0.11	8.17	0.0000	7.95	0.0272	0.22
17	8.14	0.0000	7.90	0.0136	0.24	8.36	0.0310	8.17	0.0001	0.19
18	8.15	0.0368	8.04	0.0000	0.11	8.60	0.0000	8.35	0.0000	0.24

Table 4.3: EOM-CCSD excited states energies of geometry 1 of *trans*-OSSO (optimized at MRCI/cc-pV(T+d)Z level of theory [54]) and geometry 2 (optimized at CCSD(T)/ AV(T+d)Z using two AV(D+d)Z+3 and AV(D+d)Z basis sets.

	AV(D+d)Z+3					AV(D+d)Z				
	geometry 1		geometry 2			geometry 1		geometry 2		
state	E	f	E	f	$\lvert\Delta E\rvert$	E	f	E	f	$\lvert\Delta E\rvert$
1	2.59	0.0000	2.45	0.0000	0.14	2.59	0.0000	2.45	0.0000	0.14
2	3.46	0.1043	3.34	0.0983	0.12	3.46	0.1058	3.34	0.0995	0.12
3	4.33	0.0000	4.31	0.0000	0.02	4.34	0.0000	4.32	0.0000	0.02
4	5.00	0.0238	4.88	0.0007	0.12	5.01	0.0245	4.88	0.0009	0.09
5	5.10	0.0009	4.91	0.0119	0.19	5.10	0.0011	4.92	0.0122	0.32
6	5.76	0.0000	5.34	0.0000	0.42	5.77	0.0000	5.34	0.0000	0.43
7	6.32	0.0188	6.35	0.0152	0.03	6.67	0.0165	6.44	0.0000	0.23
8	6.72	0.0000	6.44	0.0000	0.28	6.72	0.0000	6.45	0.0000	0.27
9	6.76	0.0000	6.45	0.0000	0.31	6.78	0.0000	6.69	0.0112	0.09
10	6.99	0.0000	6.93	0.3508	0.06	7.24	0.3433	6.96	0.3672	0.28
11	7.20	0.3186	6.97	0.0000	0.23	7.31	0.0000	7.23	0.0000	0.08
12	7.28	0.0000	7.23	0.0042	0.05	7.60	0.0172	7.50	0.0176	0.10
13	7.32	0.0018	7.33	0.0000	0.01	7.65	0.0000	7.53	0.0034	0.12
14	7.43	0.0000	7.44	0.0000	0.01	7.82	0.0000	7.61	0.0000	0.19
15	7.77	0.0038	7.52	0.0000	0.25	7.83	0.0003	7.82	0.1272	0.01
16	7.87	0.0000	7.78	0.1191	0.09	8.13	0.1211	7.83	0.0000	0.30
17	8.88	0.0056	7.89	0.0014	0.99	8.32	0.0018	8.36	0.0005	0.04
18	7.99	0.1177	7.90	0.0000	0.09	8.69	0.0000	8.55	0.0000	0.14

4.2.3 Atmospheric implications

Using the percentage yields reported by Frandsen *et al.* [54], we calculate the weighted cross section for a mixture of the two *cis* and *trans* conformers of OSSO. The weighted cross section at 64 km altitude of Venus' atmosphere, where SO_2 is abundant [54], is shown in Figure 4.17. This weighted spectrum is a more realistic representation of the absorption spectrum of the naturally occurring mixture of OSSO molecule in the atmosphere of Venus.

The theoretical spectra are valuable in identifying unknown molecules and are of particular importance in case of short-lived molecules. Accurate simulated spectra greatly assist with the analysis and band assignment of the experimental spectra. The experimental spectra of the two conformers of OSSO are not yet available. Our collaborators at the University of Copenhagen are presently undertaking experimental investigation of the absorption cross section of OSSO using matrix isolation spectroscopy. Our simulated spectrum of OSSO, as a mixture of its two conformers, *cis* and *trans*-OSSO, will help in identifying and assigning the bands. In a recent experimental work, the first IR and UV/Vis spectra of OSSO were recorded by generating the monomers and dimers of SO by high vacuum flash pyrolysis (HVFP) of ethylene episulfoxide in Ar or N_2 (1:1000) at 1000 K [194]. These experimental results and our calculated spectra are compared in Figure 4.18. Due to the strong absorption of ethylene and S_2 in the UV region the experimental and simulated spectra are are only comparable in the visible region and up to 4 eV. There is a general agreement, specially for the trans conformer, between the our calculated cross section and the experimental results. However, due to the variety of the molecules that can be created during pyrolysis, there is uncertainty in assigning the absorption to different conformers of OSSO.

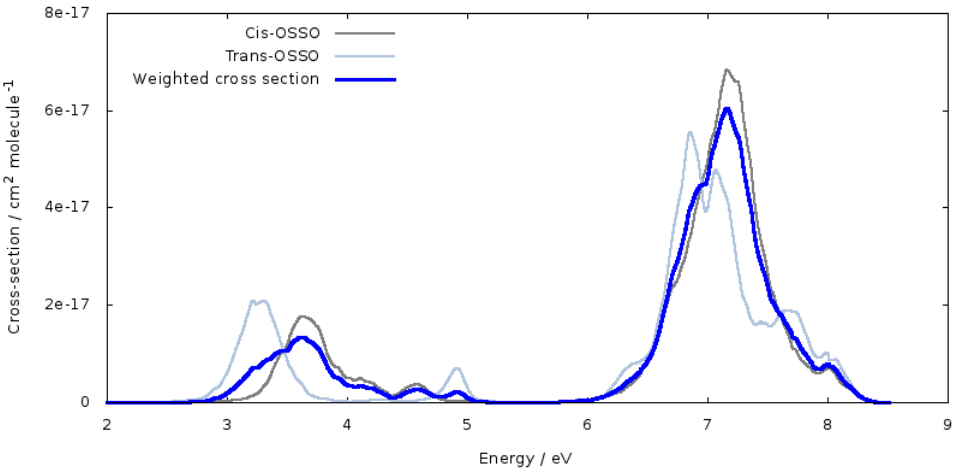

Figure 4.17: Weighted cross section for a mixture of *cis* and *trans*-OSSO at 64 km altitude.

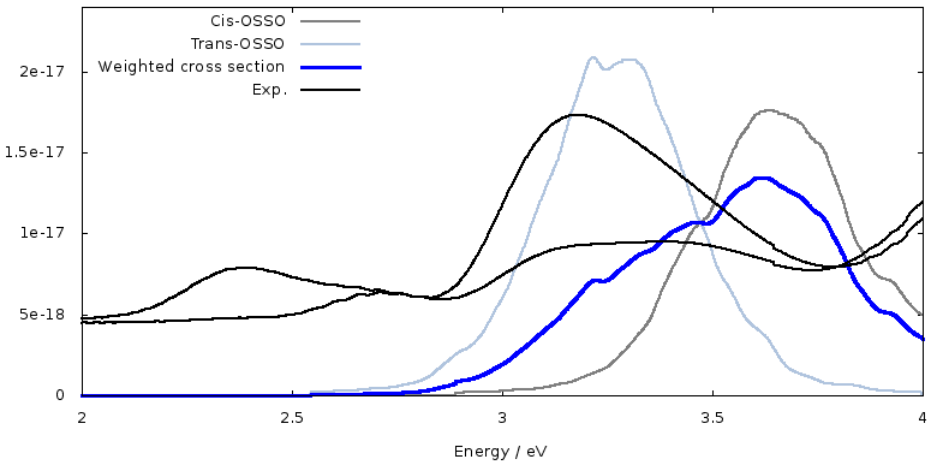

Figure 4.18: Weighted cross section for a mixture of *cis* and *trans*-OSSO at 64 km altitude, and separate calculated cross sections of the two conformers compared with the experimental results from Wu *et al.* [194].

4.3 Conclusion

We have simulated the absorption spectra of two sulfur-containing molecules, H_2SO_4 and OSSO, both with atmospheric importance. We used the nuclear ensemble approach to simulate the absorption spectra of these molecules. To have more accurate results at lower cost, we used the approximate approach 2, introduced and developed in chapter 3, to simulate the approximate EOM-CCSD/aug-cc-pV(T+d)Z+3 absorption spectra. In the simulations of both molecules, their two lowest energy conformers were involved, C_2 and C_s-H_2SO_4, and *cis* and *trans*-OSSO. The simulated spectra of the two conformers were weighted proportional to their abundance, to give a final absorption spectrum suitable for guiding experimental investigations. Our simulated spectra are in excellent agreement with the absorption region of the unknown near UV absorber of the atmosphere of Venus, (320-400 nm).

Chapter 5

Nitrous oxide spectra

In this chapter, we investigate how the formation of weakly bound complexes affects the absorption of solar radiation of N_2O in the Earth's atmosphere. The complexes considered in this chapter include the most abundant atmospheric complexes of N_2O, namely Ar-N_2O, N_2-N_2O, O_2-N_2O and H_2O-N_2O. First, we simulate and benchmark the absorption spectrum for N_2O, using different electronic structure methods to determine the most efficient approach, in terms of cost and accuracy. We then investigate the change in the absorption spectrum of N_2O upon complexation. The findings in this chapter, are also used in chapter 6, where we simulate the photodissociation dynamics of the H_2O-N_2O complex.

5.1 Photodissociation of N_2O in the Earth's atmosphere

Nitrous oxide (N_2O) is now the single most important ozone depleting substance (ODS) in the Earth's atmosphere [63] and the third most significant greenhouse gas [60]. The concentration of N_2O in the Earth's atmosphere

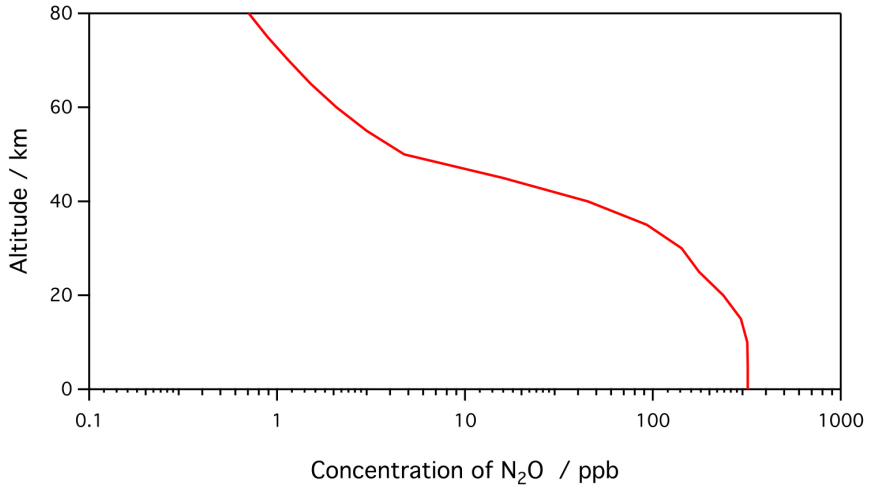

Figure 5.1: Concentration of N_2O in different altitudes [5].

has been steadily increasing over recent history, primarily due to human activities. These anthropogenic sources are now responsible for about 50% of N_2O emissions, with the agriculture sector being the single largest producer [55]. The global atmospheric budget of N_2O is poorly quantified in terms of emission sources [56]. As such, most of the atmospheric models use the rate of N_2O photodissociation to estimate the amount of N_2O that is emitted to the atmosphere [76, 77].

Nitrous oxide has a long lifetime in the Earth's atmosphere, approximately 114 years, with the major loss process being photodissociation in the stratosphere by absorbing UV light [63, 195]. This can be observed in the atmospheric abundances of N_2O, which is highest at Earth's surface and decreases rapidly in the stratosphere and higher altitudes, as can be seen in Figure 5.1. The long atmospheric lifetime of N_2O comes from the fact that there are only a few, relatively slow processes that cause it to breakdown in the atmosphere;

Photodissociation of N_2O; Equation 5.1, represents the dominant loss

$$N_2O + h\nu \rightarrow N_2 + O(^1D) \qquad 90\% \qquad (5.1)$$

$$N_2O + O(^1D) \rightarrow N_2 + O_2 \qquad (5.2)$$

$$10\%$$

$$N_2O + O(^1D) \rightarrow 2NO \qquad (5.3)$$

process of N_2O, accounting for 90% of N_2O loss in the Earth's atmosphere [63]. This primarily occurs in the stratosphere by absorbing UV photons with wavelengths of 180-230 nm [8, 73, 196] via a dipole forbidden ($1A' \rightarrow 2A'$) excitation [197, 198], which only becomes weakly allowed by coupling to its bending mode [72–74]. The absorption spectrum of N_2O monomer has been studied experimentally, [199–201] as well as theoretically [72, 73, 197], and is shown in Figure 5.2 along with the solar flux. Centered at about 180 nm, the first absorption band has a broad Gaussian shape, which is indicative of a direct photodissociation reaction [72, 75].

N_2O is also lost from the Earth's atmosphere by reaction with $O(^1D)$ (Equations 5.1 and 5.2). Collectively, these two reactions are responsible for a 10% of N_2O loss. $O(^1D)$ is a key intermediate in the Chapman cycle, in which ozone (O_3) is continually regenerated in the Earth's atmosphere. As reaction of $O(^1D)$ with N_2O is irreversible, this makes N_2O an ozone-depleting substance (ODS).

The low temperature of the stratosphere and the availability of other stratospheric gases, provides conditions that allow formation of weakly-bonded complexes. The abundance of N_2O complexes in the Earth's atmosphere was previously investigated by Salmon *et al.* and is shown as a function of altitude in Figure 5.3. Salmon *et al.* showed that the vibrational

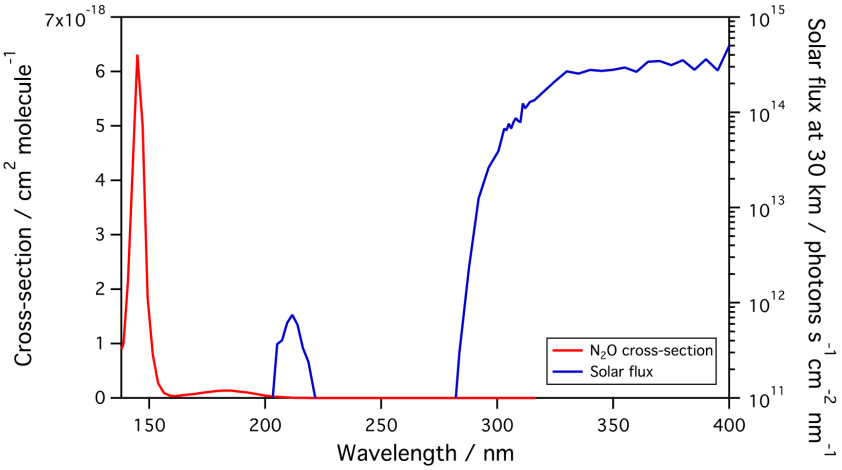

Figure 5.2: Solar flux at 30 km and N_2O experimental cross-section [1].

frequencies of N_2O are perturbed upon complexation [71]. This result is significant as the absorption cross section of N_2O is strongly dependent on coupling to the vibrational modes [72–74]. Given that N_2O undergoes a direct photodissociation process [72, 75], it follows that the photodissociation rate of N_2O is also expected to be affected by complex formation. This effect has been previously observed across various isotopologues of N_2O, which have slightly different vibrational frequencies and correspondingly different photodissociation rates [72]. As it was mentioned in chapter 1, photodissociation rate constants (J) depend on the flux of photons of a given wavelength $I(\lambda)$, the quantum yield at a given wavelength $\Phi(\lambda)$ and the absorption cross section. This possible change in the cross section, even if it is to a small extent, could influence the photodissociation rate of N_2O significantly, due to the normally very small overlap of N_2O cross section and solar flux in the stratosphere, as shown in Figure 5.2.

While the absorption spectrum and photodissociation dynamics of N_2O monomer are well-known, to the best of our knowledge, there have been

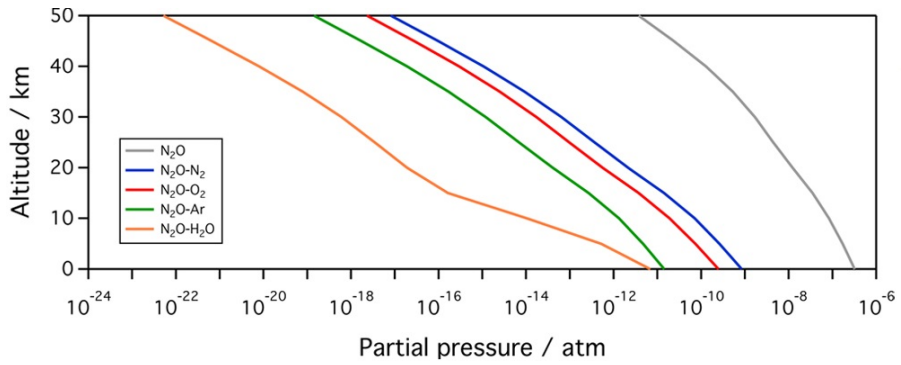

Figure 5.3: Atmospheric abundance of weakly bound complexes involving N_2O as a function of altitude [202].

no previous theoretical or experimental photodissociation investigations for the Ar-N_2O, N_2-N_2O and O_2-N_2O complexes. There has been some limited experimental photodissociation investigations of the H_2O-N_2O complex [203, 204], however much more work is required to understand its atmospheric importance.

5.2 N_2O structure and vibrational frequencies

As mentioned in the previous section, one of the features that is expected to affect the photodissociation of N_2O complexes, is the vibrational frequencies. To ensure that these are approximately described, we have investigated the sensitivity of the calculated geometry and vibrational frequencies of monomeric N_2O, where experimental results are readily available for comparison.

In Table 5.1, we present the optimized equilibrium geometry and harmonic frequencies of N_2O obtained using some common methods and same basis sets. Also in Table 5.1, we include the experimental vibrationally-averaged bond lengths of N_2O as well as the experimentally calculated fun-

damental vibrational frequencies. Although ν_1 and ν_2 are degenerate, we present them separately to keep consistency in the monomer and complex results tables as the degeneracy can be broken in complexes. The bond lengths calculated using DFT and CCSD methods, show a decreasing trend with increasing the size of basis set from aug-cc-pVDZ to aug-cc-pVQZ. This decrease in the bond lengths results in an increasing trend in the calculated harmonic frequencies with the increase in the size of basis set used. This decreasing trend in the bond lengths and increasing trend in frequencies, are more significant between aug-cc-pVDZ and aug-cc-pVTZ basis sets than that between aug-cc-pVTZ and aug-cc-pVQZ basis sets indicating good convergence of the bond lengths and harmonic frequencies with increase in the size of basis set. This also indicates that aug-cc-pVTZ basis set can produce bond lengths and harmonic frequencies at close accuracy to those calculated with the larger aug-cc-pVQZ basis set. This similarity is more highlighted for the vibrational frequencies calculated using CCSD method where the frequency results from the two aug-cc-pVTZ and aug-cc-pVQZ are the same with only 0.1 cm^{-1} difference for the N-N stretching frequency. The exceptions are the bending vibrational frequencies calculated with DFT methods where the calculated frequencies with aug-cc-pVQZ basis set show a slight decrease.

Considering the lower computational cost of CAM-B3LYP method compared with the more computationally expensive CCSD and CCSD(T) methods, we see good description of bond lengths and frequencies in our CAM-B3LYP results compared with the experimental results. Therefore, we extensively investigate the CAM-B3LYP bond lengths and harmonic frequencies of N_2O with a variety of basis sets and present the results in Table 5.2. The general trend in the bond length is the same as trend seen in Table 5.2 and

the bond lengths decrease with increasing size of the basis set. While the trend in harmonic frequencies is not increasing with increase in the size of basis set in all the cases, they are all consistent in having higher value than experimental fundamental frequencies.

Table 5.1: Bond lengths (in Å) and harmonic frequencies [a] (in cm^{-1}) of N_2O calculated at different *ab initio* levels of theory.

Method	Basis	R_{N-N}	R_{N-O}	ν_1	ν_2	ν_3	ν_4
CAM-B3LYP	aug-cc-pVDZ	1.126	1.187	608.5	608.5	1356.9	2400.9
	aug-cc-pVTZ	1.113	1.179	632.9	632.9	1352.0	2407.3
	aug-cc-pVQZ	1.112	1.178	632.2	632.2	1383.9	2397.3
M06	aug-cc-pVDZ	1.132	1.180	624.6	624.6	1318.1	2351.3
	aug-cc-pVTZ	1.118	1.172	656.0	656.0	1386.8	2410.8
	aug-cc-pVQZ	1.118	1.170	651.4	651.4	1391.5	2416.5
CCSD	aug-cc-pVDZ	1.137	1.197	593.4	593.4	1306.0	2322.8
	aug-cc-pVTZ	1.120	1.186	621.6	621.6	1318.1	2351.2
CCSD(T)	aug-cc-pVTZ	1.133	1.191	593.2	593.2	1286.8	2266.5
Expt		1.127[b]	1.185 [b]	588.8[c]	595.9 [c]	1301.9 [c]	2281.2 [c]

[a] Bending (ν_1 and ν_2), N-O stretching (ν_3) and N-N stretching (ν_4)
[b]Equilibrium experimental results from Teffo *et al.* [205].
[c] Experimentally derived fundamental frequencies from Bryant *et al.* [206].

Table 5.2: Bond lengths (in Å) and harmonic frequencies [a] (in cm^{-1}) of N_2O using different basis sets with CAM-B3LYP method.

Basis	R_{N-N}	R_{N-O}	ν_1	ν_2	ν_3	ν_4
6-31G(d)	1.127	1.188	616.5	616.5	1375.2	2430.9
6-31+G(d)	1.125	1.190	596.6	596.6	1358.5	2410.8
6-311++G(2d,2p)	1.114	1.183	627.3	627.3	1341.7	2374.9
cc-pVDZ	1.126	1.183	623.6	623.6	1379.6	2425.0
cc-pVTZ	1.114	1.179	637.3	637.3	1359.1	2405.5
cc-pVQZ	1.113	1.178	635.6	635.6	1359.2	2399.9
aug-cc-pVDZ	1.126	1.187	608.5	608.5	1356.9	2400.9
aug-cc-pVTZ	1.113	1.179	632.9	632.9	1352.0	2396.7
aug-cc-pVQZ	1.112	1.178	632.2	632.2	1356.9	2397.3
Expt	1.128[b]	1.184 [b]	588.8[c]	588.8 [c]	1284.9 [c]	2223.8 [c]

[a] Bending (ν_1 and ν_2), N-O stretching (ν_3) and N-N stretching (ν_4)
[b]Experimental results from Teffo *et al.* [205].
[c]Experimental fundamental frequencies from Tidwell *et al.* [207] and Bruch *et al.* [208].

5.3 N_2O cross section

In this section, we extensively benchmark different Newton-X and electronic structure parameters to see how these affect the accuracy of simulated N_2O cross sections. Our simulated spectra are validated against the experimental cross section of N_2O monomer. These results will be used later in section 5.4.3, where we simulate the absorption spectra of N_2O complexes, and in chapter 6, where we simulate the photodissociation dynamics of N_2O and H_2O-N_2O.

5.3.1 Newton-X parameters benchmark

In this subsection, we benchmark the Newton-X parameters for N_2O monomer using the EOM-CCSD/aug-cc-pVDZ method. In subsection 5.3.2, we will consider other electronic structure methods. The experimental results with which we validate our simulated cross section against, are from Nicolet *et al.* [209] and Yushino *et al.* [210], Exp 1 and Exp 2 respectively in Figure 5.4.

Using a Wigner distribution, we sample a certain number of geometries in the ground vibrational state of the ground electronic state. To keep consistency, the same level of theory is used for geometry optimization, harmonic frequencies and vertical excitation energies calculations. In Figure 5.5, we present the simulated absorption spectra of N_2O from ensembles of 500, 1000, 2000 and 5000 geometries. We find the spectrum simulated from 2000 geometries is smooth enough and with reasonably small associated numerical integration error. In Figure 5.6, we present our simulated cross section convoluted with a Gaussian band shape with a phenomenological broadening (δ) of 0.01, 0.05, 0.1 and 0.2 eV and in Figure 5.7, we present the same results, this time convoluted with a Lorentzian band shape and

the same range of phenomenological broadening. The band shape and δ can significantly affect the shape of the simulated spectrum particularly at the tails of the absorption bands. We can find that, the Lorentzian band shape gives results in closer agreement with the experiment when smaller values of δ are used. When the cross sections are convoluted with the Gaussian band shape, the overall shape of the bands with different values of δs seem quite consistent and in agreement with the experimental results. Overall, the Gaussian band shape of 0.1 and 0.2 eV broadenings appear to show the best agreement with the experimental results and hence, the narrower 0.1 eV broadening will be used to simulate the rest of the spectra in this chapter.

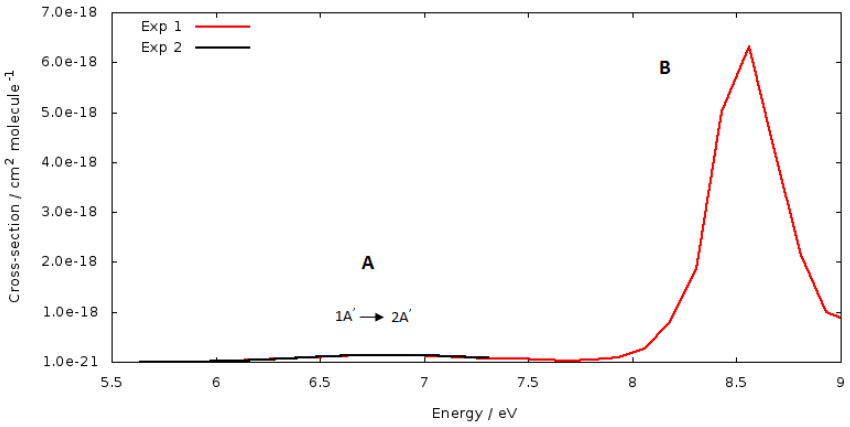

Figure 5.4: Experimental absorption spectra of N_2O from Nicolet *et al.* (Exp 1) [209] and Yushino *et al.* (Exp 2) [210].

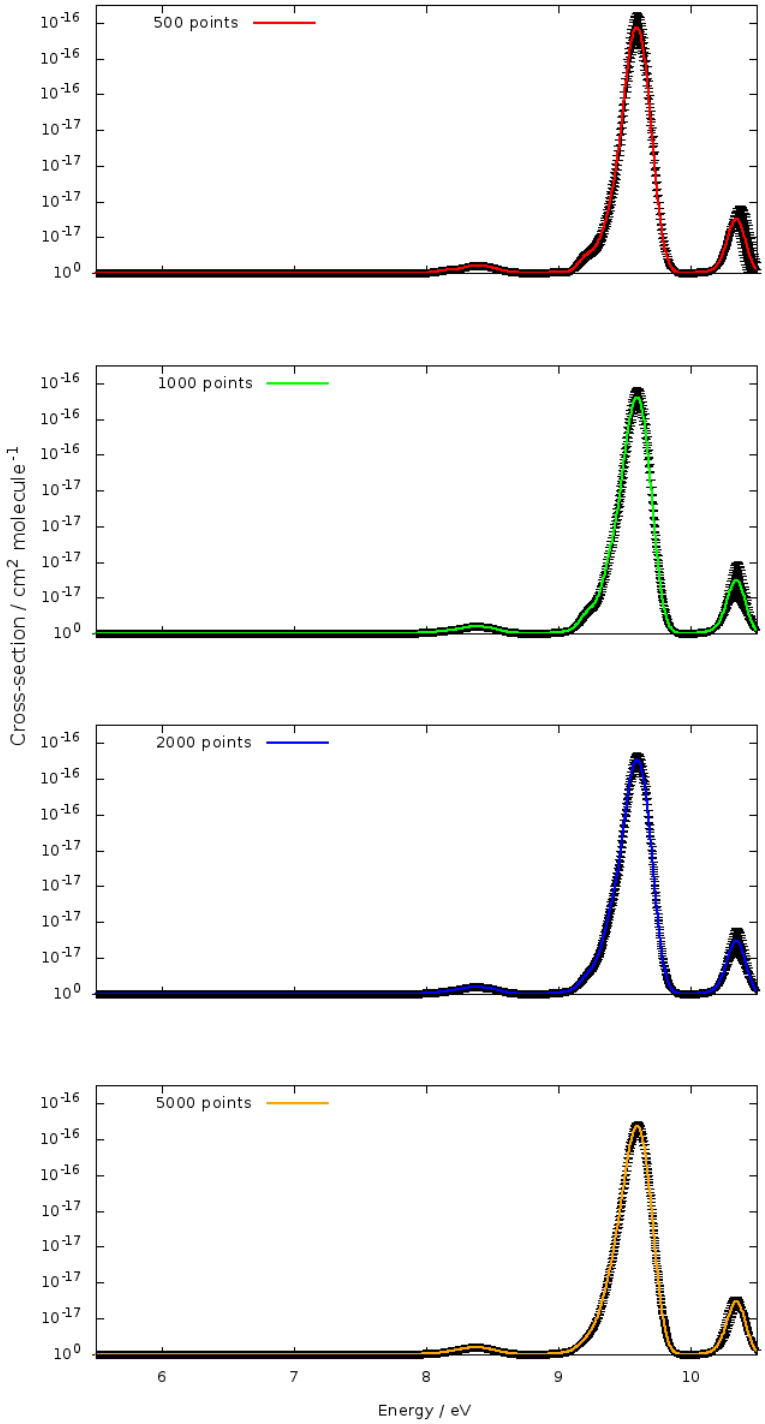

Figure 5.5: EOM-CCSD/aug-cc-pVDZ absorption cross sections of N_2O and error bars for 500, 1000, 2000 and 5000 points in the ensemble convoluted with a Gaussian band shape of 0.1 eV broadening.

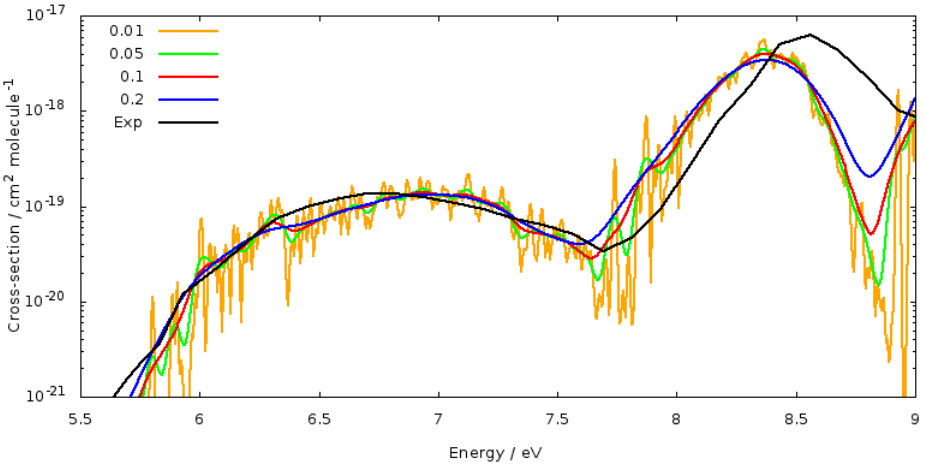

Figure 5.6: N_2O absorption cross sections convoluted with a Gaussian band shape from four phenomenological broadenings of the spectrum (eV) for 2000 points at EOM-CCSD/aug-cc-pVDZ level of theory, compared with the experimental cross section from Nicolet *et al.* [209].

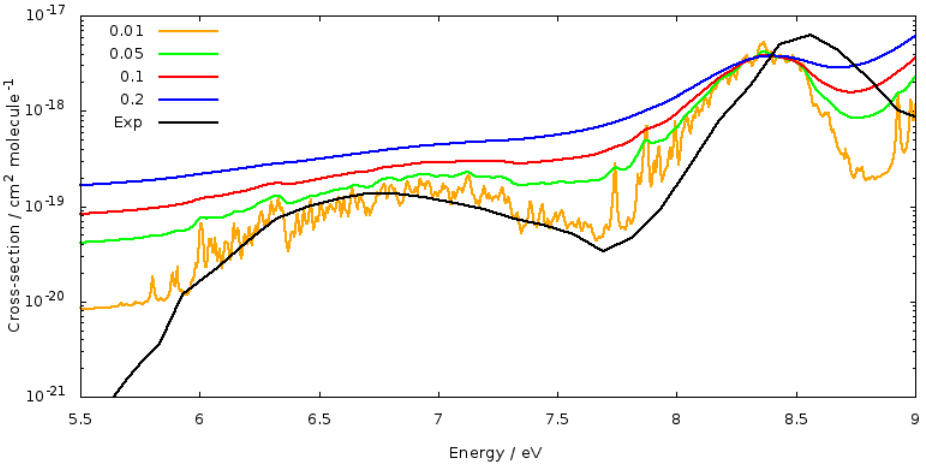

Figure 5.7: N_2O absorption cross sections convoluted with a Lorentzian band shape from four phenomenological broadenings of the spectrum (eV) for 2000 points at EOM-CCSD/aug-cc-pVDZ level of theory compared with the experimental cross section from Nicolet *et al.* [209].

5.3.2 Electronic structure benchmark

In chapter 3, the EOM-CCSD/aug-cc-pVTZ level of theory was shown to generate electronic absorption spectra that are in good agreement with experimental results for a range of sulfur-containing molecules. Although simulating the EOM-CCSD/aug-cc-pVTZ absorption spectrum of N_2O is feasible at reasonable cost, simulating the absorption spectra and photodissociation dynamics of the complexes will be much more computationally demanding. To have a rough comparison, we compare the computational cost of spectra simulation with 1000 points for the two EOM-CCSD and CAM-B3LYP methods with the same number of states. It takes about 30 minutes CPU time to calculate the excited states for one point with the EOM-CCSD method, while this time is about 22 seconds for the same calculation with the CAM-B3LYP method. Also, for dynamics simulations gradients are needed. These gradients are analytically calculated in DFT but are calculated numerically with EOM-CCSD and hence, the calculations become even more expensive. This difference in the computational cost is even more significant when we simulate the absorption spectra and photodissociation dynamics of the complexes where there are more electrons.

To find a method that gives reasonable results at lower cost, we first simulate the absorption spectrum of N_2O using EOM-CCSD and two DFT methods, CAM-B3LYP and M06, and compare the simulated spectra with the experimental results in Figure 5.8. While EOM-CCSD spectrum shows a better agreement with the experimental results, the CAM-B3LYP method produces reasonably accurate spectra for the two bands (A and B in Figure 5.4. In the lower energy region about 5.5-7.5 eV where the photodissociation of N_2O occurs there is reasonably good agreement among the three methods. The lower intensity of the simulated A band was also previously

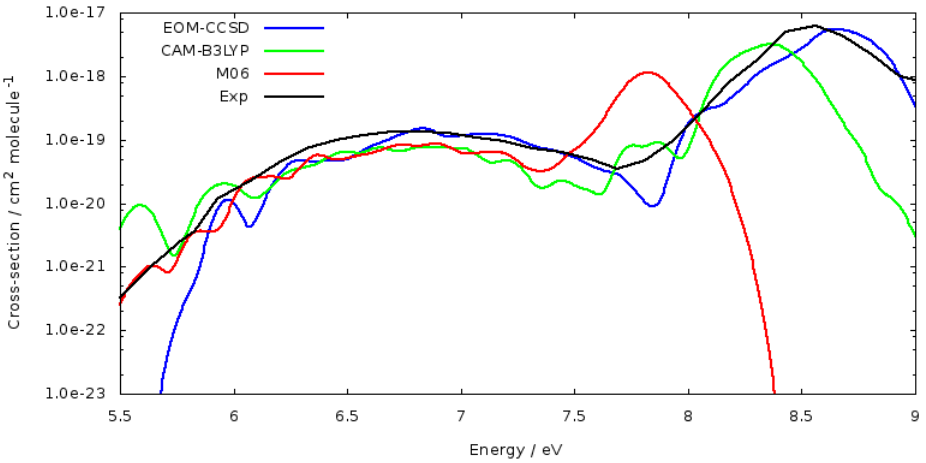

Figure 5.8: Aug-cc-pVTZ cross section of N_2O with different methods together with the experimental cross section of Nicolet *et al.* [210].

reported by Schinke [73] despite treating the photodissociation cross section of N_2O at the MRCI/aug-cc-pVQZ level of theory. Schinke multiplied his simulated cross section, shown in Figure 5.9, by a factor of 1.37 to shift up the calculated cross section to match the experimental results [73]. The low intensity problem in the spectrum of N_2O was improved by Daud *et al.* by taking into account the coupling of angular momentum and the parity of the molecule [211]. However, this approach is far more sophisticated than the nuclear ensemble approach available in Newton-X.

Given the promising CAM-B3LYP results in Figure 5.8, we further investigate the effect of changing basis set in Figure 5.10. We use three groups of basis sets to investigate the trend and consistency of our CAM-B3LYP results. The basis sets used include the Pople basis sets, 6-31G(d), 6-31+G(d) and 6-311++G(2d,2p), and the correlated consistent basis sets, cc-pVXZ and aug-cc-pVXZ, where X=D, T and Q. While the basis sets without diffused functions can reasonably simulate band A, diffused functions are needed to describe band B. This makes 6-31G(d) and cc-pVXZ basis sets un-

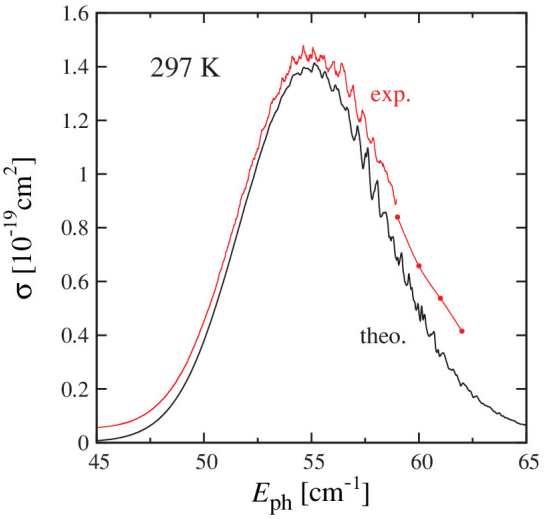

Figure 5.9: MRCI/aug-cc-pVQZ cross section of N_2O from Schinke [73] multiplied by a factor of 1.37 together with the experimental spectrum from Yushino *et al.* [210].

suitable for simulating the electronic absorption spectrum of N_2O in higher energy region, where Rydberg states are described. While the 6-31+G(d) and 6-311++G(2p,2d) basis sets show good agreement with the experimental spectrum, the aug-cc-pVXZ seem to give the best description of the two bands among the three groups of basis sets investigated in Figure 5.10. Also, these basis set comparisons show that the spectra simulated from aug-cc-pVXZ basis sets exhibit the least sensitivity to the basis set size, resulting in similar simulated absorption spectra.

From the comparisons made in this section for the monomeric N_2O, and considering the significant increase in computational cost for the complexes, we recommend using CAM-B3LYP and M06 methods for simulating the absorption cross section and photodissociation dynamics of the complexes. We are mostly interested in band A, the region where CAM-B3LYP and M06 methods can simulate spectra in good agreement with experimental spectra, and therefore, these two methods will be used for complexes, knowing that

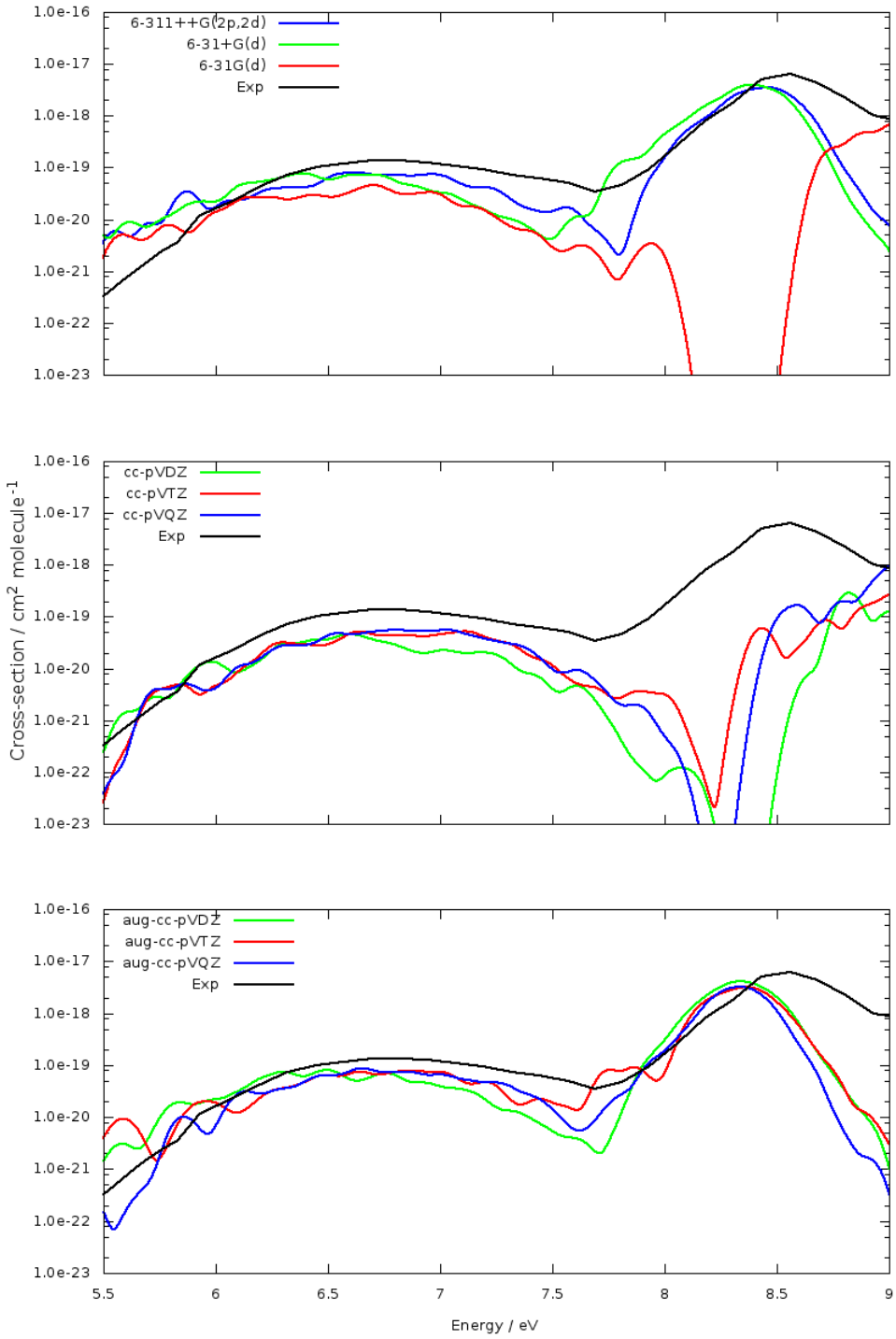

Figure 5.10: CAM-B3LYP cross section of N_2O with Pople, cc-pVXZ and aug-cc-pVXZ basis sets compared with the experimental cross section of Yushino *et al.* [209].

some accuracy is sacrificed to have feasible and faster simulations.

5.4 N_2O complexes structure and vibrational frequencies

As discussed in section 5.1, an accurate description of the structure and vibrational frequencies of N_2O complexes is important understand their significance in terms of N_2O photodisociation. In the following subsections, the previous experimental and theoretical investigations of the N_2O complexes are briefly explained and compared to our results.

5.4.1 Ar-N_2O

The first Ar-N_2O structure study was carried out back in 1981 by Joyner *et al.* [212]. Their spectroscopic constants determined a nearly T-shaped vibrationally averaged structure for the complex. The isotopic substitution showed that the argon atom was slightly tilted towards the oxygen atom of the N_2O. Later, Hodge and his coworkers reported the vibrationally resolved infrared spectrum of the Ar-N_2O van der Waals complex [213]. They confirmed the consistency between the rotational constants and a planar structure. In 1993, another rotationally resolved infrared spectrum together with improved molecular constants and new combination band results were reported by Hu *et al.* [214]. Leung *et al.* studied the Ar-N_2O rotational spectrum hyperfine structure in the microwave region with Fourier-transform microwave spectrometers and reported the rotational as well as centrifugal constants [215, 216]. Similar study was done by Ngari and Jager in 1998 on the two N_2O isotopomers complexes with Ar, Ar-$^{15}N^{14}N^{16}O$ and Ar-$^{14}N^{15}N^{16}O$ [217]. A rovibrational spectrum of the Ar-N_2O complex in the N_2O ν_1 region was recorded by Gimmler *et al.* in 2001 [218]. They reported the rotational and centrifugal distortion constants and showed a blue-shift

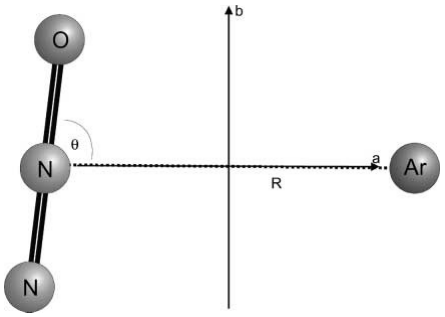

Figure 5.11: The structure of Ar-N_2O complex by Gimmler *et al.* [219] with R=3.460 Å and θ=7.4 degree.

of 0.2158(2) cm^{-1} compared to the N_2O spectrum. They calculated the two R=3.46(2) Å and θ=82.9(7)° parameters as shown in Figure 5.11.

Table 5.3: CAM-B3LYP/aug-cc-pVDZ and CCSD/aug-cc-pVDZ optimized geometries (in Å and degree) of Ar-N_2O complex compared with CCSD(T)-F12b results from Salmon *et al.* [202] with aug-cc-pV(T+d)Z/aug-cc-pV(Q+d)Z basis set pair extrapolated to CBS limit.

	CAM-B3LYP	CCSD	CCSD(T)-F12b
$R(N_1N_2)$	1.125	1.137	1.128[a]
$R(N_2O_1)$	1.187	1.197	1.186[b]
$R(N_2...Ar)$	3.540	3.551	3.396[b]
$\theta(N_1N_2$ ...Ar)	88.7	93.95	93.77[b]
$\theta(N_1N_2O_1)$	179.93	179.96	179.86[b]

[a]Theoretical results from Salmon *et al.* [202].
[b]Theoretical results from Salmon *et al.* [202].

The most recent theoretical study on Ar-N_2O complex was done by Salmon *et al.* [202], where they present the optimized structures, vibrational modes and binding energies of the complex [202]. In table in Table 5.3, we

Table 5.4: CAM-B3LYP/aug-cc-pVDZ and CCSD/aug-cc-pVDZ harmonic frequencies (in cm^{-1}) of Ar-N_2O complex compared with CCSD(T)-F12b results from Salmon *et al.* [202] with aug-cc-pV(T+d)Z/aug-cc-pV(Q+d)Z basis set pair extrapolated to CBS limit.

	CAM-B3LYP	CCSD	CCSD(T)-F12b	Expt
ν_1	24.9	33.0	38.9[a]	32.2[b], 31.4[c]
ν_2	33.0	35.7	45.9[b]	40.1[d], 38.1[c]
ν_3	607.7	591.9	599.9[b]	
ν_4	608.5	592.6	599.9[b]	
ν_5	1357.1	1306.1	1303.8[b]	1285.12[e]
ν_6	2401.0	2323.1	2289.1[b]	2223.91[f]

[a]Theoretical results from Salmon *et al.* [202].
[b]Experimental fundamental frequencies from Ngari *et al.* [217].
[c]Experimental fundamental frequencies from Hu *et al.* [214].
[d]Experimental fundamental frequencies from Ngari *et al.* [217].
[e]Experimental results from fundamental frequencies *et al.* [219].
[f]Experimental results from fundamental frequencies *et al.* [213].

compare the Ar-N_2O equilibrium geometry calculated at CAM-B3LYP/aug-cc-pVDZ and CCSD/aug-cc-pVDZ levels of theory with that from Salmon *et al.* calculated at the CCSD(T)-F12b complete basis set limit. In Table 5.4, we compare the corresponding vibrational frequencies obtained with the same methods and where available, they are compared with the experimental fundamental frequencies. While our intermolecular N_2O distances and angle calculated with CAM-B3LYP and CCSD methods are in good agreement with those from Salmon *et al.*, the intermolecular R(N_2...Ar) distance from both methods are 0.144 and 0.155 Å higher than the CCSD(T)-F12b distance by Salmon *et al.*. Also, the N_1N_2 ...Ar angle calculated with CAM-

B3LYP method is about 5 degree lower than the corresponding CCSD and CCSD(T)-F12b values. As expected, our calculated CCSD vibrational frequencies except for the intermolecular ν_2 frequency, show higher values than the fundamental experimental frequencies. In case of CAM-B3LYP, the two ν_1 and ν_2 frequencies are lower than the corresponding fundamental frequencies. While the CCSD and CAM-B3LYP intermolecular frequencies are higher than those calculated with CCSD(T)-F12b, they are consistent with the monomeric N_2O results. The disagreements in intramolecular geometry parameters and vibrational frequencies are due to the lower binding energies calculated with DFT and CCSD compared with CCSD(T)-F12b method.

5.4.2 N_2-N_2O

Randall *et al.* published the absorption spectrum of the N_2-N_2O complex in the ν_3 region of N_2O and reported a blue shift in the ν_3 band of the N_2O monomer [220]. They reported the structure of the complex as planar with a near T-shaped geometry and the N_2 molecule pointing towards the central nitrogen of the N_2O molecule. In 1999, Leung recorded the $^{15}N_2$-$^{14}N_2O$ rotational spectrum and confirmed the T-shaped structure. Venayagamoorthy and Ford published their *ab initio* study on the structure, interaction energies and vibrational spectra of N_2-N_2O in 2001 [221]. They confirmed a reasonably good agreement between their calculated centre-of-mass separation with that calculated by Randall *et al.*. In 2011, Zheng *et al.* calculated the *ab initio* two dimensional potential energy surface for the N_2-N_2O complex and recorded its ro-vibrational spectrum in the N_2O ν_1 region [222], which was similar to that detected by Randall *et al.* in the N_2 ν_3 region [220]. They also calculated the rotational and centrifugal distortion constants and determined the complex structure from the rotational constants. The CCSD(T) method with the aug-cc-pVDZ basis set were chosen to calculate the potential energy surface. In 2014, Rezaei *et al.* observed a new infrared absorption band of the N_2-N_2O complex using a quantum cascade laser arising from low frequency intermolecular modes combinations [223]. They reported a resulting intermolecular frequency of 22.334(1) cm^{-1} for this complex, although they could not identify the nature of this mode due to the lack of the theoretical predictions. This theoretical study happened later in 2015 by Zheng *et al.* [224]. Employing the CCSD(T) method with the aug-cc-pVTZ basis set, they calculated a four-dimensional intermolecular potential energy surface and determined two equivalent nearly T-shaped global minima in which the O atom is closer to the N_2 than N atom in N_2O. Their calculated

intermolecular distortion mode; 23.086 cm^{-1}, was in good agreement with the experimental result; 22.334 cm^{-1}, from Rezaei *et al.* [223].

In Table 5.5, we compare the N_2-N_2O equilibrium geometry calculated at CAM-B3LYP/aug-cc-pVDZ and CCSD/aug-cc-pVDZ levels of theory with that from Salmon *et al.* calculated at the CCSD(T)-F12b complete basis set limit. In Table 5.6, we compare the corresponding vibrational frequencies obtained with the same methods and where available, they are compared with the experimental fundamental frequencies. Our both CAM-B3LYP and CCSD geometry results except for the intermolecular (N_2...N_3N_4) angle, show good agreement with results from Salmon *et al.*. While the calculated CAM-B3LYP and CCSD ν_1- ν_6 harmonic frequencies show good agreement with the CCSD(T)-F12b, our calculated intramolecular ν_7 and ν_8 frequencies are a bit higher than those calculated by Salmon *et al.*. However, these two interamolecular frequencies are consistent with those from the monomeric N_2O. We also compare the two ν_1 and ν_8 calculated frequencies with their available corresponding experimental fundamental frequencies, and as expected they show higher values than experimental results.

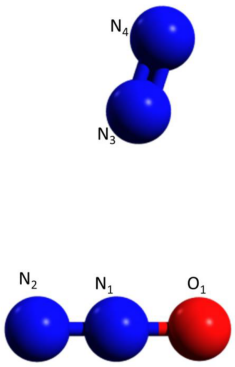

Figure 5.12: Optimized equilibrium structures of N_2-N_2O complex at CCSD(T)-F12b/CBS limit using the aug-cc-pVTZ/aug-cc-pVQZ basis set pair from Salmon *et al.* [202].

Table 5.5: CAM-B3LYP/aug-cc-pVDZ and EOM-CCSD/aug-cc-pVDZ optimized geometries (in Å and degree) of N_2-N_2O complex compared with CCSD(T)-F12b results from Salmon *et al.* [202] with aug-cc-pVTZ/aug-cc-pVQZ basis set pair extrapolated to CBS limit.

	CAM-B3LYP	CCSD	CCSD(T)-F12b
$R(N_1N_2)$	1.125	1.112	1.127[a]
$R(N_2O_1)$	1.186	1.197	1.186[b]
$R(N_3N_4)$	1.100	1.114	1.099[b]
$R(N_2...N_3)$	3.173	3.141	3.113[b]
$\theta(N_1N_2O_1)$	179.97	179.97	179.91[b]
$\theta(N_1N_2...N_3)$	96.0	94.76	95.22[b]
$\theta(N_2...N_3N_4)$	164.87	164.87	167.90[b]

[a]Theoretical results from Salmon *et al.* [202].
[b]Theoretical results from Salmon *et al.* [202].

Table 5.6: CAM-B3LYP/aug-cc-pVDZ and CCSD/aug-cc-pVDZ harmonic frequencies (in cm^{-1}) of N_2-N_2O complex compared with CCSD(T)-F12b results from Salmon *et al.* [202] with aug-cc-pVTZ/aug-cc-pVQZ basis set pair extrapolated to CBS limit.

	CAM-B3LYP	CCSD	CCSD(T)-F12b	Expt
ν_1	27.0	24.5	25.9[a]	22.3[b]
ν_2	38.4	35.7	35.1[b]	
ν_3	52.6	59.3	61.3[b]	
ν_4	80.0	81.5	84.0[b]	
ν_5	607.6	590.7	600.3[b]	
ν_6	608.9	592.6	600.8[b]	
ν_7	1358.0	1306.5	1304.7[b]	
ν_8	2403.6	2325.9	2291.8[b]	2225.99[bcd]
ν_9	2498.9	2394.6	2364.2[b]	

[a]Theoretical results from Salmon *et al.* [202].
[b]Experimental fundamental frequencies from Rezaei *et al.* [223].
[c]Experimental fundamental frequencies from Randall *et al.* [220]
[d]Experimental fundamental frequencies from Zheng *et al.* [222]

5.4.3 O_2-N_2O

The first experimental investigation on the O_2-N_2O complex was reported by Bahou *et al.* in 1996 using low-resolution infrared spectroscopy and matrix isolation techniques and related the small shifts in the ν_1 and ν_3 regions of the absorption of N_2O to the weak interaction between the N_2O and O_2 molecules [225]. Soon after, Qian *et al.* published their work on high resolution spectroscopy and structure of the O_2-N_2O complex [226]. They calculated the rotational constants and reported a planar equilibrium structure. In 2014, Li *et al.* measured the ro-vibrational spectrum of O_2-N_2O complex in the ν_1 region of monomeric N_2O [227] and reported a red shift in the band origin of monomeric N_2O. They also measured the rotational constants of O_2-N_2O complex. Recently, Salmon *et al*, investigated the structures of O_2-N_2O complex with the lowest energy using the CCSD(T)-F12b method and identified the minima structures and calculated the vibrational frequencies [228]. They reported a local minimum at -159 cm^{-1} and a global minimum at -191 cm^{-1}. This is while Qian *et al.* had reported two minima with a first order saddle point.

In Table 5.7, we compare the O_2-N_2O equilibrium geometry calculated at CAM-B3LYP/aug-cc-pVDZ and CCSD/aug-cc-pVDZ levels of theory with that from Salmon *et al.* calculated at the CCSD(T)-F12b complete basis set limit. In Table 5.8, we compare the corresponding vibrational frequencies obtained with the same methods and where available, they are compared with the experimental fundamental frequencies. We find that our calculated CCSD/aug-cc-pVDZ geometry parameters, both intermolecular and intramolecular, are in good agreement with CCSD(T)-F12b results. While most of the calculated CAM-B3LYP/aug-cc-pVDZ geometry parameters show good agreement with CCSD(T)-F12b results from Salmon *et al.*,

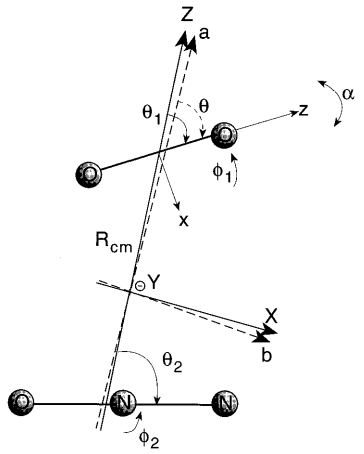

Δ''/u Å^2	−0.61(13)
Δ'/u Å^2	−0.53(10)
R''/Å	3.4232(10)
R'/Å	3.4243(6)
θ_1 /^{0}	58 or 122
θ_2 /^{0}	77 or 100
α/^{0}	20.53(5)

Figure 5.13: The suggested planar structure from Qian *et al.* [226]

.

the two intermolecular ($N_1N_2...O_2$) and ($N_2...O_2O_3$) angles are higher than their corresponding CCSD(T)-F12b values by 2.75 and 5.34 degrees. Our CAM-B3LYP and CCSD vibrational frequencies are in reasonable agreement with the CCSD(T)-F12b results from Salmon *et al.* and our calculated ν_7 and ν_9 are higher than the corresponding available experimental fundamental frequencies as expected. However, the two CAM-B3LYP ν_3 and ν_4 vibrational frequencies are lower than both CCSD and CCSD(T)-F12b frequencies. Also, our two calculated N_2O intramolecular ν_7 and ν_9 frequencies are higher than the CCSD(T)-F12b frequencies calculated by Salmon *et al.* which is consistent with the monomeric N_2O results.

Table 5.7: CAM-B3LYP/aug-cc-pVDZ and CCSD/aug-cc-pVDZ optimized geometries (in Å and degree) of O_2-N_2O complex compared with CCSD(T)-F12b results from Salmon *et al.* [202] with aug-cc-pVTZ/aug-cc-pVQZ basis set pair extrapolated to CBS limit.

	CAM-B3LYP	CCSD	CCSD(T)-F12b
$R(N_1N_2)$	1.125	1.135	1.127[a]
$R(N_2O_1)$	1.187	1.197	1.186[b]
$R(O_2O_3)$	1.198	1.210	1.206[b]
$R(N_2...O_2)$	3.144	3.099	3.068[b]
$\theta(N_1N_2O_1)$	179.94	179.94	179.85[b]
$\theta(N_1N_2...O_2)$	97.85	94.59	95.10[b]
$\theta(N_2...O_2O_3)$	118.24	114.37	113.875[b]

[a]Theoretical results from Salmon *et al.* [202].
[b]Theoretical results from Salmon *et al.* [202].

Table 5.8: CAM-B3LYP/aug-cc-pVDZ and CCSD/aug-cc-pVDZ harmonic frequencies (in cm^{-1}) of O_2-N_2O complex compared with CCSD(T)-F12b results from Salmon *et al.* [202] with aug-cc-pVTZ/aug-cc-pVQZ basis set pair extrapolated to CBS limit.

	CAM-B3LYP	CCSD	CCSD(T)-F12b	Expt
ν_1	22.18	23.8	21.7[a]	
ν_2	23.86	32.7	27.3[b]	
ν_3	36.91	44.3	45.9[b]	
ν_4	65.88	66.4	70.0[b]	
ν_5	607.88	597.7	599.0[b]	
ν_6	608.31	600.3	599.0[b]	
ν_7	1356.60	1389.6	1302.5[b]	1284.75[b]
ν_8	1721.70	1642.3	1613.0[b]	
ν_9	2401.89	2325.7	2287.5[b]	2224.12[c]

[a]Theoretical results from Salmon *et al.* [202].
[b]Experimental fundamental frequencies from Qian *et al.* [226].
[c]Experimental fundamental frequencies from Li *et al.* [227].

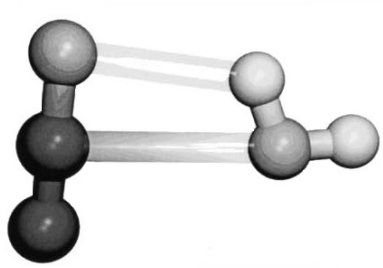

Figure 5.14: The calculated structure from infrared work with intermolecular distance of 2.964 Å and water tilt angle (θ) of 82 degree from Gimmler *et al.* [231].

5.4.4 H_2O-N_2O

The first study on H_2O-N_2O complex was a theoretical investigation of the structure, vibrational frequencies and IR intensities by Sadlej and Sicinski [229]. They showed small changes in frequencies and a clear perturbation in the spectrum due to the complex formation and suggested planar structures for the complex. Later, Zoland *et al.* reported the rotational spectrum of H_2O-N_2O in the microwave region using molecular beam electric resonance techniques and presented two close global minima and two local minima using electrostatic modeling [230].

Gimmler *et al.* reported the first IR ro-vibrational spectrum of the H_2O-N_2O complex and proposed a planar structure with the assumption that the structures of monomers do not change upon complexation [231]. Their proposed structure is shown in Figure 5.14.

In 2001, Wójcik *et al.* theoretically investigated the structure and vibrational modes of H_2O-N_2O complex which were in qualitative agreement with previous works [232]. They employed a higher level of theory, MP2/ 6-31++G**, and presented a better description of the interactions in the complex.

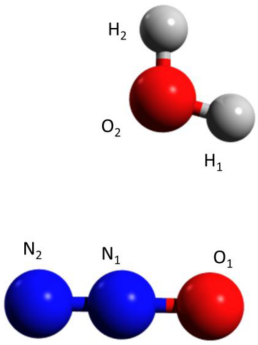

Figure 5.15: Optimized equilibrium structures of H_2O-N_2O complex at CCSD(T)-F12b/CBS limit using the aug-cc-pV(T+d)Z/aug-cc-pV(Q+d)Z basis set pair from Salmon *et al.* [202].

Recently, Földes *et al.* reported planar structures for both local and global minima of H_2O-N_2O complex, using CCSD(T)-F12a/aug-cc-pVQZ level of theory [233]. They confirmed the overall agreement between their calculated global minimum and those from IR spectroscopy [231] and microwave study [230]. They also calculated the harmonic vibrational frequencies using the same method and slightly smaller basis set, aug-cc-pVTZ.

In Table 5.9, we compare the H_2O-N_2O equilibrium geometry calculated at M06/aug-cc-pVDZ, CAM-B3LYP/aug-cc-pVDZ and CCSD/aug-cc-pVDZ levels of theory with that from Salmon *et al.* calculated at the CCSD(T)-F12b complete basis set limit. In Table 5.10, we compare the corresponding vibrational frequencies obtained with the same methods and where available, they are compared with the experimental fundamental frequencies. We also include M06 equilibrium geometry and vibrational frequencies in these tables, as this method is used in chapter 6, where we simulate the photodissociation dynamics of N_2O monomer and H_2O-N_2O complex. Our CAM-B3LYP and CCSD calculated geometries are in good agreement with the CCSD(T)-F12b results from Salmon *et al.*. Excep-

tion are the two CAM-B3LYP and CCSD intermolecular ($N_1N_2...O_2$) and ($N_2...O_2H_1$) angles, which show slightly higher and lower values compared with CCSD(T)-F12b respectively. While the intermolecular vibrational frequencies are in reasonable agreement with CCSD(T)-F12b results, the intermolecular ν_2 and ν_5 harmonic frequencies are higher than the corresponding CCSDT(T)-F12b frequencies. This difference is the highest for the ν_5 calculated with M06 method. Comparing the calculated N-N stretching vibrational frequencies with the only experimental fundamental frequency available for this complex, shows that our calculated frequencies with the three methods are all higher than the corresponding experimental frequency, as expected. The N_2O intermolecular vibrational frequencies are slightly higher than the CCSD(T)-F12b results, which is consistent with the results from monomeric N_2O.

Table 5.9: M06/aug-cc-pVDZ, CAM-B3LYP/aug-cc-pVDZ and CCSD/aug-cc-pVDZ optimized geometries (in Å and degree) of H_2O-N_2O complex compared with CCSD(T)-F12b results from Salmon *et al.* [202] with aug-cc-pVTZ/aug-cc-pVQZ basis set pair extrapolated to CBS limit.

	M06	CAM-B3LYP	CCSD	CCSD(T)-F12b
$R(N_1N_2)$	1.130	1.123	1.134	1.125[a]
$R(N_2O_1)$	1.182	1.189	1.201	1.188[b]
$R(O_2H_2)$	0.962	0.964	0.965	0.958[b]
$R(O_2H_1)$	0.958	0.962	0.964	0.959[b]
$R(N_2...O_2)$	2.900	2.889	2.893	2.849[b]
$\theta(N_1N_2O_1)$	179.435	179.46	179.51	179.58[b]
$\theta(H_1O_2H_2)$	105.28	105.86	104.78	105.05[b]
$\theta(N_1N_2...O_2)$	102.24	105.21	101.43	100.54[b]
$\theta(N_2...O_2H_1)$	83.53	79.39	77.45	85.78[b]

[a]Theoretical results from Salmon *et al.* [202].
[b]Theoretical results from Salmon *et al.* [202].

Table 5.10: M06/aug-cc-pVDZ, CAM-B3LYP/aug-cc-pVDZ and CCSD/aug-cc-pVDZ harmonic frequencies (in cm^{-1}) of H_2O-N_2O complex compared with CCSD(T)-F12b results from Salmon *et al.* [202] with aug-cc-pVTZ/aug-cc-pVQZ basis set pair extrapolated to CBS limit.

	M06	CAM-B3LYP	CCSD	CCSD(T)-F12b	Expt
ν_1	69.0	60.2	66.9	66.7[a]	
ν_2	105.4	129.1	129.4	77.5[b]	
ν_3	150.2	131.2	132.7	121.5[b]	
ν_4	182.4	166.4	173.5	157.0[b]	
ν_5	303.5	227.8	233.8	205.9[b]	
ν_6	622.0	604.6	588.3	597.6[b]	
ν_7	624.1	606.2	588.8	598.9[b]	
ν_8	1376.8	1349.8	1295.6	1299.4[b]	
ν_9	1621.3	1604.5	1643.2	1642.4[b]	
ν_{10}	2413.7	2413.0	2333.9	2298.7[b]	2232.17[b]
ν_{11}	3864.3	3832.8	3821.5	3831.5[b]	
ν_{12}	3989.9	3944.5	3939.1	3943.7[b]	

[a]Theoretical results from Salmon *et al.* [202].
[b]Experimental fundamental frequencies from Gimmler *et al.* [231].

5.5 N_2O complexes absorption cross section

In this section, we investigate the changes in the cross section of N_2O upon complexation with four abundant stratospheric species namely, Ar, N_2, O_2 and H_2O. We simulate the absorption cross section of the complexes and N_2O monomer using the same Newton-X and electronic structure parameters.

We initially simulated the absorption cross sections with the CAM-B3LYP/aug-cc-pVTZ method and present these in Figure 5.16. In the spectra simulation of Ar-N_2O complex, the EOM-CCSD cross section of monomeric N_2O from 6 states is compared with that of Ar-N_2O complex. To have a better description of Ar's electrons, we use aug-cc-pV(D+d)Z basis set on Ar atom. For Ar-N_2O, N_2-N_2O and H_2O-N_2O complexes 6 states involved in the energy calculations. In the case of O_2-N_2O, the cross section is simulated from 16 states as O_2 has many low lying states. For each comparing graph, the absorption cross section of monomeric N_2O is calculated with the same simulations parameters used for the related complex. As we are interested in the changes in the N_2O photodissociation region, i.e. band A in Figure 5.4, these spectra are zoomed in this region. We find that, the absorption cross section of Ar-N_2O and N_2-N_2O complexes are almost the same as the cross section of N_2O monomer. However, for O_2-N_2O and H_2O-N_2O complexes, the absorption cross section of the complex in the the N_2O photodissociation region is significantly higher than that of N_2O monomer.

On the basis of this exciting preliminary result, we initiated a collaboration with the Kable group at the University of New South Wales, to experimentally investigate the photodissociation dynamics of the two O_2-N_2O and H_2O-N_2O complexes. The effective absorption cross section of N_2O dimer and O_2-N_2O complexes and monomeric N_2O were recorded us-

ing the photon-fragment excitation ion spectroscopy (PHOFEX). The mixture of N_2O and O_2 in He went through supersonic cooling and skimming in the source chamber to make a molecular beam. This molecular beam was then crossed by lasers from two-laser and one-laser arrangements. In two-laser arrangement, N_2O is photolysed and the fragments are resonantly ionized. In the one-laser arrangement, N_2O is dissociated the fragments are probed. This preliminary experimental result is presented in Figure 5.17 which showed a small increase in the intensity of the O_2-N_2O cross section compared to that of N_2O in 210-216 nm (5.74-5.90 eV) region of energy. Therefore, we tried higher level of theory and more computationally expensive EOM-CCSD method to simulate the spectra. The efforts to record the cross section of H_2O-N_2O complex was unsuccessful due to challenges in maintaining fixed water vapour pressure. In Ar-N_2O and N_2-N_2O complexes, N_2O is aggregated with two inert species, they do not seem to produce any interesting products upon photodissociation of N_2O or cause any significant change in the intensity of the N_2O absorption spectra. Hence they are not our priorities to investigate their experimental photodissociation dynamics.

The EOM-CCSD method was previously showed to produce reliable spectra and in good agreement with experimental results for a range of sulfur-containing molecules in chapter 3. The simulated EOM-CCSD/aug-cc-pVDZ absorption spectra of the four complexes are presented and compared with the absorption spectrum of monomeric N_2O in Figure 5.18.

Comparing the CAM-B3LYP/aug-cc-pVTZ and EOM-CCSD/aug-cc-pVDZ simulated spectra, shows that the EOM-CCSD cross sections are more than 30% higher in intensity than CAM-B3LYP for Ar-N_2O and N_2-N_2O complexes. In the case of O_2-N_2O, the intensity increases more significantly and

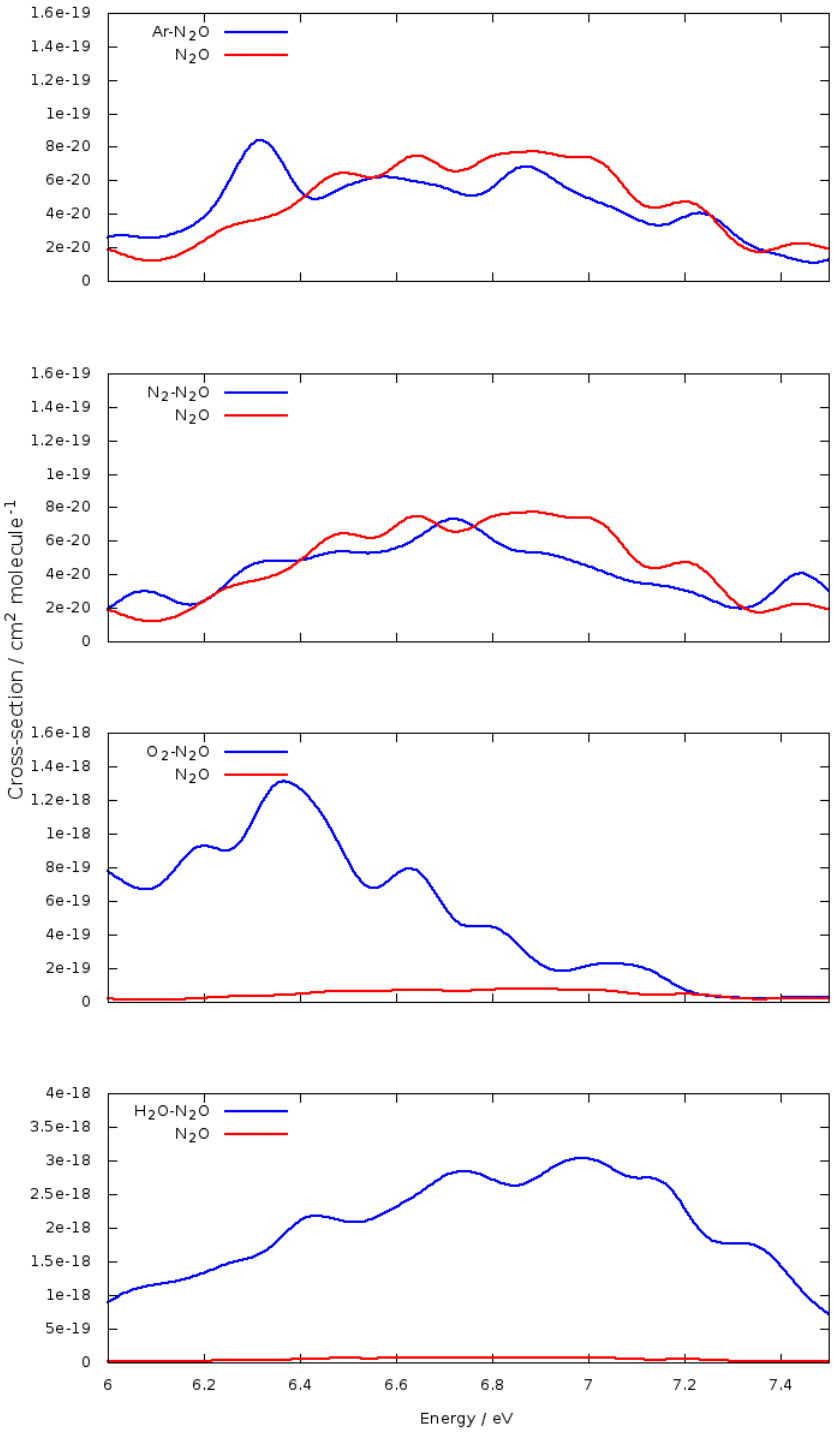

Figure 5.16: Absorption cross section of N_2O monomer and the four N_2O complexes. The level of theory and number of states involved in these simulations are CAM-B3LYP/aug-cc-pVTZ with 6 states for Ar-N_2O and H_2O-N_2O and N_2-N_2O complexes, and 15 states for O_2-N_2O complexe.

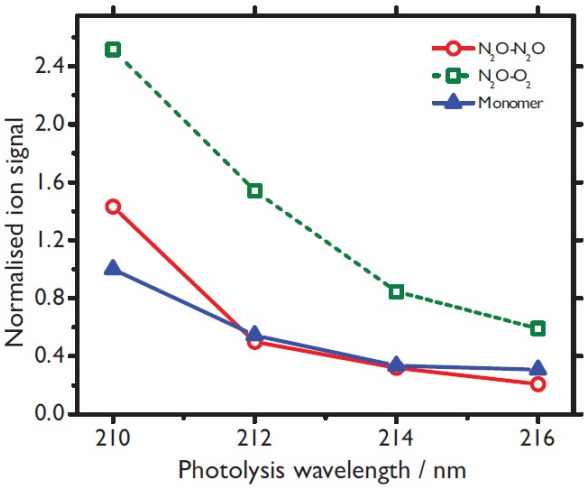

Figure 5.17: The preliminary PHOFEX experimental effective absorption cross sections of N_2O-N_2O, N_2O-O_2 complexes and N_2O monomer.

the absorption band in the region of N_2O band A, is blue shifted by about 1.0 eV. This is due to the difference between the CCSD and CAM-B3LYP geometries and vibrational frequencies. For H_2O-N_2O, a slight blue shift of about 0.2 eV is observed in the EOM-CCSD simulated band and the intensity looks to be about 25% higher than CAM-B3LYP. Despite these differences between the EOM-CCSD and CAM-B3LYP simulated spectra of complexes, they are consistent in predicting a significant increase in the cross sections of H_2O-N_2O and O_2-N_2O complexes and no specific change in the absorption spectra of Ar-N_2O and N_2-N_2O complexes.

A great amount of effort was put into the recording the effective absorption cross section of the N_2O-N_2O, O_2-N_2O complexes and N_2O monomer again by our experimentalist collaborators. The wavelength dependence standardized ion yield of N_2O-N_2O and O_2-N_2O complexes and N_2O monomer were measured and the results are shown in Figure 5.19. This time, no significant enhancement in the absorption of the O_2-N_2O complex was ob-

served. This disagreement should be due to our theoretical approach in simulating the absorption spectra of complexes, which is surprising as the same approach worked reasonably well for N_2O monomer and gave excellent accuracy for sulfur-containing molecules in chapter 3.

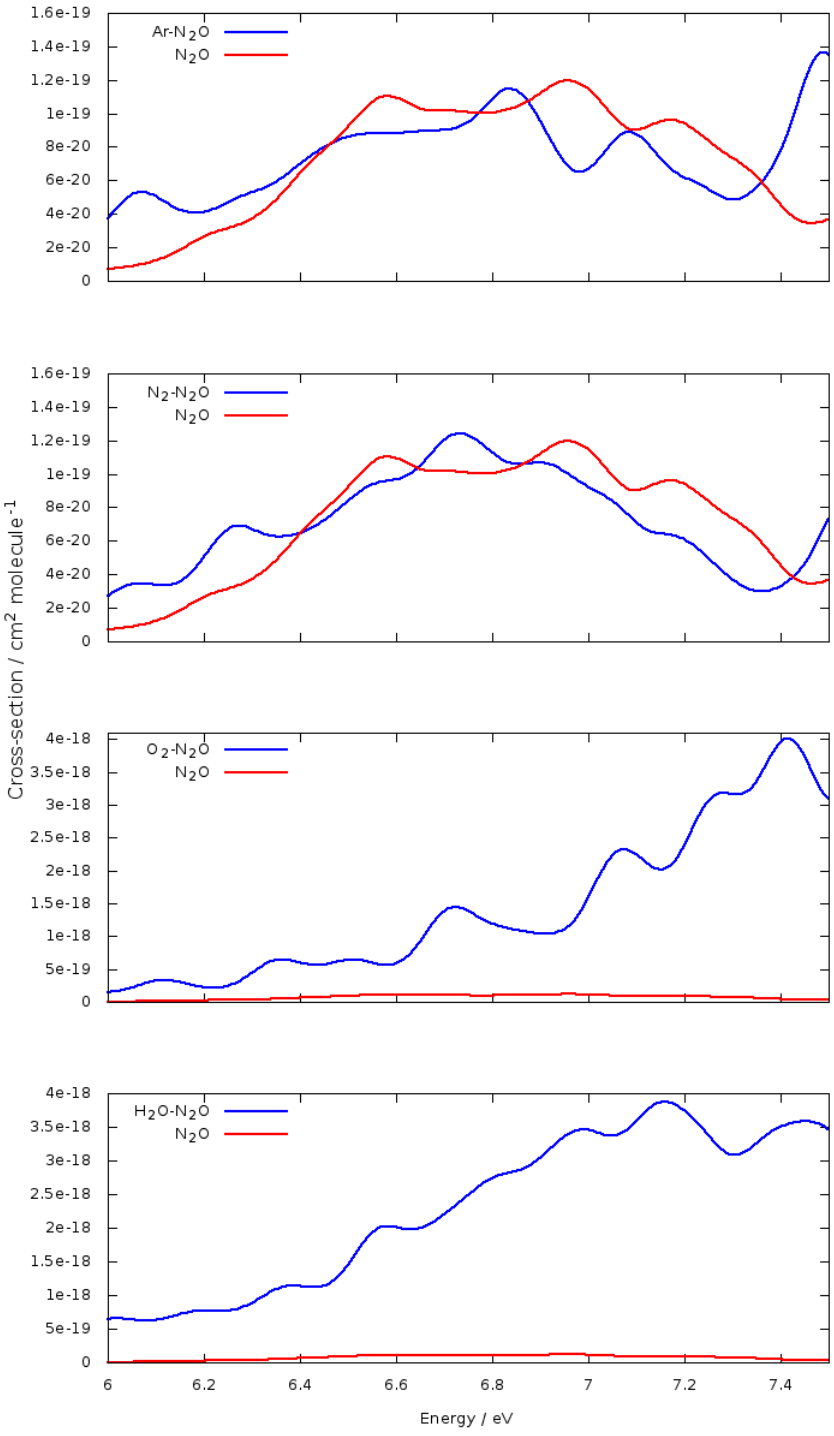

Figure 5.18: Absorption cross section of N_2O monomer and the four N_2O complexes. The level of theory and number of states involved in these simulations are EOM-CCSD/aug-cc-pVDZ with 6 states for Ar-N_2O and H_2O-N_2O and N_2-N_2O complexes, and 15 states for O_2-N_2O complexe.

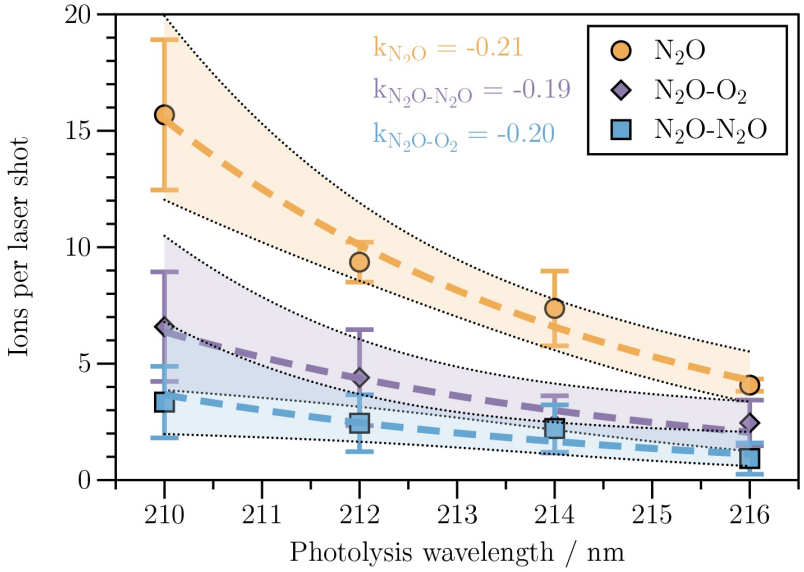

Figure 5.19: The repeated PHOFEX experimental effective absorption cross sections of N_2O-N_2O, O_2-N_2O complexes and N_2O monomer.

We suggest, however, Newton-X can simulate absorption cross section of individual molecules with reasonably high accuracy, it is not capable of generating accurate cross section for aggregated molecules. We believe that how energy is partitioned and geometries are sampled and distributed in the ensemble is different from the cases where only one molecule is involved in the spectra simulations. Also, we find that for the energy regions where the aggregated molecule with N_2O shows high absorbance, the change in the calculated cross section can be overestimated. For example, in the simulated spectrum of O_2-N_2O complex, the highest contribution to the complex spectrum, seems to be from the O_2 excitations. Two geometries from the O_2-N_2O ensemble with the highest oscillator strengths are shown in Figure 5.20, and their geometry parameters are presented in Table 5.11. To check whether the O_2 excitations contribute significantly to the increased intensity, we calculate the EOM-CCSD/aug-cc-pVDZ vertical excitations and oscillator strengths of O_2 monomer, with the same distance as given in Table 5.11 for O-O bond in the complex. Our calculated vertical excitations and oscillator strengths of O_2 monomer are very close to those from the complex, suggesting that the O_2 excitations contribute significantly to the simulated spectra of this complex.

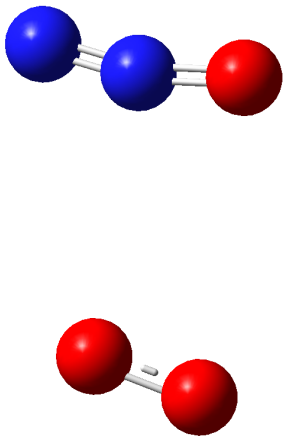

(a) Geometry 1

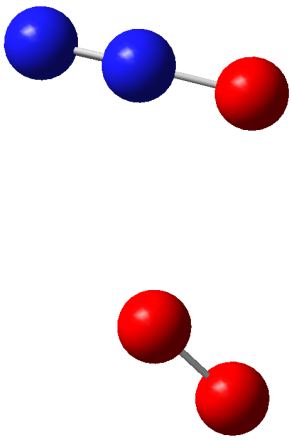

(b) Geometry 2

Figure 5.20: Two examples of geometries with the very high oscillator strengths in the ensemble of O_2-N_2O complex.

Table 5.11: CCSD/aug-cc-pVDZ geometry parameters (in Å and degree) of two examples of O_2-N_2O complex with non-physical geometries.

	Geometry 1	Geometry 2
$R(N_1N_2)$	1.147	1.131
$R(N_2O_1)$	1.213	1.297
$R(O_2O_3)$	1.232	1.277
$R(N_2...O_2)$	3.102	2.945
$\theta(N_1N_2O_1)$	166.74	169.99
$\theta(N_1N_2...O_2)$	98.61	104.56
$\theta(N_2...O_2O_3)$	102.74	135.70

5.6 Conclusion

The geometry and harmonic frequencies of N_2O monomer and its four complexes with Ar, N_2, O_2 and H_2O species were calculated using both CCSD and DFT methods. Some of the spectra simulation parameters were benchmarked for N_2O monomer and the simulated spectra were compared with the experimental spectrum. The absorption spectra of the four complexes of N_2O were simulated and compared to that of the monomeric N_2O to see any changes upon complexation. Our preliminary CAM-B3LYP simulated spectra of the complexes showed a significant increase in the absorption spectrum of N_2O for O_2-N_2O and H_2O-N_2O and no significant change for the Ar-N_2O and N_2-N_2O complexes. The initial experimental results on O_2-N_2O complex were promising showing a small increase in the cross section

of the complex. Following these consistent preliminary results, we improved the accuracy of our simulated spectra of the complexes by applying a higher level of theory in our simulations, EOM-CCSD/aug-cc-pVDZ, which had given results with good agreement with experimental results for a range of sulfur-containing molecules in chapter 3. Our EOM-CCSD/aug-cc-pVDZ simulated spectra gave consistent results with CAM-B3LYP/aug-cc-pVTZ spectra and hence, the experiment was repeated for the O_2-N_2O complex to find any change in the cross section of the complex. This subsequent experiment could not confirm the earlier findings.

While, the absorption cross section of N_2O shows no significant change upon complexation, the photodissociation dynamics of these complexes are interesting to study, as complicated potential energy surfaces of the complexes might open other photodissociation channels, where atmospherically important species, rather than the known products from photodissociation of monomeric N_2O, can be produced. For example, in chapter 6, we simulate the photodissociation dynamics of H_2O-N_2O complex to investigate the possible products and changes in the photodissociation dynamics of N_2O monomer upon complexation.

Chapter 6

Photodissociation dynamics of H_2O-N_2O

Chapter 5 showed that the electronic absorption spectra of the Ar-N_2O, N_2-N_2O, O_2-N_2O and H_2O-N_2O complexes were not substantially different to that of N_2O monomer. However, these complexes could still be important if photodissociation leads to different products than N_2O monomer. In this chapter, we simulate the photodissociation dynamics of H_2O-N_2O, and compare these to that of N_2O monomer. Previous experimental results showed that photodissociation of H_2O-N_2O with 193 nm light produces OH radical, although the mechanism is unknown.

6.1 Photodissociation of N_2O complexes

Several previous studies on the photodissociation dynamics of N_2O [199,205, 234–236] showed that the UV photodissociation of N_2O exclusively produces N_2 molecule and atomic $O(^1D)$ through the following reaction:

$$N_2O + h\nu \rightarrow N_2 + O(^1D) \tag{6.1}$$

The photodissociation dynamics of N_2O in the UV region at about 200 nm have been experimentally studied in detail, using different experimental techniques [235–245]. Some of these studies showed that the N_2 fragment in the UV photodissociation is vibrationally cold but rotationally excited [235,241–243]. Also, other studies investigated the photodissociation of N_2O in the vacuum ultraviolet (VUV) region where other dissociation channels are energetically accessible and new fragments can be produced through the following reactions [205, 246]:

$$N_2O + h\nu \rightarrow N_2 + O(^1S_0) \tag{6.2}$$

$$N_2O + h\nu \rightarrow N_2 + O(^3P_J) \tag{6.3}$$

$$N_2O + h\nu \rightarrow N(^2D) + NO \tag{6.4}$$

$$N_2O + h\nu \rightarrow N(^2P) + NO \tag{6.5}$$

There are also some detailed theoretical studies on N_2O photodissociation and its energy partitioning using quantum mechanical wave packet and classical trajectory calculations [73, 247]. Previous simulations and experiments have largely been carried out on the isolated N_2O molecule and with a limited energy window for photodissociation. This is why investigating the dynamics of N_2O complexes under atmospheric conditions might reveal new features of atmospheric chemistry and photodissociation dynamics.

The most interesting part of photodissociation dynamics of N_2O complexes, is that the more complicated potential energy surfaces of the complexes might lead to some new channels and products of photodissociation. Depending on the aggregated molecules, the new products could be of high atmospheric importance. It was previously shown that formation of the O_3-H_2O complex can change the photodissociation products of O_3 from atomic oxygen as the main product to OH radical instead [70]. We list the possible products of photodissociation of the four complexes investigated in chapter 5 below:

$$N_2O - Ar + h\nu \rightarrow N_2 + O + Ar \tag{6.6}$$

$$N_2O - N_2 + h\nu \rightarrow N_2 + N_2O \tag{6.7}$$

$$N_2O - O_2 + h\nu \rightarrow N_2 + O_3 \tag{6.8}$$

$$N_2O - H_2O + h\nu \rightarrow N_2 + 2OH \tag{6.9}$$

The products of the two Ar-N_2O and N_2-N_2O complexes are not of high atmospheric importance, as no new species are produced. In reaction 6.6, the atomic O produced from the photodissociation of N_2O cannot react with the non-reactive Ar atom. In the case of N_2-N_2O, if atomic O reacts with N_2 molecule, it likely just regenerates N_2O. This could be interesting as regeneration of N_2O could increase its lifetime in the atmosphere but it would be experimentally difficult to follow the formation of N_2O molecules. However, in the case of the other two complexes, H_2O-N_2O and O_2-N_2O,

interesting atmospheric species such as OH radical and O_3 can be produced. In this chapter, we focus our attention on the H_2O-N_2O complex as there are no previous experimental results for the O_2-N_2O complex.

In 1997, Tanaka *et al.* investigated the photodissociation dynamics of the H_2O-N_2O complex, using an excimer laser at 193 nm to cause photodissociation [203]. They reported the production of OH radical as a new product, formed upon complexation and in a reactant-pair photodissociation reaction [203]. In this work, Tanaka *et al.* used heavy water ($H_2{}^{18}O$) and measured the vibrational-rotational distribution of the OH radicals. This study suggested a strong sideways kick-out of O from N_2O, coming from the highly rotationally excited N_2, that could interact with water molecule to produce OH radical. Their calculated equilibrium geometry of the H_2O-N_2O complex is shown in Figure 6.1. However, it is worth noting that more recent and accurate investigations [202, 233] show different structure as discussed in subsection 5.4.4. On the basis of their dynamics results, Tanaka *et al.* proposed some channels through which OH radical could be produced. Using their measured vibrational and rotational distributions of ^{18}OH and ^{16}OH, and comparing these results with the previously studied O_3-H_2O system [248], an intermediate of $OH^{18}OH$ that could be responsible for their observations, was proposed. They also suggested more experimental results to understand this process fully, although these have not been forthcoming.

In the section 6.3, the photodissociation dynamics of H_2O-N_2O are simulated and compared with that of N_2O. As the photodissociation process of N_2O is well known, we first simulate the photodissociation dynamics of N_2O to validate our stimulation approach against previous results.

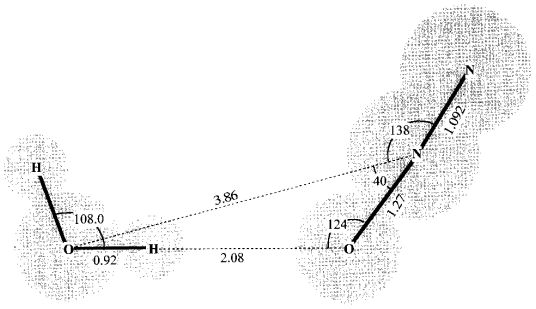

Figure 6.1: Experimental structure of H_2O- N_2O molecule from Tanaka *et al.* [203].

6.2 N_2O photodissociation dynamics

As described in chapter 2, we use trajectory surface hopping (TSH) approach to simulate the photodissociation dynamics of N_2O. The probability of nonadiabatic transition is calculated by applying the Tully's fewest switches algorithm [160], as implemented in Newton-X [169]. We first prepare the initial conditions by defining an ensemble of 10000 geometries around the equilibrium geometry and then, promote the initial condition to the excited state. To do so, we use a Wigner distribution of the harmonic vibrational modes [155]. The initial condition can be also prepared by running a long ground state dynamics and later, randomly choosing the geometries at defined time intervals; however, this can make distribution of the initial conditions too narrow [159].

The trajectories are chosen from a previously distributed ensemble and by imposing some energy restrictions, to reflect the energies of stratospheric photons: [1.2-7.2 eV (1033.2-172.2 nm)], we focus on conditions relevant for Earth's atmosphere. The on-the-fly electronic structure calculations are the most expensive part of the dynamics simulations. Complexes with medium size like H_2O-N_2O, are not neither very small to use a high level of theory at reasonable cost, nor too large where running high level calculations

is almost impossible. So, it is critical to find a balance between cost and accuracy for these systems. In chapter 5, we showed that CAM-B3LYP/aug-cc-pVDZ and M06/aug-cc-pVDZ could give reasonably accurate geometries and vibrational frequencies for N_2O at much lower computational cost than CCSD(T), which makes them acceptable candidates for photodissociation dynamics simulations. For N_2O monomer, we also simulate the photodissociation dynamics using RASSCF(4,6) in MOLCAS [166], 4 electrons in 6 orbitals, and aug-cc-pVDZ basis set. In RASSCF simulations, bond breaking processes such as photodissociation are better described and static correlation energy is also taken into account. Hence, the RASSCF simulation results can be used to validate our DFT results and find the similarities and differences between the two series of results.

In the electronic structure calculations, three excited states are included, of which the second and the third are degenerate. It was previously shown by Shincke *et al.* [73] and Daud *et al.* [211] that the three lowest excited states contribute to the first broad band of N_2O centered at about 182 nm, which is responsible for the photodissociation of N_2O in the stratosphere. The dynamics simulations are started on the third excited state with time step of 0.5 fs. We let the dynamics simulations continue to 500 fs and kill any trajectories with more than 5.0 eV jump in the potential energies. For the on-the-fly electronic structure calculations, we use CAM-B3LYP/aug-cc-pVDZ and M06/aug-cc-pVDZ functionals and basis sets. In the RASSCF simulation, the dynamics runs for 1000 steps with a 10 a.u. (0.24 fs) interval.

As we are investigating bond breaking processes with single reference DFT methods, we need to carefully define what distance constitutes a "broken" bond. If our definition is too long, convergence errors are likely before dissociation occurs whereas if our definition is too short, we may overesti-

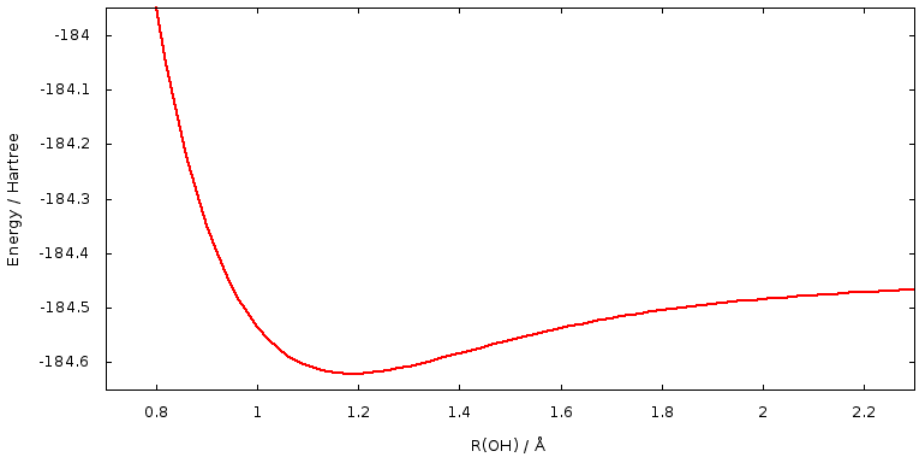

Figure 6.2: The changes in the potential energy of N_2O monomer with increasing N-O bond distance at CAM-B3LYP/aug-cc-pVDZ level of theory.

mate the number of trajectories where dissociation occurs. We define 2.0 Å as the distance where the N-O bond is considered broken as it is unlikely that the bond will reform if there is sufficient kinetics energy. In Figure 6.2, we show the changes in the potential energy of N_2O with increasing N-O distance. This Figure shows that N-O bond at distances around 2.0 Å is almost dissociated and it is not likely that it is back to reform the bond.

Multireference methods give a better description of photodissociation process than single reference methods and as a result, the dynamics calculations of almost all of the trajectories finish normally without any convergence error no matter what the bond distances are during the dissociation process. While in the case of DFT calculations, the situation is different. To check if the convergence errors in DFT simulations affect our DFT simulation results, we investigate if these convergence errors happen after the photodissociation is almost completed. We plot the number of trajectories against the N-O bond distance at the time when convergence error occurs for both CAM-B3LYP and M06 simulations in Figure 6.3. As this graph

clearly shows, the majority of trajectories have a convergence error after the photodissociation is completed, i.e. $R_{N-O} > 2.0$ $\mathring{A}$. We also double check this by comparing the percentage of trajectories at each N-O distance from 1.1 $\mathring{A}$, less than the N-O equilibrium distance, to 5.2 $\mathring{A}$, more than twice our defined N-O dissociation distance for the three CAM-B3LYP, M06 and RASSCF methods in Table 6.1. From these calculated percentages of trajectories at different N-O distances, 98.1% and 97.5% of trajectories of M06 and CAM-B3LYP simulations respectively, still exist in the dynamics calculation at 2.2 $\mathring{A}$, compared with 87.2% for the RASSCF simulation. The reduced percentage from 100% at this distance is due to the products of the other photodissociation channel of N_2O, and the non-dissociated trajectories as well and not necessarily due to the error convergence. In the case of RASSCF this reduced percentage is entirely from the NO+N production and the non-dissociated trajectories. These results confirm that while RASSCF can handle N-O bond distances to more than 5.0 $\mathring{A}$ without ending in error convergence, the two M06 and CAM-B3LYP DFT methods are able to treat reasonably well at R_{N-O} dissociation distances around 2.0 $\mathring{A}$.

After imposing the energy window, for CAM-B3LYP/aug-cc-pVDZ simulation 178 points and for M06/aug-cc-pVDZ 113 points are sampled from the Wigner distribution of 10000 geometries in the ensemble. While, in RASSCF simulation we have to sample the trajectories only by taking snapshots of a long ground state dynamics as it is the only sampling way implemented in MOLCAS package. This results in 39 trajectories for the RASSCF simulations. We determine the time when each trajectory undergoes dissociation, i.e. $R_{N-O} \geqslant 2.0$ $\mathring{A}$, and plot the normalized number of trajectories that have dissociated as a function of time. These graphs are presented and compared in Figure 6.4. The three methods show similar trends, with

the majority of the trajectories photodissociating to give N_2 + O and this occurs mostly in the first 150 fs of the photodissociation, which agrees with Schinke's findings on photodissociation dynamics of N_2O [73]. The two DFT simulation results are consistent with each other, while the RASSCF results show photodissociation occurring at a slightly later time. This can be due to the different nature of the on-the-fly electronic structure calculations, where RASSCF provides more space for the bonds which can result in slower dissociation after a longer period of stretching and bending. The other reason can be the different sampling approaches used in DFT and RASSCF simulations. In RASSCF simulation, the trajectories are taken from long ground state dynamics and when the energy is well distributed in the system. This way of sampling can result in late start in photodissociation.

The plotted N-O bond distance over time for all the trajectories and for the two DFT applied methods in the simulations also confirms that N_2O is mostly dissociated through the main N_2 + O channel and that the photodissociation is almost finished at 300 fs. These plots are presented in appendices A.33 and A.34. The percentage of trajectories that photodissociate through the main channel is 91.2% with the CAM-B3LYP method and 91.0% with the M06 method. This compares reasonably to the RASSCF results, where 82.1% of trajectories are found to photodissociate through the main channel.

We also calculate the percentage of trajectories that undergo dissociation through the second channel, i.e. NO+N production, as 2.2% and 2.6% for CAM-B3LYP and M06 simulations respectively. Our RASSCF dynamics simulations results in 10.25% of trajectories photodissociating through the second channel. While the percentage of minor channel from the three calculations are not exactly the same, our calculated results consistently identify the primary channel which agrees with the previous results in liter-

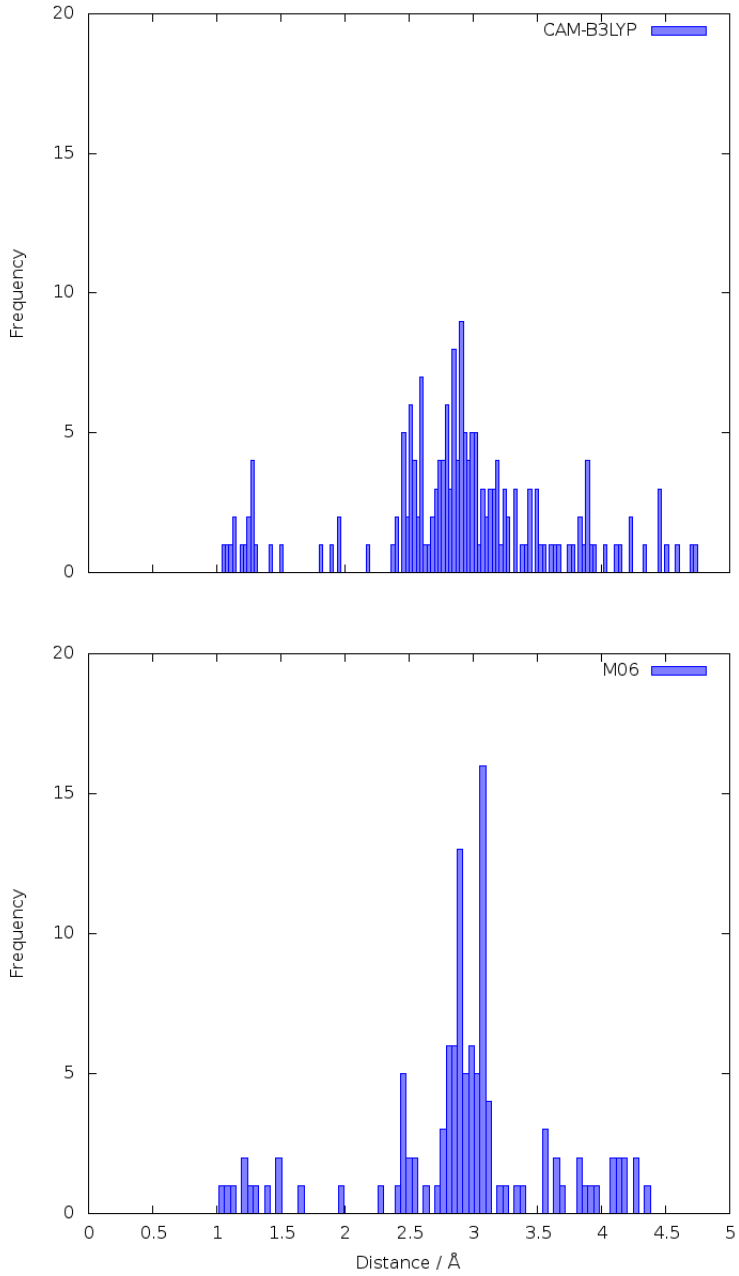

Figure 6.3: Number of trajectories that end in a convergence error at a given CAM-B3LYP (top) and M06 (bottom) N-O bond length for N_2O.

Table 6.1: The percentage of trajectories at different N-O bond distances for the three CAM-B3LYP, M06 and RASSCF methods.

	Trajectories%		
R_{N-O} /Å	M06	CAM-B3LYP	RASSCF
1.1	100.0	100.0	100.0
1.2	100.0	100.0	94.7
1.3	100.0	100.0	89.7
1.4	100.0	100.0	89.7
1.5	100.0	100.0	89.7
1.6	100.0	100.0	89.7
1.7	99.0	100.0	87.2
1.8	99.0	100.0	87.2
1.9	99.0	99.4	87.2
2.0	98.1	97.5	87.2
2.1	98.1	97.5	87.2
2.2	98.1	96.9	87.2
2.3	97.1	96.9	87.2
2.4	97.1	95.7	87.2
2.5	89.3	90.7	87.2
2.6	87.4	79.6	87.2
2.7	86.4	76.5	87.2
2.8	81.6	66.7	87.2
2.9	61.3	56.2	87.2
3.0	48.5	43.8	87.2
3.1	25.2	36.4	87.2
3.2	23.3	30.2	87.2
3.3	21.4	25.9	87.2
3.4	19.4	23.5	87.2
3.5	19.4	19.8	87.2
3.6	16.5	17.9	87.2
3.7	13.6	16.0	87.2
3.8	13.6	14.8	87.2
3.9	10.7	10.5	87.2
4.0	8.7	9.3	87.2
4.1	6.8	8.6	87.2
4.2	3.9	7.4	87.2
4.3	1.0	6.2	87.2
4.4	0.0	5.6	87.2
4.5	0.0	3.7	87.2
4.6	0.0	2.5	87.2
4.7	0.0	2.5	87.2
4.8	0.0	1.2	87.2
4.9	0.0	1.2	87.2
5.0	0.0	1.2	87.2
5.1	0.0	0.6	87.2
5.2	0.0	0.0	87.2

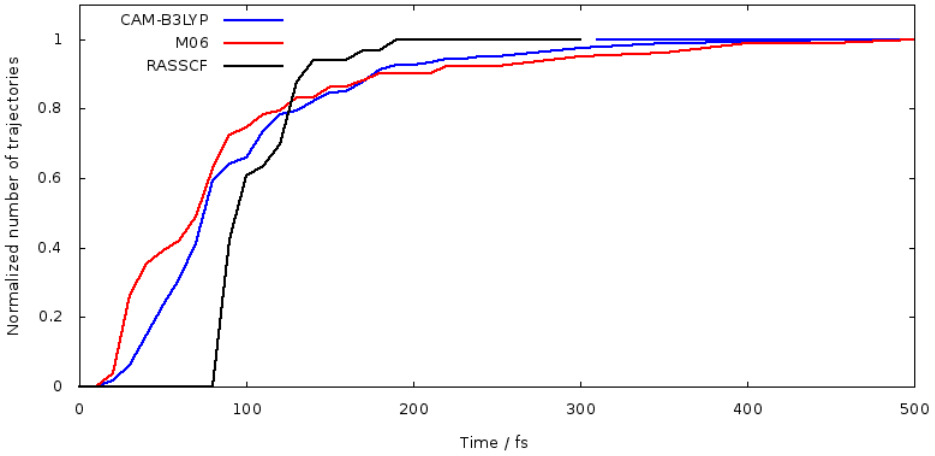

Figure 6.4: The normalized number of trajectories with dissociated N-O bond against time.

ature where the exclusive products of N_2O photodissociation is mentioned N_2+O [63, 205, 247].

We also find that a small fraction of the trajectories do not dissociate within the time limit due to different reasons such as being trapped in a potential barrier, previously mentioned by Schinke *et al.* [73], or ending in convergence error without giving the final products. The percentages for these trajectories are calculated 6.7%, 6.2% and 7.7% for CAM-B3LYP, M06 and RASSCF methods respectively. While, understanding more accurate results can be achieved with higher level electronic structure methods e.g. CASPT2, the agreement between our results and previous experimental and theoretical results is good enough to apply it on H_2O-N_2O and see the possible changes in photodissociation of N_2O upon complexation.

6.3 H_2O-N_2O photodissociation dynamics

We computationally investigate the photodissociation dynamics of the H_2O-N_2O complex using the same electronic structure methods and simulation

parameters as N_2O.

We optimize the geometry of the complex at both CAM-B3LYP/aug-cc-pVDZ and M06/aug-cc-pVDZ levels of theory and calculate their harmonic frequencies using the same method and basis sets. As previously discussed in section 6.2, three excited states contribute to the photodissociation of N_2O and therefore, four states are involved in the calculations and the N_2O dynamics starts on the fourth state. We compare the first lower states of monomer and the complex and find that the involved states in the phodissociation dynamics simulations of the complex are the same as those of monomer. Consequently, for the H_2O-N_2O complex, the same four states are involved in the simulations.

We apply the same energy restrictions to the H_2O-N_2O ensemble as was used for N_2O. This results in 155 starting points to run trajectories from for the CAM-B3LYP/aug-cc-pVDZ method and 259 starting points for the M06/aug-cc-pVDZ method. The changes in N-O bond distance against time for the H_2O-N_2O complex and from the two CAM-B3LYP and M06 simulations are plotted and presented in appendices in Figures A.37 and A.38 respectively. Comparing the changes in N-O bond distance over time for the complex and the monomer shows that the N_2+ O remains the main photodissociation channel in the photodissociation of the complex.

To make a direct comparison with photodissociation dynamics simulations of monomeric N_2O, we once again apply the dissociation criteria, i.e. $R_{N-O} > 2.0$ $\mathring{A}$, as our dissociation reference and plot the normalized accumulated number of trajectories against time for both monomeric N_2O and H_2O-N_2O complex for the two CAM-B3LYP and M06 simulations. These comparing graphs are presented in Figures 6.5 and 6.6 showing a small change in the photodissociation dynamics of N_2O upon complexation.

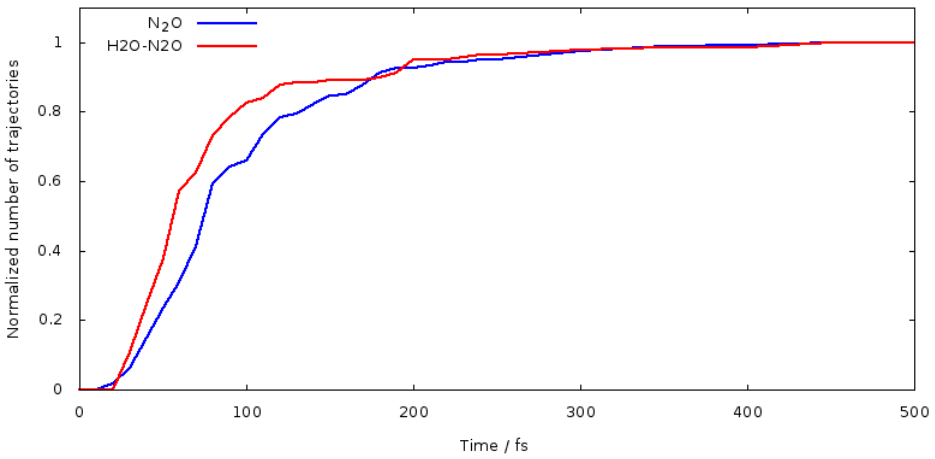

Figure 6.5: The normalized number of trajectories with dissociated N-N bond against time in CAM-B3LYP/aug-cc-pVDZ photodissociation dynamics of N_2O monomer and H_2O-N_2O complex.

While the two simulations show slightly different graphs, they are consistent in the overall change. Therefore, apart from the production of OH radicals in photodissociation of H_2O-N_2O, we find that N-O bond breaking in the H_2O-N_2O complex occurs faster than in monomeric N_2O.

We find that in 7.1% and 5.8% of trajectories in CAM-B3LYP and M06 simulations, the N_2O molecule does not dissociate within the time limit, which is consistent with the dynamics results of the monomeric N_2O. Out of the selected trajectories, 2.6% from CAM-B3LYP and 0.8% from M06 simulation undergo the second photodissociation channel and produce NO+ N.

We are also interested in changes in the O-H bonds in the water molecule and plot the changes for the CAM-B3LYP/aug-cc-pVDZ in Figures A.39 and A.41, and for the M06/aug-cc-pVDZ method in Figures A.40 and A.42. Comparing these changes in the two O-H bonds of the water molecule over time from the two simulations reveals that the two O-H bonds experiences almost the same disturbance. However, the results from the two methods

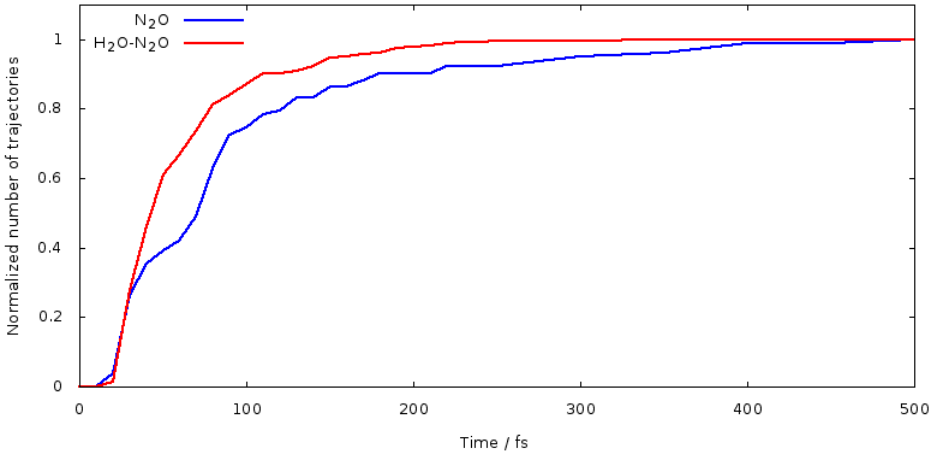

Figure 6.6: The normalized number of trajectories with dissociated N-N bond against time in M06/aug-cc-pVDZ photodissociation dynamics of N_2O monomer and H_2O-N_2O complex.

are slightly different, where the M06/aug-cc-pVDZ results show more dissociation in O-H bonds and the CAM-B3LYP/aug-cc-pVDZ results exhibit more stretching in the bonds rather than dissociation.

We find 1.9% of trajectories in CAM-B3LYP simulation produce two OH radicals. This percentage is 3.9% for the M06 simulation. Our results in terms of producing OH radicals from photodissociation of H_2O-N_2O van der Waals complex, collaborates with the experimental results of Tanaka *et al.* [203]. However, the results from the two DFT methods are quite different. The OH radical is one of the most important oxidants in the atmosphere and even in low concentration can play important atmospheric roles. Due to its high reactivity, this radical has a short lifetime of approximately 1 second.

We plot the potential energy of OH radical with changing O-H distance in Figure 6.7. In trajectories where OH is produced, the trajectories typically stop with a convergence error when the OH distance is 0.8-1.2 Å. This OH distance range falls in the bonding range of the potential energy graph of

O-H bond shown in Figure 6.7.

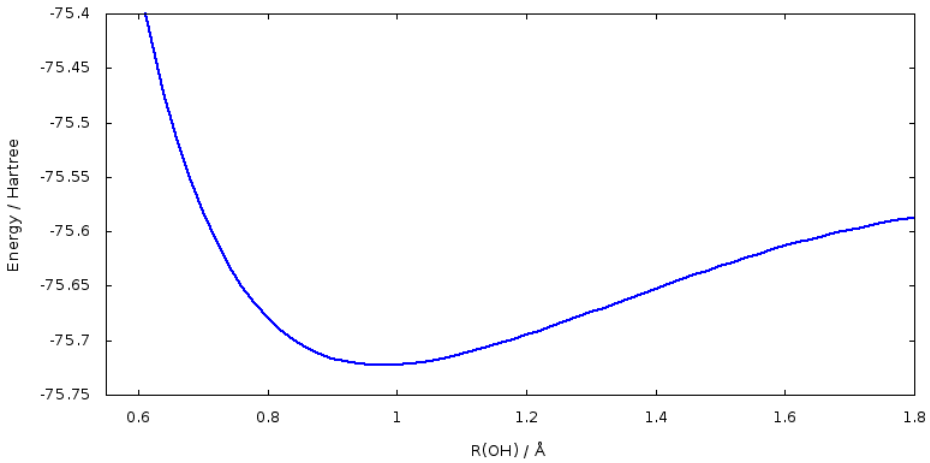

Figure 6.7: The changes in the potential energy of OH radical with decreasing O-H bond distance at CAM-B3LYP/aug-cc-pVDZ level of theory.

In our dynamics simulations, we find that OH radicals are most likely to be produced through two main mechanisms. Representative structures from the trajectories that illustrate these, are shown in Figure 6.8. In the first mechanism, O of N_2O and H of H_2O bridge between the two molecules, when the O of N_2O is not fully dissociated and the two molecules are close. In the second mechanism and where the dissociated O from N_2O is in a further distance to the rotating N_2, an O1H1O2H2 structure briefly forms, and soon after two OH radicals are generated. We find that, in about 70% of the productive trajectories, the H1-O1-H2-O2 is formed through genuine complex production, structure (a) in Figure 6.8, rather than through monomer dissociation, structure (b). The two mechanisms collaborate with Tanaka's proposed dissociation mechanism of H_2O-N_2O [203] through an O1H1O2H2 intermediate.

In the mix of trajectories there some random results from which some are worth mentioning. One trajectory from the CAM-B3LYP/aug-cc-pVDZ

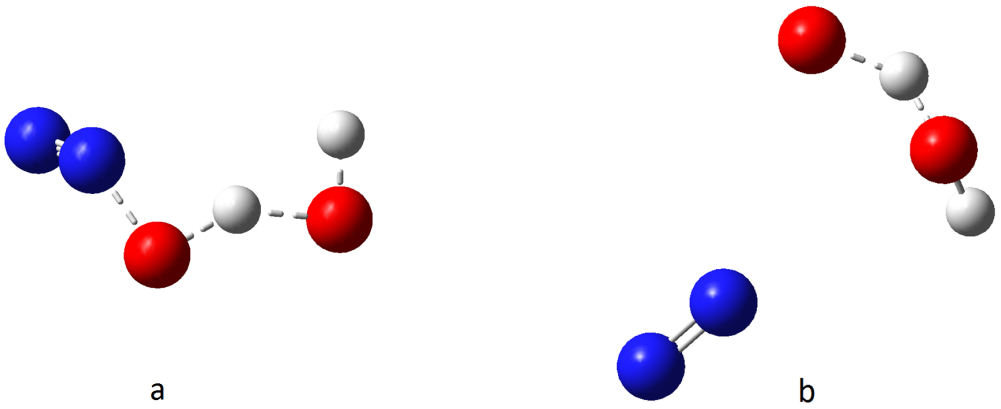

Figure 6.8: Snapshots before OH radical formation of H_2O-N_2O complex.

and two trajectories in M06/aug-cc-pVDZ simulations, produce OH radical shortly and the complex go through further dissociation and bond formation and the OH radicals do not exist after a short time. We also find that one trajectory in M06/aug-cc-pVDZ method, undergoes photodissociation through a unique channel. After the OH radicals are produced, the O1-H1 (O from N_2O and H of H_2O at closer distance to O of N_2O) radical takes the second H from O2-H2 (left from water) through forming H1-O1-H2-O2 and produces H_2O, where the O in water is actually exchanged with that of N_2O. This channel, however with low probability, could be experimentally validated using isotope exchange technique.

6.4 Conclusion

We simulated the photodissociation dynamics of monomeric N_2O and the H_2O-N_2O complex using on-the-fly *ab initio* molecular dynamics using the TSH approach. We studied photodissociation of N_2O using the two CAM-B3LYP/aug-cc-pVDZ, M06/aug-cc-pVDZ methods. We then simulated the photodissociation dynamics of N_2O with RASSCF method and used the results to validate our DFT simulations. Our results from the three methods consistently identified the primary photodissociation channel, i.e. N_2+O production, which agrees with the experimental results.

Then we applied the two CAM-B3LYP/aug-cc-pVDZ and M06/aug-cc-pVDZ methods with the same simulation parameters on the H_2O-N_2O complex, to investigate its photodissociation dynamics and identify any change compared to that of monomeric N_2O.

Our results show that, the N-O bond breaking, as the main photodissociation channel of N_2O, occurs slightly faster in H_2O-N_2O complex compared to the N-O bond breaking in photodissociation of monomeric N_2O. We also find that photodissociation of H_2O-N_2O complex leads to a new product, the atmospherically important OH radical. This OH radical production agrees with the only experimental reslut on H_2O-N_2O where the photodissociation dynamics of this complex were investigated with 193 nm light. Our simulated photodissociation dynamics of H_2O-N_2O also reveals that OH radical production occurs via formation of H1-O1-H2-O2 mostly through complex production.

Chapter 7

Conclusion

In this work, the absorption spectra and photodissociation dynamics of some atmospherically important molecules and complexes have been simulated. For these species, there are no available experimental results due to either technical challenges or being very recently identified. We have used a nuclear ensemble approach to simulate the electronic absorption spectra, as most of the species considered photodissociate via a direct mechanism. The photodissociation dynamics simulations were undertaken with on-the-fly *ab initio* molecular dynamics, using a transition surface hopping approach.

In chapter 3, we simulated the absorption spectra of some sulfur-containing molecules, namely SO_2, H_2S, CS_2, OCS and SO_3, and validated our results against their available experimental spectra. We developed and introduced a new approximation approach in simulating absorption cross section where the accuracy of the calculated spectrum from EOM-CCSD/aug-cc-pV(D+d)Z+3 was improved to very close to that of the spectrum simulated from EOM-CCSD/aug-cc-pV(T+d)Z+3 with just a small number of calculations with the larger aug-cc-pV(T+d)Z+3 basis set. This significantly reduces the computational cost of obtaining a spectrum of EOM-CCSD/aug-

cc-pV(T+d)Z+3 accuracy. We found that this approach gave electronic absorption spectra in very good agreement with the experiment.

In chapter 4, we applied the theoretical approach developed in chapter 3 to simulate electronic absorption spectra of H_2SO_4 and OSSO ; two atmospherically relevant sulfur-containing molecules where there are no experimental spectra. We improved the previous empirically convoluted absorption spectra of these molecules by directly simulating the spectra using the nuclear ensemble approach. Also in the case of H_2SO_4, we considered both the C_2 and C_s conformers, which are both of appreciable abundance under atmospherically relevant conditions.

In chapter 5, we investigated if formation of weakly bond complexes affected the electronic absorption spectrum of N_2O. The absorption spectra of four atmospheric complexes of N_2O, namely Ar-N_2, N_2-N_2O, O_2-N_2O and H_2O-N_2O, were simulated. We first benchmarked the absorption cross section of N_2O monomer to set a reference for comparison with the complexes and also to come up with the most efficient electronic structure parameters, in terms of cost and accuracy. An increase in the intensities of the cross section of O_2-N_2O and H_2O-N_2O were detected; however, it was not supported by the experimental investigations of our collaborators.

In chapter 6, we investigated the photodissociation dynamics of H_2O-N_2O using *ab initio* molecular dynamics simulations to show if complex formation could make other exit channels available under atmospheric conditions. We showed that the photodissocition of N_2O through N_2+O channel happens earlier when it is aggregated with a water molecule. Also, our results showed that, a new photodissociation channel opens for the H_2O-N_2O complex, which produces the atmospherically important OH radical.

Based on the results of this thesis, we propose the following ideas for

future works.

From our H_2SO_4 calculated J-values, the dominant photodissociation mechanism is predicted to be different from the previous results in literature. The J-values results are very sensitive to cross section overlap with solar flux, and an accurate absorption cross section, especially in the lower energy region tail of the spectrum, is needed to clarify this ambiguity in the significance and order of the H_2SO_4 photodissociation mechanisms. The current available experimental results are only three upper limits and for a clear understanding of the photodissociation mechanism of H_2SO_4, an accurate experimental absorption cross section must be used to validate our results. The experimental absorption cross section of OSSO is also unknown; however, the experiments are underway to measure the absorption spectrum of OSSO by our collaborators from University of Copenhagen using the matrix isolation spectroscopy facilities in University of Helsinki. Our simulated electronic absorption spectrum will be used for identifying and assigning the measured cross section.

The current absorption spectra simulation packages are not able to accurately simulate the cross section of the complexes, where more than one molecule are involved. We have found that this is due to the sampling the geometries and also not accurately partitioning the energies in the complexes, which leads to unphysical change in the simulated cross section. The high importance of complexes in the chemistry of planetary atmospheres, implicates that a more accurate treatment is needed for generating the absorption spectra of complexes. Also, we have used single reference DFT methods to simulate the photodissociation dynamics of the H_2O-N_2O complex, which is not the most accurate way of treating the photodissociation process, where bonds are broken and formed. Hence, to validate our pre-

liminary DFT results for the H_2O-N_2O complex, and to simulate its photodissociation dynamics more accurately, further work with multireference methods is needed.

Bibliography

[1] R. P. Wayne, *Chemistry of atmospheres: an introduction to the chemistry of the atmospheres of Earth, the planets, and their satellites*, volume 3rd (Oxford University Press, Oxford, 2000).

[2] J. H. Seinfeld, *Atmospheric chemistry and physics: from air pollution to climate change* (Hoboken, New Jersey: John Wiley & Sons, Inc., 2016), 3rd edition.

[3] J. H. Butler and S. A. Montzka, "NOAA's annual greenhouse gas index", Technical report.

[4] W. DeMore, S. Sander, D. Golden, R. Hampson, M. Kurylo, C. Howard, A. Ravishankara, C. Kolb, and M. Molina, "Chemical kinetics and photochemical data for use in stratospheric modeling, JPL Pub", Evaluation (1994).

[5] G. P. Anderson, J. H. Chetwynd, S. A. Clough, E. P. Sheitle, and F. Kneizys, "AFGL Atmospheric Constituent Profiles (0-120km)", (1986).

[6] I. Lagzi, R. Mészáros, G. Gelybo, and A. Leelössy, *Atmospheric chemistry* (Eötvös Loránd University, 2013).

[7] P. Warneck, editor, *Chapter 10 Sulfur Compounds in the Atmosphere* (Academic Press, 1988), volume 41, 484–542.

[8] B. J. Finlayson-Pitts and J. N. Pitts, *Chemistry of the Upper and Lower Atmosphere: Theory, Experiments, and Applications* (Academic, 1999).

[9] J. B. Burkholder, M. Mills, and S. McKeen, "Upper limit for the UV absorption cross sections of H_2SO_4", Geophysical Research Letters **27**, 2493–2496 (2000).

[10] V. Vaida, H. G. Kjaergaard, P. E. Hintze, and D. J. Donaldson, "Photolysis of Sulfuric Acid Vapor by Visible Solar Radiation", Science **299**, 1566–1568 (2003).

[11] M. J. Mills, O. B. Toon, V. Vaida, P. E. Hintze, H. G. Kjaergaard, D. P. Schofield, and T. W. Robinson, "Photolysis of sulfuric acid vapor by visible light as a source of the polar stratospheric CN layer", Journal of Geophysical Research: Atmospheres **110** (2005).

[12] D. J. Hofmann and J. M. Rosen, "Condensation nuclei events at 30 km and possible influences of solar cosmic rays", Nature **302**, 511 (1983).

[13] D. J. Hofmann, J. M. Rosen, J. A. Harder, and S. R. Rolf, "Ozone and aerosol-measurements in the springtime Antarctic stratosphere in 1985", Geophysical Research Letters **13**, 1252–1255 (1986).

[14] F. F. Crim, "Selective Excitation Studies of Unimolecular Reaction Dynamics", Annual Review of Physical Chemistry **35**, 657–691 (1984).

[15] F. F. Crim, "Bond-Selected Chemistry: Vibrational State Control of Photodissociation and Bimolecular Reaction", The Journal of Physical Chemistry **100**, 12725–12734 (1996).

[16] R. Feng, G. Cooper, G. R. Burton, C. E. Brion, and L. Avaldi, "Absolute photoabsorption oscillator strengths by electron energy loss methods: the valence and s2p and 2s inner shells of sulphur dioxide in the discrete and continuum regions (3.5 - 260 eV)", Chemical Physics **240**, 371–386 (1999).

[17] P. E. Hintze, H. G. Kjaergaard, V. Vaida, and J. B. Burkholder, "Vibrational and Electronic Spectroscopy of Sulfuric Acid Vapor", The Journal of Physical Chemistry A **107**, 1112–1118 (2003).

[18] B. J. B. and M. Stuart, "UV absorption cross sections for SO_3", Geophysical Research Letters **24**, 3201–3204 (1997).

[19] R. Feng, G. Cooper, and C. E. Brion, "Absolute oscillator strengths for hydrogen sulphide: I. Photoabsorption in the valence-shell and the S 2p and 2s inner-shell regions (4–260 eV)", Chemical Physics **244**, 127–142 (1999).

[20] H. Grosch, A. Fateev, and S. Clausen, "UV absorption cross-sections of selected sulfur-containing compounds at temperatures up to 500 $°C$", Journal of Quantitative Spectroscopy and Radiative Transfer **154**, 28–34 (2015).

[21] R. Feng, G. Cooper, and C. E. Brion, "Quantitative studies of the photoabsorption of carbonyl sulphide in the valence-shell, S 2p,2s and C 1s inner-shell regions (4–360 eV) by dipole electron impact spectroscopies", Chemical Physics **252**, 359–378 (2000).

[22] K. Sunanda, A. Shastri, A. K. Das, and B. N. Raja Sekhar, "Electronic states of carbon disulphide in the 5.5–11.8eV region by VUV photo

absorption spectroscopy", Journal of Quantitative Spectroscopy and Radiative Transfer **151**, 76–87 (2015).

[23] S. J. Wrenn, L. J. Butler, G. A. Rowland, C. J. H. Knox, and L. F. Phillips, "The necessity for multiphoton processes in the 193-nm photochemistry of sulphuric acid aerosols", Journal of Photochemistry and Photobiology A: Chemistry **129**, 101–104 (1999).

[24] T. W. Robinson, D. P. Schofield, and H. G. Kjaergaard, "High level ab initio studies of the excited states of sulfuric acid and sulfur trioxide", The Journal of Chemical Physics **118**, 7226–7232 (2003).

[25] J. R. Lane and H. G. Kjaergaard, "Calculated Electronic Transitions in Sulfuric Acid and Implications for Its Photodissociation in the Atmosphere", The Journal of Physical Chemistry A **112**, 4958–4964 (2008).

[26] R. L. Kuczkowski, R. D. Suenram, and F. J. Lovas, "Microwave spectrum, structure, and dipole moment of sulfuric acid", Journal of the American Chemical Society **103**, 2561–2566 (1981).

[27] V. Krasnopolsky, *A photochemical model for the Venus atmosphere at 47–112 km*, volume 218 (2012).

[28] X. Zhang, M. C. Liang, F. P. Mills, D. A. Belyaev, and Y. L. Yung, "Sulfur chemistry in the middle atmosphere of Venus", Icarus **217**, 714–739 (2012).

[29] L. W. Esposito, M. Copley, R. Eckert, L. Gates, A. I. F. Stewart, and H. Worden, "Sulfur dioxide at the Venus cloud tops, 1978–1986", Journal of Geophysical Research: Atmospheres **93**, 5267–5276 (1988).

[30] T. Encrenaz, T. K. Greathouse, M. J. Richter, J. Lacy, T. Widemann, B. Bézard, T. Fouchet, C. deWitt, and S. K. Atreya, "HDO and SO_2 thermal mapping on Venus", A&A **559**, A65 (2013).

[31] E. Marcq, D. Belyaev, F. Montmessin, A. Fedorova, J.-L. Bertaux, A. C. Vandaele, and E. Neefs, *An investigation of the SO_2 content of the venusian mesosphere using SPICAV-UV in nadir mode*, volume 211 (2011).

[32] Y. L. Yung and W. B. Demore, "Photochemistry of the stratosphere of Venus: Implications for atmospheric evolution", Icarus **51**, 199–247 (1982).

[33] K. L. Jessup, E. Marcq, F. Mills, A. Mahieux, S. Limaye, C. Wilson, M. Allen, J.-L. Bertaux, W. Markiewicz, T. Roman, A.-C. Vandaele, V. Wilquet, and Y. Yung, "Coordinated Hubble Space Telescope and Venus Express Observations of Venus' upper cloud deck", Icarus **258**, 309–336 (2015).

[34] E. S. Barker, "Detection of SO_2 in the UV spectrum of Venus", Geophysical Research Letters **6**, 117–120 (1979).

[35] J. B. Pollack, O. B. Toon, R. C. Whitten, R. Boese, B. Ragent, M. Tomasko, L. Esposito, L. Travis, and D. Wiedman, "Distribution and source of the UV absorption in Venus' atmosphere", Journal of Geophysical Research: Space Physics **85**, 8141–8150 (1980).

[36] V. A. Krasnopolsky, "Chemical composition of Venus atmosphere and clouds: Some unsolved problems", Planetary and Space Science **54**, 1352 – 1359 (2006).

[37] K. Molaverdikhani, K. McGouldrick, and L. W. Esposito, "The abundance and vertical distribution of the unknown ultraviolet absorber in the venusian atmosphere from analysis of Venus Monitoring Camera images", Icarus **217**, 648 – 660 (2012).

[38] E. S. Barker, J. H. Woodman, M. A. Perry, B. A. Hapke, and R. Nelson, "Relative Spectrophotometry of Venus from 3067 to 5960 Å", Journal of the Atmospheric Sciences **32**, 1205–1211 (1975).

[39] L. D. Travis, "On the Origin of Ultraviolet Contrasts on Venus", Journal of the Atmospheric Sciences **32**, 1190–1200 (1975).

[40] L. Zasova, V. Krasnopolsky, and V. Moroz, "Vertical distribution of SO2 in upper cloud layer of Venus and Origin of U.V.-absorption", Advances in Space Research **1**, 13 – 16 (1981).

[41] W. Markiewicz, E. Petrova, O. Shalygina, M. Almeida, D. Titov, S. Limaye, N. Ignatiev, T. Roatsch, and K. Matz, "Glory on Venus cloud tops and the unknown UV absorber", Icarus **234**, 200 – 203 (2014).

[42] O. B. Toon, R. P. Turco, and J. B. Pollack, "The ultraviolet absorber on Venus: Amorphous sulfur", Icarus **51**, 358 – 373 (1982).

[43] K. K. Hartley, A. R. Wolff, and L. D. Travis, "Croconic acid: An absorber in the Venus clouds?", Icarus **77**, 382 – 390 (1989).

[44] C. Na, L. Esposito, W. McClintock, and C. Barth, "Sulfur Dioxide in the Atmosphere of Venus: II. Modeling Results", Icarus **112**, 389 – 395 (1994).

[45] E. Marcq, J.-L. Bertaux, F. Montmessin, and D. Belyaev, "Variations of sulphur dioxide at the cloud top of Venus's dynamic atmosphere", Nature geoscience **6**, 25 (2013).

[46] D. V. Titov, H. Svedhem, D. McCoy, J. P. Lebreton, S. Barabash, J. L. Bertaux, P. Drossart, V. Formisano, B. Haeusler, O. I. Korablev, W. Markiewicz, D. Neveance, M. Petzold, G. Piccion, T. L. S. Zhang, F. W. Taylor, E. Lellouch, D. Koschny, O. Witasse, M. Warhaut, A. Acomazzo, J. Rodrigues-Cannabal, J. Fabrega, T. Schirmann, A. Clochet, and M. Coradini, "Venus Express: Scientific goals, instrumentation, and scenario of the mission", Cosmic Research **44** (2006).

[47] L. W. Esposito and L. D. Travis, "Polarization studies of the Venus uv contrasts: Cloud height and haze variability", Icarus **51**, 374 – 390 (1982).

[48] C. J. Marsden and B. J. Smith, "An ab initio study of many isomers of S_2O_2. A combined theoretical and experimental analysis of the harmonic force field and molecular structure of cis-planar OSSO", Chemical Physics **141**, 335 – 353 (1990).

[49] C. W.-K. L. Jun-Qian, Z. Y.-F. D. Kai-Ning, and L. Yi, "DFT Study of the Stabilities of Disulfur Dioxide Isomers", Chinese Journal of Structural Chemistry **4**, 024 (2004).

[50] M. Goodarzi, M. Vahedpour, and F. Nazari, "Theoretical study on the atmospheric formation of cis and trans-OSSO complexes", Chemical Physics Letters **494**, 315 – 322 (2010).

[51] Y. Murakami, S. Onishi, T. Kobayashi, N. Fujii, N. Isshiki, K. Tsuchiya, A. Tezaki, and H. Matsui, "High Temperature Reaction of S + SO_2 → SO + SO: Implication of S_2O_2 Intermediate Complex Formation", The Journal of Physical Chemistry A **107**, 10996–11000 (2003).

[52] A. Ramírez-Solís, F. Jolibois, and L. Maron, "Born–Oppenheimer DFT molecular dynamics studies of S_2O_2: Non-harmonic effects on the lowest energy isomers", Chemical Physics Letters **510**, 21 – 26 (2011).

[53] V. A. Krasnopolsky, "A photochemical model for the Venus atmosphere at 47–112km", Icarus **218**, 230 – 246 (2012).

[54] B. N. Frandsen, P. O. Wennberg, and H. G. Kjaergaard, "Identification of OSSO as a near-UV absorber in the Venusian atmosphere.", Geophysical Research Letters **11**, 146–155 (2016).

[55] A. Syakila and C. Kroeze, "The global nitrous oxide budget revisited", Greenhouse Gas Meas. Manage. **1**, 17–26 (2011).

[56] J. Huang, A. Golombek, R. Prinn, R. Weiss, P. Fraser, P. Simmonds, E. J. Dlugokencky, B. Hall, J. Elkins, P. Steele, R. Langenfelds, P. Krummel, G. Dutton, and L. Porter, "Estimation of regional emissions of nitrous oxide from 1997 to 2005 using multinetwork measurements, a chemical transport model, and an inverse method", Journal of Geophysical Research: Atmospheres **113**, D17313 (2008).

[57] "Drawing down N_2O to protect climate and the ozone layer", Report, United Nations Environment Programme (UNEP) (2013).

[58] A.-G. E. Ausseil, M. U. Kirschbaum, R. M. Andrew, S. McNeill, J. R. Dymond, F. Carswell, and N. W. Mason, "Climate regulation in New Zealand: contribution of natural and managed ecosystems", Plant and Soil **309**, 25–42 (2008).

[59] "Greenhouse Gas Inventory Report", Report, Ministry for the Environment (2018).

[60] "Climate change synthesis report", Report, IPCC, Geneva, Switzerland (2014).

[61] D. J. Hofmann, J. H. Butler, E. J. Dlugokencky, J. W. Elkins, K. Masarie, S. A. Montzka, and P. Tans, "The role of carbon dioxide in climate forcing from 1979 to 2004: introduction of the Annual Greenhouse Gas Index", Tellus, Ser. B **58B**, 614–619 (2006).

[62] "Climate Change 2014: Mitigation of Climate Change", Report, IPCC, Geneva, Switzerland (2014).

[63] A. R. Ravishankara, J. S. Daniel, and R. W. Portmann, "Nitrous oxide (N_2O): The dominant ozone-depleting substance emitted in the 21st century", Science **326**, 123–125 (2009).

[64] P. J. Crutzen, "Influence of nitrogen oxides on atmospheric ozone content", Quarterly Journal of the Royal Meteorological Society **96**, 320–325 (1970).

[65] D. J. Wuebbles, "Nitrous oxide: no laughing matter", Science **326**, 56–57 (2009).

[66] A. Deepak, T. D. Wilkerson, and L. H. Ruhnke, *Atmospheric Water Vapor* (Academic Press, 1980).

[67] V. Vaida and J. E. Headrick, "Physicochemical Properties of Hydrated Complexes in the Earth's Atmosphere", The Journal of Physical Chemistry A **104**, 5401–5412 (2000).

[68] V. Vaida, J. S. Daniel, H. G. Kjaergaard, L. M. Goss, and A. F. Tuck, "Atmospheric absorption of near infrared and visible solar radiation by the hydrogen bonded water dimer", Quarterly Journal of the Royal Meteorological Society **127**, 1627–1643 (2001).

[69] L. Brown and V. Vaida, "Photoreactivity of oxygen dimers in the ultraviolet", Journal of Physical Chemistry **100**, 7849–7853 (1996).

[70] G. Frost and V. Vaida, "Atmospheric implications of the photolysis of the ozone-water weakly bound complex", Journal of Geophysical Research-Atmospheres **100**, 18803–18809 (1995).

[71] S. R. Salmon, "An estimation of the concentration of atmospheric nitrous oxide containing complexes,", (2015).

[72] J. A. Schmidt, M. S. Johnson, and R. Schinke, "Isotope effects in N_2O photolysis from first principles", Atmos. Chem. Phys. **11**, 8965–8975 (2011).

[73] R. Schinke, "Photodissociation of N_2O: Potential energy surfaces and absorption spectrum", J. Chem. Phys. **134**, 064313–064325 (2011).

[74] H. Kawamata, H. Kohguchi, T. Nishide, and T. Suzuki, "Photodissociation of nitrous oxide starting from excited bending levels", Journal of Chemical Physics **125**, 133312–133322 (2006).

[75] R. Schinke, *Photodissociation Dynamics* (Cambridge University Press, 1993).

[76] A. I. Hirsch, A. M. Michalak, L. M. Bruhwiler, W. Peters, E. J. Dlugokencky, and P. P. Tans, "Inverse modeling estimates of the global nitrous oxide surface flux from 1998-2001", Global Biogeochemical Cycles **20**, 17p (2006).

[77] R. L. Thompson, P. Bousquet, F. Chevallier, P. J. Rayner, and P. Ciais, "Impact of the atmospheric sink and vertical mixing on nitrous oxide fluxes estimated using inversion methods", Journal of Geophysical Research-Atmospheres **116**, 14p (2011).

[78] M. Born and R. Oppenheimer, "Zur Quantentheorie der Molekeln", Annalen der Physik **389**, 457–484 (1927).

[79] M. Born, *Dynamical theory of crystal lattices* (Clarendon, Oxford :, 1954).

[80] F. Jensen, *Introduction to Computational Chemistry* (John Wiley & Sons, 2006).

[81] J. O. T. Helgaker, P. Jorgensen, *Molecular Electronic-Structure Theory* (John Wiley & Sons, 2000).

[82] A. Szabo and N. Ostlund, *Modern Quantum Chemistry: Introduction to Advanced Electronic Structure Theory* (Dover Publications, 1996).

[83] H. Lischka, D. Nachtigallová, A. J. A. Aquino, P. G. Szalay, F. Plasser, F. B. C. Machado, and M. Barbatti, "Multireference Approaches for Excited States of Molecules", Chemical Reviews **118**, 7293–7361 (2018).

[84] W. Kutzelnigg, "R12-Dependent terms in the wave function as closed sums of partial wave amplitudes for large l", Theoretica chimica acta **68**, 445–469 (1985).

[85] W. Kutzelnigg and W. Klopper, "Wave functions with terms linear in the interelectronic coordinates to take care of the correlation cusp. I. General theory", The Journal of Chemical Physics **94**, 1985–2001 (1991).

[86] S. Ten-no, "Initiation of explicitly correlated Slater-type geminal theory", Chemical Physics Letters **398**, 56–61 (2004).

[87] D. P. Tew and W. Klopper, "New correlation factors for explicitly correlated electronic wave functions", The Journal of Chemical Physics **123**, 074101 (2005).

[88] K. M. d. Lange and J. R. Lane, "Explicit correlation and intermolecular interactions: Investigating carbon dioxide complexes with the CCSD(T)-F12 method", The Journal of Chemical Physics **134**, 034301 (2011).

[89] D. P. Tew, W. Klopper, C. Neiss, and C. Hättig, "Quintuple-ζ quality coupled-cluster correlation energies with triple-ζ basis sets", Physical Chemistry Chemical Physics **9**, 1921–1930 (2007).

[90] T. B. Adler, G. Knizia, and H.-J. Werner, "A simple and efficient CCSD(T)-F12 approximation", The Journal of Chemical Physics **127**, 221106 (2007).

[91] O. Marchetti and H.-J. Werner, "Accurate calculations of intermolecular interaction energies using explicitly correlated wave functions", Physical Chemistry Chemical Physics **10**, 3400–3409 (2008).

[92] G. Knizia, T. B. Adler, and H.-J. Werner, "Simplified CCSD(T)-F12 methods: Theory and benchmarks", The Journal of Chemical Physics **130**, 054104 (2009).

[93] C. Møller and M. S. Plesset, "Note on an Approximation Treatment for Many-Electron Systems", Physical Review **46**, 618–622 (1934).

[94] P. Hohenberg and W. Kohn, "Inhomogeneous Electron Gas", Physical Review **136**, B864–B871 (1964).

[95] W. Kohn and L. J. Sham, "Self-Consistent Equations Including Exchange and Correlation Effects", Physical Review **140**, A1133–A1138 (1965).

[96] T. Yanai, D. P. Tew, and N. C. Handy, "A new hybrid exchange–correlation functional using the Coulomb-attenuating method (CAM-B3LYP)", Chemical Physics Letters **393**, 51–57 (2004).

[97] Y. Zhao and D. G. Truhlar, "The M06 suite of density functionals for main group thermochemistry, thermochemical kinetics, noncovalent interactions, excited states, and transition elements: two new functionals and systematic testing of four M06-class functionals and 12 other functionals", Theoretical Chemistry Accounts **120**, 215–241 (2008).

[98] Y. Zhao and D. G. Truhlar, "Density Functionals with Broad Applicability in Chemistry", Accounts of Chemical Research **41**, 157–167 (2008).

[99] J.-D. Chai and M. Head-Gordon, "Long-range corrected hybrid density functionals with damped atom–atom dispersion corrections", Physical Chemistry Chemical Physics **10**, 6615–6620 (2008).

[100] O. A. von Lilienfeld, I. Tavernelli, U. Rothlisberger, and D. Sebastiani, "Optimization of Effective Atom Centered Potentials for London Dispersion Forces in Density Functional Theory", Physical Review Letters **93**, 153004 (2004).

[101] A. Tkatchenko and M. Scheffler, "Accurate Molecular Van Der Waals Interactions from Ground-State Electron Density and Free-Atom Reference Data", Physical Review Letters **102**, 073005 (2009).

[102] S. Grimme, "Accurate description of van der Waals complexes by density functional theory including empirical corrections", Journal of Computational Chemistry **25**, 1463–1473 (2004).

[103] U. Zimmerli, M. Parrinello, and P. Koumoutsakos, "Dispersion corrections to density functionals for water aromatic interactions", The Journal of Chemical Physics **120**, 2693–2699 (2004).

[104] B. O. Roos, P. R. Taylor, and P. E. Sigbahn .

[105] P. A. Malmqvist, A. Rendell, and B. O. Roos, "The restricted active space self-consistent-field method, implemented with a split graph unitary group approach", The Journal of Physical Chemistry **94**, 5477–5482 (1990).

[106] K. Andersson, P. A. Malmqvist, B. O. Roos, A. J. Sadlej, and K. Wolinski, "Second-order perturbation theory with a CASSCF reference function", The Journal of Physical Chemistry **94**, 5483–5488 (1990).

[107] K. Andersson, P. Malmqvist, and B. O. Roos, "Second-order perturbation theory with a complete active space self-consistent field reference function", The Journal of Chemical Physics **96**, 1218–1226 (1992).

[108] K. Hirao, "Multireference Møller—Plesset perturbation theory for high-spin open-shell systems", Chemical Physics Letters **196**, 397–403 (1992).

[109] K. Hirao, "Multireference Møller—Plesset method", Chemical Physics Letters **190**, 374–380 (1992).

[110] K. Hirao, "Multireference Møller–Plesset perturbation treatment of potential energy curve of N_2", International Journal of Quantum Chemistry **44**, 517–526 (1992).

[111] C. Angeli, M. Pastore, and R. Cimiraglia, "New perspectives in multireference perturbation theory: the n-electron valence state approach", Theoretical Chemistry Accounts **117**, 743–754 (2007).

[112] J. P. Zobel, J. J. Nogueira, and L. González, "The IPEA dilemma in CASPT2", Chemical Science **8**, 1482–1499 (2017).

[113] P. G. Szalay, T. Müller, G. Gidofalvi, H. Lischka, and R. Shepard, "Multiconfiguration Self-Consistent Field and Multireference Configuration Interaction Methods and Applications", Chemical Reviews **112**, 108–181 (2012).

[114] I. Levine, *Quantum Chemistry*, Pearson advanced chemistry series (Pearson, 2014).

[115] D. Walter and E. A. Carter, "Multi-reference weak pairs local configuration interaction: efficient calculations of bond breaking", Chemical Physics Letters **346**, 177 – 185 (2001).

[116] D. Walter, A. Venkatnathan, and E. A. Carter, "Local correlation in the virtual space in multireference singles and doubles configuration interaction", The Journal of Chemical Physics **118**, 8127–8139 (2003).

[117] D. B. Krisiloff and E. A. Carter, "Approximately size extensive local multireference singles and doubles configuration interaction", Physical Chemistry Chemical Physics **14**, 7710–7717 (2012).

[118] A. Venkatnathan, A. B. Szilva, D. Walter, R. J. Gdanitz, and E. A. Carter, "Size extensive modification of local multireference configura-

tion interaction", The Journal of Chemical Physics **120**, 1693–1704 (2004).

[119] T. Shiozaki, G. Knizia, and H.-J. Werner, "Explicitly correlated multireference configuration interaction: MRCI-F12", The Journal of Chemical Physics **134**, 034113 (2011).

[120] R. J. Bartlett and G. D. P. III, "Molecular Applications of Coupled Cluster and Many-Body Perturbation Methods", Physica Scripta **21**, 255 (1980).

[121] G. D. P. III and R. J. Bartlett, "A full coupled-cluster singles and doubles model: The inclusion of disconnected triples", The Journal of Chemical Physics **76**, 1910–1918 (1982).

[122] J. Noga and R. J. Bartlett, "The full CCSDT model for molecular electronic structure", The Journal of Chemical Physics **86**, 7041–7050 (1987).

[123] O. Christiansen, H. Koch, and P. Jørgensen, "The second-order approximate coupled cluster singles and doubles model CC2", Chemical Physics Letters **243**, 409–418 (1995).

[124] J. F. Stanton and J. Gauss, "Perturbative treatment of the similarity transformed Hamiltonian in equation-of-motion coupled-cluster approximations", The Journal of Chemical Physics **103**, 1064–1076 (1995).

[125] K. Raghavachari, G. W. Trucks, J. A. Pople, and M. Head-Gordon, "A fifth-order perturbation comparison of electron correlation theories", Chemical Physics Letters **157**, 479–483 (1989).

[126] H. Koch, O. Christiansen, P. Jørgensen, A. M. S. d. Merás, and T. Helgaker, "The CC3 model: An iterative coupled cluster approach including connected triples", The Journal of Chemical Physics **106**, 1808–1818 (1997).

[127] H. J. Monkhorst, "Calculation of properties with the coupled-cluster method", International Journal of Quantum Chemistry **12**, 421–432 (1977).

[128] H. Sekino and R. J. Bartlett, "A linear response, coupled-cluster theory for excitation energy", International Journal of Quantum Chemistry **26**, 255–265 (1984).

[129] H. Koch and P. Jørgensen, "Coupled cluster response functions", The Journal of Chemical Physics **93**, 3333–3344 (1990).

[130] J. F. Stanton and R. J. Bartlett, "The equation of motion coupled-cluster method. A systematic biorthogonal approach to molecular excitation energies, transition probabilities, and excited state properties", The Journal of Chemical Physics **98**, 7029–7039 (1993).

[131] D. C. Comeau and R. J. Bartlett, "The equation-of-motion coupled-cluster method. Applications to open- and closed-shell reference states", Chemical Physics Letters **207**, 414–423 (1993).

[132] H. Koch, H. J. A. Jensen, P. Jørgensen, and T. Helgaker, "Excitation energies from the coupled cluster singles and doubles linear response function (CCSDLR). Applications to Be, CH^+, CO, and H_2O", The Journal of Chemical Physics **93**, 3345–3350 (1990).

[133] A. B. Trofimov and J. Schirmer, "An efficient polarization propagator approach to valence electron excitation spectra", Journal of Physics B: Atomic, Molecular and Optical Physics **28**, 2299 (1995).

[134] A. B. Trofimov, G. Stelter, and J. Schirmer, "A consistent third-order propagator method for electronic excitation", The Journal of Chemical Physics **111**, 9982–9999 (1999).

[135] P. H. P. Harbach, M. Wormit, and A. Dreuw, "The third-order algebraic diagrammatic construction method (ADC(3)) for the polarization propagator for closed-shell molecules: Efficient implementation and benchmarking", The Journal of Chemical Physics **141**, 064113 (2014).

[136] R. J. Bartlett, "Coupled-cluster theory and its equation-of-motion extensions", Wiley Interdisciplinary Reviews: Computational Molecular Science **2**, 126–138 (2012).

[137] B. Jeziorski and H. J. Monkhorst, "Coupled-cluster method for multideterminantal reference states", Physical Review A **24**, 1668–1681 (1981).

[138] D. Mukherjee, "Normal ordering and a Wick-like reduction theorem for fermions with respect to a multi-determinantal reference state", Chemical Physics Letters **274**, 561–566 (1997).

[139] W. Kutzelnigg and D. Mukherjee, "Normal order and extended Wick theorem for a multiconfiguration reference wave function", The Journal of Chemical Physics **107**, 432–449 (1997).

[140] J. Gräfenstein and D. Cremer, "Development of a CAS-DFT method covering non-dynamical and dynamical electron correlation in a balanced way", Molecular Physics **103**, 279–308 (2005).

[141] M. E. CASIDA, *Time-Dependent Density Functional Response Theory for Molecules* (1995), 155–192.

[142] F. Furche and R. Ahlrichs, "Adiabatic time-dependent density functional methods for excited state properties", The Journal of Chemical Physics **117**, 7433–7447 (2002).

[143] R. Mitrić, U. Werner, M. Wohlgemuth, G. Seifert, and V. Bonačić-Koutecký, "Nonadiabatic Dynamics within Time-Dependent Density Functional Tight Binding Method", The Journal of Physical Chemistry A **113**, 12700–12705 (2009).

[144] S. F. Boys, "Electronic Wave Functions. I. A General Method of Calculation for the Stationary States of Any Molecular System", Proceedings of the Royal Society of London A: Mathematical, Physical and Engineering Sciences **200**, 542–554 (1950).

[145] R. Krishnan, J. S. Binkley, R. Seeger, and J. A. Pople, "Self-consistent molecular orbital methods. XX. A basis set for correlated wave functions", The Journal of Chemical Physics **72**, 650–654 (1980).

[146] T. H. Dunning, "Gaussian basis sets for use in correlated molecular calculations. I. The atoms boron through neon and hydrogen", The Journal of Chemical Physics **90**, 1007–1023 (1989).

[147] Y. Jung, A. Sodt, P. M. W. Gill, and M. Head-Gordon, "Auxiliary basis expansions for large-scale electronic structure calculations", Proceedings of the National Academy of Sciences **102**, 6692–6697 (2005).

[148] L. Kong, F. A. Bischoff, and E. F. Valeev, "Explicitly Correlated R12/F12 Methods for Electronic Structure", Chemical Reviews **112**, 75–107 (2012).

[149] S. Kritikou and J. G. Hill, "Auxiliary Basis Sets for Density Fitting in Explicitly Correlated Calculations: The Atoms H–Ar", Journal of Chemical Theory and Computation **11**, 5269–5276 (2015).

[150] K. B. Wiberg, A. E. de Oliveira, and G. Trucks, "A Comparison of the Electronic Transition Energies for Ethene, Isobutene, Formaldehyde, and Acetone Calculated Using RPA, TDDFT, and EOM-CCSD. Effect of Basis Sets", The Journal of Physical Chemistry A **106**, 4192–4199 (2002).

[151] R. Crespo-Otero and M. Barbatti, "Spectrum simulation and decomposition with nuclear ensemble: formal derivation and application to benzene, furan and 2-phenylfuran", Theoretical Chemistry Accounts **131**, 1237 (2012).

[152] J. P. Bergsma, P. H. Berens, K. R. Wilson, D. R. Fredkin, and E. J. Heller, "Electronic spectra from molecular dynamics: a simple approach", The Journal of Physical Chemistry **88**, 612–619 (1984).

[153] J. G. Saven and J. L. Skinner, "A molecular theory of the line shape: Inhomogeneous and homogeneous electronic spectra of dilute chromophores in nonpolar fluids", The Journal of Chemical Physics **99**, 4391–4402 (1993).

[154] W. Case, *Wigner functions and Weyl transforms for pedestrians*, volume 76 (2008).

[155] M. Barbatti, A. J. A. Aquino, and H. Lischka, "The UV absorption of nucleobases: Semi-classical ab initio spectra simulations", Phys. Chem. Chem. Phys. **12**, 4959–4967 (2010).

[156] R. Crespo-Otero and M. Barbatti, "$Cr(CO)_6$ photochemistry: Semi-classical study of UV absorption spectral intensities and dynamics of photodissociation", The Journal of Chemical Physics **134**, 164305 (2011).

[157] M. Barbatti, "The role of tautomers in the UV absorption of urocanic acid", Physical Chemistry Chemical Physics **13**, 4686–4692 (2011).

[158] P. G. Szalay, A. J. A. Aquino, M. Barbatti, and H. Lischka, "Theoretical study of the excitation spectrum of azomethane", Chemical Physics **380**, 9–16 (2011).

[159] M. Barbatti, "Nonadiabatic dynamics with trajectory surface hopping method", Wiley Interdisciplinary Reviews: Computational Molecular Science **1**, 620–633 (2011).

[160] J. C. Tully, "Molecular dynamics with electronic transitions", The Journal of Chemical Physics **93**, 1061–1071 (1990).

[161] D. J. Garton, A. L. Brunsvold, T. K. Minton, D. Troya, B. Maiti, and G. C. Schatz, "Experimental and Theoretical Investigations of the Inelastic and Reactive Scattering Dynamics of O(3P) + D_2", The Journal of Physical Chemistry A **110**, 1327–1341 (2006).

[162] E. Fabiano, T. W. Keal, and W. Thiel, "Implementation of surface hopping molecular dynamics using semiempirical methods", Chemical Physics **349**, 334–347 (2008).

[163] W. R. Duncan, W. M. Stier, and O. V. Prezhdo, "Ab Initio Nonadiabatic Molecular Dynamics of the Ultrafast Electron Injection across the Alizarin-TiO_2 Interface", Journal of the American Chemical Society **127**, 7941–7951 (2005).

[164] C. F. Craig, W. R. Duncan, and O. V. Prezhdo, "Trajectory Surface Hopping in the Time-Dependent Kohn-Sham Approach for Electron-Nuclear Dynamics", Physical Review Letters **95**, 163001 (2005).

[165] H.-J. Werner, P. J. Knowles, G. Knizia, F. R. Manby, and M. Schütz, "Molpro: a general-purpose quantum chemistry program package", Wiley Interdisciplinary Reviews: Computational Molecular Science **2**, 242–253 (2012).

[166] F. Aquilante, J. Autschbach, R. K. Carlson, L. F. Chibotaru, M. G. Delcey, L. De Vico, I. Fdez. Galván, N. Ferré, L. M. Frutos, L. Gagliardi, M. Garavelli, A. Giussani, C. E. Hoyer, G. Li Manni, H. Lischka, D. Ma, P. Å. k. Malmqvist, T. Müller, A. Nenov, M. Olivucci, T. B. Pedersen, D. Peng, F. Plasser, B. Pritchard, M. Reiher, I. Rivalta, I. Schapiro, J. Segarra-Martí, M. Stenrup, D. G. Truhlar, L. Ungur, A. Valentini, S. Vancoillie, V. Veryazov, V. P. Vysotskiy, O. Weingart, F. Zapata, and R. Lindh, "Molcas 8: New capabilities for multiconfigurational quantum chemical calculations across the periodic table", Journal of Computational Chemistry **37**, 506–541 (2016).

[167] J. F. Stanton, J. Gauss, M. Harding, P. Szalay, A. Auer, R. Bartlett, U. Benedikt, C. Berger, D. Bernholdt, Y. Bomble, L. Cheng, O. Christiansen, M. Heckert, O. Heun, C. Huber, T.-C. Jagau, D. Jonsson, J. Jusélius, K. Klein, W. Lauderdale, D. Matthews, T. Metzroth,

L. Mück, D. O'Neill, D. Price, E. Prochnow, C. Puzzarini, K. Ruud, F. Schiffmann, W. Schwalbach, C. Simmons, S. Stopkowicz, A. Tajti, J. Vázquez, F. Wang, and J. Watts, "CFOUR, Version 1.0", .

[168] M. J. Frisch, G. W. Trucks, H. B. Schlegel, G. E. Scuseria, M. A. Robb, J. R. Cheeseman, G. Scalmani, V. Barone, G. A. Petersson, H. Nakatsuji, M. Caricato, A. Marenich, J. Bloino, G. Janesko, B, R. Gomperts, B. Mennucci, H. P. Hratchian, J. V. Ortiz, X. Li, A. F. Izmaylov, J. L. Sonnenberg, D. Williams-Young, F. Ding, F. Lipparini, F. Egidi, J. Goings, B. Peng, A. Petrone, T. Henderson, D. Ranasinghe, V. G. Zakrzewski, J. Gao, N. Rega, G. Zheng, W. Liang, M. Hada, M. Ehara, K. Toyota, R. Fukuda, J. Hasegawa, M. Ishida, T. Nakajima, Y. Honda, O. Kitao, H. Nakai, T. Vreven, K. Throssell, J. A. Montgomery Jr., J. E. Peralta, F. Ogliaro, M. Bearpark, J. J. Heyd, E. Brothers, K. N. Kudin, V. N. Staroverov, T. Keith, R. Kobayashi, J. Normand, K. Raghavachari, A. Rendell, J. C. Burant, S. S. Iyengar, J. Tomasi, M. Cossi, J. M. Millam, M. Klene, C. Adamo, R. Cammi, J. W. Ochterski, R. L. Martin, K. Morokuma, O. Farkas, J. B. Foresman, and D. J. Fox, "Gaussian 09 Revision D.01", Gaussian Inc. Wallingford CT 2016.

[169] M. Barbatti, G. Granucci, M. Ruckenbauer, F. Plasser, R. Crespo-Otero, J. Pittner, M. Persico, and H. Lischka, "NEWTON-X: A package for Newtonian dynamics close to the crossing seam.", (2016).

[170] "TURBOMOLE V6.2 2010, a development of University of Karlsruhe and Forschungszentrum Karlsruhe GmbH, 1989-2007, TURBOMOLE GmbH, since 2007; available from `http://www.turbomole.com`.", .

[171] S. Farahani, B. N. Frandsen, H. G. Kjaergaard, and J. R. Lane, "Simulated Electronic Absorption Spectra of Sulfur-Containing Molecules Present in Earth's Atmosphere", The Journal of Physical Chemistry A **123**, 6605–6617 (2019).

[172] S. L. Manatt and A. L. Lane, "A compilation of the absorption cross-sections of SO_2 from 106 to 403 nm", Journal of Quantitative Spectroscopy and Radiative Transfer **50**, 267–276 (1993).

[173] R. Crespo-Otero and M. Barbatti, "Recent Advances and Perspectives on Nonadiabatic Mixed Quantum–Classical Dynamics", Chemical Reviews **118**, 7026–7068 (2018).

[174] H. B. Niemann, S. K. Atreya, G. R. Carignan, T. M. Donahue, J. A. Haberman, D. N. Harpold, R. E. Hartle, D. M. Hunten, W. T. Kasprzak, P. R. Mahaffy, T. C. Owen, N. W. Spencer, and S. H. Way, "The Galileo Probe Mass Spectrometer: Composition of Jupiter's Atmosphere", Science **272**, 846–849 (1996).

[175] D. B. Nash and R. R. Howell, "Hydrogen Sulfide on IO: Evidence from Telescopic and Laboratory Infrared Spectra", Science **244**, 454–457 (1989).

[176] W. D. Watson, "Interstellar molecule reactions", Reviews of Modern Physics **48**, 513–552 (1976).

[177] G. K. Kolluru, X. Shen, S. C. Bir, and C. G. Kevil, "Hydrogen sulfide chemical biology: Pathophysiological roles and detection", Nitric Oxide **35**, 5–20 (2013).

[178] I. Cacelli, V. Carravetta, and R. Moccia, "H_2S photoabsorption and photoionization cross sections by Stieltjes imaging", Chemical Physics **120**, 51 – 64 (1988).

[179] L. C. Lee, X. Wang, and M. Suto, "Quantitative photoabsorption and fluorescence spectroscopy of H_2S and D2S at 49–240 nm", The Journal of Chemical Physics **86**, 4353–4361 (1987).

[180] C. Brion, Y. Iida, and J. Thomson, "Absolute oscillator strengths for the photoabsorption, ionic photofragmentation and photoionization of H_2S (10–40 eV)", Chemical Physics **101**, 449 – 460 (1986).

[181] T. Ibuki, H. Koizumi, T. Yoshimi, M. Morita, S. Arai, K. Hironaka, K. Shinsaka, Y. Hatano, Y. Yagishita, and K. Ito, "Photoabsorption cross section of H_2S", Chemical Physics Letters **119**, 327 – 330 (1985).

[182] C. Y. R. Wu and F. Z. Chen, "Temperature-dependent photoabsorption cross sections of H_2S in the 1600–2600Å region", Journal of Quantitative Spectroscopy and Radiative Transfer **60**, 17–23 (1998).

[183] A. Rich and J. Patel, "Carbon Disulfide (CS_2) Mechanisms in Formation of Atmospheric Carbon Dioxide (CO2) Formation from Unconventional Shale Gas Extraction and Processing Operations and Global Climate Change", Environmental Health Insights **9**, 35 (2015).

[184] J. Logan, M. B. Mcelroy, S. Wofsy, and M. Prather, "Oxidation of CS_2 and COS - sources for atmospheric SO_2", Nature **281** (1979).

[185] S. P. McGlynn, J. W. Rabalais, J. R. McDonald, and V. M. Scherr, "Electronic spectoscopy of isoelectronic molecules. II. Linear triatomic groupings containing sixteen valence electrons", Chemical Reviews **71**, 73–108 (1971).

[186] D. C. Thornton, A. R. Bandy, B. W. Blomquist, and B. E. Anderson, "Impact of anthropogenic and biogenic sources and sinks on carbonyl sulfide in the North Pacific troposphere", Journal of Geophysical Research: Atmospheres **101**, 1873–1881 (1996).

[187] T. S. Bates, B. K. Lamb, A. Guenther, J. Dignon, and R. E. Stoiber, "Sulfur emissions to the atmosphere from natural sourees", Journal of Atmospheric Chemistry **14**, 315–337 (1992).

[188] H. G. Bingemer, S. Bürgermeister, R. L. Zimmermann, and H.-W. Georgii, "Atmospheric OCS: Evidence for a contribution of anthropogenic sources", Journal of Geophysical Research: Atmospheres **95**, 20617–20622 (1990).

[189] L. T. Molina, J. J. Lamb, and M. J. Molina, "Temperature dependent UV absorption cross sections for carbonyl sulfide", Geophysical Research Letters **8**, 1008–1011 (1981).

[190] P. Limão-Vieira, F. F. d. Silva, D. Almeida, M. Hoshino, H. Tanaka, D. Mogi, T. Tanioka, N. J. Mason, S. V. Hoffmann, M.-J. Hubin-Franskin, and J. Delwiche, "Electronic excitation of carbonyl sulphide (COS) by high-resolution vacuum ultraviolet photoabsorption and electron-impact spectroscopy in the energy region from 4 to 11 eV", The Journal of Chemical Physics **142**, 064303 (2015).

[191] J. Demaison, M. Herman, J. Liévin, and H. D. Rudolph, "Equilibrium Structure of Sulfuric Acid", The Journal of Physical Chemistry A **111**, 2602–2609 (2007).

[192] Y. Miller, R. B. Gerber, and V. Vaida, "Photodissociation yields for vibrationally excited states of sulfuric acid under atmospheric conditions", Geophysical Research Letters **34** (2007).

[193] K. J. Feierabend, D. K. Havey, S. S. Brown, and V. Vaida, "Experimental absolute intensities of the $4\nu9$ and $5\nu9$ O-H stretching overtones of H_2SO_4", Chemical Physics Letters **420**, 438–442 (2006).

[194] Z. Wu, H. Wan, J. Xu, B. Lu, Y. Lu, A. K. Eckhardt, P. R. Schreiner, C. Xie, H. Guo, and X. Zeng, "The near-UV absorber OSSO and its isomers", Chemical Communications **54**, 4517–4520 (2018).

[195] S. Solomon, D. Qin, M. Manning, Z. Chen, M. Marquis, K. Averyt, M. Tignor, and H. Miller, "Climate Change 2007: The physical science basis. Contribution of Working Group I to the Fourth Assessment Report of the Intergovernmental Panel on Climate Change", Report (2007).

[196] N. R. Carlon, D. K. Papanastasiou, E. L. Fleming, C. H. Jackman, P. A. Newman, and J. B. Burkholder, "UV absorption cross sections of nitrous oxide (N_2O) and carbon tetrachloride (CCl_4) between 210 and 350 K and the atmospheric implications", Atmospheric Chemistry and Physics **10**, 6137–6149 (2010).

[197] D. G. Hopper, "Ab initio multiple root optimization MCSCF study of the $C_{\infty V}$ /C_s excitation spectra and potential energy surface of N_2O", Journal of Chemical Physics **80**, 4290–4316 (1984).

[198] R. Schinke and J. A. Schmidt, "Photodissociation of N_2O: Excitation of ^{1}A" States", Journal of Physical Chemistry A **116**, 11083–11087 (2012).

[199] S. P. McGlynn, J. W. Rabalais, J. R. McDonald, and V. M. Scherr, "Electronic spectoscopy of isoelectronic molecules. II. Linear triatomic groupings containing sixteen valence electrons", Chemical Reviews **71**, 73–108 (1971).

[200] G. S. Selwyn and H. S. Johnston, "Ultraviolet absorption spectrum of nitrous oxide as function of temperature and isotopic substitution", Journal of Chemical Physics **74**, 3791–3803 (1981).

[201] K. Yoshino, D. E. Freeman, and W. H. Parkinson, "High resolution absorption cross-section measurements of N_2O at 295–299 K in the wavelength region 170–222 nm", Planetary and Space Science **32**, 1219–1222 (1984).

[202] S. R. Salmon, K. M. de Lange, and J. R. Lane, "Structure and Abundance of Nitrous Oxide Complexes in Earth's Atmosphere", The Journal of Physical Chemistry A **120**, 2096–2105 (2016).

[203] N. Tanaka, U. Nagashima, M. Takayanagi, H. L. Kim, and I. Hanazaki, "Photochemical Reaction Dynamics of the N_2O-$H_2{}^{18}O$ van der Waals Complex", The Journal of Physical Chemistry A **101**, 507–512 (1997).

[204] H. L. Kim, M. Takayanagi, and I. Hanazaki, "Photochemistry of $N_2O.H_2O$ complexes produced in supersonic jets", Chemical Physics Letters **222**, 431 – 435 (1994).

[205] J. L. Teffo and A. Chédin, "Internuclear potential and equilibrium structure of the nitrous oxide molecule from rovibrational data", Journal of Molecular Spectroscopy **135**, 389–409 (1989).

[206] M. S. Bryant, S. W. Reeve, and W. A. Burns, "Observation and Analysis of N_2O Rotation–Vibration Spectra", Journal of Chemical Education **85**, 121 (2008).

[207] E. D. Tidwell, E. K. Plyler, and W. S. Benedict, "Vibration-Rotation Bands of N_2O", Journal of the Optical Society of America **50**, 1243–1263 (1960).

[208] D. E. Burch and D. Williams, "Total Absorptance by Nitrous Oxide Bands in the Infrared", Applied Optics **1**, 473–482 (1962).

[209] M. N. Peeterman and W., "The production of nitric oxide in the stratosphere by oxidation of nitrous oxide", Ann. Geophys. **28**, 751–762 (1972).

[210] K. Yoshino, D. E. Freeman, and W. H. Parkinson, "High resolution absorption cross-section measurements of N_2O at 295–299 K in the wavelength region 170–222 nm", Planetary and Space Science **32**, 1219–1222 (1984).

[211] M. N. Daud, "Accurate treatment of total photoabsorption cross sections by an ab initio time-dependent method", The European Physical Journal D **68**, 267 (2014).

[212] C. H. Joyner, T. A. Dixon, F. A. Baiocchi, and W. Klemperer, "The structure of Ar-N_2O", The Journal of Chemical Physics **75**, 5285–5290 (1981).

[213] J. Hodge, G. D. Hayman, T. R. Dyke, and B. J. Howard, "Molecular-beam infrared spectroscopy of the Ar-N_2O van der Waals molecule", Journal of the Chemical Society, Faraday Transactions 2 Molecular and Chemical Physics **82**, 1137–1142 (1986).

[214] T. A. Hu, E. L. Chappell, and S. W. Sharpe, "Infrared, diode laser spectroscopy of the Ar-N_2O complex: Observation of the intermolecular bending mode in combination with the highest frequency intramolecular stretching mode", The Journal of Chemical Physics **98**, 6162–6169 (1993).

[215] H. O. Leung, "Nuclear quadrupole hyperfine structure in the rotational spectra of HCCH-N_2O and Ar-N_2O", Chemical Communications 2525–2526 (1996).

[216] H. O. Leung, D. Gangwani, and J.-U. Grabow, "Nuclear Quadrupole Hyperfine Structure in the Microwave Spectrum of Ar-N_2O", Journal of Molecular Spectroscopy **184**, 106–112 (1997).

[217] M. S. Ngarıi and W. Jäger, "Ground State Average and Partial Substitution Structures of the Ar-N_2O van der Waals Dimer", Journal of Molecular Spectroscopy **192**, 452–454 (1998).

[218] G. Gimmler and M. Havenith, "High-Resolution IR Spectroscopy of the N_2O-H_2O and N_2O-D_2O van der Waals Complexes", Journal of Molecular Spectroscopy **216**, 315–321 (2002).

[219] G. Gimmler and M. Havenith, "Free-jet infrared diode laser spectroscopy of the ν2-band of the Ar-N_2O van der Waals complex", Journal of Molecular Structure **599**, 117–123 (2001).

[220] R. W. Randall, T. R. Dyke, and B. J. Howard, "Infrared spectroscopy of the N_2-N_2O van der Waals complex", Faraday Discussions of the Chemical Society **86**, 21–29 (1988).

[221] M. Venayagamoorthy and T. A. Ford, "Ab initio molecular orbital studies of the vibrational spectra of some van der Waals complexes.

Part 1. Complexes of molecular nitrogen with carbon dioxide, nitrous oxide, carbonyl sulphide and carbon disulphide", Journal of Molecular Structure **565–566**, 399–409 (2001).

[222] R. Zheng, Y. Zhu, S. Li, M. Fang, and C. Duan, "Rovibrational spectrum and potential energy surface of the N_2-N_2O van der Waals complex", Journal of Molecular Spectroscopy **265**, 102–105 (2011).

[223] M. Rezaei, K. H. Michaelian, and N. Moazzen-Ahmadi, "New combination bands of N_2O-CO_2, N_2O-OCS, and N_2O-N_2 complexes in the N_2O $\nu 1$ region", The Journal of Chemical Physics **140**, 044332 (2014).

[224] R. Zheng, L. Zheng, Y. Lu, and M. Yang, "Theoretical studies for the N_2-N_2O van der Waals complex The potential energy surface, intermolecular vibrations, and rotational transition frequencies", The Journal of Chemical Physics **143**, 154304 (2015).

[225] M. Bahou, L. Schriver-Mazzuoli, C. Camy-Peyret, A. Schriver, T. Chiavassa, and J. P. Aycard, "Infrared matrix spectra of the N_2O...O_2 complex in solid nitrogen. The N_2O...O_2+O thermal diffusion limited reaction", Chemical Physics Letters **265**, 145–153 (1997).

[226] H.-B. Qian, D. Seccombe, and B. J. Howard, "Spectroscopy and structure of the open-shell complex O_2-N_2O", The Journal of Chemical Physics **107**, 7658–7666 (1997).

[227] S. Li, R. Zheng, and C.-X. Duan, "Infrared diode laser spectroscopy of O_2-N_2O van der Waals complex in the $\nu 1$ symmetric stretch region of N_2O", Chinese Physics B **23**, 123301 (2014).

[228] S. R. Salmon and J. R. Lane, "The structure of the O_2-N_2O complex", The Journal of Chemical Physics **143**, 124303 (2015).

[229] J. Sadlej and M. Siciński, "Investigations of the anaesthetic activity of nitrous oxide by quantum-chemical calculations", Journal of Molecular Structure: THEOCHEM **204**, 1–14 (1990).

[230] D. Zolandz, D. Yaron, K. I. Peterson, and W. Klemperer, "Water in weak interactions: The structure of the water–nitrous oxide complex", The Journal of Chemical Physics **97**, 2861–2868 (1992).

[231] G. Gimmler and M. Havenith, "High-Resolution IR Spectroscopy of the N_2O-H_2O and N_2O-D_2O van der Waals Complexes", Journal of Molecular Spectroscopy **216**, 315–321 (2002).

[232] M. J. Wójcik, M. Boczar, and T. A. Ford, "Ab initio study of energies, structures and vibrational spectra of the complexes of water with carbon oxysulfide and nitrous oxide", Chemical Physics Letters **348**, 126–130 (2001).

[233] T. Földes, C. Lauzin, T. Vanfleteren, M. Herman, J. Liévin, and K. Didriche, "High-resolution, near-infrared CW-CRDS, and ab initio investigations of N_2O–HDO", Molecular Physics **113**, 473–482 (2014).

[234] A. Brown, P. Jimeno, and G. G. Balint-Kurti, "Photodissociation of N_2O. I. Ab Initio Potential Energy Surfaces for the Low-Lying Electronic States X ^{1}A', 2 ^{1}A', and 1 ^{1}A"", The Journal of Physical Chemistry A **103**, 11089–11095 (1999).

[235] P. Felder, B. M. Haas, and J. Robert Huber, "The photoreaction N_2O $\rightarrow$ O(^1D)+N_2($^1\Sigma$) at 193 nm studied by photofragment translational spectroscopy", Chemical Physics Letters **186**, 177–182 (1991).

[236] J. M. Teule, G. C. Groenenboom, D. W. Neyer, D. W. Chandler, and M. H. M. Janssen, "State-to-state photodynamics of nitrous oxide

and the effect of long-range interaction on the alignment of O(^{1}D$_2$)", Chemical Physics Letters **320**, 177–185 (2000).

[237] M. Ahmed, E. R. Wouters, D. S. Peterka, O. S. Vasyutinskii, and A. G. Suits, "Atomic orbital alignment and coherence in N_2O photodissociation at 193.3 nm", Faraday Discussions **113**, 425–436 (1999).

[238] D. W. Neyer, A. J. R. Heck, and D. W. Chandler, "Photodissociation of N_2O: J-dependent anisotropy revealed in N_2 photofragment images", The Journal of Chemical Physics **110**, 3411–3417 (1999).

[239] D. W. Neyer, A. J. R. Heck, D. W. Chandler, J. M. Teule, and M. H. M. Janssen, "Speed-Dependent Alignment and Angular Distributions of O(1D2)from the Ultraviolet Photodissociation of N_2O", The Journal of Physical Chemistry A **103**, 10388–10397 (1999).

[240] T. Suzuki, H. Katayanagi, Y. Mo, and K. Tonokura, "Evidence for multiple dissociation components and orbital alignment in 205 nm photodissociation of N_2O", Chemical Physics Letters **256**, 90–95 (1996).

[241] T. F. Hanisco and A. C. Kummel, "State-resolved photodissociation of nitrous oxide", The Journal of Physical Chemistry **97**, 7242–7246 (1993).

[242] L. L. Springsteen, S. Satyapal, Y. Matsumi, L. M. Dobeck, and P. L. Houston, "Anisotropy and energy disposal in the 193-nm nitrous oxide photodissociation measured by VUV laser-induced fluorescence of oxygen atom (^1D)", The Journal of Physical Chemistry **97**, 7239–7241 (1993).

[243] N. Shafer, K. Tonokura, Y. Matsumi, S. Tasaki, and M. Kawasaki, "The Doppler spectra of $O(^1D)$ from the photodissociation of O_2, NO_2, and N_2O", The Journal of Chemical Physics **95**, 6218–6223 (1991).

[244] A. M. Rijs, E. H. G. Backus, C. A. d. Lange, M. H. M. Janssen, K. Wang, and V. McKoy, "Rotationally resolved photoelectron spectroscopy of hot N_2 formed in the photofragmentation of N_2O", The Journal of Chemical Physics **114**, 9413–9420 (2001).

[245] T. Nishide and T. Suzuki, "Photodissociation of Nitrous Oxide Revisited by High-Resolution Photofragment Imaging: Energy Partitioning", The Journal of Physical Chemistry A **108**, 7863–7870 (2004).

[246] G. Black, R. L. Sharpless, T. G. Slanger, and D. C. Lorents, "Quantum yields for the production of $O(^1S)$, $N(^2D)$, and $N_2(A^3\Sigma_u^+)$ from the vacuum UV photolysis of N_2O", The Journal of Chemical Physics **62**, 4266–4273 (1975).

[247] J. A. Schmidt, M. S. Johnson, U. Lorenz, G. C. McBane, and R. Schinke, "Photodissociation of N_2O: Energy partitioning", J. Chem. Phys. **135**, 024311–024321 (2011).

[248] D. S. King, D. G. Sauder, and M. P. Casassa, "Cluster effects in O_3/ H_2S photochemistry: Dynamics of the $O + H_2O \rightarrow 2OH$ reaction photoinitiated in the O_3-H_2O dimer", The Journal of Chemical Physics **100**, 4200–4210 (1994).

Appendices

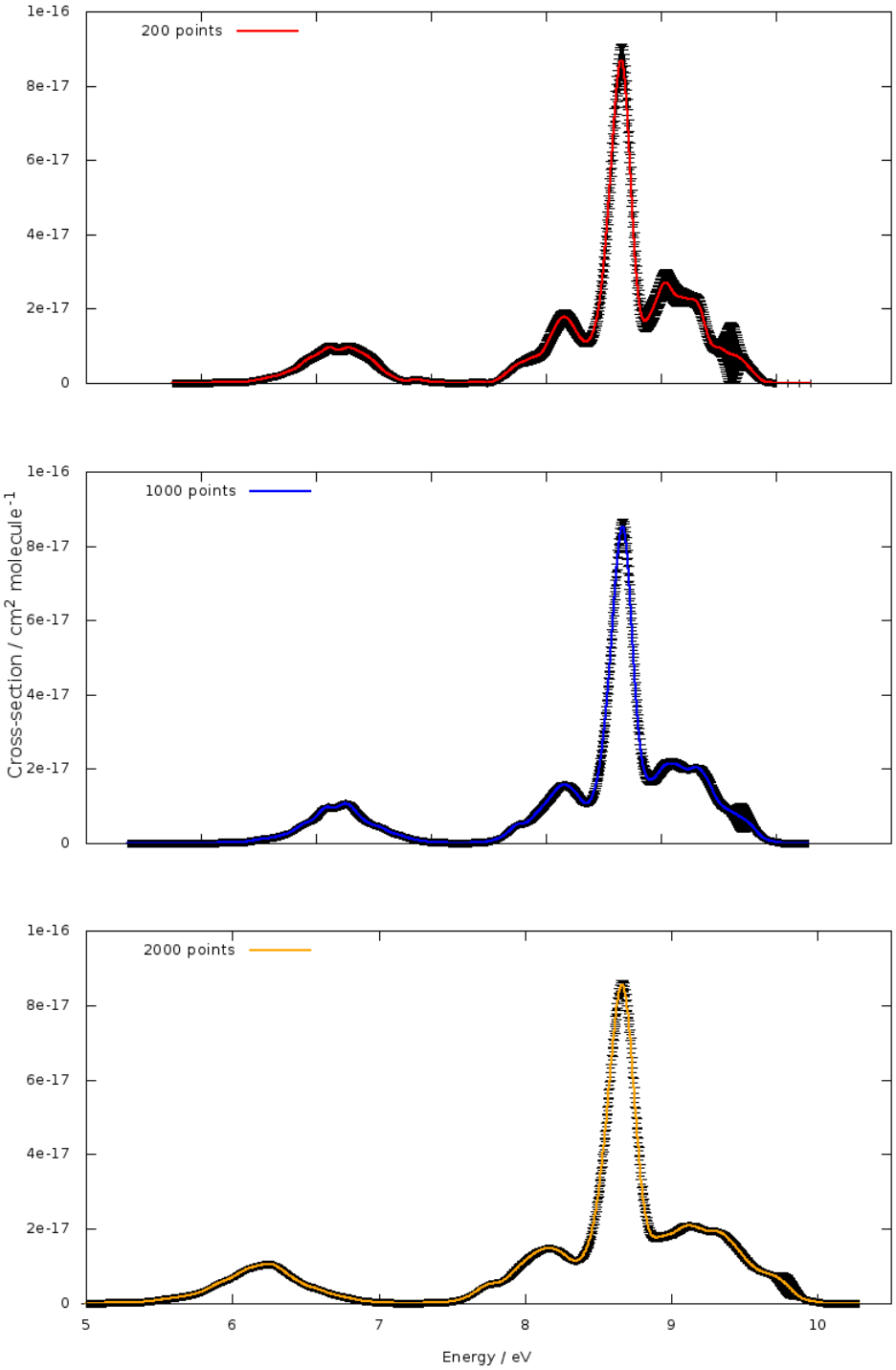

Figure A.1: EOM-CCSD/aug-cc-pV(D+d)Z absorption spectra of H_2S and error bars for 200, 1000 and 2000 points.

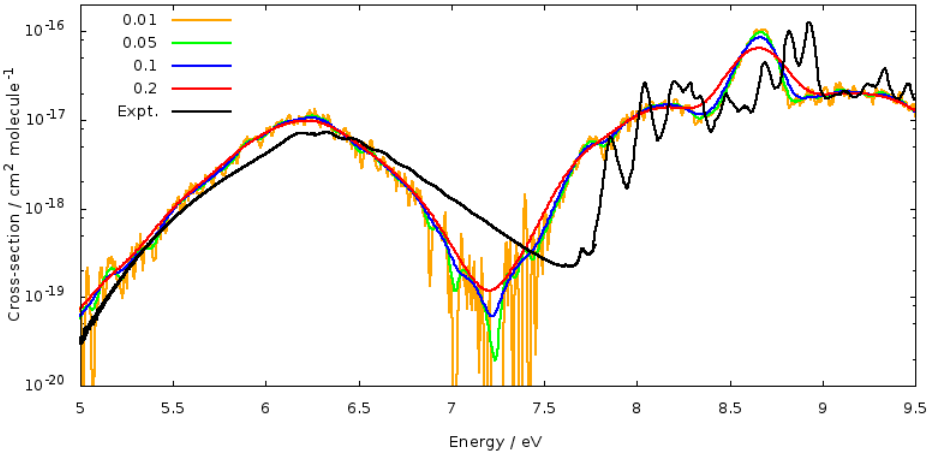

Figure A.2: H_2S absorption spectra from four phenomenological broadenings (eV) for 2000 points at EOM-CCSD/aug-cc-pV(D+d)Z+3 level of theory and the experimental spectrum from Grosch *et. al* [20] (5.0-6.3 eV) at 294.8 K, Wu and Chen [182] (6.3-7.7 eV) at 295 K and Feng *et al.* (7.7-9.6 eV) [19].

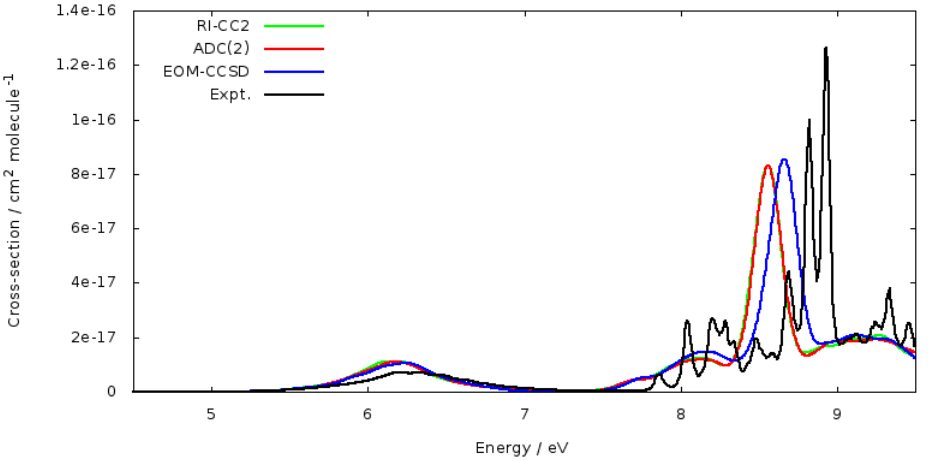

Figure A.3: H_2S simulated spectra from EOM-CCSD, RI-CC2 and ADC(2) methods with aug-cc-pV(D+d)Z+3 basis set and the experimental spectrum from Grosch *et. al* [20] (5.0-6.3 eV) at 294.8 K, Wu and Chen [182] (6.3-7.7 eV) at 295 K and Feng *et al.* (7.7-9.6 eV) [19].

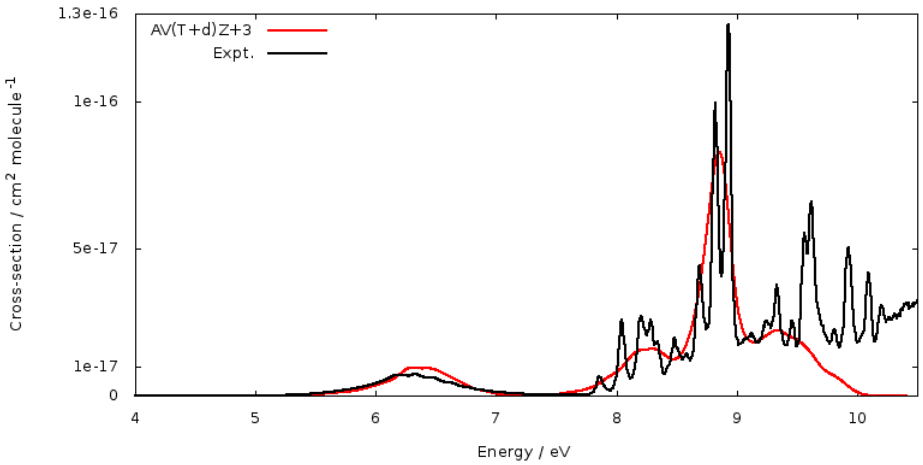

Figure A.4: EOM-CCSD/aug-cc-pV(T+d)Z+3 simulated spectra of H_2S and the experimental spectrum from Grosch *et. al* [20] (5.0-6.3 eV) at 294.8 K, Wu and Chen [182] (6.3-7.7 eV) at 295 K and Feng *et al.* (7.7-9.6 eV) [19].

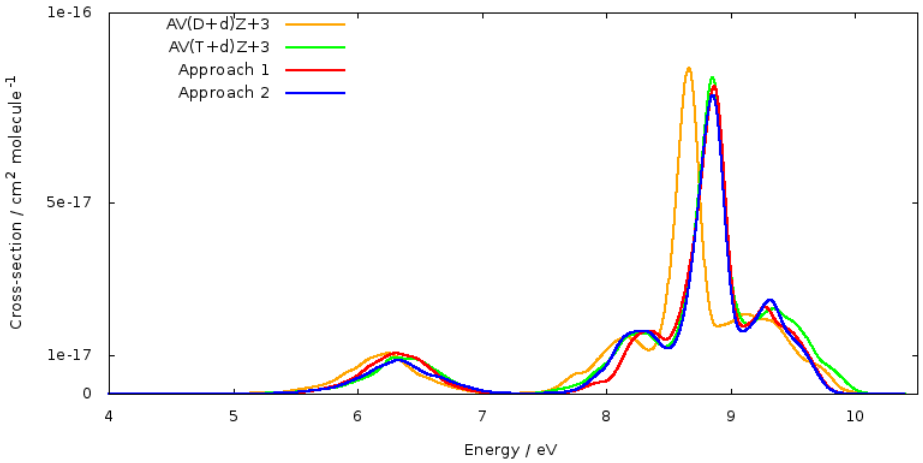

Figure A.5: Approximated EOM-CCSD/aug-cc-pV(T+d)Z+3 spectra of H_2S from approaches 1 and 2 compared with EOM-CCSD calculated spectrum from aug-cc-pV(T+d)Z+3 and aug-cc-pV(D+d)Z+3.

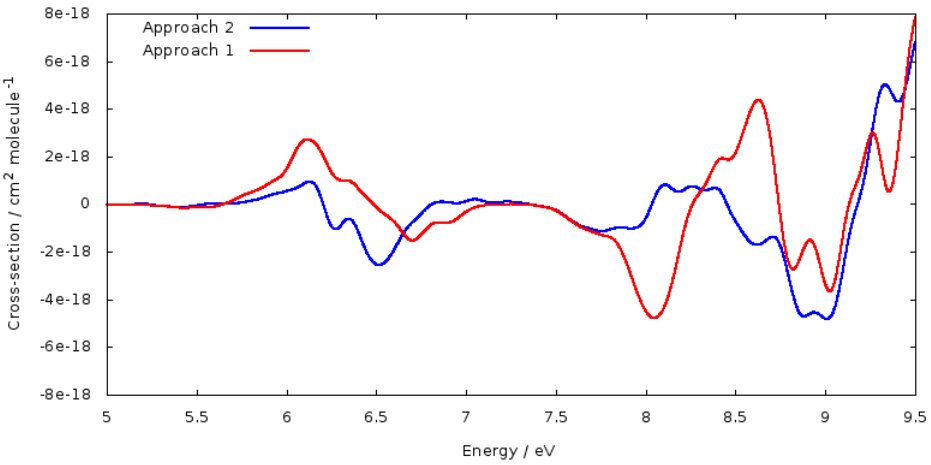

Figure A.6: Difference graphs from comparing H_2S approach 1 and 2 spectra with calculated EOM-CCSD/aug-cc-pV(T+d)Z+3 spectrum.

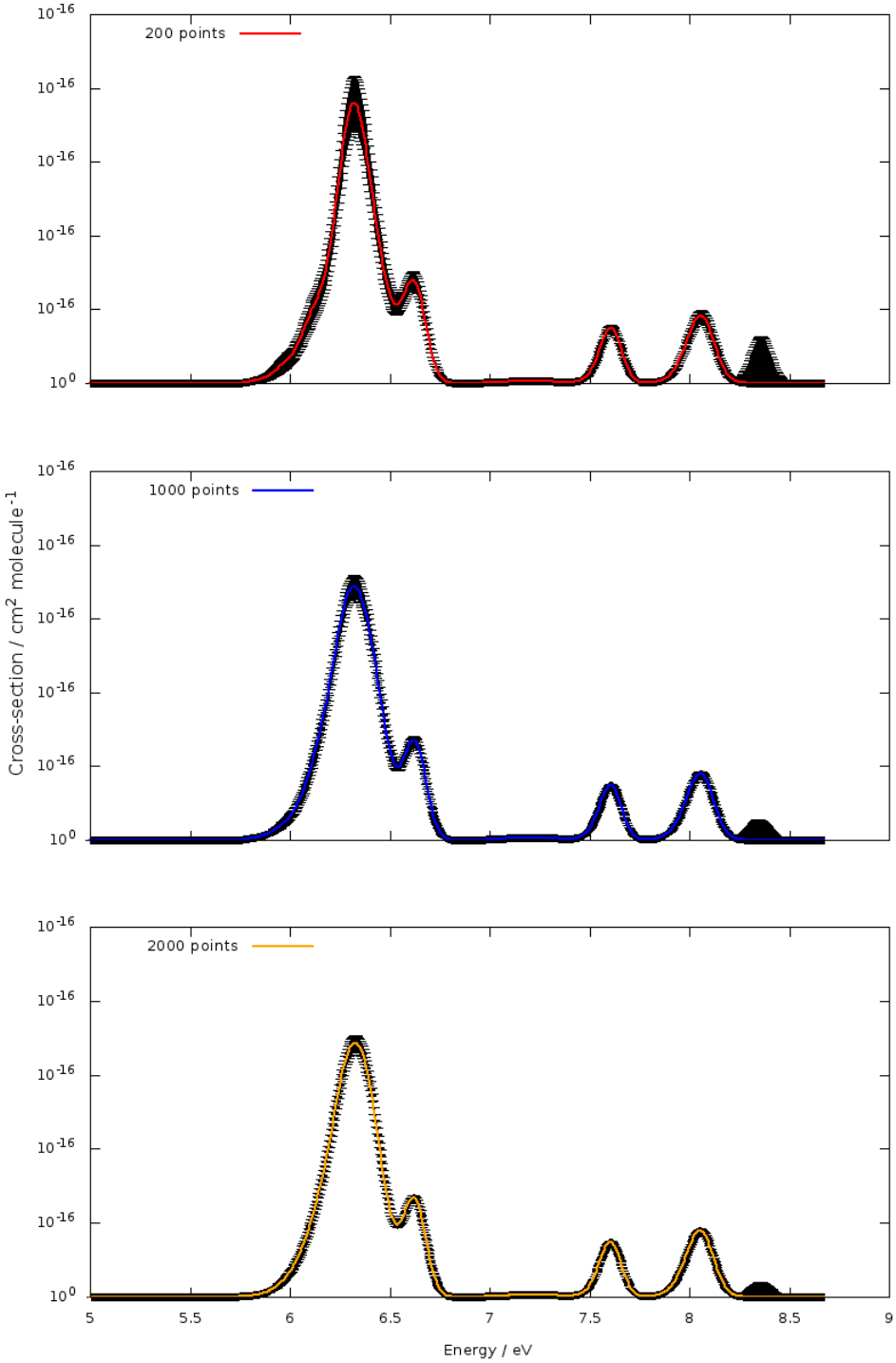

Figure A.7: EOM-CCSD/aug-cc-pV(D+d)Z absorption spectra of CS_2 and error bars for200, 1000 and 2000 points.

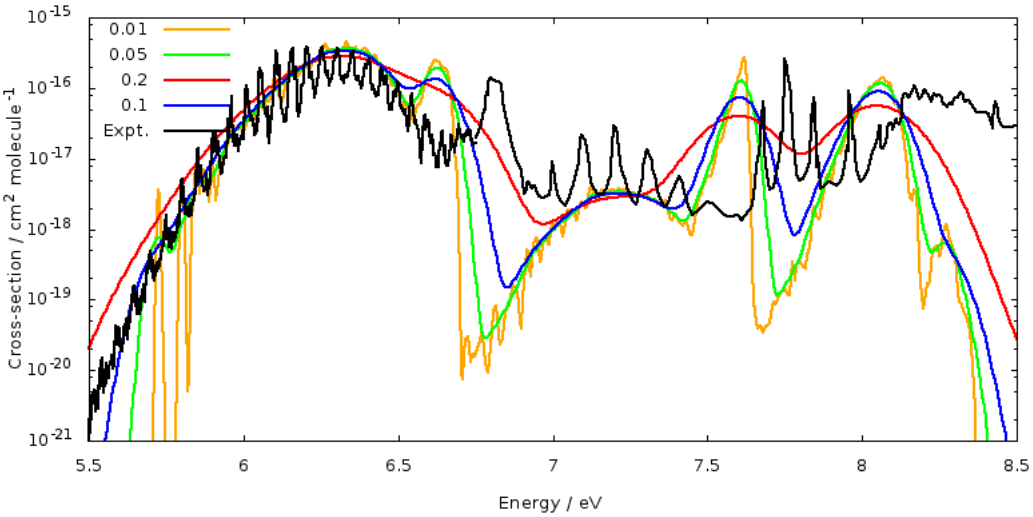

Figure A.8: CS_2 absorption spectra from four phenomenological broadenings (eV) for 2000 points at EOM-CCSD/aug-cc-pV(D+d)Z+3 level of theory and the experimental spectrum from Grosch *et. al* [20] (3.3-6.0 eV) at 294.8 K, Sunanda *et. al* [22] (6.0-6.7 eV) at 298 K and Rabalais *et. al* [185] (6.7-8.2 eV) at 298 K.

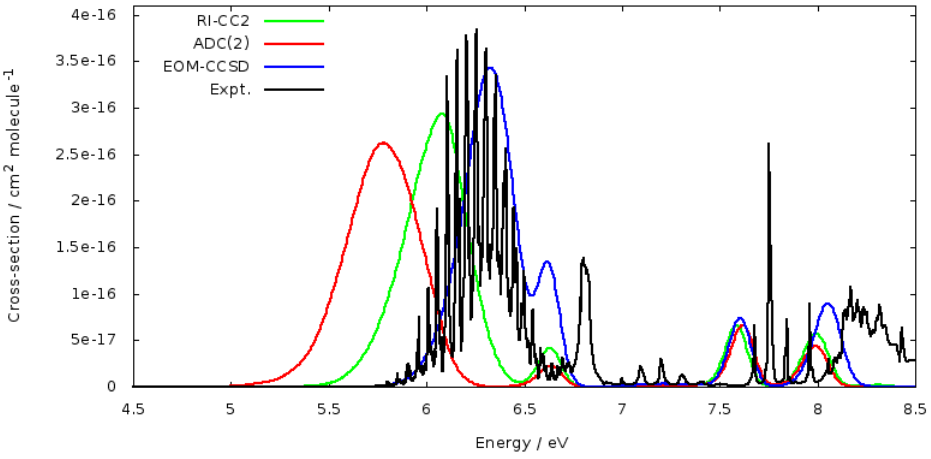

Figure A.9: CS_2 simulated spectra from EOM-CCSD, RI-CC2 and ADC(2) methods with aug-cc-pV(D+d)Z+3 basis set and the experimental spectra from Grosch *et. al* [20] (3.3-6.0 eV) at 294.8 K, Sunanda *et. al* [22] (6.0-6.7 eV) at 298 K and Rabalais *et. al* [185] (6.7-8.2 eV) at 298 K.

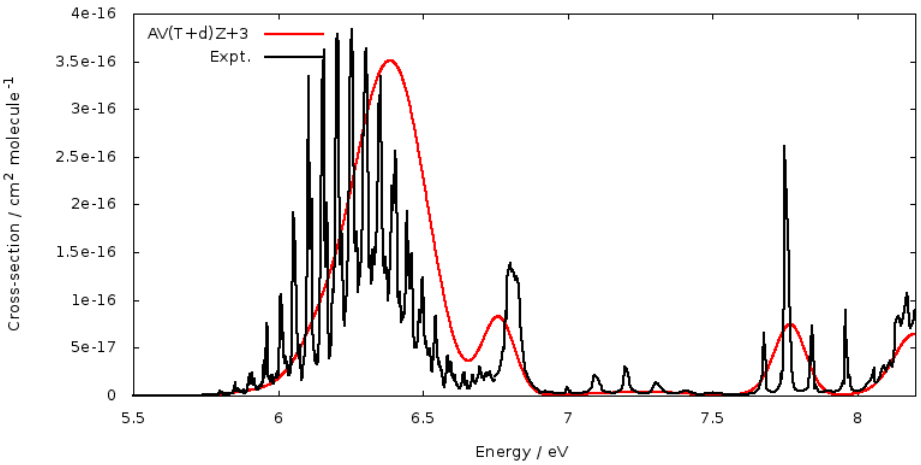

Figure A.10: EOM-CCSD/aug-cc-pV(T+d)Z+3 simulated spectrum of CS_2 and the experimental spectrum from Grosch *et. al* [20] (3.3-6.0 eV) at 294.8 K, Sunanda *et. al* [22] (6.0-6.7 eV) at 298 K and Rabalais *et. al* [185] (6.7-8.2 eV) at 298 K.

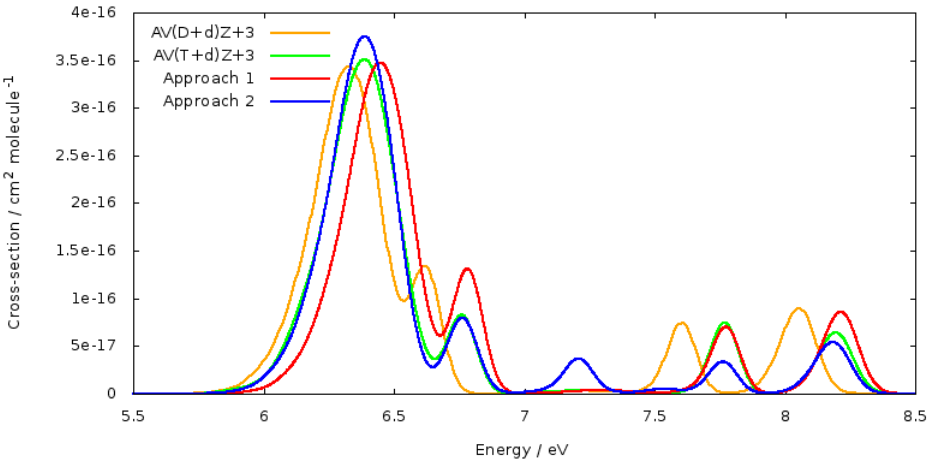

Figure A.11: Approximated EOM-CCSD/aug-cc-pV(T+d)Z+3 spectra of CS_2 from approaches 1 and 2 compared with EOM-CCSD calculated spectrum from aug-cc-pV(T+d)Z+3 and aug-cc-pV(D+d)Z+3.

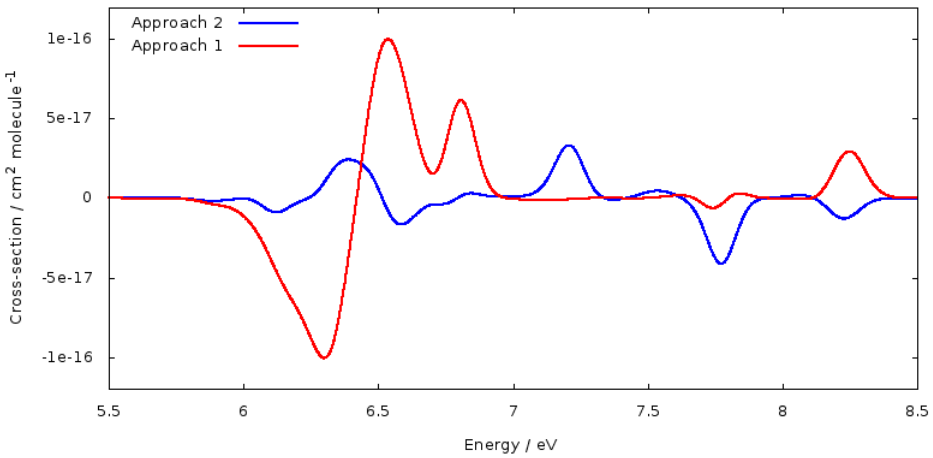

Figure A.12: Difference graphs from comparing CS_2 approach 1 and 2 spectra with calculated EOM-CCSD/aug-cc-pV(T+d)Z+3 spectrum.

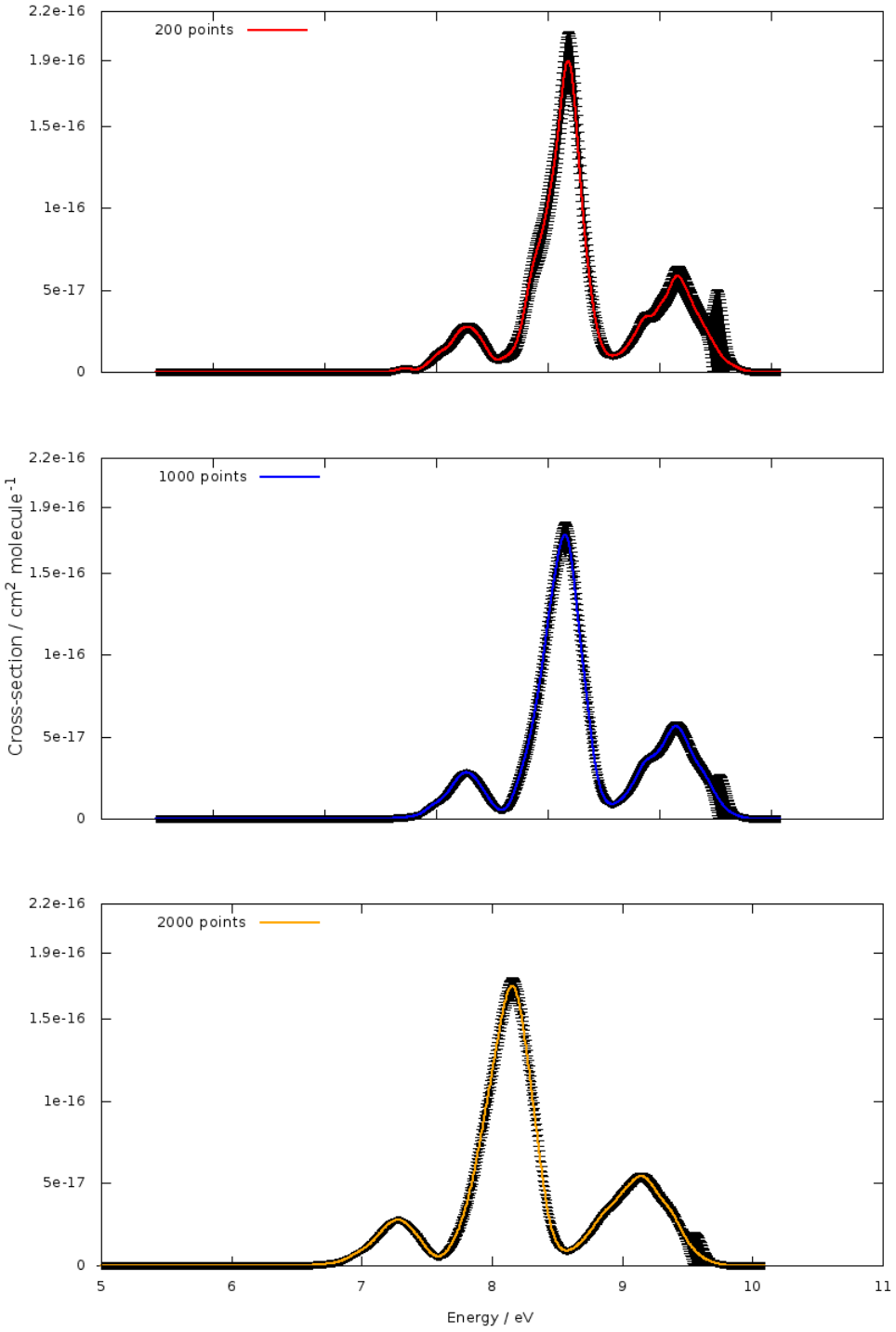

Figure A.13: EOM-CCSD/aug-cc-pV(D+d)Z absorption spectra of OCS and error bars for 200, 1000 and 2000 points.

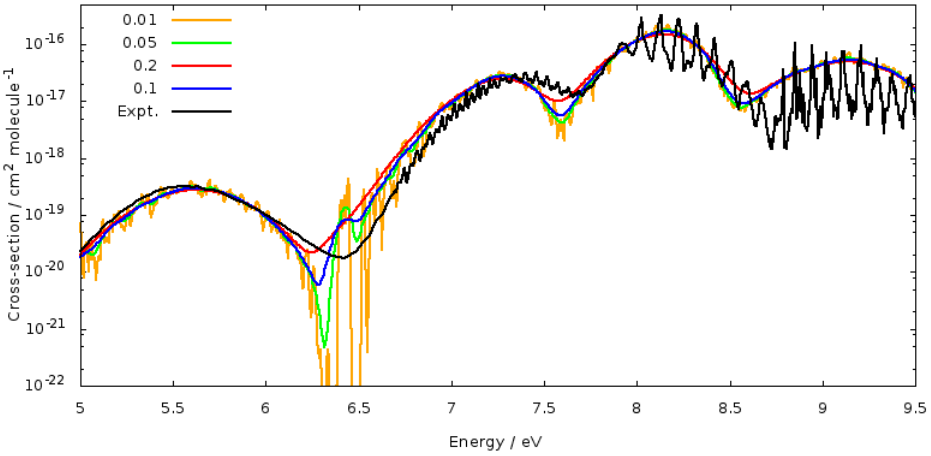

Figure A.14: OCS absorption spectra from four phenomenological broadenings (eV) for 2000 points at EOM-CCSD/aug-cc-pV(D+d)Z+3 level of theory and the experimental spectrum from Molina *et al.* [189] (4.1-4.8 eV) at 295 K and Limao-Vieira *et al.* [190] (4.8-9.3 eV) at 298 K.

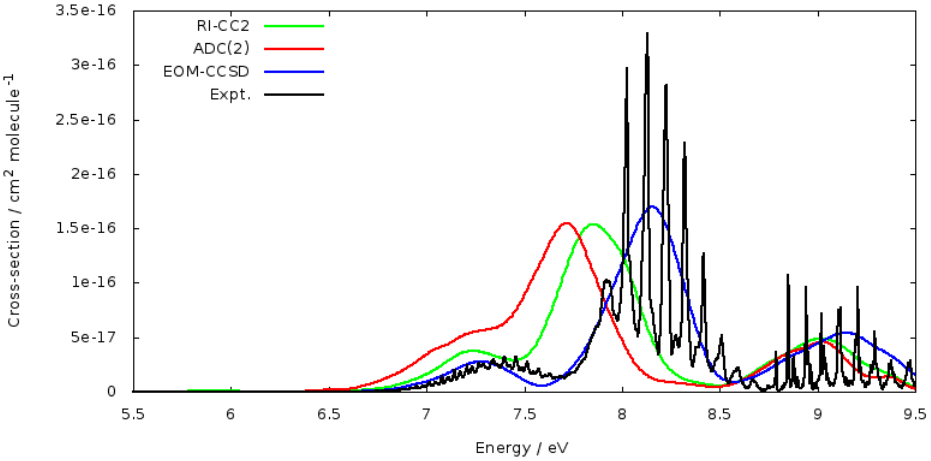

Figure A.15: OCS simulated spectra from EOM-CCSD, RI-CC2 and ADC(2) methods with aug-cc-pV(D+d)Z+3 basis set and the experimental spectraum from Molina *et al.* [189] (4.1-4.8 eV) at 295 K and Limao-Vieira *et al.* [190] (4.8-9.3 eV) at 298 K.

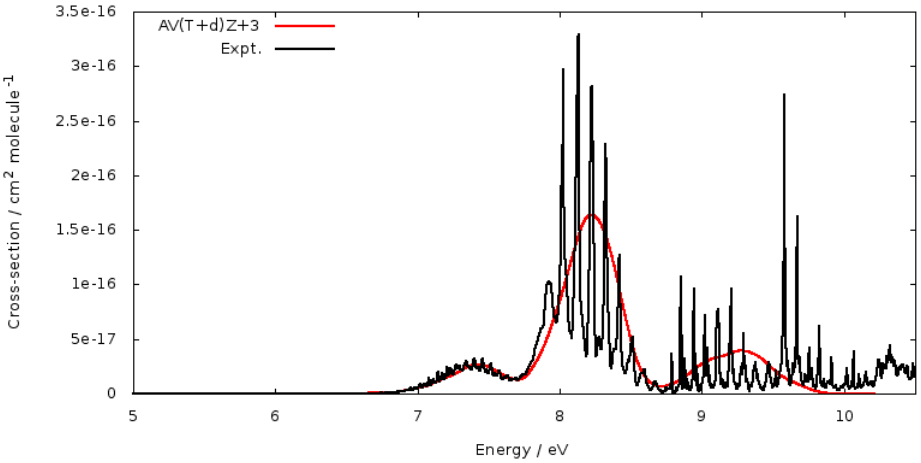

Figure A.16: EOM-CCSD/aug-cc-pV(T+d)Z+3 simulated spectra of OCS and the experimental spectrum from Molina *et al.* [189] (4.1-4.8 eV) at 295 K and Limao-Vieira *et al.* [190] (4.8-9.3 eV) at 298 K.

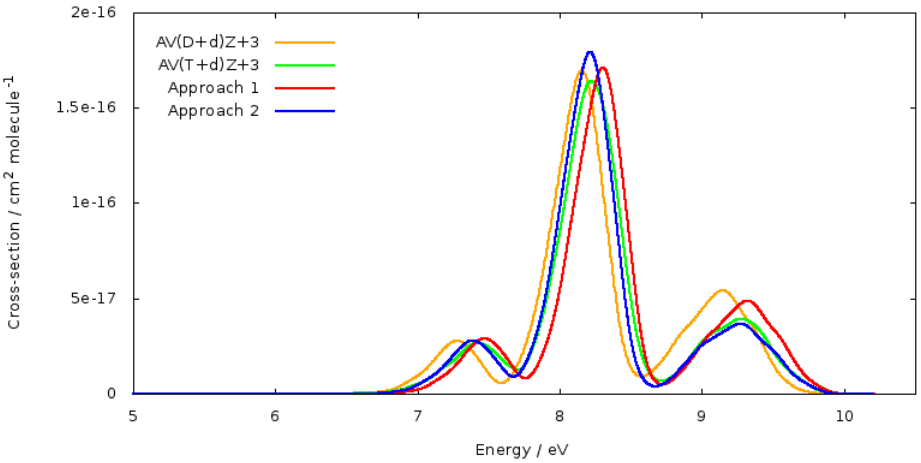

Figure A.17: Approximated EOM-CCSD/aug-cc-pV(T+d)Z+3 spectra of OCS from approaches 1 and 2 compared with EOM-CCSD calculated spectrum from aug-cc-pV(T+d)Z+3 and aug-cc-pV(D+d)Z+3.

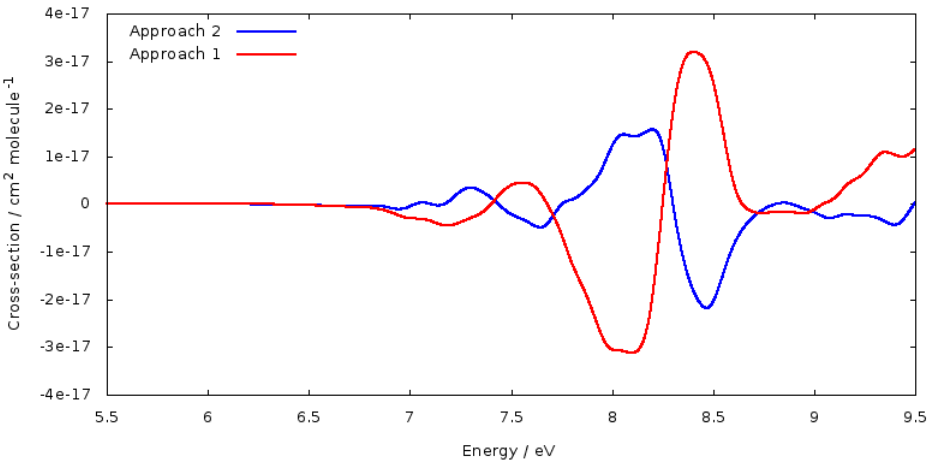

Figure A.18: Difference graphs from comparing OCS approach 1 and 2 spectra with calculated EOM-CCSD/aug-cc-pV(T+d)Z+3 spectrum.

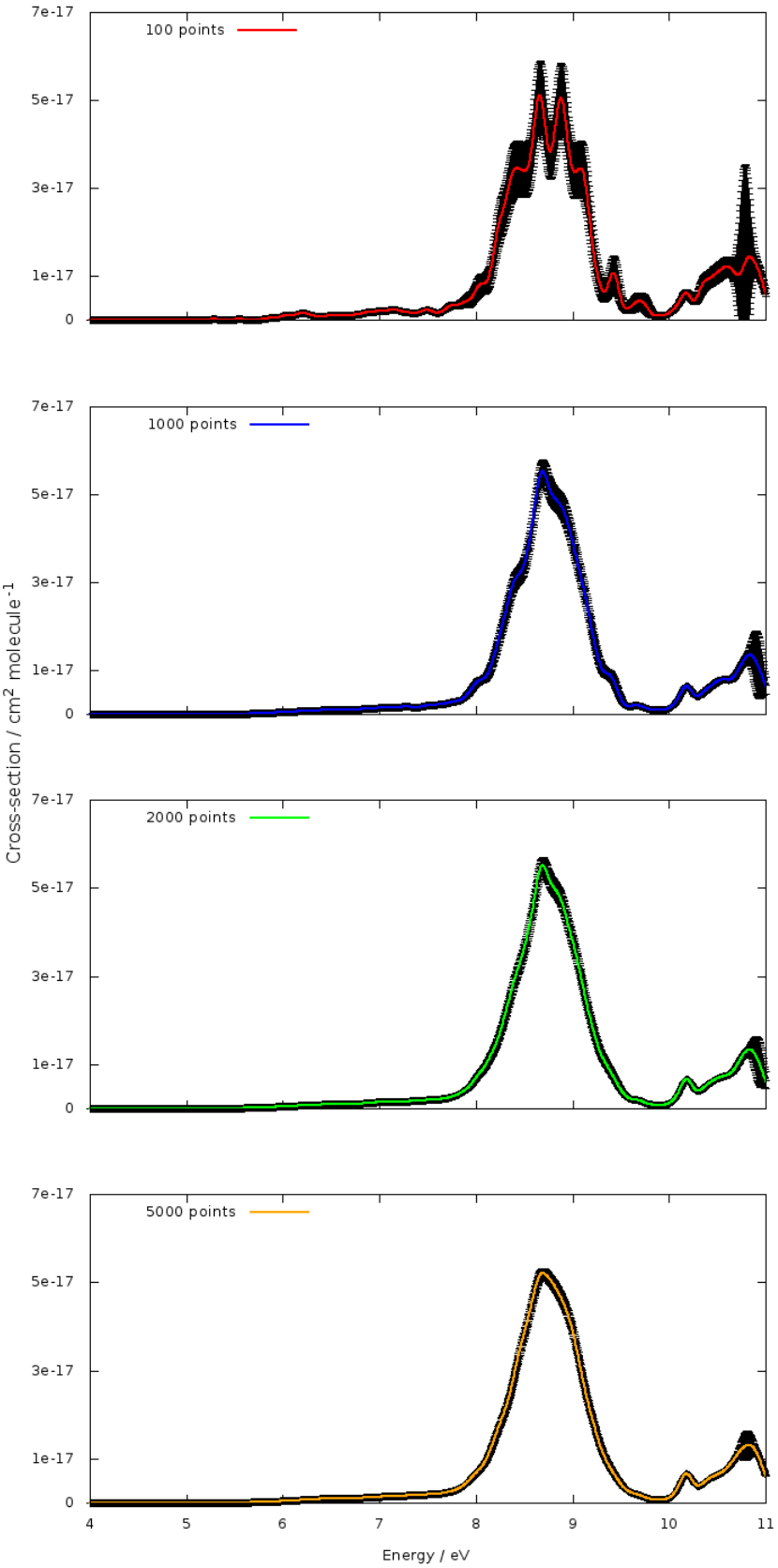

Figure A.19: EOM-CCSD/aug-cc-pV(D+d)Z+3 absorption spectra SO_3 and error bars for 100, 1000, 2000 and 5000 points.

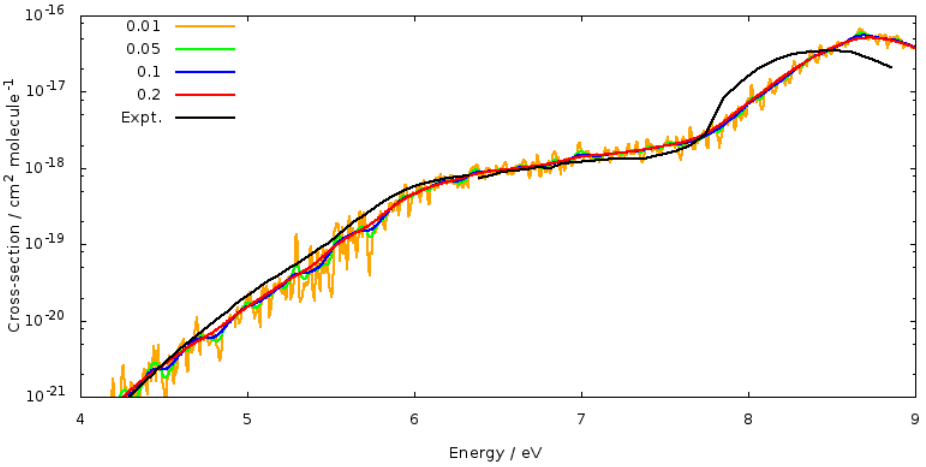

Figure A.20: SO_3 absorption spectra from four phenomenological broadenings (eV) for 2000 points at EOM-CCSD/aug-cc-pV(D+d)Z+3 level of theory and the experimental spectrum from Burkholder *et. al* [18] (4.8-6.4 eV) and Hintz *et. al* [17] (6.4-8.9 eV) at 403 K.

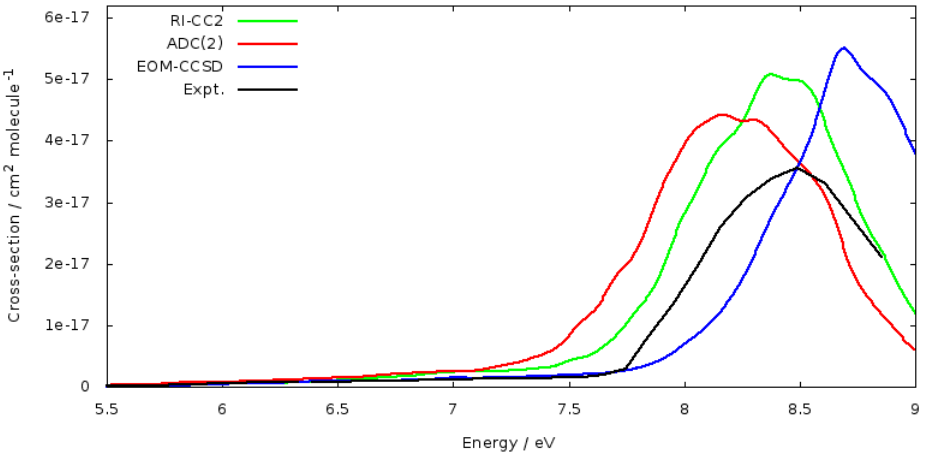

Figure A.21: SO_3 simulated spectra from EOM-CCSD, RI-CC2 and ADC(2) methods with aug-cc-pV(D+d)Z+3 basis set and the experimental spectrum from Burkholder *et. al* [18] (4.8-6.4 eV) and Hintz *et. al* [17] (6.4-8.9 eV) at 403 K.

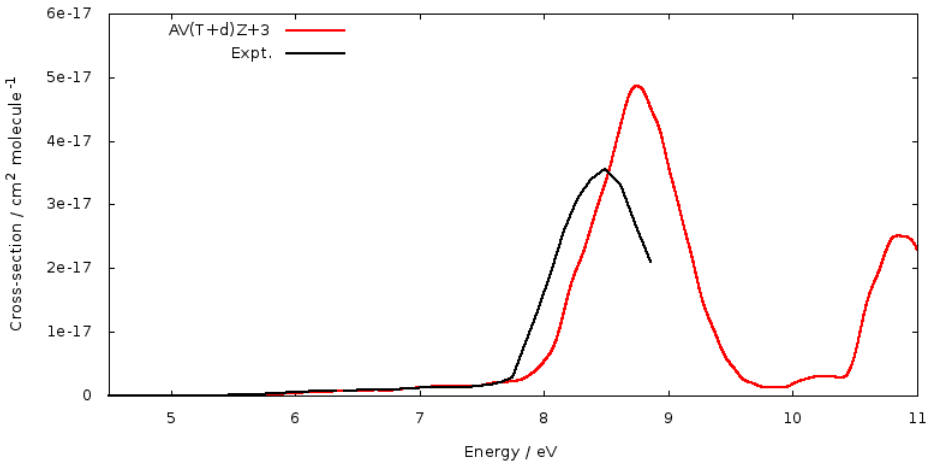

Figure A.22: EOM-CCSD/aug-cc-pV(T+d)Z+3 simulated spectra of SO_3 and the experimental spectrum from Burkholder *et. al* [18] (4.8-6.4 eV) and Hintz *et. al* [17] (6.4-8.9 eV) at 403 K.

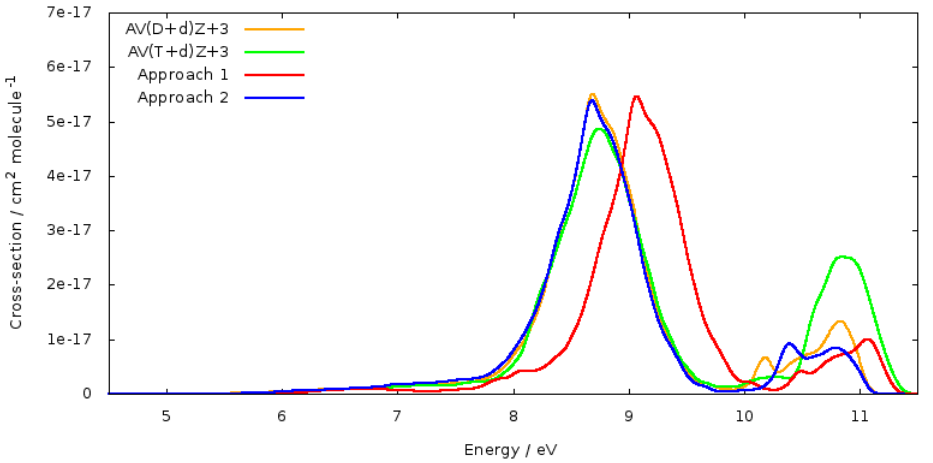

Figure A.23: Approximated EOM-CCSD/aug-cc-pV(T+d)Z+3 spectra of SO_3 from approaches 1 and 2 compared with EOM-CCSD calculated spectraum from aug-cc-pV(T+d)Z+3 and aug-cc-pV(D+d)Z+3.

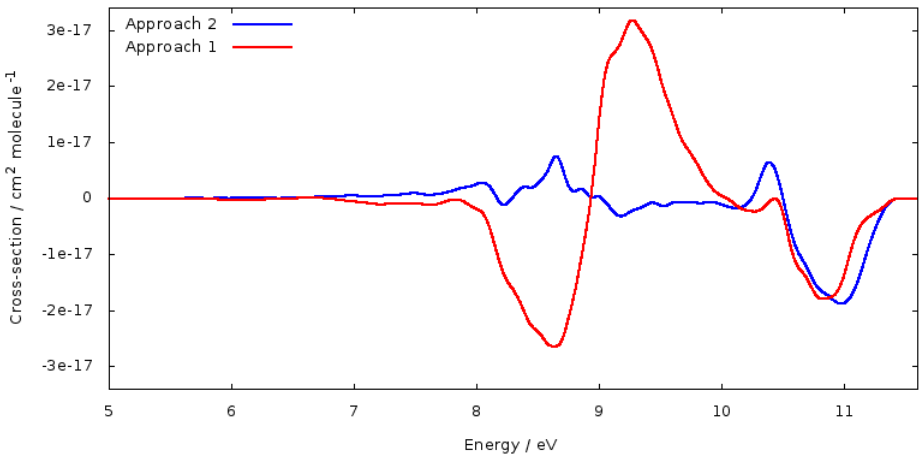

Figure A.24: Difference graphs from comparing SO_3 approach 1 and 2 spectra with calculated EOM-CCSD/aug-cc-pV(T+d)Z+3 spectrum.

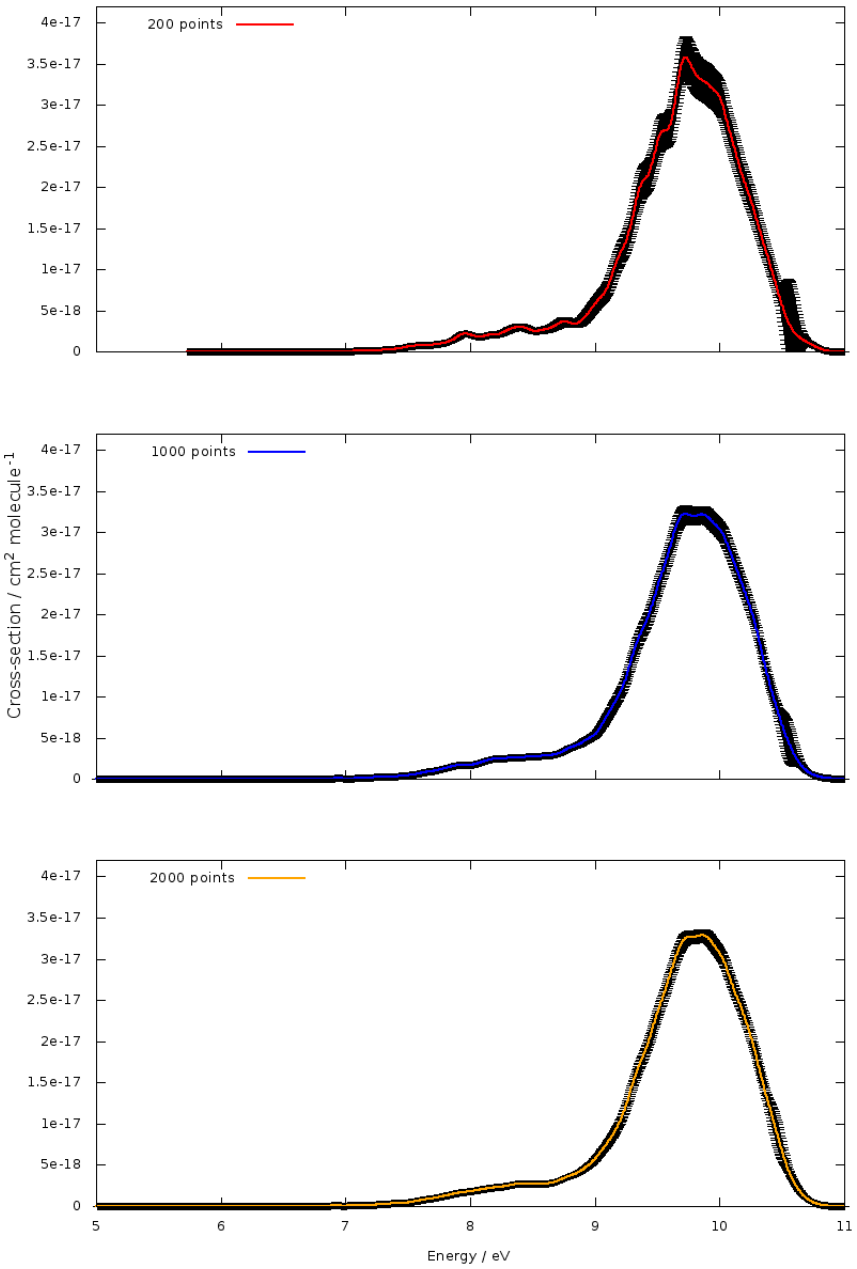

Figure A.25: EOM-CCSD/aug-cc-pV(D+d)Z+3 absorption spectra of C_2-H_2SO_4 and error bars for 200, 1000 and 2000 points.

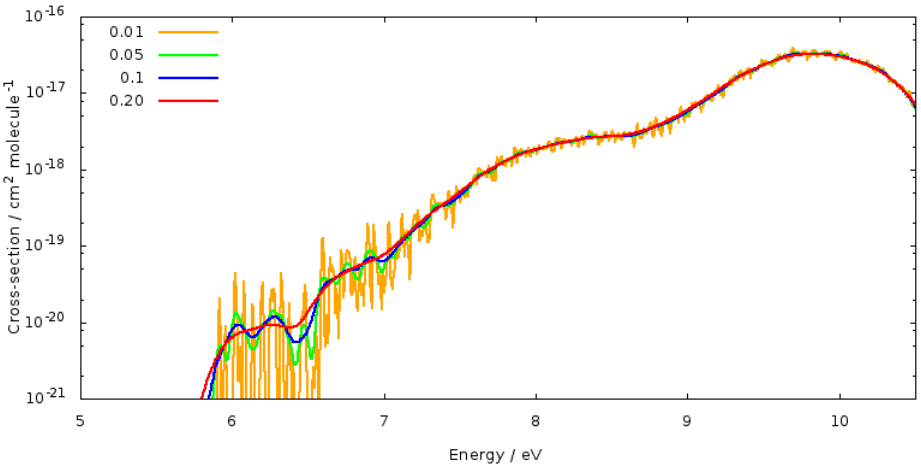

Figure A.26: C_2-H_2SO_4 absorption spectra from four phenomenological broadenings (eV) for 2000 points at EOM-CCSD/aug-cc-pV(D+d)Z+3 level of theory.

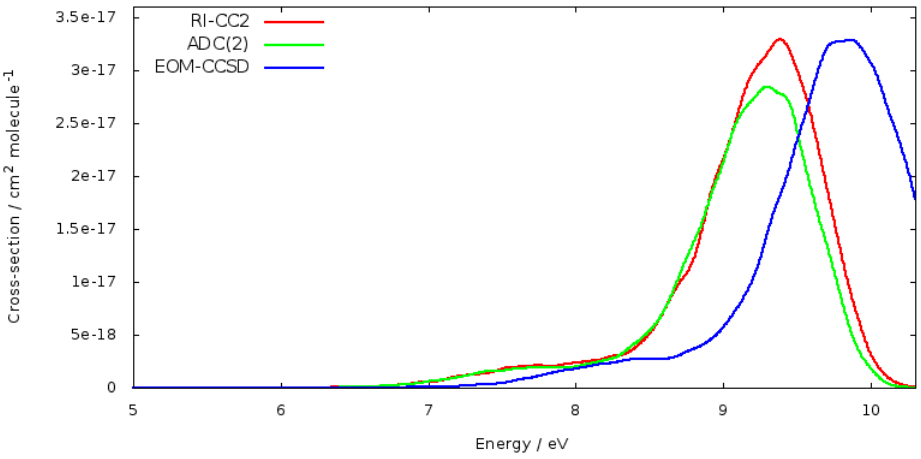

Figure A.27: C_2-H_2SO_4 simulated spectra from EOM-CCSD, RI-CC2 and ADC(2) methods with aug-cc-pV(D+d)Z+3 basis set and 2000 points.

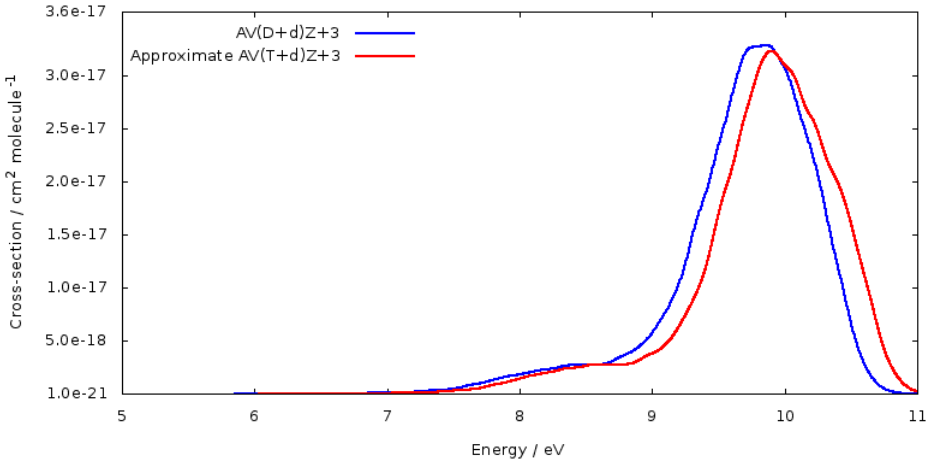

Figure A.28: Approximate EOM-CCSD/aug-cc-pV(T+d)Z+3 and calculated EOM-CCSD/aug-cc-pV(D+d)Z+3 spectra of C_2-H_2SO_4.

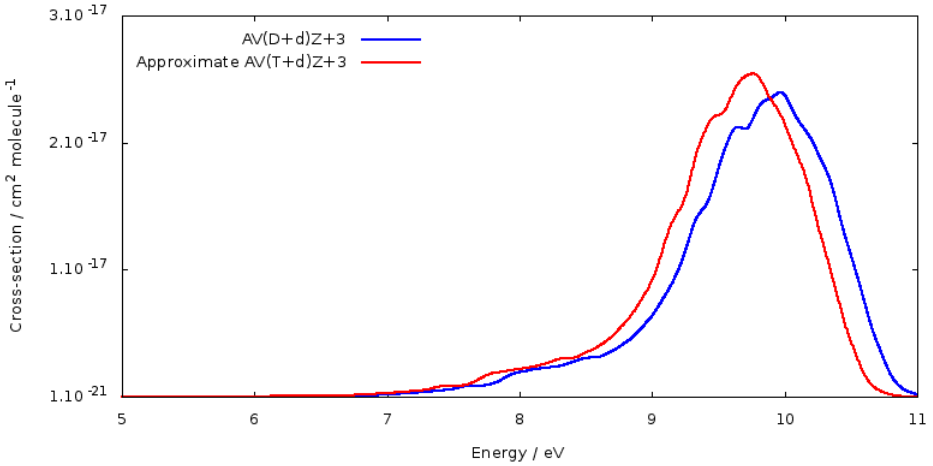

Figure A.29: Approximate EOM-CCSD/aug-cc-pV(T+d)Z+3 and calculated EOM-CCSD/aug-cc-pV(D+d)Z+3 spectra of C_s-H_2SO_4.

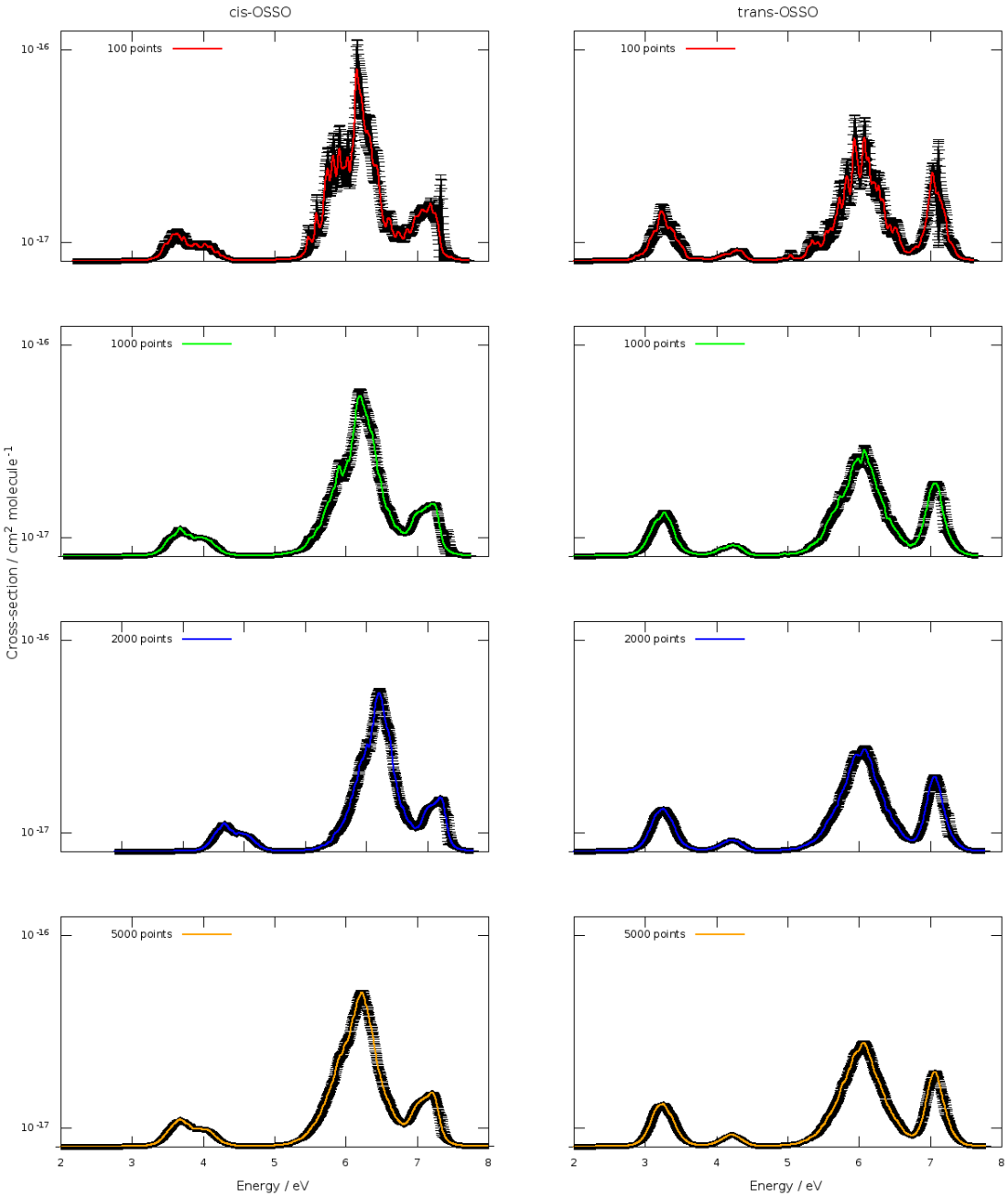

Figure A.30: EOM-CCSD/aug-cc-pV(D+d)Z+3 absorption spectra of *cis* and *trans*-OSSO and error bars for 100, 500, 1000 and 5000 points.

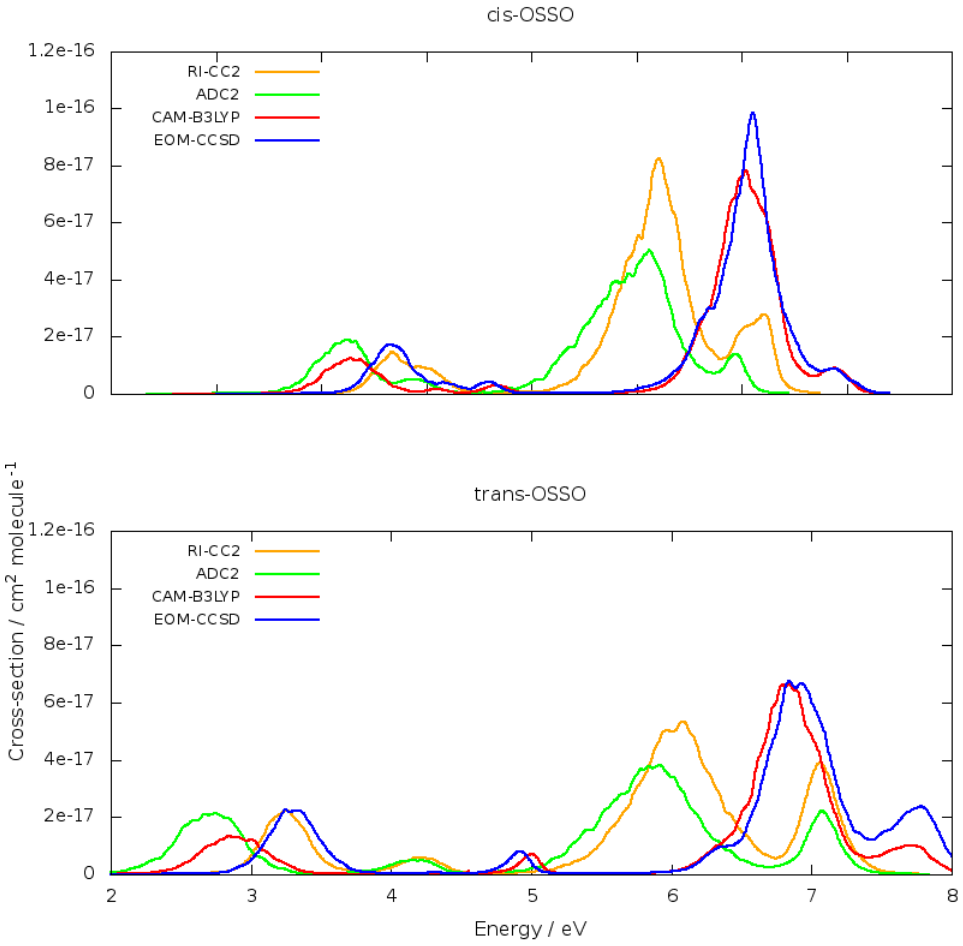

Figure A.31: Aug-cc-pV(D+d)Z+3 absorption spectra of *cis* and *trans*-OSSO with different *ab initio* methods.

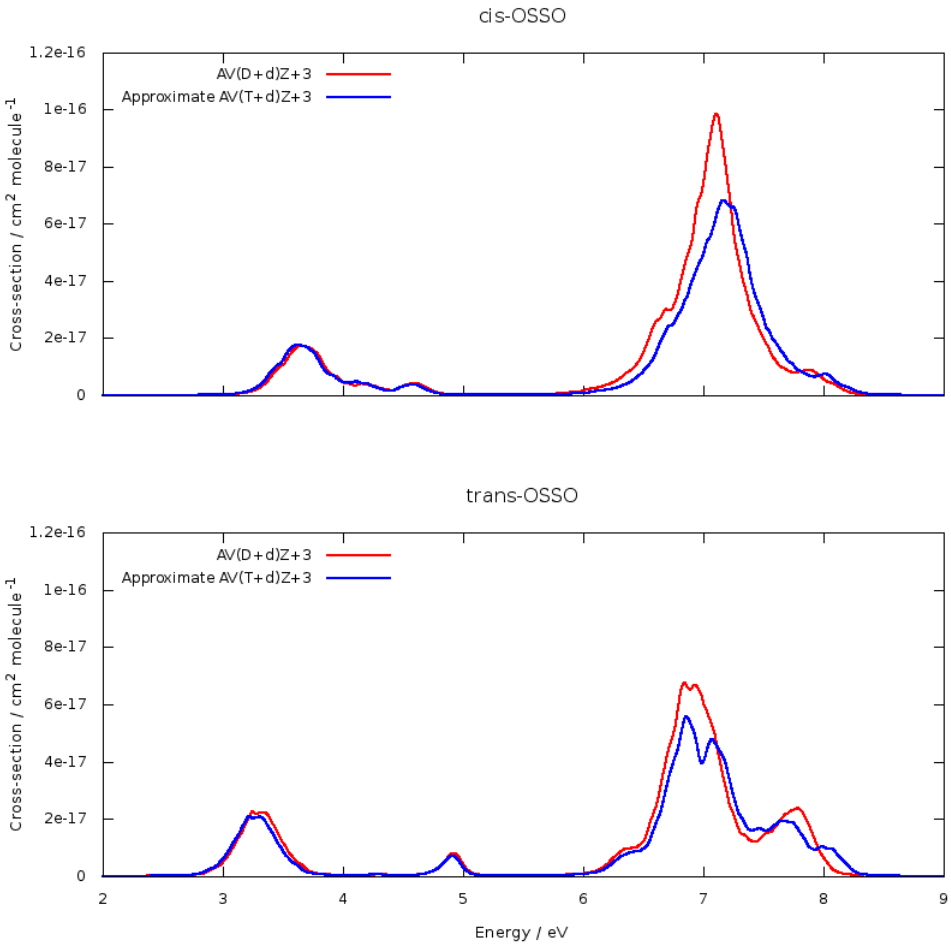

Figure A.32: The calculated EOM-CCSD/aug-cc-pV(D+d)Z+3 and approximate EOM-CCSD/aug-cc-pV(T+d)Z+3 absorption spectra of *cis* and *trans*-OSSO.

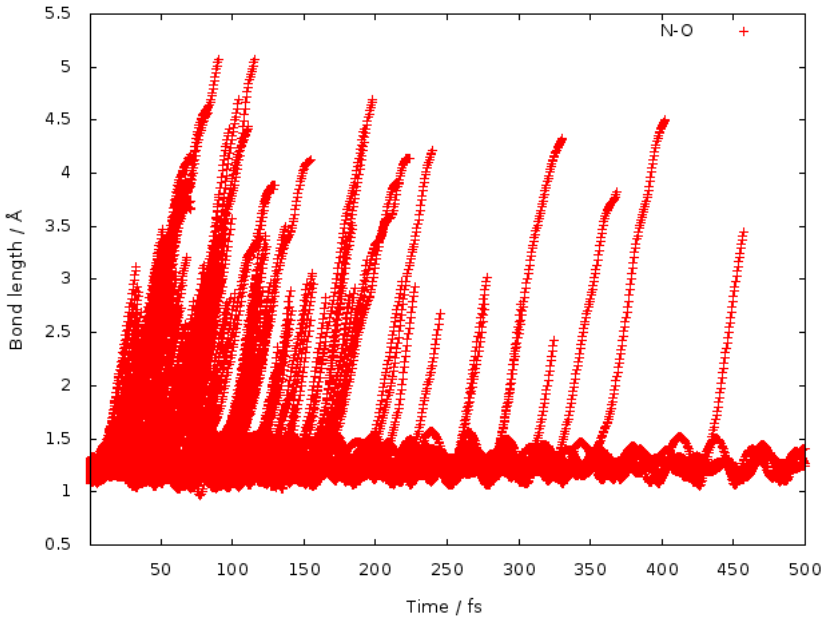

Figure A.33: Changes in N-O bond lengths over time from CAM-B3LYP/aug-cc-pVDZ N_2O photodissociation dynamics simulation.

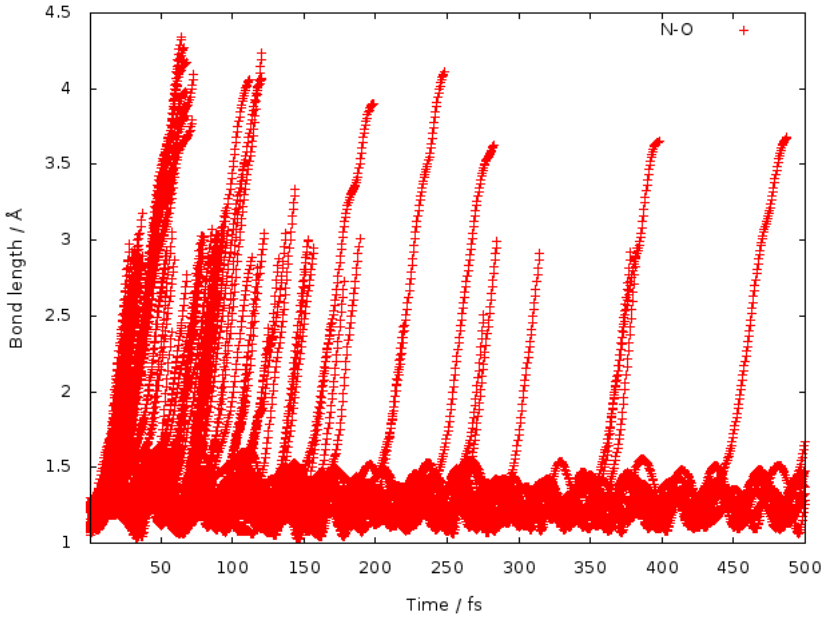

Figure A.34: Changes in N-O bond lengths over time from M06/aug-cc-pVDZ N_2O photodissociation dynamics simulation.

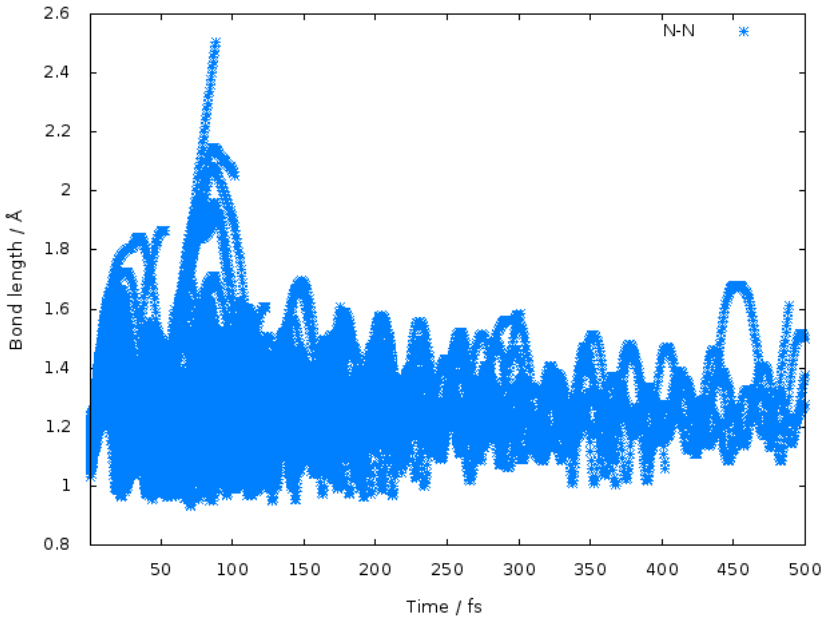

Figure A.35: Changes in N-N bond lengths over time from CAM-B3LYP/aug-cc-pVDZ N_2O photodissociation dynamics simulation.

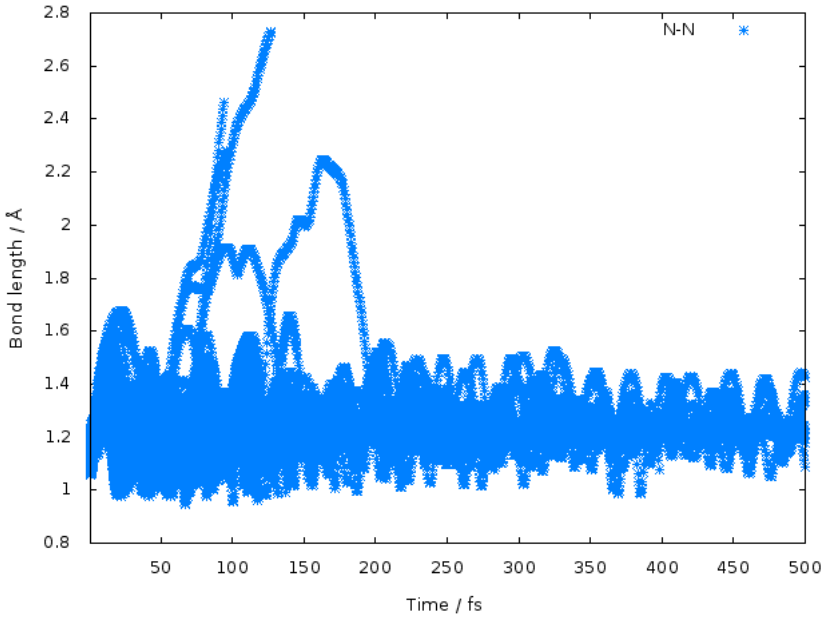

Figure A.36: Changes in N-N bond lengths over time from M06/aug-cc-pVDZ N_2O photodissociation dynamics simulation.

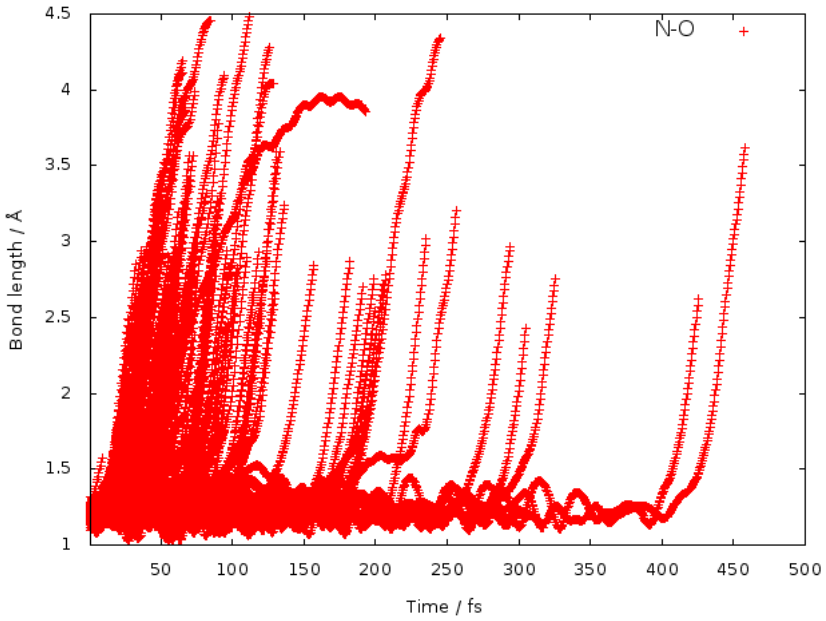

Figure A.37: Changes in N-O bond lengths over time from CAM-B3LYP/aug-cc-pVDZ H_2O-N_2O photodissociation dynamics simulation.

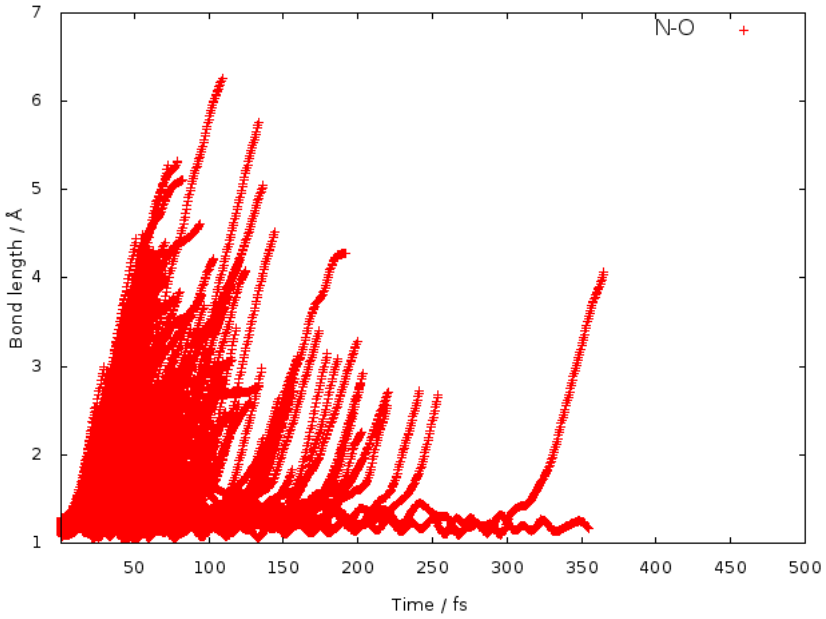

Figure A.38: Changes in N-O bond lengths over time from M06/aug-cc-pVDZ H_2O-N_2O photodissociation dynamics simulation.

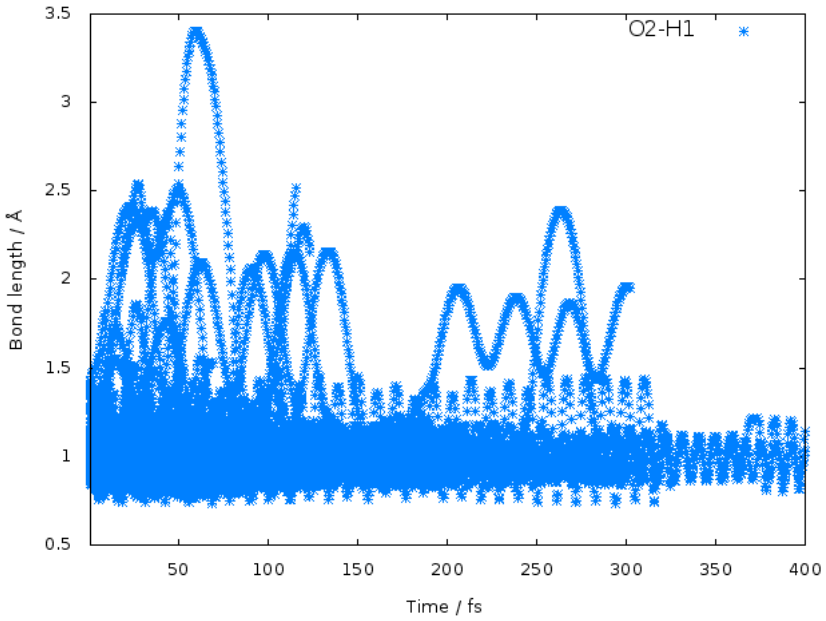

Figure A.39: Changes in O-H1 (bond in a closer distance to O in N_2O) bond lengths over time from CAM-B3LYP/aug-cc-pVDZ H_2O-N_2O photodissociation dynamics simulation.

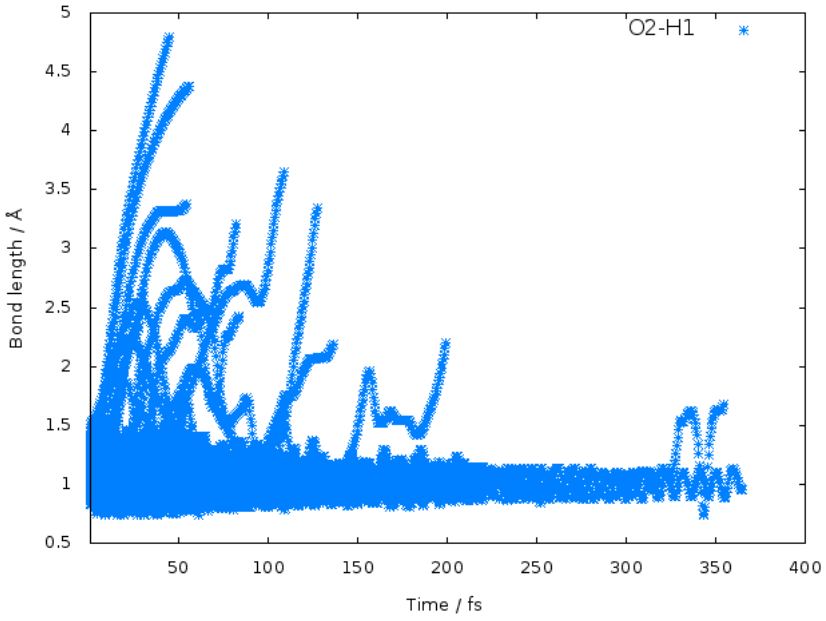

Figure A.40: Changes in O-H1 (bond in a closer distance to O in N_2O)bond lengths over time from M06/aug-cc-pVDZ H_2O-N_2O photodissociation dynamics simulation.

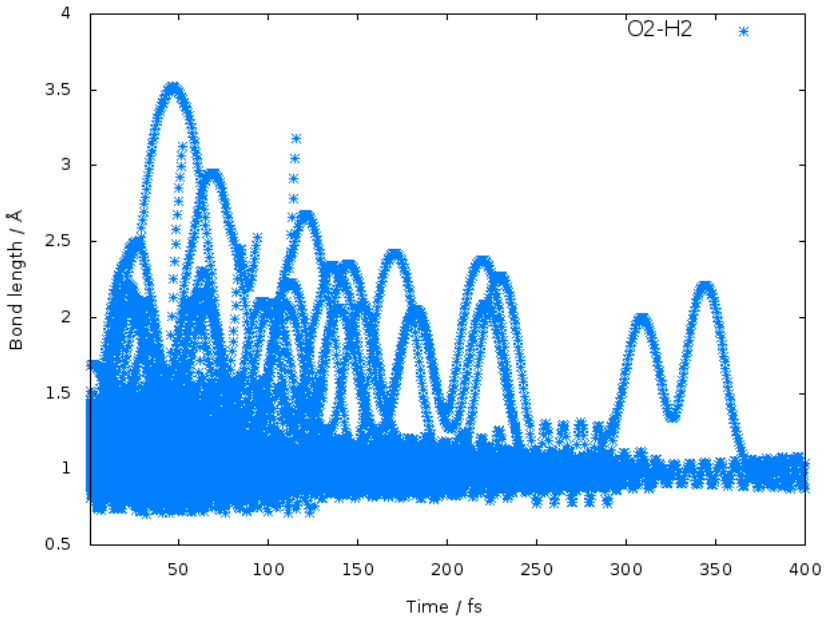

Figure A.41: Changes in O-H2 (bond in a further distance to O in N_2O) bond lengths over time from CAM-B3LYP/aug-cc-pVDZ H_2O-N_2O photodissociation dynamics simulation.

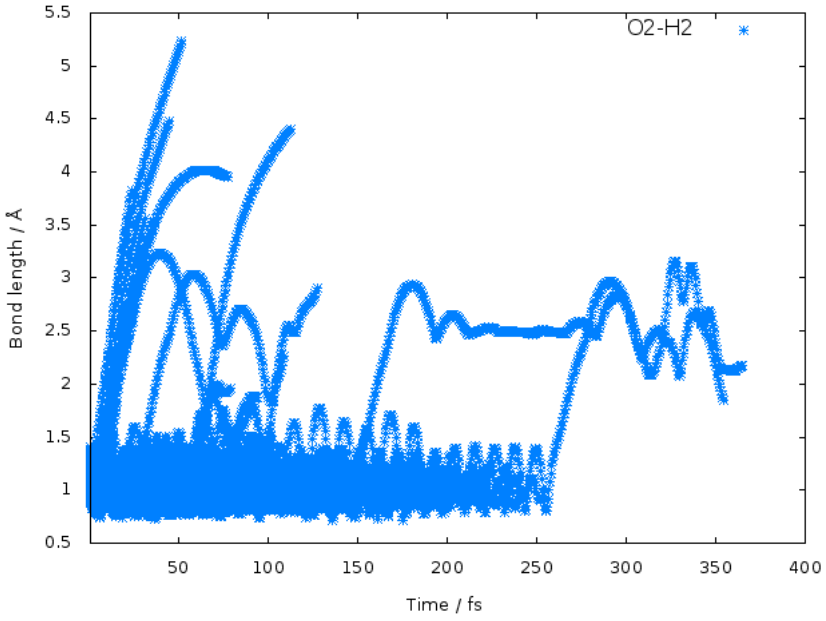

Figure A.42: Changes in O-H2 (bond in a further distance to O in N_2O) bond lengths over time from M06/aug-cc-pVDZ H_2O-N_2O photodissociation dynamics simulation.